

REPORT DOCUMENTATION PAGEForm Approved
OMB No. 0704-0188

Public reporting burden for this collection of information is estimated to average 1 hour per response, including the time for reviewing instructions, searching data sources, gathering and maintaining the data needed, and completing and reviewing the collection of information. Send comments regarding this burden estimate or any other aspect of this collection of information, including suggestions for reducing this burden to Washington Headquarters Service, Directorate for Information Operations and Reports, 1215 Jefferson Davis Highway, Suite 1204, Arlington, VA 22202-4302, and to the Office of Management and Budget, Paperwork Reduction Project (0704-0188) Washington, DC 20503.

PLEASE DO NOT RETURN YOUR FORM TO THE ABOVE ADDRESS.

1. REPORT DATE (DD-MM-YYYY) 06/27/2007		2. REPORT TYPE Final		3. DATES COVERED (From - To) 04/01/2004 to 09/30/2006	
4. TITLE AND SUBTITLE NMR System for a Type II Quantum Computer				5a. CONTRACT NUMBER	
				5b. GRANT NUMBER FA9550-04-1-0212	
				5c. PROGRAM ELEMENT NUMBER	
6. AUTHOR(S) Cory, David G.				5d. PROJECT NUMBER	
				5e. TASK NUMBER	
				5f. WORK UNIT NUMBER	
7. PERFORMING ORGANIZATION NAME(S) AND ADDRESS(ES) Massachusetts Institute of Technology 77 Massachusetts Avenue Cambridge, MA 02139-4307				8. PERFORMING ORGANIZATION REPORT NUMBER ISRN MIT--2007-6895936-F	
9. SPONSORING/MONITORING AGENCY NAME(S) AND ADDRESS(ES) Air Force Office of Scientific Research Arlington, VA 22203 8715 N Randolph St Arlington VA 22203 Dr John S. Grogan, NE				10. SPONSOR/MONITOR'S ACRONYM(S) AFOSR	
12. DISTRIBUTION AVAILABILITY STATEMENT Approved for public release; distribution is unlimited.					
13. SUPPLEMENTARY NOTES This final technical report was prepared with the support of the United States Air Force Office of Scientific Research award number FA9550-04-1-0212. However, any opinions, findings, conclusions, or recommendations expressed herein are those of the author(s) and do not necessarily reflect the view of the AFOSR.					
14. ABSTRACT This project was to use liquid state nuclear magnetic resonance (NMR) as a test-bed to explore the control of information for Type-II quantum computing (QC) and for quantum information processing approaches to quantum simulations. During the first stages of the project we demonstrated NMR based implementations of type-II QC algorithms including the diffusion equation and Burger's equation. These demonstrations relied on a spatial encoding of non-interacting quantum systems. One of the challenges of quantum simulations is the growth of errors during a lattice type calculation. We demonstrated that we could reduce the errors by introducing random operations that commute with the map. This improved the simulation fidelity but important errors still remained. We then attacked these errors directly by exploring both the transients in our implementation (which led to the largest errors) and a series of more robust optimal control pulses. Finally during this last period we focused on quantum simulations of exchange operations over lattices and demonstrated that quantum interference effects involving multiple paths between the exchanging qubits can lead to higher fidelity operations.					
15. SUBJECT TERMS nuclear magnetic resonance (NMR); quantum information processing (QIP); quantum computing (QC)					
16. SECURITY CLASSIFICATION OF:			17. LIMITATION OF ABSTRACT UU	18. NUMBER OF PAGES 399	19a. NAME OF RESPONSIBLE PERSON David G. Cory
a. REPORT U	b. ABSTRACT U	c. THIS PAGE U			19b. TELEPHONE NUMBER (Include area code) (617) 253-3806

AFRL-SR-AR-TR-07-0262

TABLE OF CONTENTS

Page Number of Report File

SF298	1
Table of Contents.....	2
Executive Summary.....	3-4
Final Report.....	5-13
Bibliography.....	14-15
Appendix.....	16
Zhiying (Debra) Chen Thesis.....	17-128
Karen (Ka Yan) Lee Thesis.....	129-189
Suddhasattwa Sinha Thesis.....	190-295
Michael Kevin Henry, Jr., Thesis.....	296-399

Executive Summary

This project was to use nuclear magnetic resonance (NMR) to investigate quantum information processing (QIP) that is nearer term than full quantum computing (QC). The two areas of most relevance are type-II quantum computing and quantum simulation. In early work we demonstrated type-II algorithms and quantified the errors associated with their implementations. Since these algorithms have rather limited quantum speedups only very large-scale implementations have potential for exceeding the capabilities of classical processors. Therefore we turned more of our attention to quantum simulations over the past couple of years. There are three new results to report here:

- the implementation of the quantum saw-tooth map,
- a cyclic manipulation of quantum entanglement that reveals the structure of errors,
- the theoretical study of path interference for state transfers.

The Quantum Saw-Tooth map is a quantized version of a classically chaotic map. This map was implemented on a 3-qubit NMR QIP and repeated cycles of the map were performed. We demonstrated that the expected quantum localization was observed when errors were sufficiently small and that otherwise the expected diffusive behavior was seen. We were also able to characterize the types of errors (coherent, incoherent and decoherent) that were responsible for the transition away from localized dynamics. This work has been reported in the peer-reviewed literature.

The cyclic manipulation of entanglement enables one to efficiently characterize incoherent errors without the need for fidelity decay experiments. Incoherence is important to identify in a QIP since the errors accumulate rapidly and there are relatively straightforward approaches to avoiding this. The challenges are that at short times incoherence looks like decoherence, and that in a time-reversal experiment (such as is required for fidelity decay studies) the influences of incoherence are not necessarily reversed. So fidelity decay often again associates the incoherent errors with decoherence. By exploring a cyclic process the map has an effective propagator of the identity matrix and so fidelity decay type measurements are possible without time-reversal and still the dynamics show partial recurrences. We have demonstrated this in a three-qubit system and reported this in a peer-reviewed publication.

The transfer of coherent information between two qubits is a fundamental building block of all QIP. In order to improve the fidelity of this operation we explore state transfers when there are multiple paths available. The presence of multiple paths permits quantum interference and can speedup the transfer (resulting in reduced errors). This work has not yet been reported and is described more fully below.

In conclusion over this project we have shown that useful quantum simulations can be explored via NMR/QIP and we are moving to systems where the Hilbert space size permits non-trivial computations. In separate work we have reported on entanglement of 11 spins and we are working on a processor that contains 15 spins. Although perfectly unitary operations on these processors can be simulated on classical computers, processes that include incoherence and

decoherence start to be too large for classical systems and are certainly more efficiently investigated on the NMR/QIP test-bed.

Cumulative List of Persons Involved in the Research Effort

Professor David G. Cory, Principal Investigator, Nuclear Science & Engineering
Dr. Timothy F. Havel, Principal Research Scientist, Nuclear Science & Engineering
Dr. Anatoly Dementyev, Postdoctoral Associate, Francis Bitter Magnet Laboratory
Ms. Zhiying (Debra) Chen, Graduate Student, Nuclear Science & Engineering
Mr. Michael Kevin Henry, Jr., Graduate Student, Nuclear Science & Engineering
Ms. Karen Ka Yan Lee, Graduate Student, Electrical Engineering & Computer Science
Mr. Siddhasattwa Sinha, Graduate Student, Physics
Mr. Conner Galloway, Undergraduate Student, Nuclear Science & Engineering

Theses derived from AFOSR support

Zhiying (Debra) Chen "Experimental Demonstration and Exploration of Quantum Lattice Gas Algorithm" February 2005. Please see Appendix pdf file pages 17-128.

Karen (KaYan) Lee "Investigations on Resource-Limited Quantum Control Through NMR Pulses" June 2006. Please see Appendix pdf file pages 129-189.

Siddhasattwa Sinha "Coherent Control of Dipolar Coupled Spins in Large Hilbert Spaces" April 2006. Please see Appendix pdf file pages 190-295.

Michael Kevin Henry, Jr., "Coherent Control in QIP" June 2007. Please see Appendix pdf file pages 296-399.

Chapter 1

Introduction

Recent research [1, 2, 3] has demonstrated that the computational advantages theoretically shown attainable through quantum information processing [4, 5] are realizable, at the most elementary level, in a variety of controllable physical systems. Attempts to identify and develop the most promising of these systems draw increasing interest to several practical issues associated with fundamentally quantum mechanical computation. Chief among these is the faithful transportation of non-classical information over a set distance, for example, as a quantum wire necessary for quantum teleportation [6] or as a quantum data bus between two distinct quantum devices. It is implicitly assumed that such devices be sufficiently distant as to remove the possibility of direct coupling, yet not so distant as to warrant the introduction of a potentially lossy interface to an optical fiber.

The simplest solution to meet this end is a series of concatenated SWAP gates spatially connecting the initial and final state locations. This is, though, far from ideal as the application of each gate, regardless of implementation, currently requires fine dynamical control over the chosen system which necessarily increases the potential for error and decoherence. More intricate solutions have been proposed utilizing photons in cavity QED [7] and phonons in ion traps [8] yet are not applicable to several quantum information processing implementations, such as optical lattices [9] and arrays of quantum dots [10], which inherently rely on collective phenomena to transport quantum states as opposed to the singular phonons and photons used as

individual information carriers in the proposed.

Another solution, considered here, is the use of specialized coupling geometries in unmodulated nuclear spin lattices. Initially investigated as a linear spin chain evolving under uniform nearest neighbor coupling [11], this paper seeks to investigate specific geometries utilizing designed, time-independent couplings as a potential realization of a robust quantum data bus.

In the most general case, a sample of N spin- $\frac{1}{2}$ particles evolves under the time-independent Hamiltonian

$$\hat{\mathcal{H}} = - \sum_{i,j} J_{ij} \vec{\sigma}^i \cdot \vec{\sigma}^j - \sum_{i=1}^N B_i \sigma_z^i. \quad (1.1)$$

$\vec{\sigma}^i = (\sigma_x^i, \sigma_y^i, \sigma_z^i)$ are the Pauli matrices for the i^{th} spin, $J_{ij} \geq 0$ is the coupling strength between spins i and j , and $B_i \geq 0$ is the magnitude of an external magnetic field at spin i . The coupling and magnetic field strengths are both required static in time for ease of implementation, yet are allowed arbitrary through the utilization of the fictitious spins and the “column method” of [12] as described in [13]. The Hamiltonian explicitly excludes the utilization of radio frequency pulses in a further attempt to reduce possible sources of error.

It is assumed that a sender, Alice, is able to attach a single spin in an arbitrary, unknown state parameterized by θ ,

$$|\psi_{in}\rangle = \cos \frac{\theta}{2} |\downarrow\rangle + e^{i\phi} \sin \frac{\theta}{2} |\uparrow\rangle. \quad (1.2)$$

to the s^{th} spin without error. Inputs involving multiple qubits, including entanglement, are considered later. Further assuming that all other lattice spins are initialized in the ground state $|\downarrow\rangle$, the state of the chain is described by the wave function

$$|\Psi(t)\rangle = \cos \frac{\theta}{2} |0\rangle + e^{i\phi} \sin \frac{\theta}{2} \sum_{j=1}^N \langle j | e^{-i\hat{\mathcal{H}}t/\hbar} |s\rangle |j\rangle \quad (1.3)$$

where the notation $|j\rangle$ is utilized to denote the state in which only the j^{th} spin is in

the state $|\uparrow\rangle$. $|0\rangle$ designates the lattice ground state.

While general, Eq. 1.3 does not directly reveal any useful information until a Hamiltonian is selected. Still, several useful quantities can be obtained, as shown in [11], before specifying further. If a receiver, Bob, is able to detach a spin from the r^{th} site without error at time t_0 , he will obtain the generally mixed state

$$|\psi_{out}(t)\rangle = \frac{1}{\sqrt{P(t)}} \left(\cos \frac{\theta}{2} |\downarrow\rangle + e^{i\phi} f_{s,r}^N(t) \sin \frac{\theta}{2} |\uparrow\rangle \right), \quad (1.4)$$

where $P(t) \equiv \cos^2(\frac{\theta}{2}) + \sin^2(\frac{\theta}{2}) |f_{r,s}^N(t)|^2$ and $f_{r,s}^N(t) \equiv \langle r | e^{-i\mathcal{H}t/\hbar} | s \rangle$, the transition amplitude of an excitation from the s^{th} site to the r^{th} site. From this, one can obtain the fidelity averaged over all possible input states

$$F = \frac{|f_{r,s}^N(t_0)| \cos \gamma}{3} + \frac{|f_{r,s}^N(t_0)|^2}{6} + \frac{1}{2} \quad (1.5)$$

which is maximized by choosing B_i such that $\gamma \equiv \arg(f_{r,s}^N(t_0))$ is a multiple of 2π . It is further shown that the entanglement between the s^{th} and r^{th} spins, as measured by concurrence [14], will be

$$\epsilon = |f_{r,s}^N(t_0)|. \quad (1.6)$$

Thus, for any nonzero $f_{r,s}^N(t_0)$, entanglement shared through the channel can be distilled into pure singlets, and used for teleportation [15, 16].

By specifying that Alice and Bob sit at opposite ends of a one dimensional spin chain of uniform coupling in a constant magnetic field, it has been shown [11] that for chains of $N \leq 80$ fidelity exceeds the upper bound of classical transmission [17] including several near perfect fidelities for chains with $N \leq 20$.

Consideration of coupling geometries extending to two and three spatial dimensions has yielded several important restrictions and constructions for classes of lattices geometries exhibiting perfect fidelity. Notable among these is a method for the construction of unity fidelity geometries as the Cartesian product of two geometries known to exhibit perfect fidelity [18]. The produced graph will display perfect trans-

fer at the least common multiple of the transfer times of its constructing graphs. In this way, one could conceivably construct a geometry for perfect swap over arbitrarily large distances in constant time, though with substantial overhead.

This paper seeks to investigate nuclear spin geometries which produce unity fidelity state transfer without dependence on any external manipulation. This investigation is pursued on a purely theoretical basis through simulation using a Hamiltonian reduced on the restriction that $[\mathcal{H}, \sigma_{tot}^z] = 0$, reducing dimensionality from 2^N to NC_ℓ . The result is identical to the graph adjacency matrix. These simulations produced a complete set of geometries with $N \leq 8$ known to display perfect fidelity with uniform coupling or with a single coupling variable. Several interesting cases are examined in detail. Further, a method for finding necessary and sufficient conditions for perfect fidelity in geometries with a fixed number of spins is found by use of the inverse Laplace transform. Finally, the problem of solving Eq. 1.3 generally is related to several problems of known difficulty, and the use of such lattices structures for transport of multiple qubits, including entanglement and the performance of arbitrary in-transit quantum logic operations, is examined.

Chapter 2

Small-Spin Simulations

Due to the difficulty of reducing the evolution operator for a general geometry and the usefulness of a robust data set for verification of results, simulations were performed using the reduced Hamiltonian to examine the evolution of a single input excitation in all coupling geometries with $N \leq 8$ and uniform coupling or a single coupling variable. Since $[\mathcal{H}, \sigma_{tot}^z] = 0$, simulation of the evolution of a single input excitation may be used as a direct measure of fidelity, simplifying simulations over what would be required to simulate a more general input state, Eq. 1.2.

All graphs found to exhibit perfect swap are replicated in Table 2.1. Except for special, denoted cases where fidelity is known to be exactly unity, fidelities were shown perfect to at least four decimal places. Where listed, all hitting times are relative to the time scale set the single link chain.

At first glance, one notices the frequency of simple ratios both in the required coupling ratios and the hitting times. Further, all satisfying graphs are mirror symmetric with regard to the input and output spins and are thus subject to the conditions set forth in [18]. As such, the entire lattice wave function must be periodic which is equivalent to the requirement that the ratios of the differences of the eigenvalues are rational.





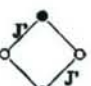
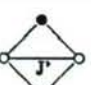



Coupling Geometry	Maximum Fidelity	Coupling Restrictions	Hitting Times
	1.0	$\forall J$	$\frac{\pi\pi}{4J}$
	0.9999	$J' = \frac{13}{4}J$	$\frac{\pi\pi}{3}$
	0.9999	$J' = \frac{35}{4}J$	$\pi\pi$
	1.0	$\forall J$	$\frac{\pi\pi}{4J}$
	0.9999	$J' = \frac{8}{3}J$	
	0.9999	$J' = 3J$	$\frac{\pi\pi}{4}$
	0.9999	$J' = 2J$	$\frac{\pi\pi}{4}$
	0.9999	$J' = 3J$	
	0.9999	$J' = 0.446162J$	2.71546
	0.9999	$J' = 2.24134J$	1.21153
	1.0	$\forall J$	$\frac{\pi\pi}{4J}$

Table 2.1: All coupling geometries generating perfect fidelity of $N \leq 8$ with one coupling variable. The input and output spins are marked as white circles with black circles as intermediary spins. All unlabeled couplings are of strength J .

Chapter 3

A Method for Finding a Necessary and Sufficient Condition for Perfect Fidelity for Given N

As stated, Eqs. 1.3, 1.4, and 1.5 are not particularly useful due to the difficulty in conveniently expressing $f_{r,s}^N(t_0)$ for a general Hamiltonian. However, it is possible to draw a necessary and sufficient condition for perfect swap from Eq. 1.5 when one makes use of the following identity:

$$\mathcal{L}[e^{At}] = (s\mathbf{1} - A)^{-1}. \quad (3.1)$$

As the input and output states of a lattice are predetermined, only one matrix element of the infinite expansion $e^{i\mathcal{H}t/\hbar}$ is of importance in determining fidelity. Because the Laplace transform, and likewise, the inverse Laplace transform are linear, their presence does not prevent access to the single important matrix element. In this way, the condition for perfect fidelity may evolve as follows:

$$\begin{aligned}
F = 1 &= \frac{|f_{r,s}^N(t)| \cos \gamma}{3} + \frac{|f_{r,s}^N(t)|^2}{6} + \frac{1}{2} \\
&= \frac{|\langle r | e^{-i\mathcal{H}t/\hbar} | s \rangle| \cos \gamma}{3} + \frac{|\langle r | e^{-i\mathcal{H}t/\hbar} | s \rangle|^2}{6} + \frac{1}{2} \\
&= \frac{|\langle r | \mathcal{L}^{-1} [(s\mathbb{1} - i\mathcal{H}/\hbar)^{-1}] | s \rangle| \cos \gamma}{3} + \frac{|\langle r | \mathcal{L}^{-1} [(s\mathbb{1} - i\mathcal{H}/\hbar)^{-1}] | s \rangle|^2}{6} + \frac{1}{2} \\
&= \frac{\mathcal{L}^{-1} [\langle r | (s\mathbb{1} - i\mathcal{H}/\hbar)^{-1} | s \rangle] \cos \gamma}{3} + \frac{\mathcal{L}^{-1} [\langle r | (s\mathbb{1} - i\mathcal{H}/\hbar)^{-1} | s \rangle]^2}{6} + \frac{1}{2}
\end{aligned} \tag{3.2}$$

The above may not seem like a significant improvement over the original expression due to the required matrix inversion. However, the selection of a dimensionality, N , will allow for the reduction of the inversion to a more general expression obtained through blockwise inversion. The application of the inverse Laplace transform will result in a final condition on the coupling Hamiltonian that is satisfied if and only if a geometry demonstrates perfect fidelity. Here we continue to find such an expression for all 3-spin systems.

Consider the most general 3-spin Hamiltonian

$$\begin{aligned}
\mathcal{H} &= \begin{bmatrix} 0 & a & b \\ a & 0 & c \\ b & c & 0 \end{bmatrix} \\
\Rightarrow s\mathbb{1} - i\mathcal{H}/\hbar &= \begin{bmatrix} s & -ia/\hbar & -ib/\hbar \\ -ia/\hbar & s & -ic/\hbar \\ -ib/\hbar & -ic/\hbar & s \end{bmatrix}
\end{aligned} \tag{3.3}$$

The inversion of a general 3×3 matrix is known to be

$$\begin{bmatrix} d & e & f \\ h & i & j \\ k & l & m \end{bmatrix}^{-1} = \frac{1}{ejk + fhl + dim - fik - djl - ehm} \begin{bmatrix} im - jl & fl - em & ej - fi \\ jk - hm & dm - fk & fh - dj \\ hl - ik & ek - dl & di - eh \end{bmatrix} \tag{3.4}$$

$$\Rightarrow (s1 - i\mathcal{H}/\hbar)^{-1} = \left(\frac{2iabc}{\hbar^3} + \frac{(a^2 + b^2 + c^2)s}{\hbar^2} + s^3 \right)^{-1} \begin{bmatrix} c^2/\hbar + s^2 & ias/\hbar - bc/\hbar & ibs/\hbar - ac/\hbar^2 \\ ias/\hbar - bc/\hbar^2 & s^2 + b^2/\hbar^2 & ics/\hbar - ab/\hbar^2 \\ ibs/\hbar - ac/\hbar^2 & ics/\hbar - ab/\hbar^2 & s^2 + a^2/\hbar \end{bmatrix} \quad (3.5)$$

If it is arbitrarily taken that a transfer is desired between the first and third spins, all matrix elements may be removed except for the corner off-diagonal element.

Bibliography

- [1] D. Cory, A. Fahmy, and T. Havel, "Ensemble quantum computing by nmr spectroscopy," *Proc. Natl. Acad. Sci.*, vol. 94, pp. 1634–1639, 1997.
- [2] I. Chuang, N. Gershenfeld, and M. Kubinec, "Experimental implementation of fast quantum searching," *Phys. Rev. Lett.*, vol. 80, Apr. 1998.
- [3] I. Chuang, M. Vandersypen, X. Zhou, D. Leung, and S. Lloyd, "Experimental realization of a quantum algorithm," *Nature*, vol. 393, no. 6681, pp. 143–146, 1998.
- [4] P. W. Shor, "Algorithms for quantum computation: Discrete logarithms and factoring," in *IEEE Symposium on Foundations of Computer Science*, pp. 124–134, 1994.
- [5] L. Grover, "A fast quantum mechanical algorithm for database search," ACM, 1996.
- [6] C. H. Bennett, G. Brassard, C. Crépeau, R. Jozsa, A. Peres, and W. K. Wootters, "Teleporting an unknown quantum state via dual classical and einstein-podolsky-rosen channels," *Phys. Rev. Lett.*, vol. 70, pp. 1895–1899, Mar 1993.
- [7] G. Guthöhrlein, M. Keller, K. Hayasaka, W. Lange, and H. Walther, "A single ion as a nanoscopic probe of an optical field," *Nature*, vol. 414, pp. 49–51, Nov 2001.
- [8] D. Leibfried, B. Demarco, V. Meyer, D. Lucas, M. Barrett, J. Britton, W. Itano, B. Jelenkovi, C. Langer, T. Rosenband, and D. Wineland *Nature*, vol. 442, no. 412, 2003.
- [9] O. Mandel, M. Greiner, A. Widera, T. Rom, T. W. Hänsch, and I. Bloch, "Controlled collisions for multi-particle entanglement of optically trapped atoms," *Nature*, vol. 425, pp. 937–940, Aug 2003.
- [10] D. Loss and D. P. DiVincenzo, "Quantum computation with quantum dots," *Phys. Rev. A*, vol. 57, pp. 120–126, Jan 1998.
- [11] S. Bose, "Quantum communication through an unmodulated spin chain," *Phys. Rev. Lett.*, vol. 91, p. 207901, Nov 2003.

- [12] A. M. Childs, R. Cleve, E. Deotto, E. Farhi, S. Gutmann, and D. A. Spielman, "Exponential algorithmic speedup by a quantum walk," in *STOC '03: Proceedings of the thirty-fifth annual ACM symposium on Theory of computing*, (New York, NY, USA), pp. 59–68, ACM Press, 2003.
- [13] M. Christandl, N. Datta, A. Ekert, and A. J. Landahl, "Perfect state transfer in quantum spin networks," *Physical Review Letters*, vol. 92, no. 18, p. 187902, 2004.
- [14] W. K. Wootters, "Entanglement of formation of an arbitrary state of two qubits," *Phys. Rev. Lett.*, vol. 80, pp. 2245–2248, Mar 1998.
- [15] C. H. Bennett, G. Brassard, S. Popescu, B. Schumacher, J. A. Smolin, and W. K. Wootters, "Purification of noisy entanglement and faithful teleportation via noisy channels," *Phys. Rev. Lett.*, vol. 76, pp. 722–725, Jan 1996.
- [16] M. Horodecki, P. Horodecki, and R. Horodecki, "Inseparable two spin- $\frac{1}{2}$ density matrices can be distilled to a singlet form," *Phys. Rev. Lett.*, vol. 78, pp. 574–577, Jan 1997.
- [17] M. Horodecki, P. Horodecki, and R. Horodecki, "General teleportation channel, singlet fraction, and quasidistillation," *Phys. Rev. A*, vol. 60, pp. 1888–1898, Sep 1999.
- [18] M. Christandl, N. Datta, T. C. Dorlas, A. Ekert, A. Kay, and A. J. Landahl, "Perfect transfer of arbitrary states in quantum spin networks," *Physical Review A (Atomic, Molecular, and Optical Physics)*, vol. 71, no. 3, p. 032312, 2005.

APPENDIX

Theses derived from AFOSR support (as referenced in Executive Summary)

Zhiying (Debra) Chen "Experimental Demonstration and Exploration of Quantum Lattice Gas Algorithm" February 2005. Appendix pdf file pages 17-128.

Karen (KaYan) Lee "Investigations on Resource-Limited Quantum Control Through NMR Pulses" June 2006. Appendix pdf file pages 129-189.

Suddhasattwa Sinha "Coherent Control of Dipolar Coupled Spins in Large Hilbert Spaces" April 2006. Appendix pdf file pages 190-295.

Michael Kevin Henry, Jr., "Coherent Control in QIP" June 2007. Appendix pdf file pages 296-399.

Experimental Demonstration and Exploration of Quantum Lattice Gas Algorithms

by

Zhiying Chen

Submitted to the Department of Nuclear Engineering
in partial fulfillment of the requirements for the degree of
Doctor of Philosophy in Nuclear Science and Engineering

at the

MASSACHUSETTS INSTITUTE OF TECHNOLOGY

February 2005

© Massachusetts Institute of Technology 2005. All rights reserved.

Author
Department of Nuclear Engineering
February, 2005

Certified by
David G. Cory
Professor
Thesis Supervisor

Read by
Terry Orlando
Professor
Thesis Reader

Accepted by
Jeffrey A. Coderre
Chairman, Department Committee on Graduate Students

Experimental Demonstration and Exploration of Quantum Lattice Gas Algorithms

by

Zhiying Chen

Submitted to the Department of Nuclear Engineering
on February, 2005, in partial fulfillment of the
requirements for the degree of
Doctor of Philosophy in Nuclear Science and Engineering

Abstract

Recently, it has been suggested that an array of small quantum information processors sharing classical information can be used to solve selected computational problems, referred to as a type-II quantum computer. The first concrete implementation demonstrated here solves the diffusion equation, and it provides a test example from which to probe the strengths and limitations of this new computation paradigm. The NMR experiment consists of encoding a mass density onto an array of 16 two-qubit quantum information processors and then following the computation through 7 time steps of the algorithm. The results show a good agreement with the analytic solution for diffusive dynamics.

From the numerical simulations of the NMR implementations, we explore two major error sources (1) the systematic error in the collision operator and (2) the linear approximation in the initialization. Since the mass density evolving under the Burgers equation develops sharp features over time, this is a stronger test of liquid state NMR implementations of type-II quantum computers than the previous example using the diffusion equation. Small systematic errors in the collision operator accumulate and swamp all other errors. We propose, and demonstrate, that the accumulation of this error can be avoided to a large extent by replacing the single collision operator with a set of operators, that have random errors and similar fidelities. Experiments have been implemented on 16 two-qubit sites for eight successive time steps for the Burgers equation. The improvement in the experimental results suggests that more complicated modulation of error terms may offer further improvement.

An alternative approach has been suggested to encode in the Fourier space (k -space) to remove the usage of this linear approximation. This new method also provides us a simple means to implement the streaming operation quantum mechanically by controlling magnetic field gradients sandwiched with RF pulses. Therefore, this method might serve as a new tool to probe the implementations of quantum lattice gas (QLG) algorithms. Experimental demonstration of the diffusion equation has been performed on 16 two-qubit sites for four successive time steps.

Recently, much attention has been focused on constructing many identical simple

processing elements arranged in a cellular automata architecture recently. It is likely that the early quantum hardware will be built in a similar manner. Quantum lattice gas algorithms therefore provide a bridge between such hardware and potential early algorithms. We propose a quantum lattice gas model similar to the one proposed by Margolus for the classical setting. This quantum algorithm simulates the one-particle quantum random walk. The preliminary experimental design associated with the lattice gas model on a ring molecule is presented. The searches for the suitable pulses to construct the unitary operators, used in the implementations of the lattice gas model, are done and the results are encouraging.

Thesis Supervisor: David G. Cory

Title: Professor

Acknowledgments

The first person that I would like to thank is my supervisor, David Cory, for his motivation, sound advice, guidance, firm encouragement and help. David's creative and fresh ideas have kept me busy. The fruitful experience working with him not only teaches my enormous scientific knowledge, but also the way to delivery the ideas and teamwork.

It is also my pleasure to thank Jeffrey Yezpe, a wonderful and talented collaborator. In addition to his scientific knowledge, his willingness to explain our work and discuss new ways to approach the problems has made my life more enjoyable. I am also proud to have worked with Carlos Perez. The work presented in these pages contains many of his insights and contributions.

I am also grateful to the talented and enthusiastic people that have made this lab a dynamic place. I enjoyed the long streak working with Marco Pravia, thinking, and discussing. I especially want to thank to Paola Cappellaro for her consideration and willingness to spend time to discuss and explore my ideas. Yun Liu deserves special thanks for his enormous knowledge on computers as well as his insights into many fields. I am also thankful to Nicolas Boulant (Garcon), Hyong-Joon Cho, and Chandrasekhar Ramanathan for helping in many ways with experimental and simulation work. Many thanks go to my colleagues and the entire, evolving lab over the years.

The experience at MIT represents a significant portion of my life. The friendships I made in those days were extremely important. I deeply appreciate that my friends spent their precious time to assist and guide me throughout the years.

I am most appreciate the constant love and support that my parents, Baoqiu and Zhongyu, and my sister Zhiqun have given me. Without their help, I would not have made it this far.

For my mother, farther, sister, and friends at MIT

Contents

1	Introduction	21
2	Type-II Quantum Lattice Gas Algorithm	25
2.1	Lattice Gas Method	25
2.2	The 1-D Diffusion Automaton	27
2.2.1	Microscopic Regime	27
2.2.2	Mesosopic Regime	27
2.2.3	Macroscopic Regime	29
2.2.4	Transition Matrix	31
2.3	Type-II Quantum Lattice Gas Algorithm	32
3	NMR Demonstration	37
3.1	Methodology for NMR Implementations	38
3.1.1	Spin System and Control	38
3.1.2	Lattice Initialization	41
3.1.3	Collision and Swap Gates	47
3.1.4	Measurement	49
3.1.5	Streaming	51
3.2	Experiment Demonstration	51
3.3	Conclusion	51
4	Systematic Error	55
4.1	The Burgers Equation	56

4.1.1	QLG Algorithm for the Burgers Equation	56
4.1.2	First Implementation using NMR	58
4.1.3	The Collision Matrix with Higher Viscosity Term	61
4.1.4	Numerical Simulations	63
4.1.5	The Collision Operator with Modulated Phases	66
4.2	Conclusion	68
4.3	Other Error Sources	70
4.4	Discussion	70
5	Linear Approximation	73
5.1	Mapping to k -space	74
5.2	NMR Implementation	75
5.2.1	Encoding	76
5.2.2	Collision	80
5.2.3	Measurement	82
5.2.4	Streaming	82
5.3	Conclusion and Discussion	84
6	Type-I Quantum Lattice Gas Algorithms	87
6.1	Quantum lattice gas algorithms	88
6.2	Chain Architectures	92
6.3	NMR Simulations	94
6.3.1	Spin System	94
6.3.2	Logic Gates	95
6.3.3	Methodology	97
A	Quantum Simulation using NMR	101

List of Figures

- 3-1 **Labeled chloroform** Labeled chloroform consists of two qubits, the hydrogen nucleus and labeled carbon served as qubits 1 and 2. States $|0\rangle$ and $|1\rangle$ are the ground state and excited state, respectively, induced by the Zeeman interaction with the applied magnetic field. Frequencies w_1 and w_2 , defined as multiplication of the gyro-magnetic ratio γ and the magnetic field B_0 , are the resonant frequencies to flip the spins. 38
- 3-2 **Liquid sample in the coils** The lattice initialization is demonstrated. The liquid sample is placed in the middle with the gradient coils on both ends and surrounded by the RF coils. Once the gradient field is turned on, the resonant frequencies across the sample will vary corresponding to the strength and duration of the gradient. Thus, the spin ensemble can be sliced into a lattice of small blocks. 40

3-3 **Quantum lattice gas algorithm for solving the 1-D diffusion equation.** The algorithm employs N two-qubit sites to encode the discretized mass density. Each site codes for a single value of the mass density using the quantum state of the two qubits. The encoded information is subjected to a series of local transformations that evolve the system. The collision operator C is the only entangling operation in the algorithm, and it creates quantum coherences limited to each two-qubit system. The streaming is executed by classical communication, and it moves the occupation numbers up and down the lattice as denoted by the arrows. The sectioned cylinder depicts the position of the sites in the NMR sample. Each site is physically realized as an addressable slice of isotropically-labeled chloroform solution. 42

3-4 **Equalizing magnetization** Since the ratio of γ_H to γ_C is a factor of four, the spectra of H and C following a $\frac{\pi}{2}$ pulse should reflect 4 : 1 ratio in the peak heights, shown in (a). In order to compensate the different magnetization, the equalization pulse sequence is applied and results in the spectrum (b). 44

3-5 **Pseudo-pure states** The results of pseudo-pure states of hydrogen and carbon are shown in (a) and (b), respectively. 45

3-6 NMR methodology for QLG algorithm. The NMR implementation consists of four main sections, each corresponding to the prescribed QLG algorithm step. The top two lines in the diagram correspond to RF pulses applied to the proton and carbon qubits, respectively. The third line shows the application of magnetic field gradients. In the encoding section, the initial carbon magnetization is recorded on the protons before being transferred to the carbons. The starting magnetization is specified by using a RF pulse shaped as the Fourier transform of the desired magnetization. The shaped pulses are applied in the presence of gradients so that each site can be addressed. A carbon decoupling sequence prevents the scalar coupling from interfering with the low power shaped pulses. The $\frac{\pi}{2}$ at the end of the encoding move the information from the x -axis to the z -axis, as required by the QLG algorithm. The collision operator follows the encoding, and it is implemented without gradients to ensure that all of the sites in the sample feel the same transformation. The results are observed in two experiments, each time using the more sensitive proton channel. A swap gate is added when measuring the carbon magnetization. Finally, the streaming operation is applied by shifting the frequencies of the carbon and proton shapes in opposite directions. 48

3-7 Pulse sequence for the collision operator The collision operator for the diffusion equation can be generated by applying $\frac{\pi}{2}$ pulses on both channels with delay time $\frac{1}{4J}$ in between. The same sequence can be used to generate the swap gate by increasing the delay time to $\frac{1}{2J}$. 50

- 3-8 **QLG algorithm experimental results.** The experimental mass densities are plotted in the figure, together with plots of the analytical solution and the numerical simulation of the NMR experiment. Seven steps of the algorithm were implemented on 16 two-qubit sites. The simulations were performed using the actual RF nutation rates and times of the experimental setup. The calculations closely match the data, suggesting that the deviation between the analytical results and the data can be attributed imperfections in the methodology. As a result, the simulations promise to be useful in exploring the errors from alternate methods. 52
- 4-1 **QLG algorithm for the Burgers equation implemented in four steps.** Three horizontal lines represent proton spin, carbon spin and field gradients. Both starting magnetizations are encoded in proton channel first due to the high signal to noise ratio while decoupled in carbon channel to prevent interfering of scalar coupling. The collision operator is applied after the initialization. Measurement are also taken in two steps in the proton channel followed by data processing in a personal computer. 61
- 4-2 **Experiment results comparing with simulation and analytical solutions.** The experimental data (dots) are plotted together with the simulations (grey dash lines) and the analytical solutions (black solid lines) for 15 time steps on a lattice of 16 cells. The horizontal axis for each plot indicates the number of the lattice cells and vertical axis is the flow velocity. The numbers associated with each plot are the time steps. The deviation between the simulation and analytical solutions is mainly due to the accumulative errors in the collision operator. We also observed the deviation between the experimental data and simulation results, possibly introduced by inhomogeneity, self-diffusion. 62

- 4-3 **Experimental data** The experimental data (dots) are plotted, together with plots of the analytical solutions (solid lines) and the numerical simulations (dash lines) of the NMR experiment. Nine time steps (numbers) of the algorithm have been carried out on 16 two-qubit sites. The vertical axis is associated with flow speed and the horizontal axis presents the lattice sites. The simulations closely match the data, suggesting that the deviation between the analytical results and the data can be attributed to four imperfection controls, discussed below, in the implementations. 64
- 4-4 **Relative strength of four types of errors** We present the relative strength of each source here. Horizontal axis is denoted by time steps and vertical axis shows the difference between the simulation results with the analytical solutions. We notice that the deviation is mainly caused by the linear approximation at the beginning and the accumulated errors in the collision operators take over after a few time steps. 65
- 4-5 **Systematic errors** The growth of the systematic errors due to the collision operator in two NMR implementation. The single collision operator data (dots) is fit (solid line) with a line of slope 1, which shows linear growth of the error. The collision operator data with modulated phases (pluses) is the fit with a line of slope 3/4 (dashed line). The buildup of the systematic errors has been slowed down by proposed method. However, the systematic errors have not been totally converted into random errors. 67
- 4-6 **Experiment data versus analytical results** The experimental data are plotted together with the analytical solutions for 8 time steps on a lattice of 16 parallel two-qubit QIPs. Viscosity: $\frac{1}{4} \frac{\Delta x^2}{\Delta t}$. Experimental NMR data (dots) versus analytical solution (curves). Randomizing the error terms in the collision operator has improved the experimental results dramatically. 69

5-1	One step in the initialization One period of the sequence used in the initialization and corresponding changes of k values in the k -space are presented. The solid line, in the k space diagram, illustrates the shift of the wave number for the hydrogen spin while the time iterates forwards. The dash line gives the movement of k value for the carbon. At the end of the sequence, the wave numbers of the characteristic Fourier components of both spins are incremented by the same amount. Below the plot, the pulse sequence is demonstrated.	81
5-2	Readout Measurement on the hydrogen spin is illustrated here. The magnetization peaks are related to the occupation numbers at each lattice site by $n_i = \frac{1}{2}(1 + \sigma_z^i)$. The observed spectrum is imposed by a sinc function.	83
5-3	k-space experimental data versus analytical solutions The experimental data (dots) are plotted together with analytical solutions (solid lines) for four time steps on 16 two-qubit sites.	85
6-1	Collision rules for 1D QLG algorithm The collisions of the simplest one dimensional QLG algorithm. A single particle of mass $\tan \theta$ at a site has an amplitude to be scattered $i \sin \theta$	89
6-2	Partitioned cellular automata Each square represents a cell, and each oval is a unitary operator acting on two lattice cells. On odd/even steps the pairing is exchanged.	91
6-3	Spin chain architectures One-dimensional array of quantum units ($ABCABC \dots$), such as nuclear spins in a polymer, is depicted here. A series of spins ABC can be treated as a quantum information processor. Sequence of resonant pulses allow one to load information and unload results at the end of an array. Each processor has the same circuit and they can process information and exchange it with the nearest neighbors.	93

6-4	The ring model	This model shows a chain of 6 qubits. Two loading qubits are presented by X and Y respectively. All the qubits with the same labels share the same resonant frequencies.	94
6-5	The two-qubit SWAP gate	Here demonstrates the pulse sequence of the SWAP gate on two qubits and untouched the third spin. To refocus the scalar interactions between pair AC and BC , a π pulse has been performed on pair AB and separate the delay period to half. Two π pulses are performed on qubit C in the a quarter and three quarter of the delay respectively.	97
6-6	One step QLG algorithm	The NMR implementation consists of three main section, each corresponding to the prescribed QCA step. The horizontal lines in the diagram correspond to RF pluses applied to each qubit respectively. In the encoding section, the initial magnetization is recorded on loading qubits before transferred to the other qubits. The unitary operator on pair AB and swap gate between BC follow the encoding. In the next step, the unitary operator on pair CA are applied, followed by swap gate between BC again.	99
A-1	Quantum simulation scheme	Correspondence between the simulated and physical system. The initial state s evolves to $s(T)$ under the propagator U . This process is related to the evolution of state p in the physical system by an invertible map ϕ	102
A-2	Truncated quantum harmonic oscillator	NMR signals demonstrate a quantum simulation of truncated harmonic oscillator. The solid lines are fits to theoretical expectations. Evolution of the different initial states are shown: (a) evolution of $ 0\rangle$ with no oscillation (b) evolution of $ 0\rangle + i 2\rangle$, showing 2Ω oscillations (c) evolution of $ 0\rangle + 1\rangle + 2\rangle + 3\rangle$, showing Ω oscillation and (d) 3Ω oscillations. . .	103
A-3	Demonstration of system and environment	Basic model for the system, local quantum and classical environment.	104

A-4	Decay rate Simulation showing the dependence of the decay rate on the kick rate, and the onset of the decoupling limit. Beyond 900 <i>kicks/ms</i> the decay rate decreases.	105
-----	---	-----

List of Tables

6.1	Summary of the relevant characteristics for the set of transformations required for the implementation of QCA. The three columns list the pulse duration (in μs), maximum power (in kHz), and the fidelity of simulated pulse.	96
6.2	Summary of the gates fidelities. The two columns list the unitary operators, and the gate fidelity of them	98

Chapter 1

Introduction

In 1965 Intel co-founder Gordon Moore noted that the processing power (number of transistors and speed) of computer chips was almost doubling every 18 months. This trend has continued roughly since the first computer in 1946. Such an exponential and rapid acceleration in computing ability is impressive. However, the basic technologies that have enabled Moore's Law are reaching fundamental physical limits. The miniaturization of processor components, which has taken transistor sizes from one centimeter in 1965 to 0.1 microns today. If Moore's law continues unabated, then each transistor is predicted to be as small as a hydrogen atom by about 2030. At that size, the quantum nature of electrons in the atoms becomes significant. Current technologies cannot possibly continue miniaturization beyond the scale of atoms, and errors will be generated in the computation. However, it is possible to exploit the quantum physics as a new way to do computation. This new way opens up fantastic new computational power based on the superpositions of quantum states.

The field of quantum information processing (QIP) has made steady progress in the past decade, driven in part by the realization that some quantum algorithms offer a computational advantage over the best-known classical counterparts [1]. Integer factorization of large numbers is believed to be practically impossible with an ordinary computer. By comparison, a quantum computer could solve this problem very quickly [2]. This ability would allow a quantum computer to break many of the cryptographic systems in use today. It comes with no surprise that quantum computers could also

be useful for running simulations of many-body quantum systems [3, 4, 5, 6, 7]. In theory, these problems can be easily emulated with a well controlled quantum system. To reach a practical improvement, quantum algorithms require precise control in a large Hilbert space, making physical implementations difficult.

Recently, much attention has been focused on lattice gas algorithms as candidate quantum algorithms. Quantum lattice gas algorithms are the generalizations of classical lattice gas algorithms, which are implemented on a lattice of many identical simple units associated with homogeneous update rules to all the lattice sites. Such an architecture offers the experimental simplification that the early quantum hardware is likely to build in a similar manner.

Two types of quantum lattice gas algorithms are defined according to the quantum computing architectures: type-I and type-II quantum information processors. In a type-I design [8, 9, 10], the lattice points are presented by either the states of the quantum system or quantum qubits. The system wave function must remain coherent for the duration of the quantum gate sequence needed to implement a particular algorithm. An algorithm of type-I quantum lattice gas models unfolds the quantum operator into an ordered sequence of basic two-qubit quantum operations. Type-II [11] is essentially an array of small quantum information processors interconnected by classical communication channels. Quantum coherence only exist inside each processor for a short period. This particular architecture significantly simplifies the quantum controls by using magnetic resonance imaging (MRI) techniques. It may also increase the range of problems that small quantum processors can tackle and thus serve as an intermediate architecture between few-qubit and large scale quantum computers.

In the present thesis, I aim to provide a reader who is unfamiliar with the field of lattice gases and quantum lattice gases with an introduction to the lattice Boltzmann methods and recently progress in the quantum lattice gas algorithms. This thesis is divided into a comprehensive introduction which gives a detailed overview of lattice Boltzmann methods, followed by sections on the methodologies used to implement type-II quantum lattice gas algorithms using NMR. The approaches for improving the control and reducing errors during the experiments will be discussed in depth

in Chapter 4 and 5. In the last chapter, a brief introduction of type-I lattice gas algorithms is given and a preliminary experimental design using nuclear magnetic resonance (NMR) is presented.

Chapter 2

Type-II Quantum Lattice Gas Algorithm

2.1 Lattice Gas Method

The lattice gas method is a tool of computational physics used to model complex hydro-dynamical flows that are too large for a standard low-level molecular dynamics treatment. This method contains discontinuous inter-facial boundaries that prevent a high-level partial differential equation description [12, 13, 14, 15]. The basic idea underlying the lattice gas method is to statistically represent a macroscopic scale time-dependent field quantities by “averaging” repeated artificial microscopic particles scattering and propagating throughout a lattice of interconnected sites. Many particles are distributed over the lattice sites. These particles may coexist at each site at a given time, and each particle carries a unit mass and a unit momentum of energy. They interact on site by an artificial collision rule which is locally invariant under the point-group symmetries of the lattice, and, furthermore, which exactly conserves the total mass, momentum, and energy at that site. The movement of particles along the lattice is prescribed by a streaming operation that shifts particles to the nearest neighboring sites, thus endowing the particles with the property of momentum. In a

¹This section was extracted from M. A. Pravia, Z. Chen, J. Yepez, D. G. Cory, “Experimental Demonstration of Quantum Lattice Gas Computation,” QIP, 2002.

maximally discrete way, the algorithm encapsulates the microscopic scale kinematics of the particles scattering on site and moving along the lattice. The mean-free path length between collisions is about one lattice cell size, and the mean-free time between collision elapses after a single update. This is computationally simple in comparison to molecular dynamics where many thousands of updates are required to capture such particle interactions.

The mesoscopic evolution is obtained by taking the ensemble average over many steps in microscopic realization. At the mesoscopic scale, the average presence of each particle type is defined by a real-valued occupation probability. In addition, the microscopic collision and streaming rules translate into the language of kinetic theory. The behavior of the system is described by a transport equation for the occupation probabilities, and this equation is a discrete Boltzmann equation called the *lattice Boltzmann equation*.

The lattice Boltzmann equation further translates into a macroscopic, continuous, effective field theory by letting the cell size approach zero (the limit of infinite lattice resolution called the *continuum limit*). At the macroscopic scale, partial differential equations describe the evolution of the field, admitting solutions such as propagating sound wave modes and diffusive modes. The passage of the Boltzmann equation to the effective field theory begins by expanding the occupation probabilities, which have a well-defined statistical functional form in terms of the continuous macroscopic variables, such as the mass density ρ (and the velocity or energy field if they are defined in the model). This expansion usually is carried out perturbatively in a small parameter such as the Knudsen number (ratio of mean-free path to the largest characteristic length scale) or the Mach number (ratio of the sound speed to the largest characteristic flow speed) in a fashion analogous to the Chapman-Enskog expansion of kinetic theory. Conversely, the macroscopic field quantities can also be expressed as a function of the mesoscopic occupation probabilities for example, the mass density at some point is a sum over the occupation probabilities in that vicinity.

2.2 The 1-D Diffusion Automaton

2.2.1 Microscopic Regime

We here consider a one-dimensional system [16, 17] in which particles may travel upwards or downwards to the nearest sites with some probabilities. Usually, a random walk is simulated by selecting one particle in the system and transporting it at random upwards or downwards, provided that the destination site is empty. At each site z of the lattice, we define two Boolean variables $n_1(z, t)$ and $n_2(z, t)$. These quantities are occupation numbers indicating whether or not a particle is entering site z at time t in direction e_1 (up) and e_2 (down), respectively.

In the microscopic regime, random motion is obtained by shuffling the two directions of motion indecently at each lattice site and at each time step. In other words, what is traveling in direction e_1 will be exchanged with what is traveling in direction e_2 with a probability $1 - \mu(z, t)$. The micro-dynamics has two phases: collision and propagation to the nearest neighbor. A particle entering site $z + \Delta z$ at time $t + \Delta t$ with velocity pointing upwards must have been at site z at t . With a probability $\mu(z, t)$, this particle was the one with a velocity pointing upwards and with probability $1 - \mu(z, t)$ the one which had a velocity pointing downwards. Therefore, the random walk rule obeys

$$\begin{aligned} n_1(z + \Delta z, t + \Delta t) &= \mu(z, t)n_1(z, t) + (1 - \mu(z, t))n_2(z, t) \\ n_2(z - \Delta z, t + \Delta t) &= (1 - \mu(z, t))n_1(z, t) + \mu(z, t)n_2(z, t). \end{aligned} \quad (2.1)$$

The time step is denoted by Δt , while the lattice spacing is given by Δz .

2.2.2 Mesoscopic Regime

At a mesoscopic scale, the variables n_i no longer appear as Boolean quantities but rather as an ensemble average of all the Boolean quantities (varying continuously between 0 and 1). Indeed, a mesoscopic point of coordinate z designates a microscopic volume comprising many particles. Formally, this averaging $f_i(z, t) = \langle n_i(z, t) \rangle$ is

treated as an ensemble average in the sense of statistical mechanics. Since $\mu(z, t)$ is statistically independent of $n_i(z, t)$, the average of $\langle \mu n_i \rangle$ yields

$$\langle \mu(z, t) n_i(z, t) \rangle = \langle \mu(z, t) \rangle \langle n_i(z, t) \rangle = p f_i(z, t). \quad (2.2)$$

The variables $f_1(z, t)$ and $f_2(z, t)$ are the occupation probabilities for finding upward- and downward-moving particles, respectively, at the site location z and time t . Therefore, relations in Eq. 2.1 can be averaged and yield

$$\begin{aligned} f_1(z + \Delta z, t + \Delta t) &= p f_1(z, t) + (1 - p) f_2(z, t) \\ f_2(z - \Delta z, t + \Delta t) &= (1 - p) f_1(z, t) + p f_2(z, t). \end{aligned} \quad (2.3)$$

In this case, the interesting quantity of the lattice gas is the mass density field, ρ , defines as the sum of upward- and downward-moving particles

$$\rho(z, t) = \sum_{i=1}^2 f_i(z, t). \quad (2.4)$$

We can arrange Eq. 2.3 as following:

$$\begin{aligned} f_1(z + \Delta z, t + \Delta t) - f_1(z, t) &= (p - 1) [f_1(z, t) - f_2(z, t)] \\ f_2(z - \Delta z, t + \Delta t) - f_2(z, t) &= (p - 1) [f_2(z, t) - f_1(z, t)] \end{aligned} \quad (2.5)$$

By summing these two equations, we obtain

$$f_1(z + \Delta z, t + \Delta t) + f_2(z - \Delta z, t + \Delta t) - \rho(z, t) = 0. \quad (2.6)$$

This equation reflects the conservation of mass: the number of particles entering site z at time t are exiting at time $t + \Delta t$. For this reason, Eq. 2.6 is called the *continuity* equation.

The lattice gas described above is summarized by the Boltzmann equation

$$f_{1,2}(z \pm \Delta z, t + \Delta t) = f_{1,2}(z, t) + \Omega_{1,2}(z, t), \quad (2.7)$$

where the left-hand side denotes the occupation of the lattice as a function of the previous lattice configuration and where the collision terms are

$$\Omega_{1,2} = \pm(p-1)[f_1 - f_2] \quad (2.8)$$

The collision terms define different numerical problem that we desired to solve. It changes the direction of some particles, thus it is responsible for the diffusive behavior.

2.2.3 Macroscopic Regime

The Chapman-Enskog expansion technique is commonly used in statistical mechanics to derive the macroscopic laws governing the relevant physical quantities. The idea of the Chapman-Enskog expansion is the following: it is assumed that the actual occupation numbers f_i are close to the equilibrium population $f_i^{(0)}$. The occupation number can be expanded in terms of a small parameter ϵ :

$$f_i = f_i^{(0)} + \epsilon f_i^{(1)} + \epsilon^2 f_i^{(2)} + O(\epsilon^3), \quad (2.9)$$

where the $f_i^{(l)}$ s are functions of z and t to be determined.

The next step is to take a Taylor expansion of the left-hand side of Eq. 2.5. One has

$$f_i(z + \Delta z c_i, t + \Delta t) - f_i(z, t) = \left[\Delta t \partial_t + \frac{\Delta t^2}{2} \partial_t^2 + \Delta z c_i \partial_z + \frac{\Delta z^2}{2} c_i^2 \partial_z^2 + \Delta t \Delta z c_i \partial_t \partial_z \right] f_i(z, t), \quad (2.10)$$

where we have defined $c_1 = -c_2 = 1$ and neglected third-order terms in the expansion. The infinitely short time step Δt and small lattice spacing Δz are not in the same order of magnitude when they approach the continuous limit. The propagation speed

v of the particles appears as the ratio between the lattice spacing and time step $\Delta z/\Delta t$, which remains finite. It turns out that the time step goes faster to zero than the lattice spacing because of an interesting case $(\Delta z)^2/\Delta t \rightarrow \text{constant}$. As a result, we express $\Delta z \sim \epsilon \Delta z$ and $\Delta t \sim \epsilon^2 \Delta t$.

By comparing both sides of Eq. 2.5 and Eq. 2.10, order by order,

$$\left[\Delta t \partial_t + \frac{\Delta t^2}{2} \partial_t^2 + \Delta z c_i \partial_z + \frac{\Delta z^2}{2} c_i^2 \partial_z^2 + \Delta t \Delta z c_i \partial_t \partial_z \right] f_i(z, t) \quad (2.11)$$

$$= (1 - p) [f_i(z, t) - f_j(z, t)],$$

we can obtain the solutions for $f_i^{(0)}$ and higher order terms as well. For the order $O(\epsilon^0)$ we have $f_1^{(0)}(z, t) = f_2^{(0)}(z, t)$ because the left-hand term is zero. This results in

$$f_1^{(0)} = f_2^{(0)} = \frac{1}{2} \rho \quad (2.12)$$

and the condition that

$$\sum_{i=1}^2 f_i^{(l)} = 0, \text{ if } l \geq 1. \quad (2.13)$$

The next order $O(\epsilon)$ of the Boltzmann equation is given by taking the term $\Delta z c_i \partial_z f_i^{(0)}$ of the Taylor expansion and the term $f_i^{(1)}$ in the right-hand side of the equation. Since $f_i^{(0)} = \rho/2$, we obtain

$$\begin{aligned} \frac{\Delta z}{2} \partial_z \rho &= (p - 1)(f_1^{(1)} - f_2^{(1)}) \\ -\frac{\Delta z}{2} \partial_z \rho &= (p - 1)(f_2^{(1)} - f_1^{(1)}). \end{aligned} \quad (2.14)$$

The solution of Eq. 2.14 is then straightforward

$$f_i^{(1)} = \frac{\Delta z}{4(p - 1)} c_i \partial_z \rho. \quad (2.15)$$

The equation governing the evolution of ρ is given by the continuity Eq. 2.6. The order $O(\epsilon^1)$ reads

$$\sum_{i=1}^2 \Delta z c_i \partial_z f_i^{(0)} = 0, \quad (2.16)$$

which is obviously satisfied by our solution. The next order is $O(\epsilon^2)$

$$\sum_{i=1}^2 \left[\Delta t \partial_t f_i^{(0)} + \Delta z c_i \partial_z f_i^{(1)} + \frac{\Delta z^2}{2} c_i^2 \partial_z^2 f_i^{(0)} \right] = 0. \quad (2.17)$$

Using the solution for $f_i^{(0)}$ and $f_i^{(1)}$, we obtain the equation

$$\partial_t \rho + \frac{\Delta z^2}{2} \left[\frac{1}{2(p-1)} + \frac{1}{2} \right] \partial_z^2 \rho = 0 \quad (2.18)$$

and, finally

$$\partial_z \rho = D \partial_z^2 \rho \quad (2.19)$$

which is the expected diffusion equation with the diffusion constant

$$D = \frac{\Delta z^2}{\Delta t} \frac{p}{2(1-p)}. \quad (2.20)$$

Finally, in this implementation we consider an initial mass density $\rho(z, t=0)$ whose evolution obeys the periodic boundary condition $\rho(z, t) = \rho(z + L, t)$, where L is the length of the lattice. As a result, the initial mass density diffuses until the total mass is evenly dispersed throughout the lattice.

2.2.4 Transition Matrix

We introduce a *transition matrix* $A(i, i')$, which gives the probability for an input state i transformed into an output state i' in a collision process. Clearly the whole collision process can be defined by giving the full transition matrix A . $A(i, i')$ obviously has

$$\sum_{i'} A(i, i') = 1 \quad (2.21)$$

for any i (This is the normalization constraint.). In some models, the transition matrix is symmetric:

$$A(i, i') = A(i', i) \quad (2.22)$$

and one says that *detailed balance* holds. However, in general, this is not true. A weaker property is the so-called *semi-detailed balance* which only requires

$$\sum_{i'} A(i, i') = 1 \quad (2.23)$$

for any i' . Semi-detailed balance is obeyed by most lattice gas models. The matrix that satisfies the normalization but does not hold detailed balance constraint is Markov or stochastic matrix. Satisfying both the normalization and semi-detailed balance, the matrix is referred as a doubly stochastic matrix.

2.3 Type-II Quantum Lattice Gas Algorithm

Quantum lattice gas (QLG) algorithms are generalizations of the classical lattice gas algorithms described above, where quantum bits are used to encode the occupation probabilities and where the principle of quantum mechanical superposition is added to the artificial microscopic world. In this quantum case, the mesoscopic occupation probabilities are mapped onto the wave functions of quantum mechanical sites. In the case where the quantum lattice gas describes a hydrodynamic system when the time evolution of the flow field is required, we must periodically measure these occupation probabilities, making the quantum lattice gas algorithm suitable to a type-II implementation. Such type-II algorithms have been shown to solve dynamical equations such as the diffusion equation [18], the Burgers equation [19], and magnetohydrodynamic Burgers turbulence equation[20]. In this chapter, I will discuss about the QLG algorithm for the diffusion equation.

The quantum lattice gas algorithm that solves the 1-D diffusion equation derives from a classical lattice gas of particles moving up and down a 1-D lattice[18]. The corresponding quantum lattice gas algorithm description begins by encoding the occupation probabilities, and thus the mass density, in the states of a lattice of quantum objects. The streaming and collision operations are then a combination of classical and quantum operations, including measurements. The aim of the algorithm is to

take an initial mass density field and to evolve its underlying occupation probabilities according to the Boltzmann equation (2.7). A schematic of the entire quantum algorithm is shown in Fig. 3-3. A single time step of the algorithm is decomposed into four sequential operations:

1. encoding of the mass density
2. applying the collision operator \hat{C} at all sites
3. measuring the occupation numbers
4. streaming to neighboring sites.

These operations are repeated until the mass density field has evolved for the desired number of time steps. In the first time step, the encoding operation specifies the initial mass density profile, while in all the subsequent steps the encoding writes the results of the previous streaming operation. The final time step ends with the readout of the desired result, so operation 4 is not performed.

Each occupation probability is represented as the quantum mechanical expectation value of finding a two-level system, or qubit, in its excited state $|1\rangle$. As a result, the state of the qubit encoding the value $f_i(z, t)$ is

$$|f_i(z, t)\rangle = \sqrt{f_i(z, t)}|1\rangle + \sqrt{1 - f_i(z, t)}|0\rangle. \quad (2.24)$$

It follows that a single value of the mass density is recorded in two qubits, one for each occupation number. The combined two-qubit wave function for a single node becomes

$$\begin{aligned} |\psi(z, t)\rangle = & \sqrt{f_1 f_2}|11\rangle + \sqrt{f_1(1 - f_2)}|10\rangle + \\ & \sqrt{(1 - f_1)f_2}|01\rangle + \sqrt{(1 - f_1)(1 - f_2)}|00\rangle. \end{aligned} \quad (2.25)$$

The kets $|00\rangle$, $|01\rangle$, $|10\rangle$, and $|11\rangle$ span the joint Hilbert space of the two qubits, and this is the largest dimension space over which quantum superpositions are allowed. As with the classical algorithm, the constraint for local equilibrium (2.12) forces the

initial occupation probabilities at a node to be half of the corresponding mass density value.

The occupation numbers encoded in the two-qubit wave function $|\psi(z, t)\rangle$ can be recovered by measuring the expectation value of the number operator \hat{n}_i , as given in

$$f_i(z, t) = \langle \psi(z, t) | \hat{n}_i | \psi(z, t) \rangle, \quad (2.26)$$

where $\hat{n}_1 = \hat{n} \otimes \mathbf{1}$, $\hat{n}_2 = \mathbf{1} \otimes \hat{n}$, where $\mathbf{1}$ is the 2×2 identity matrix, and where the action of the single-qubit number operator \hat{n} returns 1 if the qubit is in its excited state and 0 for the ground state.

The encoded occupation probabilities evolve as specified in the Boltzmann equation by the combined action of the collision operator, the measurement, and streaming. The collision operator contributes by taking the local average of the two occupation probabilities. This averaging (not to be confused with statistical coarse-grain averaging, time averaging, or ensemble averaging) is done by choosing the collision operator \hat{C} to be the “square-root-of-swap” gate, written as

$$\hat{C} = \begin{pmatrix} 1 & 0 & 0 & 0 \\ 0 & \frac{1+i}{2} & \frac{1-i}{2} & 0 \\ 0 & \frac{1-i}{2} & \frac{1+i}{2} & 0 \\ 0 & 0 & 0 & 1 \end{pmatrix} \quad (2.27)$$

in the standard basis. The propagator \hat{C} induces local quantum entanglement. The same collision is applied simultaneously at every site, resulting in

$$|\psi'(z, t)\rangle = \hat{C}|\psi(z, t)\rangle \quad (2.28)$$

Using (2.26), the intermediate occupation probabilities of the wave function $|\psi'(z, t)\rangle$ are

$$f'_i(z, t) = \frac{1}{2} (f_1 + f_2) \quad (2.29)$$

as required for $i = 1, 2$. The third operation physically measures these intermediate

occupation probabilities $f'_i(z, t)$ at all the sites. A single time step is completed with the streaming of the occupation probabilities to the nearest neighbors, according to the rule

$$f_1(z - \Delta z, t + \Delta t) = f'_1(z, t) \quad (2.30)$$

$$f_2(z + \Delta z, t + \Delta t) = f'_2(z, t). \quad (2.31)$$

The information of each qubit is shifted to the neighboring sites in opposite directions. The streaming operation is a classical step causing global data shifting, and it is carried out in a classical computer interfaced to the quantum processors. Together, the last three operations result in

$$f_{1,2}(z \pm \Delta z, t + \Delta t) = \frac{1}{2} [f_1(z, t) + f_2(z, t)], \quad (2.32)$$

which is the exact dynamics described by the Boltzmann equation (2.7).

Chapter 3

NMR Demonstration

Here, we explore the experimental aspects of building a type-II quantum computer using NMR techniques [21]. QIP experiments utilizing NMR typically employ a liquid sample of molecules containing spin- $\frac{1}{2}$ nuclei. The sample is subjected to a strong magnetic field B_0 of order ~ 10 T creating an energy difference ΔE between the aligned and anti-aligned spin states that results in an equilibrium state with net magnetization. At room temperature, $\Delta E/k_B T$ is about 10^{-5} , so that the net magnetization is relatively small, but, given the large number of molecules in the sample ($\sim 10^{18}$), it is still easily detectable. The entire spin ensemble is accurately described by a reduced density matrix of only the intramolecular spin degrees of freedom. The ensemble nature of the NMR sample thus makes it inherently applicable to parallel computation. A type-II architecture can be mapped onto an NMR sample by creating a correspondence between the sites of the lattice and spatially distinct spin ensembles. Using magnetic field gradients and radio frequency (RF) pulses, information in the lattice can be encoded, manipulated, and read out.

¹This section was extracted from M. A. Pravia, Z. Chen, J. Yezpez, D. G. Cory, "Experimental Demonstration of Quantum Lattice Gas Computation," QIP, 2002.

3.1 Methodology for NMR Implementations

3.1.1 Spin System and Control

For this two-qubit problem, we chose a room-temperature solution of isotropically-labeled chloroform ($^{13}\text{CHCl}_3$), where the hydrogen nucleus and the labeled carbon nucleus served as qubits 1 and 2 Fig. 3-1, respectively. The chloroform sample was divided into 16 classically-connected sites of two qubits each, creating an accessible Hilbert space larger than would be available with 32 non-interacting qubits.

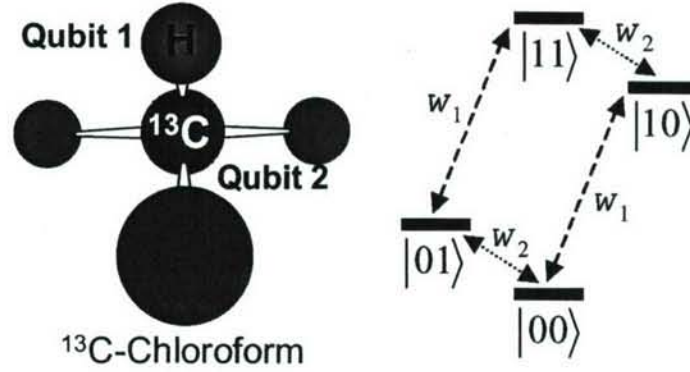


Figure 3-1: **Labeled chloroform** Labeled chloroform consists of two qubits, the hydrogen nucleus and labeled carbon served as qubits 1 and 2. States $|0\rangle$ and $|1\rangle$ are the ground state and excited state, respectively, induced by the Zeeman interaction with the applied magnetic field. Frequencies w_1 and w_2 , defined as multiplication of the gyro-magnetic ratio γ and the magnetic field B_0 , are the resonant frequencies to flip the spins.

The internal Hamiltonian of this system in a strong and homogeneous magnetic field B_0 is

$$H_{\text{internal}} = -\frac{1}{2}(\gamma_H B_0) \sigma_z^1 - \frac{1}{2}(\gamma_C B_0) \sigma_z^2 + \frac{\pi J}{2} \sigma_z^1 \sigma_z^2 \quad (3.1)$$

where the first two terms represent the Zeeman couplings of the spins with B_0 and the last term is the scalar coupling between the two spins. The operators of the form σ_k^i are Pauli spin operators for the spin i and the Cartesian direction k . In the rotating frame, the internal Hamiltonian can be reformulated as: $H_{\text{internal}} = \frac{\pi J}{2} \sigma_z^1 \sigma_z^2$. The choice of chloroform is particularly convenient because the different gyro-magnetic ratios, γ_H

and γ_C , generate widely spaced resonant frequencies. As a result, a RF pulse applied on resonance with one of the spins does not affect, to a good approximation, the other spin. In the 7 T magnet utilized for the implementation, the hydrogen and carbon frequencies were about 300 MHz and 75 MHz, respectively. The widely spaced frequencies allow us to write the two RF control Hamiltonians as acting on the two spins independently. More concretely, the externally-controlled RF Hamiltonians are written as

$$H_{RF}^i(t) = -\frac{1}{2} [w_x^i(t)\sigma_x^i + w_y^i(t)\sigma_y^i] \quad (3.2)$$

The RF Hamiltonians generate arbitrary single-spin rotations with high fidelity when the total nutation frequencies

$$\nu_{RF}^i = \frac{1}{2\pi} \sqrt{[w_x^i]^2 + [w_y^i]^2} \quad (3.3)$$

are much stronger than J , the scalar coupling constant. The scalar coupling Hamiltonian and the single-spin rotations permit the implementation of a universal set of gates, and they are the building blocks for constructing more involved gates such as the collision operator \hat{C} .

The lattice of quantum information processors shown in Fig. 3-2 is realized by superimposing a linear magnetic field gradient on the main field B_0 , adding a position dependent term to the Hamiltonian having the form

$$H_{gradient}(z) = -\frac{1}{2} \left(\gamma_H \frac{\partial B_z}{\partial z} z \right) \sigma_z^1 - \frac{1}{2} \left(\gamma_C \frac{\partial B_z}{\partial z} z \right) \sigma_z^2 \quad (3.4)$$

The variable z denotes the spatial location along the direction of the main field, while the constant $\frac{\partial B_z}{\partial z}$ specifies the strength of the gradient. The usefulness of this Hamiltonian can be appreciated by noticing that the offset frequencies $\Delta\Omega_{H,C} = \gamma_{H,C} \left(\frac{\partial B_z}{\partial z} \right) z$ of the spins vary with position when the gradient field is applied. Spins at distinct locations can thus be addressed with RF fields oscillating at the corresponding frequencies. In this way, the magnetic field gradient allows the entire spin ensemble to be sliced into a lattice of smaller, individually addressable sub-ensembles.

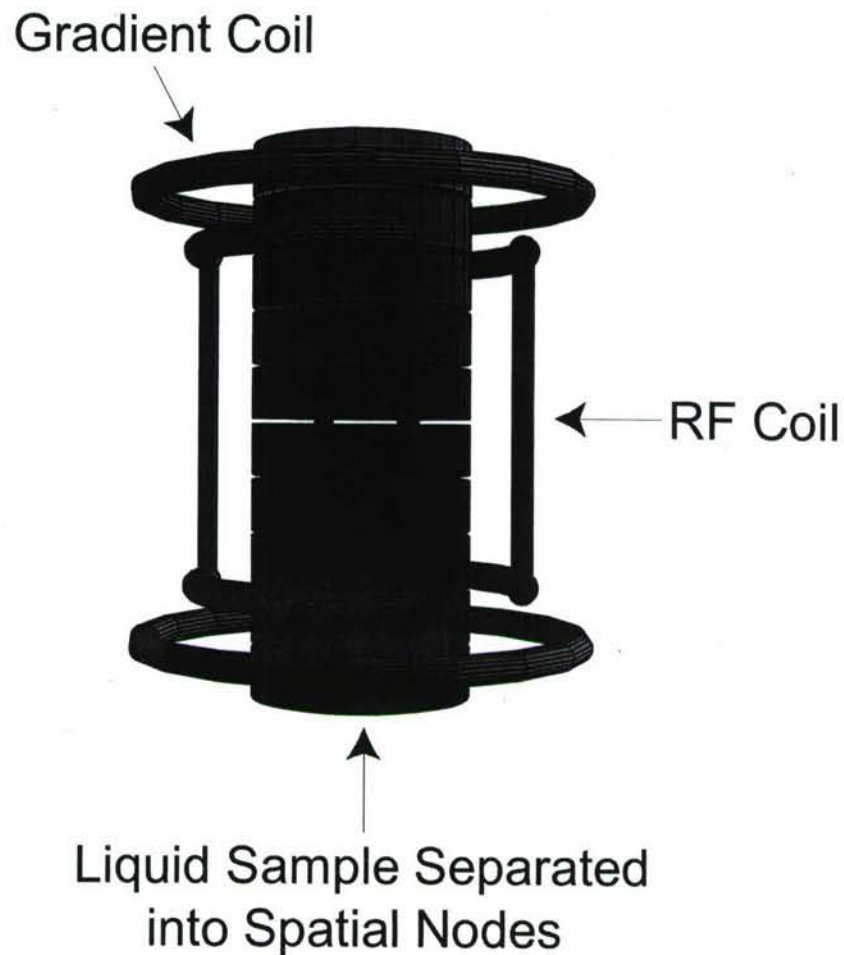


Figure 3-2: **Liquid sample in the coils** The lattice initialization is demonstrated. The liquid sample is placed in the middle with the gradient coils on both ends and surrounded by the RF coils. Once the gradient field is turned on, the resonant frequencies across the sample will vary corresponding to the strength and duration of the gradient. Thus, the spin ensemble can be sliced into a lattice of small blocks.

Using the coupling, RF, and gradient Hamiltonians described above, together with the appropriate measurement and processing tools, we can now describe in detail how the four steps of the diffusion QLG algorithm translate to experimental tasks. The lattice initialization step (1) uses the magnetic field gradients to establish sub-ensembles of varying resonant frequency addressable with the RF Hamiltonians as described in Fig. 3-3. The collision step (2) makes use of both the RF and the internal coupling Hamiltonians to generate the desired unitary operation \hat{C} . The readout (3) is accomplished by measuring the spins in the presence of a magnetic field gradient. And finally, the streaming operation (4) is performed as a processing step in a classical computer in conjunction with the next initialization step.

3.1.2 Lattice Initialization

The initialization of the lattice begins by transforming the equilibrium state of the ensemble into a starting state amenable for quantum computation. At thermal equilibrium, the density matrix is

$$\sigma_{thermal} = \frac{1}{\mathcal{Z}} \exp \left[-\frac{H_{internal}}{k_B T} \right] \approx \frac{\mathbf{1}}{2^2} + \epsilon \left[\frac{\gamma_H}{\gamma_C} \sigma_z^1 + \sigma_z^2 \right], \quad (3.5)$$

where ϵ has a value on the order of 10^{-5} and \mathcal{Z} is the partition function. The equilibrium state is highly mixed and the two spins have unequal magnetizations. To perform quantum computations, it is convenient to transform the equilibrium state into a pseudo-pure state [22, 23], a mixed state whose deviation part transforms identically to the corresponding pure state and, when measured, returns expectation values proportional to those that would be obtained by measuring the underlying pure state. Two transformations create the starting pseudo-pure state $|00\rangle$ from the thermal state. First, the magnetizations of the two spins are equalized ², illustrated

²This is achieved by applying the pulse sequence: $[\frac{\pi}{2}]_x^{H,C} \rightarrow (\frac{1}{4J}) \rightarrow [\frac{\pi}{2}]_y^{H,C} \rightarrow (\frac{1}{4J}) \rightarrow [\frac{\pi}{2}]_{-x}^{H,C} \rightarrow \text{gradient}(z)$.

in Fig. 3.1.2,

$$\sigma_{thermal} \xrightarrow{\text{Equalize}} \sigma_{equal} = \frac{1}{2^2} + \frac{\epsilon}{2} \left(1 + \frac{\gamma_H}{\gamma_C} \right) [\sigma_z^1 + \sigma_z^2] \quad (3.6)$$

followed by a pseudo-pure state creation sequence³ that results in

$$\sigma_{equal} \xrightarrow{\text{Pseudo-pure}} \sigma_{pp} = \frac{1}{2^2} + \epsilon \frac{\sqrt{3}}{4\sqrt{2}} \left(1 + \frac{\gamma_H}{\gamma_C} \right) [\sigma_z^1 + \sigma_z^2 + \sigma_z^1 \sigma_z^2]. \quad (3.7)$$

The equalization and pseudo-pure state creation sequences are described in detail in reference [24]. For clarity, we define the constant in front of the brackets to be ϵ' , allowing us to write the pseudo-pure state σ_{pp} in terms of the desired spinor $|00\rangle$ as

$$\sigma_{pp} = \left(\frac{1}{4} - \epsilon' \right) \mathbf{1} + \epsilon' |00\rangle\langle 00|. \quad (3.8)$$

Expressed in this manner, it is now more easily seen how a unitary transformation applied to σ_{pp} acts trivially on the term proportional to the identity, but it evolves the term $|00\rangle\langle 00|$ as it would a pure state as shown in Fig. 3-5.

Individually addressing the sites of the lattice, as depicted in Fig. 3-3, is accomplished by selectively addressing slices of the cylindrical sample. The procedure is related to slice-selection in magnetic resonance imaging (MRI) [25], and it works by applying the gradient Hamiltonian in the presence of suitably shaped RF pulses. First, consider the Hamiltonian for a one-spin system subjected to a linear magnetic field gradient in the z -direction and to a time-dependent RF pulse applied in the y -direction. In this case, the Hamiltonian is

$$H_{RF,G}(z, t) = -\frac{1}{2} \left(\gamma \frac{\partial B_z}{\partial z} z \right) \sigma_z - \frac{1}{2} w_y(t) \sigma_y \quad (3.9)$$

where the σ_z term is the linearly-varying static field and the σ_y term is the time-dependent RF. The Hamiltonian $H_{RF,G}(z, t)$ does not commute with itself at all times, so a closed-form and exact solution cannot be easily given without specifying the

³It is accomplished by the application of $[\frac{\pi}{4}]_x^{H,C} \rightarrow (\frac{1}{2}J) \rightarrow [\frac{\pi}{8}]_y^{H,C} \rightarrow \text{gradient}(z)$.

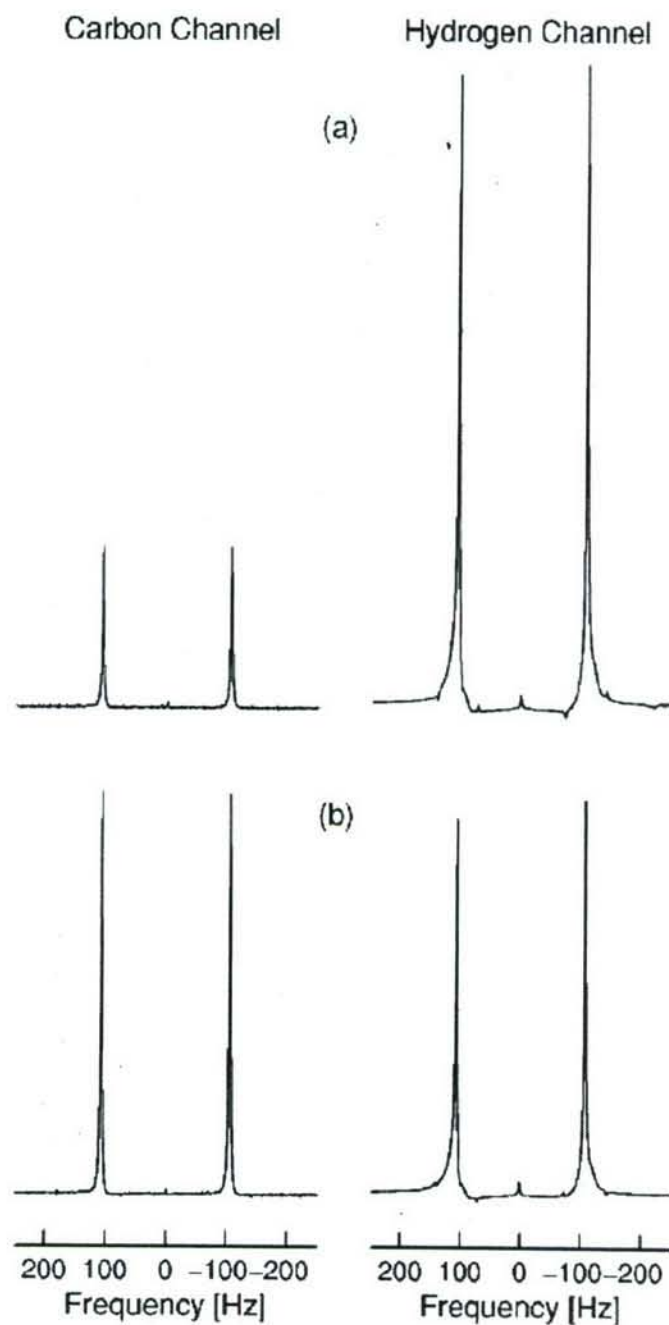


Figure 3-4: **Equalizing magnetization** Since the ratio of γ_H to γ_C is a factor of four, the spectra of H and C following a $\frac{\pi}{2}$ pulse should reflect 4 : 1 ratio in the peak heights, shown in (a). In order to compensate the different magnetization, the equalization pulse sequence is applied and results in the spectrum (b).

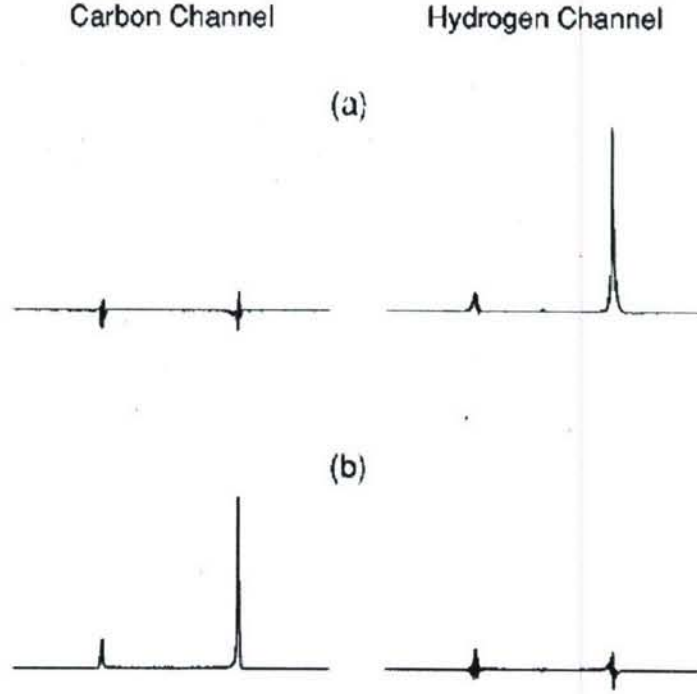


Figure 3-5: **Pseudo-pure states** The results of pseudo-pure states of hydrogen and carbon are shown in (a) and (b), respectively.

function $w_y(t)$. (The two terms in the Hamiltonian doesn't commute with each other at all times.) A valuable approach, however, is to consider the approximate evolution generated by $H_{RF,G}(z, t)$ during infinitesimal periods of the RF pulse. To first order, the evolution during the initial period Δt becomes

$$U_{RF,G}(z, t = \Delta t) \approx \exp \left[i \frac{1}{2} \left(\gamma \frac{\partial B_z}{\partial z} \Delta t \right) z \sigma_z \right] \exp \left[i \frac{w_y(\Delta t) \Delta t}{2} \sigma_y \right]. \quad (3.10)$$

By defining the term in the parenthesis as $\Delta k_z \equiv \gamma \frac{\partial B_z}{\partial z} \Delta t$, the evolution of an initial density matrix σ_z through a single period becomes

$$U_{RF,G} \sigma_z U_{RF,G}^\dagger \approx \exp \left[i \frac{\Delta k_z z}{2} \sigma_z \right] \sigma_x \exp \left[-i \frac{\Delta k_z z}{2} \sigma_z \right] w_y(\Delta t) \Delta t + \sigma_z \quad (3.11)$$

where small angle approximations have been made. The first term is a spatial helix

of the x and y magnetizations having a wavenumber Δk_z . The second term is the first order approximation to the magnetization remaining in the state σ_z . Another period of evolution will affect the σ_z term as described, creating a new magnetization helix with wavenumber Δk_z . In addition, the initial helix will have its wavenumber increased by an amount Δk_z . The final result over many periods is the formation a shaped magnetization profile having many components

$$\sigma_z \rightarrow \sum_{n=1}^N \exp \left[i \frac{n \Delta k_z z}{2} \sigma_z \right] \sigma_x \exp \left[-i \frac{n \Delta k_z z}{2} \sigma_z \right] w_y(n \Delta t) \Delta t + \sigma_z. \quad (3.12)$$

Each term in summation can be interpreted as a cylindrical Fourier component of the x - y magnetization weighted by the RF nutation rate $w_y(n \Delta t)$. The RF waveform specifies the magnitude of each spatial Fourier component, and the resulting spatial profile is the Fourier transform of the RF waveform[30]. An equivalent description is to say that, for weak RF pulses, the excited magnetization of the spins at a given resonance frequency is, to first order, proportional to the Fourier component of the RF waveform at that frequency. As a result, control of the appropriate RF Fourier component essentially translates to selective addressing of spatial frequencies, which in turn allows the excitation of particular spatial locations.

The Fourier transform approximation allows encoding of arbitrary shapes on the various spatial locations of one uncoupled nuclear species. For QIP, however, coupled spins are required to implement entangling operations. In particular, the chloroform carbons and protons are coupled together via the scalar coupling. Given that the required RF waveforms should be weak, the coupling interferes with the desired evolution. The effect of the coupling present while encoding on spin 1 is removed by applying a strong RF decoupling sequence on the second spin⁴. The decoupling modulates the σ_z^2 operator in the interaction Hamiltonian, making its average over

⁴The decoupling was accomplished by applying the pulse cycle $Q\bar{Q}Q\bar{Q}$ during the positive and negative gradients. The element Q is a composite π pulse implemented with four sequential pulses having nutation angles $80.4^\circ, 362.0^\circ, 181.6^\circ, 180.8^\circ$ and respective phases $271.3^\circ, 132.4^\circ, 292.3^\circ, 200.4^\circ$. This composite pulse was chosen over more commonly used pulse sequences for its relatively short total nutation angle and good decoupling, allowing the cycle to fit within a gradient period.

a cycle period equal to zero. As a result, the second spin feels an identity operation during the decoupling. Fig. 3-6 shows the complete RF and gradient pulse sequence. As can be seen from the diagram, the first encoding on qubit 1 was subsequently swapped to qubit 2, followed by a re-encoding of qubit 1. We chose this method because the smaller gyro-magnetic ratio of ^{13}C causes a narrower frequency dispersion in the presence of the gradients, making the carbon decoupling simpler.

As described above, the encoding process writes the desired shapes in the spatial dependence of each spin's x -magnetization. The occupation numbers, however, are proportional to the z -magnetization, as can be seen when the number operator in the equation

$$f_i(n\Delta z, m\Delta t) = \langle \psi(n\Delta z, m\Delta t) | \hat{n}_i | \psi(n\Delta z, m\Delta t) \rangle, \quad (3.13)$$

is replaced with $\hat{n}_i = \frac{1}{2}(1 + \sigma_z^i)$ resulting in

$$f_i(n\Delta z, m\Delta t) = \frac{1}{2} \left[1 + \langle \psi(n\Delta z, m\Delta t) | \sigma_z^i | \psi(n\Delta z, m\Delta t) \rangle \right]. \quad (3.14)$$

where second term in the brackets represents the z -magnetization. The encoding process is followed by a $\pi/2$ pulse that rotates the excited x -magnetization to the z direction.

3.1.3 Collision and Swap Gates

After initialization, the next step is to apply the collision operator. For the QLG algorithm solution to the diffusion equation, the collision operator \hat{C} is the square-root-of-swap gate. Expressed in terms of the Pauli operators, it is

$$\hat{C} = \exp \left[-i \frac{\pi}{8} (\sigma_x^1 \sigma_x^2 + \sigma_y^1 \sigma_y^2 + \sigma_z^1 \sigma_z^2) \right] \quad (3.15)$$

where an irrelevant global phase has been ignored. Written in this form, the operation \hat{C} can be decomposed into a sequence of implementable RF pulses and scalar coupling evolutions[33, 35] by noticing that the product operators in the exponent commute

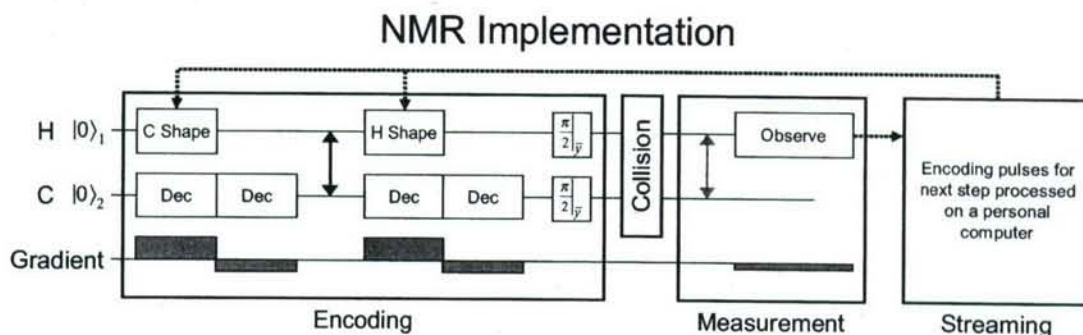


Figure 3-6: **NMR methodology for QLG algorithm.** The NMR implementation consists of four main sections, each corresponding to the prescribed QLG algorithm step. The top two lines in the diagram correspond to RF pulses applied to the proton and carbon qubits, respectively. The third line shows the application of magnetic field gradients. In the encoding section, the initial carbon magnetization is recorded on the protons before being transferred to the carbons. The starting magnetization is specified by using a RF pulse shaped as the Fourier transform of the desired magnetization. The shaped pulses are applied in the presence of gradients so that each site can be addressed. A carbon decoupling sequence prevents the scalar coupling from interfering with the low power shaped pulses. The $\frac{\pi}{2}$ at the end of the encoding move the information from the x -axis to the z -axis, as required by the QLG algorithm. The collision operator follows the encoding, and it is implemented without gradients to ensure that all of the sites in the sample feel the same transformation. The results are observed in two experiments, each time using the more sensitive proton channel. A swap gate is added when measuring the carbon magnetization. Finally, the streaming operation is applied by shifting the frequencies of the carbon and proton shapes in opposite directions.

with each other, resulting in

$$\hat{C} = \exp \left[-i \frac{\pi}{8} \sigma_y^1 \sigma_y^2 \right] \exp \left[-i \frac{\pi}{8} \sigma_z^1 \sigma_z^2 \right] \exp \left[-i \frac{\pi}{8} \sigma_x^1 \sigma_x^2 \right] \quad (3.16)$$

Expanding the first and last exponentials as scalar couplings sandwiched by the appropriate single-spin rotations results in

$$\begin{aligned} \hat{C} = & \exp \left[i \frac{\pi}{4} \sigma_x^1 \right] \exp \left[i \frac{\pi}{4} \sigma_x^2 \right] \exp \left[-i \frac{\pi}{8} \sigma_z^1 \sigma_z^2 \right] \exp \left[-i \frac{\pi}{4} \sigma_x^1 \right] \exp \left[-i \frac{\pi}{4} \sigma_x^2 \right] \cdot \\ & \exp \left[-i \frac{\pi}{8} \sigma_z^1 \sigma_z^2 \right] \cdot \\ & \exp \left[-i \frac{\pi}{4} \sigma_y^1 \right] \exp \left[-i \frac{\pi}{4} \sigma_y^2 \right] \exp \left[-i \frac{\pi}{8} \sigma_z^1 \sigma_z^2 \right] \exp \left[i \frac{\pi}{4} \sigma_y^1 \right] \exp \left[i \frac{\pi}{4} \sigma_y^2 \right] \end{aligned} \quad (3.17)$$

The exponents of terms proportional to $\sigma_z^1 \sigma_z^2$ represent internal Hamiltonian evolutions lasting for a time $t_{zz}^{col} = 1/(4J)$. The exponents of terms with single-spin operators are implemented by $\pi/2$ rotations as in Fig. 3-7. They were generated by RF pulses whose nutation rate was about 50 times greater than J . All of the pulses and delays were applied without a magnetic field gradient in order to transform all of the sites identically.

As shown in Fig. 3-6, swap gates were utilized both in the lattice initialization and in the measurement of the carbon magnetization. The pulse sequence for the swap gates was almost identical to the sequence for \hat{C} . The only difference was that the internal evolution delay was set to $t_{zz}^{swap} = 1/(2J)$.

3.1.4 Measurement

If the algorithm is performed on individual quantum systems, then the values are obtained by averaging over many strong quantum measurements of identical instances of each step. However, when the algorithm is performed using a large ensemble of quantum systems, as in the case of NMR, then a single weak measurement of the entire ensemble can provide sufficient precision to obtain $f_i'(z, t)$. The occupation numbers resulting from the collision were obtained by measuring the z -magnetizations and using equation (3.14). Since only the σ_x^i and σ_y^i operators are directly observable,

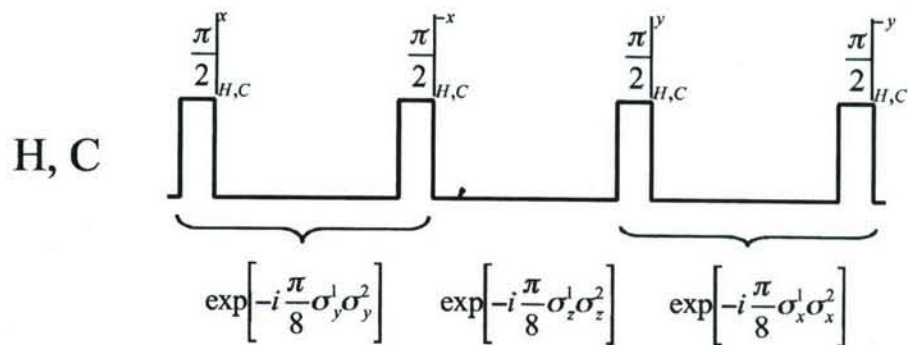


Figure 3-7: **Pulse sequence for the collision operator** The collision operator for the diffusion equation can be generated by applying $\frac{\pi}{2}$ pulses on both channels with delay time $\frac{1}{4J}$ in between. The same sequence can be used to generate the swap gate by increasing the delay time to $\frac{1}{2J}$.

a “read out” $\pi/2$ pulse transformed the z -magnetization into x -magnetization. The proton magnetization was measured directly after the collision, while the carbon magnetization was first swapped to the protons before observation. Measurements of both the ^{13}C and ^1H magnetizations were carried out separately, and in both cases via the more sensitive proton channel. The measurements were made in the presence of a weak linear magnetic field gradient, causing signals from different sites to resonate with distinguishable frequencies. The observed proton signal was digitized and Fourier transformed to record an image of the spatial variation of the spin magnetization. The observed spectrum was then processed to correct the baseline and to obtain the resulting magnetization at each site. Because each site is composed of a slice of the

sample with spins resonating in a band of frequencies, the occupation number for each site was obtained by averaging over all spins in the corresponding band.

3.1.5 Streaming

The final step involves classically streaming the results of the measurements according to Eqs. (2.30) and (2.31). For the diffusion equation, the streaming operation is applied in conjunction with the next lattice initialization step by adding a linearly varying phase to the Fourier transform of the desired shape. The added phase causes a shift in the frequency of the pulse determined by the slope of the phase. When the frequency-shifted pulse is applied in the presence of the magnetic field gradient, the shift results in spatial translation of the encoded shape. The streaming operation is thus implemented as a signal processing step in the lattice initialization procedure.

3.2 Experiment Demonstration

The results of the experiment are shown in Fig. 3-8, together with plots of the analytical solution and of numerical simulations of the NMR experiment. In total, 7 steps of the algorithm were completed using a parallel array of 16 two-qubit ensemble NMR quantum processors. The observed deviations between the data points and the analytical plots can be attributed to imperfections in the various parts of the NMR implementation.

3.3 Conclusion

Ensemble NMR techniques have been used to study the experimental details involved in quantum information processing. The astronomical number of individual quantum systems ($\sim 10^{18}$) present in typical liquid-state spin ensembles greatly facilitates the problem of measuring spin quantum coherences. In addition, the ensemble nature has been successfully utilized to create the necessary pseudo-pure states [22, 23] and to systematically generate non-unitary operations over the ensemble [26]. In this

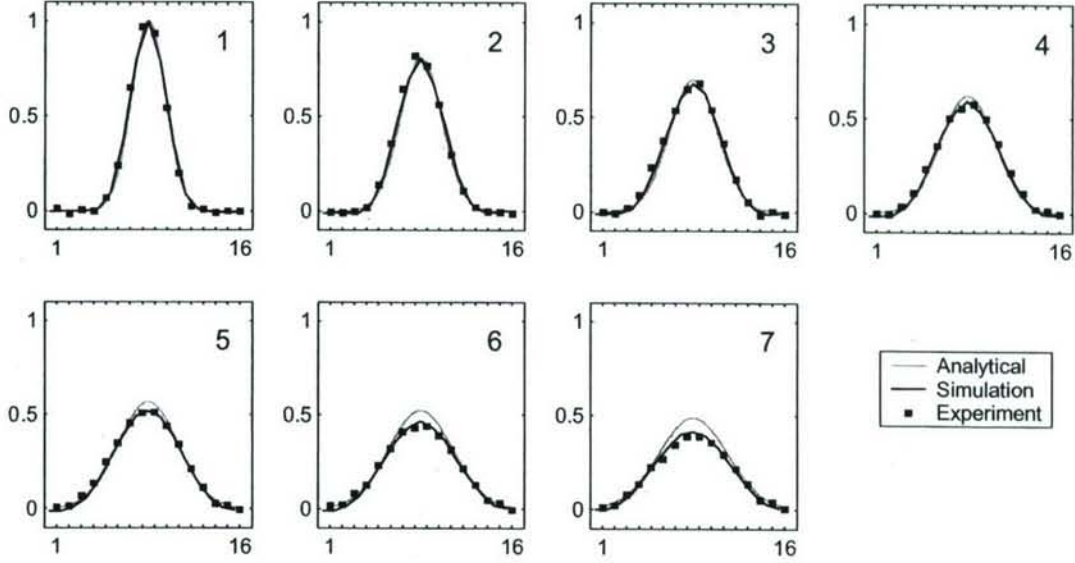


Figure 3-8: **QLG algorithm experimental results.** The experimental mass densities are plotted in the figure, together with plots of the analytical solution and the numerical simulation of the NMR experiment. Seven steps of the algorithm were implemented on 16 two-qubit sites. The simulations were performed using the actual RF nutation rates and times of the experimental setup. The calculations closely match the data, suggesting that the deviation between the analytical results and the data can be attributed imperfections in the methodology. As a result, the simulations promise to be useful in exploring the errors from alternate methods.

experiment, we again exploit the ensemble nature, but this time as a means of realizing a parallel array of quantum information processors. The novel architecture is then used to run a quantum lattice gas algorithm that solves the 1-D diffusion equation.

The closeness of the data to the analytical results is encouraging, and it demonstrates the possibility of combining the advantages of quantum computation at each node with massively parallel classical computation throughout the lattice. Currently, commercial MRI machines routinely take images with $256 \times 256 \times 256$ volume elements. As a result, the large size of the NMR ensemble provides, in principle, sufficient room to explore much larger lattices. However, in moving to implementations with more computational power, several challenges remain. The limited control employed here is sufficient for a few time steps of the algorithm, but refinements are necessary to increase the number of achievable iterations. In addition, although complicated op-

erations have been done in up to 7 NMR qubits [27, 28, 29], the problem of efficiently initializing a large lattice of few-qubit processors still remains. Our results provide a first advance in this direction, and they provide confirmation that NMR techniques can be used to test these new ideas.

Chapter 4

Systematic Error

The ensemble nature of the spin system allows us to split the sample into a spatial array of lattice sites. As we mentioned in the previous chapter, well developed methods from MRI [25] allow us to selectively address the spins in each of these sites. Typically the addressing is carried out in a space reciprocal to the spatial mapping, called k -space [30], where k is the wave-number of the corresponding Fourier components. The k -space formalism provides a recipe for writing a spatially varying spin rotation across an ensemble of spins that have been distinguished from each other by a magnetic field gradient. The k -space formalism is essentially the application of shaped RF pulses in the presence of a linear magnetic gradient field as a means of exciting selective frequencies. For most studies the full k -space formalism is not employed and a linear approximation is invoked. If the rotation angle of the shaped pulse is small, then the excited magnetization may be accurately calculated only to first order in that angle, and the excited magnetization is related to the RF waveform simply by a Fourier transform. As a result, the required RF waveform can also be determined by taking the inverse Fourier transform of the desired initial magnetization. This technique allows us to encode arbitrary magnetization profiles spanning the various spatial locations in our experiment and thereby approximating any desired initial conditions. In the previously implemented diffusion equation, higher order Fourier

¹This section was extracted from Z. Chen, J. Yezpez, D. G. Cory, "Simulation of the Burgers equation by NMR quantum information processing," submitted, 2005.

components of the number density are attenuated by the dynamics and the solution is stable even in the presence of substantial accumulated errors.

To push the development of type-II implementations we have chosen to explore the nonlinear Burgers equation to test the breakdown for the linear approximation. Over time, a shock front forms and high spatial frequencies in the magnetization profile become important and it is these high spatial frequencies that we expect to be most sensitive to errors. The numerical treatment of the QLG algorithm for the Burgers equation therefore offers a stronger proof of our NMR quantum computing approach since the effect of the nonlinear convective term in the equation generates a sharp edge as a shock develops in time that is not mimicked by spin relaxation, random self-diffusion, nor RF inhomogeneities.

4.1 The Burgers Equation

4.1.1 QLG Algorithm for the Burgers Equation

The QLG algorithm is initialized, in the NMR case, by encoding the particles' occupation probabilities as a spin-magnetization profile. To handle the one-dimensional Burgers equation [19], it is sufficient to use two qubits (two spin- $\frac{1}{2}$ nuclei) per lattice site, where each stores a single real valued occupation probability. A lattice of QIPs are related to the ensemble sample by creating a correspondence between lattice sites and spatially dependent positions in the sample. The dynamical evolution is caused by a collision operator (a quantum operation), and measurement and streaming (classical operations) according to the QLG algorithmic paradigm.

First, each occupation probability is mapped onto a lattice site as the expectation value of a number operator at a space time site z at time t . As a result, the initial state of the i^{th} qubit is $\sqrt{f_i(z, t)}|1\rangle + \sqrt{1 - f_i(z, t)}|0\rangle$. The combined wave function for a lattice site is a tensor product over the qubits:

$$|\psi\rangle = \sqrt{f_1 f_2}|11\rangle + \sqrt{f_1(1 - f_2)}|10\rangle + \sqrt{(1 - f_1)f_2}|01\rangle + \sqrt{(1 - f_1)(1 - f_2)}|00\rangle. \quad (4.1)$$

In the basis of a two-qubit system, the number operators for the occupancy of qubits are defined in terms of the single qubit number operation $\hat{n} = \begin{pmatrix} 1 & 0 \\ 0 & 0 \end{pmatrix}$ as follows: $\hat{n}_1 = 1 \otimes \hat{n}$ and $\hat{n}_2 = \hat{n} \otimes 1$. Therefore, the occupation probability is represented as follows:

$$f_i(z, t) = \langle \psi(z, t) | \hat{n}_i | \psi(z, t) \rangle. \quad (4.2)$$

The macroscopic scale dynamical quantity of the quantum lattice gas is the number density, ρ , defined as the sum of the occupancy probability. The equilibrium occupation probabilities that we use are

$$\begin{aligned} f_1^{eq} &= \frac{\rho}{2} + \frac{1}{2\alpha} \sqrt{\alpha^2 + 1} - \frac{1}{2\alpha} \sqrt{(\alpha^2 + 1) - 2\alpha^2 \rho + \alpha^2 \rho^2} \\ f_2^{eq} &= \frac{\rho}{2} - \frac{1}{2\alpha} \sqrt{\alpha^2 + 1} + \frac{1}{2\alpha} \sqrt{(\alpha^2 + 1) - 2\alpha^2 \rho + \alpha^2 \rho^2}. \end{aligned} \quad (4.3)$$

where α is denoted by $\cot \theta \cos(\zeta - \xi)$ for convenience. (θ , ξ , and ζ are the “Euler” angles introduced by the collision operator, which will be covered below.)

Second, the evolution of f_i is governed by the combined action of the collision operator, measurement and streaming. The collision operator is applied to all the lattice sites independently, resulting in $|\psi'(z)\rangle = \hat{C}|\psi(z)\rangle$, for all lattice sites. The choice of the particular components of the unitary collision operator determines the form of the macroscopic effective field theory (a parabolic partial differential equation) and the value of its transport coefficients (coefficients of the dissipative terms). A general representation of the collision operator for the Burgers equation is a block diagonal matrix. This single quantum operator has the following matrix representation:

$$\hat{C} = \begin{pmatrix} 1 & 0 & 0 & 0 \\ 0 & e^{i\phi} e^{i\xi} \cos \theta & e^{i\phi} e^{i\zeta} \sin \theta & 0 \\ 0 & -e^{i\phi} e^{-i\zeta} \sin \theta & e^{i\phi} e^{-i\xi} \cos \theta & 0 \\ 0 & 0 & 0 & 1 \end{pmatrix}, \quad (4.4)$$

where ϕ , ξ , ζ , and θ are the “Euler” angles. The corresponding nonlinear Burgers

equation reads

$$\frac{\partial \rho}{\partial t} + c \sin 2\theta \cos(\zeta - \xi) (\rho - 1) \frac{\partial \rho}{\partial z} = \frac{1}{2} \frac{\Delta z}{\Delta t} \frac{\partial^2 \rho}{\partial z^2}. \quad (4.5)$$

Here, Δt is the update time and a cell size is presented by Δz . The propagation speed c of particles is determined as the ratio of the lattice cell size to the time step interval.

Third, we measure the occupation probabilities. This process erases all the superpositions and quantum entanglement that was created by the unitary collision operator in the second step.

Fourth, and last step of the QLG algorithm, we shift the f_i obtained in the previous step to its nearest neighbor. This step requires only classical communication between neighboring sites. The time is incremented after this step. Then, we loop back to step 1 and update the field of occupation probabilities over the lattice sites. In this way, we can continue to iterate forward in time and make a time-history record of the occupation probabilities, which in turn gives us the temporal evolution of the number density field.

4.1.2 First Implementation using NMR

In the first implementation of the Burgers equation, we chose the “Euler” angles in Eq. 4.4 to be $\phi = \zeta = \xi = 0$, and $\theta = \frac{\pi}{4}$. As a result, the general collision operator reduces to the quantum gate

$$\hat{C} = \begin{pmatrix} 1 & 0 & 0 & 0 \\ 0 & \frac{1}{\sqrt{2}} & \frac{1}{\sqrt{2}} & 0 \\ 0 & -\frac{1}{\sqrt{2}} & \frac{1}{\sqrt{2}} & 0 \\ 0 & 0 & 0 & 1 \end{pmatrix}, \quad (4.6)$$

and the equilibrium occupation probabilities for the Burgers equation are expressed:

$$f_i^{eq} = \frac{\rho}{2} + \frac{e_i}{\sqrt{2}} \left[1 - \sqrt{1 - \rho \left(1 - \frac{\rho}{2} \right)} \right], \quad (4.7)$$

where e_i is ± 1 for different qubits. Then we have the Burgers equation in standard form

$$\frac{\partial u}{\partial t} - u \frac{\partial u}{\partial x} = \nu \frac{\partial^2 u}{\partial x^2} \quad (4.8)$$

where $\nu = \frac{\Delta z^2}{2\Delta t}$ is the transport coefficient (viscosity term) and the flow field is defined as $u = c(\rho - 1)$.

A room-temperature solution of isotropically-labeled chloroform ($^{13}\text{CHCl}_3$) has been chosen for implementing the Burgers experiments. The hydrogen and the labeled carbon nucleus are served as qubits 1 and 2, and the difference of the gyro-magnetic ratio of two spins generates widely spaced resonant frequencies that allows us to address each spin independently.

The initial magnetization is specified by using a RF pulse shaped by the Fourier transform of the desired magnetization (transform of the initial number density profile). While applying the shaped pulse, a carbon decoupling sequence is performed to prevent the scalar coupling from interfering with the low power shaped pulses. In addition, the $\frac{\pi}{2}$ pulse, which rotates the information from the x -axis to the z -axis, is applied separately just after each initialization. This is done to keep the valuable information along the longitudinal direction where it will not be affected by the gradient and chemical shift. The encoding of initial states on both spins is accomplished in two steps: The initial carbon magnetization is recorded on the protons before being transferred to the carbons and followed by the initialization of proton magnetization. Furthermore, a short pulse sequence, called the *clean sequence*, is executed after the first swap gate to erase the phase distortion that may be caused by the decoupling sequence.

The unitary operator \hat{C} can be decomposed of a sequence of RF pulses and scalar coupling. The product operators in the exponent commute with each other, resulting in $\hat{C} = \exp \left[-i \frac{\pi}{8} \sigma_x^H \sigma_y^C \right] \exp \left[i \frac{\pi}{8} \sigma_y^H \sigma_x^C \right]^2$. Both terms can be expanded as natural scalar

²The collision operator is achieved by the pulse sequence: $[\frac{\pi}{2}]_{-x}^{H,C} \rightarrow \frac{1}{2J} \rightarrow [\frac{\pi}{2}]_x^{H,C} \rightarrow [\frac{\pi}{2}]_{-y}^{H,C} \rightarrow [\frac{\pi}{4}]_x^H [\frac{\pi}{4}]_{-x}^C \rightarrow \frac{1}{2J} \rightarrow [\frac{\pi}{2}]_y^{H,C}$.

Hamiltonian couplings sandwiched with the appropriate single rotations, resulting in

$$\begin{aligned} \hat{C} = & \exp \left[-i\frac{\pi}{4}(\sigma_y^H + \sigma_y^C) \right] \exp \left[-i\frac{\pi}{4}\sigma_z^H \sigma_z^C \right] \exp \left[-i\frac{\pi}{8}(\sigma_x^H - \sigma_x^C) \right] \\ & \exp \left[i\frac{\pi}{4}(\sigma_y^H + \sigma_y^C) \right] \exp \left[-i\frac{\pi}{4}(\sigma_x^H + \sigma_x^C) \right] \exp \left[-i\frac{\pi}{4}\sigma_z^H \sigma_z^C \right] \exp \left[i\frac{\pi}{4}(\sigma_x^H + \sigma_x^C) \right]. \end{aligned} \quad (4.9)$$

The exponential terms of single spin rotations are implemented by $\pi/2$ and $\pi/4$ pulses. The exponents of terms with $\sigma_z^H \sigma_z^C$ represent the natural internal Hamiltonian evolutions with time period $1/2J$.

The occupation numbers of each spin are obtained following the collision step by measuring the z -magnetization according to the following equation

$$f_i(z, t) = \frac{1}{2} \left[1 + \langle \psi(z, t) | \sigma_z^i | \psi(z, t) \rangle \right]. \quad (4.10)$$

Since only σ_x and σ_y are observable in our NMR spectrometer, a $\pi/2$ pulse has been used to bring the z -magnetization into the transverse plane. The measurements are done in two separate experiments, where a SWAP gate is applied to bring the magnetization from carbon channel to the proton channel. This SWAP operation is done because the higher signal-to-noise ratio in the proton channel allows us to improve the accuracy of our implementation. During the “readout” process (Step 3), a weak magnetic field gradient is applied to distinguish different sites. The observed proton signals are digitized and Fourier transformed, allowing us to record the spatially-dependent spin magnetization profile. The four main sections of the NMR implementation of QLG algorithm are graphically depicted in Figure 4-1.

The experiments have been performed on a lattice of 16 cells for 15 time steps, shown in Fig. 4-2. After ten iterations, the deviation between the experimental data and simulation results becomes significant. This indicates that our numerical simulations do not include all the potential error sources. However, some of them are small enough to be ignored for now. As described before, the “Euler” angles of the collision matrix are tunable and determines the viscosity term in the Burgers equation. We aim to choose another collision matrix for the Burgers equation, which contains a

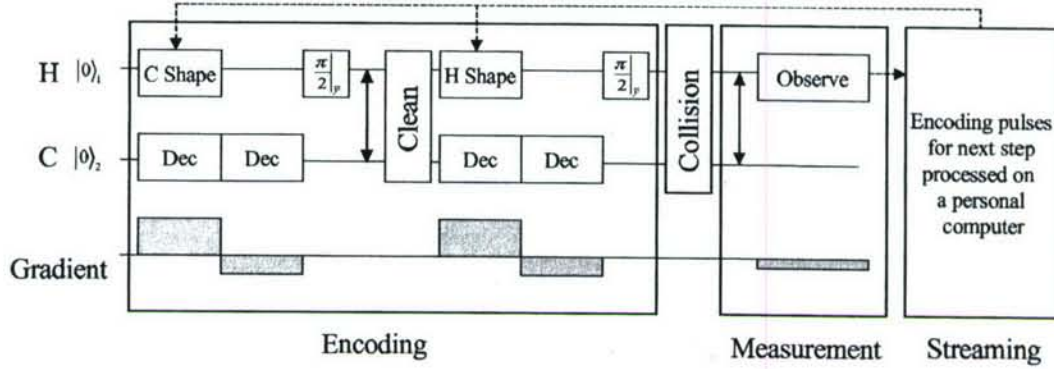


Figure 4-1: **QLG algorithm for the Burgers equation implemented in four steps.** Three horizontal lines represent proton spin, carbon spin and field gradients. Both starting magnetizations are encoded in proton channel first due to the high signal to noise ratio while decoupled in carbon channel to prevent interfering of scalar coupling. The collision operator is applied after the initialization. Measurement are also taken in two steps in the proton channel followed by data processing in a personal computer.

higher viscosity parameter, thus it takes less time steps to form the sharp front.

4.1.3 The Collision Matrix with Higher Viscosity Term

This time, ϕ , ζ , and ξ are still set to be zero, but $\cos\theta$ is selected to be 0.8 for convenience. In this particular case, the equilibrium occupation probabilities for the Burgers equation are determined by

$$f_i^{eq} = \frac{\rho}{2} + e_i \frac{5}{8} \left[1 - \sqrt{1 - \left(\frac{32\rho}{25} \right) \left(1 - \frac{\rho}{2} \right)} \right]. \quad (4.11)$$

The collision quantum operator ³ is written to be $\hat{C} = \exp \left[-i \frac{\pi}{4.882} \left(\sigma_x^H \sigma_y^C - \sigma_y^H \sigma_x^C \right) \right]$.

³The corresponding pulse sequence is the following: $[\frac{\pi}{2}]_{-x}^{H,C} \rightarrow \frac{1}{2J} \rightarrow [\frac{\pi}{2}]_x^{H,C} \rightarrow [\frac{\pi}{2}]_{-y}^{H,C} \rightarrow [\frac{\pi}{2.441}]_x^H [\frac{\pi}{2.441}]_{-x}^C \rightarrow \frac{1}{2J} \rightarrow [\frac{\pi}{2}]_y^{H,C}$.

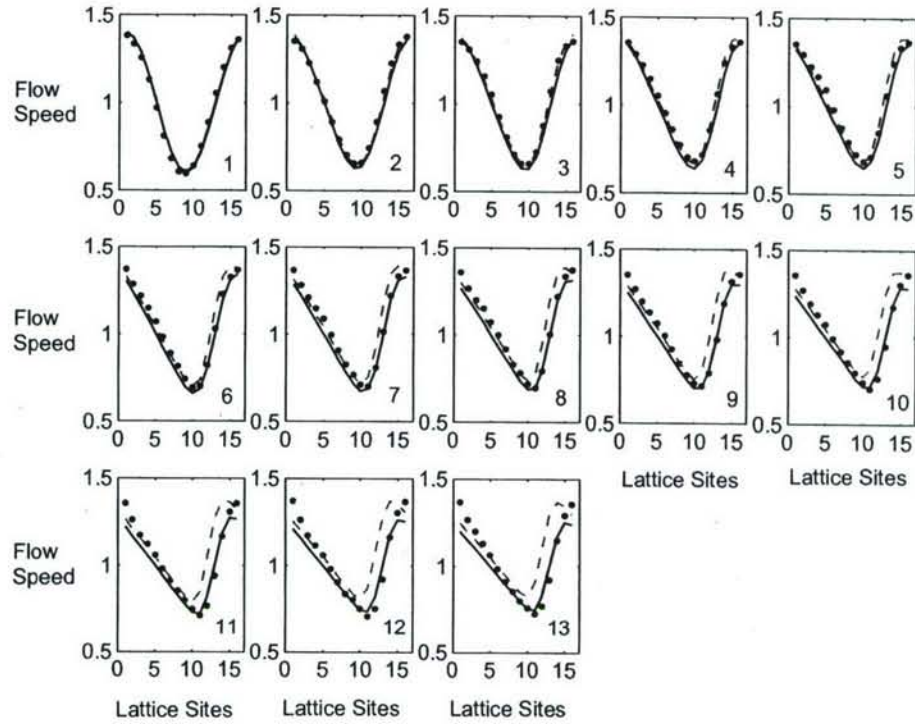


Figure 4-2: **Experiment results comparing with simulation and analytical solutions.** The experimental data (dots) are plotted together with the simulations (grey dash lines) and the analytical solutions (black solid lines) for 15 time steps on a lattice of 16 cells. The horizontal axis for each plot indicates the number of the lattice cells and vertical axis is the flow velocity. The numbers associated with each plot are the time steps. The deviation between the simulation and analytical solutions is mainly due to the accumulative errors in the collision operator. We also observed the deviation between the experimental data and simulation results, possibly introduced by inhomogeneity, self-diffusion.

The corresponding matrix representation is written as

$$\hat{C} = \begin{pmatrix} 1 & 0 & 0 & 0 \\ 0 & 0.8 & 0.6 & 0 \\ 0 & -0.6 & 0.8 & 0 \\ 0 & 0 & 0 & 1 \end{pmatrix}. \quad (4.12)$$

The viscosity term associated with this unitary operator is $\frac{1}{4} \frac{\Delta z^2}{\Delta t}$, which doubles the value in the previous one.

Nine successive time steps of the quantum algorithm have been implemented on 16 two-qubit sites, depicted in Fig. 4-3. Using the new collision matrix, the deviation between experimental data and simulation results has been reduced as we expected. Here, we have demonstrated shock-formation driven by a tunable viscosity parameter to show that the width of the shock front is not determined by implementation imperfections.

4.1.4 Numerical Simulations

The NMR numerical simulation has provided an alternative way to study the spectroscopic implementations. We have observed the deviation between the experimental data and analytical solutions due to the errors in the implementation. To explore the source and relative size of these errors, we simulated perfect experiments, each time adding controlled errors in four sections of the implementation:

- The linear approximation in the initialization
- Inefficiency of the decoupling sequence
- Swap gate errors
- Collision operator errors

The errors originating from the imperfect decoupling sequence caused least impact to the mass density, followed by the errors in the SWAP gates. The Fourier transform approximation executes a correct writing of the desired magnetization only to first

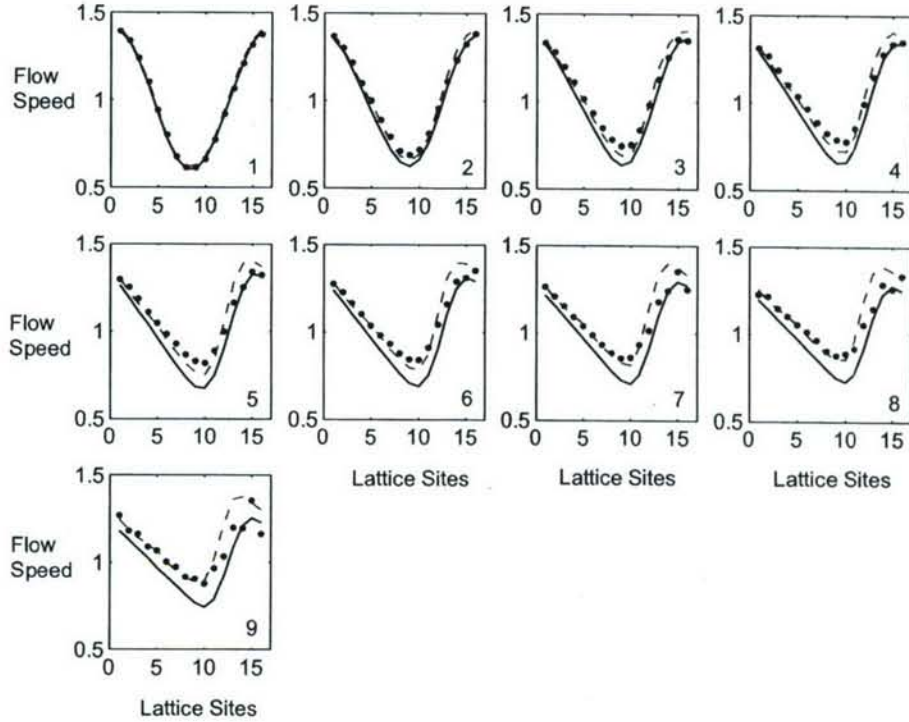


Figure 4-3: Experimental data The experimental data (dots) are plotted, together with plots of the analytical solutions (solid lines) and the numerical simulations (dash lines) of the NMR experiment. Nine time steps (numbers) of the algorithm have been carried out on 16 two-qubit sites. The vertical axis is associated with flow speed and the horizontal axis presents the lattice sites. The simulations closely match the data, suggesting that the deviation between the analytical results and the data can be attributed to four imperfection controls, discussed below, in the implementations.

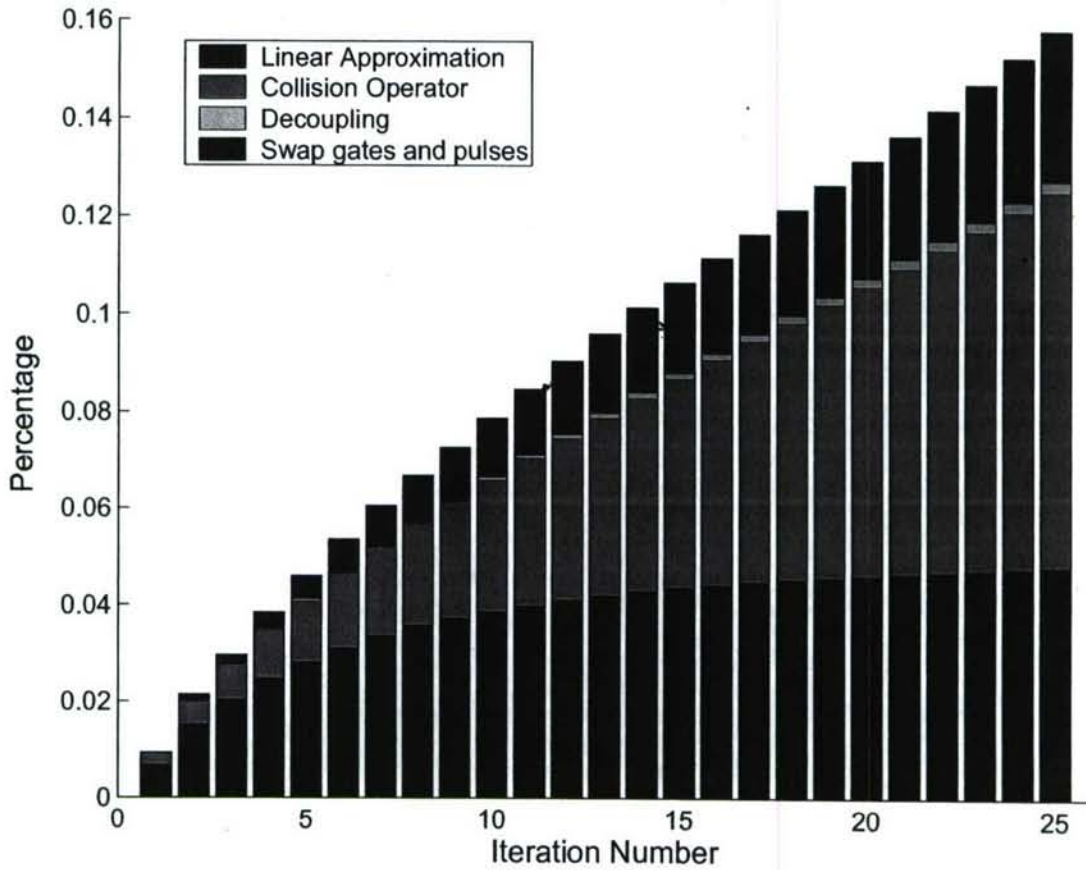


Figure 4-4: **Relative strength of four types of errors** We present the relative strength of each source here. Horizontal axis is denoted by time steps and vertical axis shows the difference between the simulation results with the analytical solutions. We notice that the deviation is mainly caused by the linear approximation at the beginning and the accumulated errors in the collision operators take over after a few time steps.

order in the overall flip angle. The largest deviations originated from realistic simulations of the collision gate. It is important to note that the simulated gate fidelities for the swap and collision gates, although imperfect, are still about 0.995. This suggests that the observed deviations are caused by the coherent buildup of errors through a few iterations, and not just by the individual errors from a single gate. The complete simulation result, showing the relative size of each error, is plotted in Fig. 4-4.

In the NMR implementations to date there are two important sources of systematic errors: (1) a linear approximation relating the excited magnetization to the

Fourier components of the shaped RF pulse; and (2) errors from the repeated collision operators. Here we explore the impact of these errors on a simple computation and illustrate a simple means of reducing the accumulated errors. In summary, one of the most important challenges to implement a useful type-II quantum architecture is to avoid the accumulation of systematic errors. In the next section, our discussion aims to an alternative method to mitigate the growth of systematic errors.

4.1.5 The Collision Operator with Modulated Phases

The first-order accurate Fourier approximation was expected to be the dominant error source in the NMR implementation. However, NMR simulations with controlled errors shows that the systematic error induced by the experimental implementation of the unitary collision operator associated with the QLQ algorithm is the major challenge. Replacing the single collision operator with a set of operators to randomize errors allows us to improve the robustness of the implementation.

In the implementation of the Burgers equation, we also observed deviations between the numerically predicted data points and analytically predicted solutions. The major error sources in the NMR implementation are known, so to explore the source and relative strength of these errors, we have simulated the NMR experiments. The major error source in this implementation is the collision operator, and it is introduced by ignoring the scalar coupling between proton and carbon during the RF pulses. When applying a RF pulse on the proton qubit, the Hamiltonian in the rotating form is $H = 2\pi J\sigma_z^H\sigma_z^C + \gamma_H B_1\sigma_x^H$, where B_1 is the strength of the RF pulse. With the presence of the scalar coupling, a small portion of the proton magnetization has been transferred to the carbon qubit. Therefore, the applied propagator can be recast as $U = U_{\text{desired}}U_{\text{error}}$.

The error in the collision operator is a systematic error that builds up throughout the successive time steps. Although this is not the significant error at the beginning of the implementation, it eventually dominates the first-order error due to the Fourier approximation and becomes the dominant issue after just several time step interactions. Notice that while the reduction of the initial magnetization from the Fourier

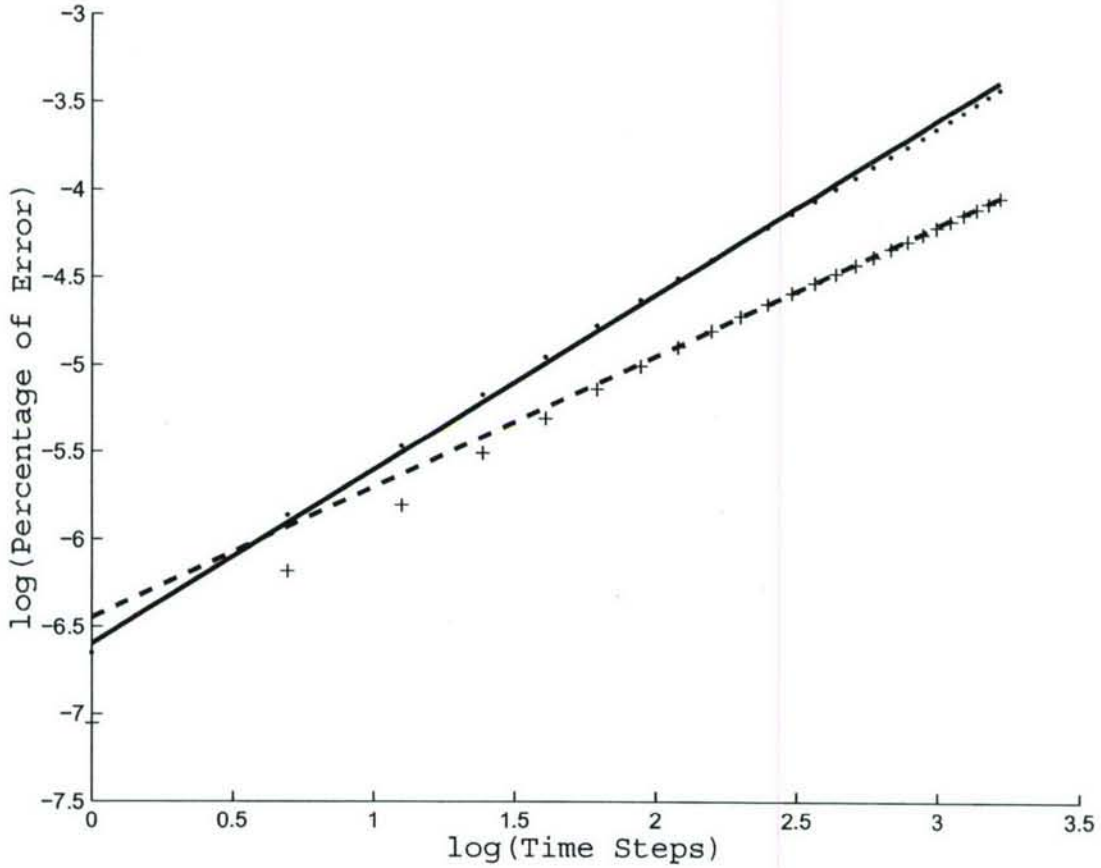


Figure 4-5: **Systematic errors** The growth of the systematic errors due to the collision operator in two NMR implementation. The single collision operator data (dots) is fit (solid line) with a line of slope 1, which shows linear growth of the error. The collision operator data with modulated phases (pluses) is the fit with a line of slope 3/4 (dashed line). The buildup of the systematic errors has been slowed down by proposed method. However, the systematic errors have not been totally converted into random errors.

transform is systematic, since the magnetization profile is changing the errors are not precisely repeated. In the collision operator, however, the errors are exactly the same from step to step. In addition we expect that the radio frequency inhomogeneity leads to strongly correlated errors in the lattice encoding. Hence, we have proposed replacing a single collision operator with a set of collision operators that have similar fidelity but randomized error terms.

Since the collision operator for the Burgers equation is a zero-order coherence term, the collision operator commutes with the rotation operator. Therefore, we

apply a 90° rotation operator to the collision operator at each step to mitigate error growth. Consequently, a dramatic improvement is observed as shown in Fig. 4-5. On a logarithmic plot, the simulation results fit a line with a slope of $3/4$. If the error terms in the collision operators were totally randomized and hence followed a Gaussian distribution, the best-fit regression line should have had a slope of $1/2$. The deviation between our simulation data and the ideal Gaussian case indicates residual systematic error in the collision operator. In a future study, we may use strongly modulated pulses to randomize the error terms [31].

The experimental number densities are over-plotted in Fig. 4-6 with the exact analytical solutions. Eight successive time steps of the quantum algorithm were implemented on 16 two-qubit sites. An improvement of our present experimental approach using collision operators with modulated phases is observed. The agreement of the data to the analytical solutions is encouraging and suggests that totally randomizing error terms in the collision operator may offer further improvement.

4.2 Conclusion

From the simulation, we find the major error sources are due to imperfect control of the quantum spin system and the Fourier approximation associated with setting its magnetization profile. Our proposed method for converting the systematic errors into random errors is effective. The improvement we achieve relative to the previous experiment is encouraging, and it demonstrates the possibility of using the same technique in future studies. The closeness of the numerical data to the exact analytical results for the nonlinear Burgers equation further proves the practicality of implementing the QLG algorithm using a spatial NMR technique. In addition, although the limitation of the Fourier approximation is not dominant, the problem of precisely initializing a lattice of QIPs still remains an open issue.

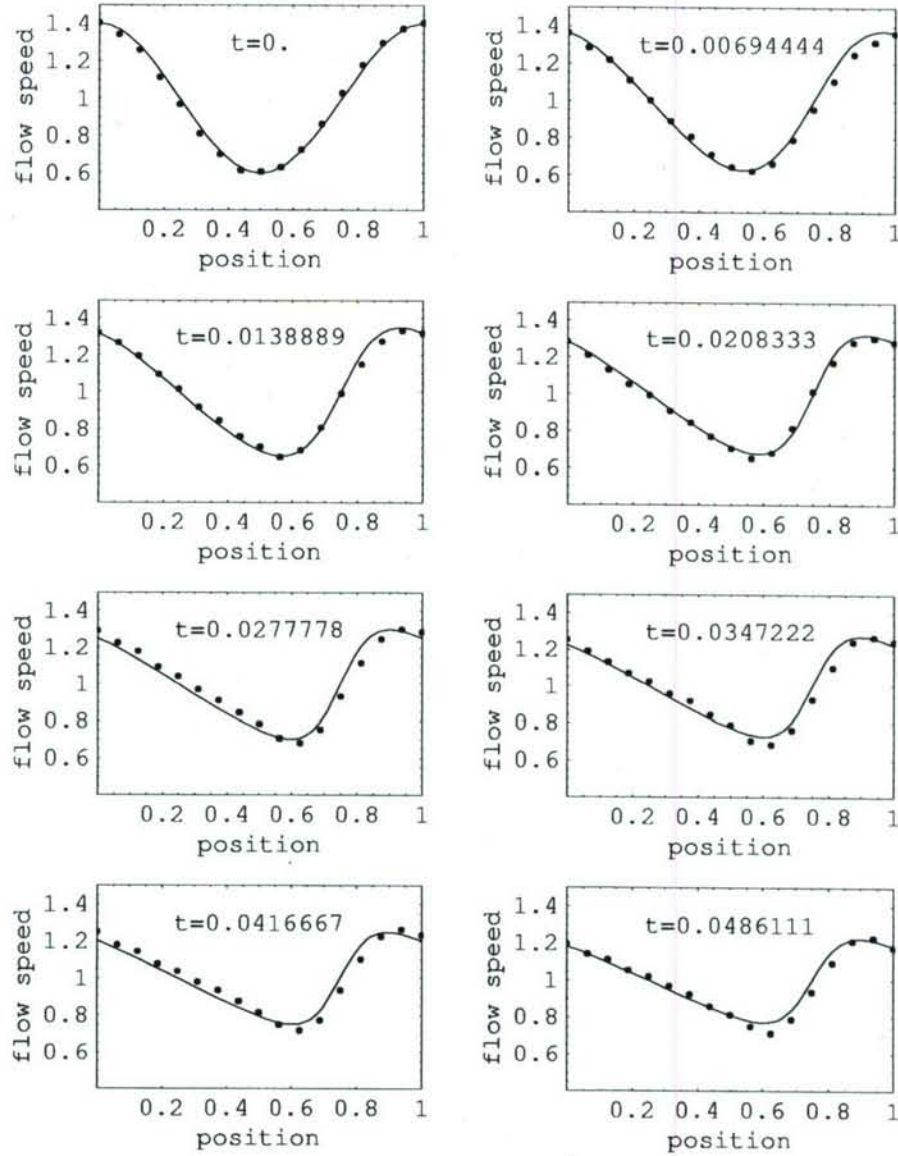


Figure 4-6: **Experiment data versus analytical results** The experimental data are plotted together with the analytical solutions for 8 time steps on a lattice of 16 parallel two-qubit QIPs. Viscosity: $\frac{1}{4} \frac{\Delta x^2}{\Delta t}$. Experimental NMR data (dots) versus analytical solution (curves). Randomizing the error terms in the collision operator has improved the experimental results dramatically.

4.3 Other Error Sources

Other potential sources of errors include signal to noise, the state fidelity of the starting pseudo pure state, and gradient switching time. In addition, the random self-diffusion of the liquid molecules in the presence of a strong gradient can result in a substantial loss of signal. Although these errors were not significant in our implementation, they are likely to become important as more complicated algorithms are executed on larger lattices.

In particular, molecular diffusion over the time of an operation places a lower bound on the physical size of the volume element corresponding to each site in the computation. In the 1-D case discussed here, the root-mean-squared displacement ($\Delta z = \sqrt{2Dt}$) for chloroform ($D = 2.35 \times 10^{-5} \text{ cm}^2/\text{s}$) is about $10.8 \mu\text{m}$ over the 25 ms needed for encoding and the collision operator. Since the actual volume element were about $625 \mu\text{m}$ across, this resulted in a negligible mixing of the information in adjacent sites. However, it is clear that for this approach to type-II quantum computer to remain viable for large matrixes and more complex collision operators the physical size of the sample must grow with the size of the problem.

4.4 Discussion

It has been suggested by Peter Love in [32] that the transition matrix \mathbf{A} in the type-II lattice gas algorithms for the Burgers equation may not be a doubly stochastic matrix. It should be clear here that the transition matrix defining the lattice Boltzmann equation is not the collision operator defined in the algorithms. We begin the discussion by deriving the transition matrix \mathbf{A} from the unitary collision operator \hat{C} . The occupation numbers in the classical Boltzmann model are encoded as the diagonal terms in the density matrix $\mathbf{n} = [(1 - f_1)(1 - f_2), (1 - f_2)f_1, f_2(1 - f_1), f_1f_2]$. The collision step of the Boltzmann model is given by the multiplication of the vector \mathbf{n} by the transition matrix that satisfies normalization and semi-detailed balance. In our type-II simulation, the result of the collision step is reproduced by conjugating

the density matrix by the collision operator. The transition matrix is denoted by the effect of this conjugation on the diagonal elements in the density matrix.

As mentioned earlier in this chapter, the collision transformation can be expressed by a general block-diagonal unitary matrix with complex coefficient:

$$\hat{C} = \begin{pmatrix} 1 & 0 & 0 & 0 \\ 0 & e^{i\phi} e^{i\xi} \cos \theta & e^{i\phi} e^{i\zeta} \sin \theta & 0 \\ 0 & -e^{i\phi} e^{-i\zeta} \sin \theta & e^{i\phi} e^{-i\xi} \cos \theta & 0 \\ 0 & 0 & 0 & 1 \end{pmatrix}. \quad (4.13)$$

Therefore, quantum transition map on the diagonal elements in the density matrix can be written as:

$$\begin{aligned} \rho'_{11} &= \rho_{11} \\ \rho'_{22} &= \cos^2 \theta \rho_{22} + \sin^2 \theta \rho_{33} + e^{-i(\xi-\zeta)} \cos \theta \sin \theta \rho_{32} + e^{i(\xi-\zeta)} \cos \theta \sin \theta \rho_{23} \\ \rho'_{33} &= \sin^2 \theta \rho_{22} + \cos^2 \theta \rho_{33} - e^{-i(\xi-\zeta)} \cos \theta \sin \theta \rho_{32} - e^{i(\xi-\zeta)} \cos \theta \sin \theta \rho_{23} \\ \rho'_{44} &= \rho_{44} \end{aligned} \quad (4.14)$$

The transition matrix then contains two components: classical diffusive part and quantum mechanical part as described:

$$\mathbf{A} = \begin{pmatrix} 1 & 0 & 0 & 0 \\ 0 & \cos^2 \theta & \sin^2 \theta & 0 \\ 0 & \sin^2 \theta & \cos^2 \theta & 0 \\ 0 & 0 & 0 & 1 \end{pmatrix} + \frac{1}{2} \cos 2\theta \begin{pmatrix} 0 & 0 & 0 & 0 \\ 0 & e^{-i(\xi-\zeta)} \frac{\rho_{32}}{\rho_{22}} & e^{i(\xi-\zeta)} \frac{\rho_{23}}{\rho_{33}} & 0 \\ 0 & -e^{-i(\xi-\zeta)} \frac{\rho_{32}}{\rho_{22}} & -e^{i(\xi-\zeta)} \frac{\rho_{23}}{\rho_{33}} & 0 \\ 0 & 0 & 0 & 0 \end{pmatrix}, \quad (4.15)$$

where the quantum mechanical part gives rise non-diffusive behavior, the nonlinear shock formation characteristic of the Burgers equation. Furthermore, the quantum mechanical part brings the off-diagonal information to the diagonal elements, introducing local quantum superposition and entanglement. Thus, the new values of the occupation probabilities in the lattice Boltzmann model is not, exclusively, determined by the occupation numbers in the previous step.

The unitarity of \hat{C} implies that the classical part of the transition matrix A obeys normalization and semi-detailed balance. It is trivial to realize that the sum of each column in the second term is zero. Thus, any arbitrary collision operator for the Burgers equation obeys the semi-detailed balance. To formulate a sufficient normalization constraint, we simplify the constraint to be

$$e^{-i(\xi-\zeta)} \frac{\rho_{32}}{\rho_{22}} + e^{i(\xi-\zeta)} \frac{\rho_{23}}{\rho_{33}} = 0. \quad (4.16)$$

Only when Eq. 4.16 is satisfied, the collision transformation is a doubly stochastic matrix. Therefore, it leaves us an open issue about the algorithms and further discussion should be invoked.

The systematic error that we discussed in this chapter is not caused by this open problem, but introduced by the imperfect implementations. Details about the quantum control of the NMR system are accessible in [36, 37, 38, 39].

Chapter 5

Linear Approximation

We utilize the magnetic image technique to slice NMR spin ensemble into a lattice of cells and address all the spatial locations simultaneously. This technique is essentially the application of shaped RF pulses in the presence of a gradient field as a means of exciting selective frequencies. If the flip angle of the shaped pulse is small and the excited magnetizations, to a good approximation, are proportional to the Fourier transform of the RF waveform. As a result, the RF waveform can also be determined by the inverse Fourier transform of the desired transverse magnetization. The above technique allows the encoding of arbitrary shapes at the various spatial locations in our experiment. However, this Fourier approach for determining the frequency selectivity of a pulse sequence is only accurate to the first order and generates potential error sources.

We aim to remove the linear approximation by mapping lattice cells to a set of Fourier components in the k -space, a space reciprocal to the spatial locations. This new approach gives us the freedom to perform the streaming step quantum mechanically by controlling the linear magnetic field gradients. It may arise new applications using this particular architecture for quantum lattice gas algorithms.

We have chosen to the diffusion equation to explore the NMR implementation using the k -space mapping. Diffusion equation provides a neat and robust test since low frequencies Fourier components in the magnetization profile are less sensitive to errors.

5.1 Mapping to k -space

In a type-II quantum lattice gas algorithm, the occupation probabilities are encoded to the wave function of lattice sites. Each occupation probability $f_i(z, t)$ is represented as the quantum mechanical expectation value of finding a two-level system in its excited state. The combined two-qubit wave function for a single node becomes $|\psi(z, t)\rangle = \sqrt{f_1 f_2}|11\rangle + \sqrt{f_1(1-f_2)}|10\rangle + \sqrt{(1-f_1)f_2}|01\rangle + \sqrt{(1-f_1)(1-f_2)}|00\rangle$. The collision operator is a unitary evolution matrix applied homogeneously across all the lattice sites causing local quantum superposition and entanglement, $|\psi'(z, t)\rangle = \hat{C}|\psi(z, t)\rangle$. Measurement process is a non-unitary action that destroys all the superpositions and entanglements caused by the previous step, resulting in $f_i(z, t) = \langle\psi(z, t + \Delta t)|\hat{n}_i|\psi(z, t + \Delta t)\rangle$, where \hat{n}_i are the number operators. In practice, the occupation numbers must be determined by repeated measurement of a single realization or by a single measurement over a statistical ensemble. The NMR ensemble nature make this measurement particular simple.

The wave function method outlined above is adequate for simple problems that consists of few spins, but becomes tedious to describe more complicated cases involving more spins. The magnetic state of the NMR ensemble, therefore, is conveniently defined using the density matrix formalism. The density matrix corresponded to the wave functions is

$$\rho(z, t) = |\psi(z, t)\rangle\langle\psi(z, t)|. \quad (5.1)$$

and the collision step can be reformulated as

$$\rho'(z, t) = \hat{C}\rho(z, t)\hat{C}^\dagger. \quad (5.2)$$

The measurement process consists in taking the trace of the measurement operator acting on the density matrix of the system being measured:

$$\langle n_i \rangle = \text{tr} [\rho(z, t)\hat{n}_i]. \quad (5.3)$$

A similar presentation of the lattice can be formulated in the k -space by creating

the correspondence between a lattice node with a Fourier component, generated by magnetic field gradients. Once a static field gradient is applied, the spin procession frequency varies linearly with the position along the z direction. It induces the transverse phase to accumulate linearly with position as well. The gradient field, therefore, modulate the transverse magnetization into a spatial helix, referred as a Fourier component characterized with its wave number k . A RF pulse can modulate the phase and amplitude of each Fourier helix and also produce amplitude modulated magnetization gratings along z direction by transforming the transverse magnetizations to longitudinal direction. However, a RF pulse does not change the pitch of the grating and only the gradients can change the k value of each component to another in the k -space. Due to the linear nature of the k -space, each separate Fourier component may be treated independently. The corresponding formalism of the density matrix 5.1 results in

$$\rho(k, t) = |\psi(k, t)\rangle\langle\psi(k, t)|, \quad (5.4)$$

where k indicates a lattice cell. The evolution of the collision step is described by the following equation

$$\rho'(k, t) = \hat{C}\rho(k, t)\hat{C}^\dagger. \quad (5.5)$$

Then, the measurement is given by

$$\langle \hat{n}_i \rangle = \text{tr} [\rho(k, t)\hat{n}_i]. \quad (5.6)$$

5.2 NMR Implementation

The same room-temperature solution of labeled chloroform used in the previous experiments has been selected. The resonant frequencies of the two spins, hydrogen and labeled carbon, in this heteronuclear molecule is about 225MHz apart in 10 T magnet. Therefore, a single pulse on resonance with one spin will not affect the other. The interaction term between the spins can be characterized by the scalar coupling constant $J = 214\text{Hz}$. More details about the sample can be found in Chapter 3.

5.2.1 Encoding

Individual addressing the sites of the lattice is established by a sequence of RF pulses followed by the gradient Hamiltonians. We begin by studying the evolution of a one-spin system and the small angle approximation is invoked here to simplify the calculation. Then the discussion moves to a weakly coupled two-spin system. In this system, there are two important challenges to implement a type-II quantum architecture: (1) lattice initialization to an identical Fourier component; and (2) the internal Hamiltonian interfering information between spins. We demonstrate that the usage of π pulses on one spin in conjunction with two static gradients for the same duration can give the desired results. Wisely selecting the gradient strengths, the Fourier helices associated with both spins can have same wave number even though they have different gyro-magnetic ratios. The π pulses modulate the interaction Hamiltonian and refocus scalar term after one period of the sequence: the system, thus, can be treated independently as two one-spin systems.

First, consider the Hamiltonian for a one-spin system subjected to a RF pulse applied in the y -direction followed by a linear field gradient in the z -direction. The RF Hamiltonian is

$$H_{RF} = -\frac{1}{2}\omega_y\sigma_y. \quad (5.7)$$

and the gradient Hamiltonian is

$$H_G = -\frac{1}{2}\left(\gamma\frac{\partial B_z}{\partial z}z\right)\sigma_z = -\frac{1}{2}\gamma Gz\sigma_z, \quad (5.8)$$

where ω_y is a constant value during the pulse time τ and the gradient term is a linearly varying static field. The static gradient strength is denoted by G . The evolution of the period $\tau + \Delta t$ becomes

$$U(t = \tau + \Delta t) = \exp\left[\frac{i}{2}\Delta k_z z\sigma_z\right] \exp\left[\frac{i}{2}\omega_y\tau\sigma_y\right] \quad (5.9)$$

where Δk_z is the wavenumber, parametered as $\Delta k_z = \gamma\frac{\partial B_z}{\partial z}\Delta t$. The evolution of an

initial density matrix $\rho_0 = \sigma_z$ through a single period yields

$$\rho(\tau + \Delta t) = U \sigma_z U^\dagger = \sin(\omega_y \tau) \exp\left[\frac{i}{2} \Delta k_z z \sigma_z\right] \sigma_x \exp\left[-\frac{i}{2} \Delta k_z z \sigma_z\right] + \cos(\omega_y \tau) \sigma_z. \quad (5.10)$$

If the small angle approximation applies, the density matrix becomes

$$\rho(\tau + \Delta t) \approx \omega_y \tau \exp\left[\frac{i}{2} \Delta k_z z \sigma_z\right] \sigma_x \exp\left[-\frac{i}{2} \Delta k_z z \sigma_z\right] + \sigma_z. \quad (5.11)$$

Another period evolution will affect the σ_z term as described above, creating the new magnetization helix and incrementing wavenumber by Δk_z . The final result is the formation of many Δk_z components

$$\sigma_z \rightarrow \sum_{n=1}^N \omega_y(n) \tau \exp\left[\frac{i}{2} n \Delta k_z z \sigma_z\right] \sigma_x \exp\left[-\frac{i}{2} n \Delta k_z z \sigma_z\right] + \sigma_z. \quad (5.12)$$

Each term in summation can be interpreted as a cylindrical Fourier component of the transverse magnetization weighted by the RF nutation rate $\omega_y(n)$.

Next step, we will consider the evolution of two weakly coupled spins with gyro-magnetic ratio γ_H and γ_C , respectively. The RF Hamiltonian is expressed as the sum of two single RF terms because of the realization that both spins are addressed independently through two channels.

$$H_{RF} = -\frac{1}{2} \omega_y^1 \sigma_y^1 - \frac{1}{2} \omega_y^2 \sigma_y^2 \quad (5.13)$$

and the gradient Hamiltonian gives

$$H_G = -\frac{1}{2} (\gamma_H + \gamma_C) \frac{\partial B_z}{\partial z} z \sigma_z = -\frac{1}{2} (\gamma_H + \gamma_C) G z \sigma_z, \quad (5.14)$$

Consequently, the evolution operator of a single period consists of two exponential terms: a single spin rotation and gradient evolution term. Since the internal Hamiltonian commutes with the gradient Hamiltonian, the gradient evolution can be expressed

by two separate terms as well,

$$\begin{aligned}
U(t = \tau + \Delta t) &= \exp \left[\frac{i}{2} (\Delta k_z^1 \sigma_z^1 + \Delta k_z^2 \sigma_z^2) z + \frac{i\pi J}{2} \sigma_z^1 \sigma_z^2 \Delta t \right] \exp \left[\frac{i}{2} (\omega_y^1 \sigma_y^1 + \omega_y^2 \sigma_y^2) \tau \right] \\
&= \exp \left[\frac{i}{2} (\Delta k_z^1 \sigma_z^1 + \Delta k_z^2 \sigma_z^2) z \right] \exp \left[\frac{i\pi J}{2} \sigma_z^1 \sigma_z^2 \Delta t \right] \\
&\quad \exp \left[\frac{i}{2} (\omega_y^1 \sigma_y^1 + \omega_y^2 \sigma_y^2) \tau \right],
\end{aligned} \tag{5.15}$$

where the exponential terms of $\sigma_z^1 \sigma_z^2$ are attributed to the internal Hamiltonian. One may realize that the scalar coupling evolution has not been considered during the RF pulse. It has been neglected because the total nutation frequencies induced by the RF Hamiltonians are much stronger than the interaction constant.

An initial density matrix $\sigma_z^1 + \sigma_z^2$ through a single period becomes

$$\begin{aligned}
\rho = U(\sigma_z^1 + \sigma_z^2)U^\dagger &= \sigma_z^1 + \sigma_z^2 + \exp \left[\frac{i}{2} (\Delta k_z^1 \sigma_z^1 + \Delta k_z^2 \sigma_z^2) z \right] \\
&\quad \exp \left[\frac{i\pi J}{2} \sigma_z^1 \sigma_z^2 \Delta t \right] (\omega_y^1 \tau \sigma_x^1 + \omega_y^2 \tau \sigma_x^2) \exp \left[\frac{-i\pi J}{2} \sigma_z^1 \sigma_z^2 \Delta t \right] \\
&\quad \exp \left[\frac{-i}{2} (\Delta k_z^1 \sigma_z^1 + \Delta k_z^2 \sigma_z^2) z \right].
\end{aligned} \tag{5.16}$$

A string of π pulses on the first spin is applied to modulate the Fourier components, remove the chemical shift, and refocus the scalar interactions. The π pulse along x modulates σ_z , σ_y terms with minus signs and leaves σ_x operator unchanged: $\sigma_x \rightarrow \sigma_x$, $\sigma_y \rightarrow -\sigma_y$, $\sigma_z \rightarrow -\sigma_z$. After a single π pulse along x on qubit 1, the density matrix picks up a minus sign for all the terms which contain σ_z^1 and σ_y^1 :

$$\begin{aligned}
\rho &= -\sigma_z^1 + \sigma_z^2 + \exp \left[\frac{-i}{2} (-\Delta k_z^1 \sigma_z^1 + \Delta k_z^2 \sigma_z^2) z \right] \exp \left[\frac{-i\pi J}{2} \sigma_z^1 \sigma_z^2 \Delta t \right] \\
&\quad (\omega_y^1 \tau \sigma_x^1 + \omega_y^2 \tau \sigma_x^2) \exp \left[\frac{i\pi J}{2} \sigma_z^1 \sigma_z^2 \Delta t \right] \exp \left[\frac{i}{2} (-\Delta k_z^1 \sigma_z^1 + \Delta k_z^2 \sigma_z^2) z \right].
\end{aligned} \tag{5.17}$$

The operator, given by the application of a static gradient for another period Δt with a variant strength, causes the internal Hamiltonian average over at the end of the

period,

$$\begin{aligned} \rho = & -\sigma_z^1 + \sigma_z^2 + \exp \left\{ \frac{i}{2} [(\Delta k_z^{1'} - \Delta k_z^1)\sigma_z^1 + (\Delta k_z^{2'} + \Delta k_z^2)\sigma_z^2] z \right\} \\ & (\omega_y^1 \tau \sigma_x^1 + \omega_y^2 \tau \sigma_x^2) \exp \left\{ \frac{-i}{2} [(\Delta k_z^{1'} - \Delta k_z^1)\sigma_z^1 + (\Delta k_z^{2'} + \Delta k_z^2)\sigma_z^2] z \right\}, \end{aligned} \quad (5.18)$$

where wave numbers of corresponding Fourier components on both spins are increased by $\Delta k_z^{1'}$ and $\Delta k_z^{2'}$ respectively. Another π pulse, following the magnetic gradient, is performed to reverse the minus signs on all the σ_z^1 terms,

$$\begin{aligned} \rho = & \sigma_z^1 + \sigma_z^2 + \exp \left\{ \frac{i}{2} [(\Delta k_z^1 - \Delta k_z^{1'})\sigma_z^1 + (\Delta k_z^2 + \Delta k_z^{2'})\sigma_z^2] z \right\} \\ & (\omega_y^1 \tau \sigma_x^1 + \omega_y^2 \tau \sigma_x^2) \exp \left\{ \frac{-i}{2} [(\Delta k_z^1 - \Delta k_z^{1'})\sigma_z^1 + (\Delta k_z^2 + \Delta k_z^{2'})\sigma_z^2] z \right\}. \end{aligned} \quad (5.19)$$

We can rewrite Eq. 5.19 as Eq. 5.20 if the actions of the gradient Hamiltonians on both qubits are identical, $\Delta k_z^1 - \Delta k_z^{1'} = \Delta k_z^2 + \Delta k_z^{2'} = \Delta k_z$.

$$\rho = \sigma_z^1 + \sigma_z^2 + \exp \left[\frac{i}{2} \Delta k_z (\sigma_z^1 + \sigma_z^2) z \right] (\omega_y^1 \tau \sigma_x^1 + \omega_y^2 \tau \sigma_x^2) \exp \left[\frac{-i}{2} \Delta k_z (\sigma_z^1 + \sigma_z^2) z \right]. \quad (5.20)$$

Effects of both field gradients accumulate on the carbon nucleus, while the second gradient attenuates, to some extent, the first one for the proton spin. Thus, the deviation between the k values caused by the different gyro magnetic ratios is compensated by applying the above pulse sequence. The condition is satisfied if the ratio of two gradients obeys

$$\frac{G_1}{G_2} = \frac{\gamma_H + \gamma_C}{\gamma_H - \gamma_C}. \quad (5.21)$$

The procedure described above is illustrated in Fig. 5-1.

After n periods application of the composition of RF pulses and gradients, it gives

$$\begin{aligned} \sigma_z^1 + \sigma_z^2 & \rightarrow \sigma_z^1 + \sigma_z^2 + \\ & \sum_{n=1}^N \exp \left[\frac{i}{2} n \Delta k_z (\sigma_z^1 + \sigma_z^2) z \right] [\omega_y^1(n) \tau \sigma_x^1 + \omega_y^2(n) \tau \sigma_x^2] \exp \left[\frac{-i}{2} n \Delta k_z (\sigma_z^1 + \sigma_z^2) z \right]. \end{aligned} \quad (5.22)$$

The exact solution can be achieved and it is given in [30],

$$\begin{aligned} \sigma_z^1 + \sigma_z^2 &\rightarrow \prod_{n=1}^N \cos(\omega_y^1(n)\tau) \sigma_z^1 + \prod_{n=1}^N \cos(\omega_y^2(n)\tau) \sigma_z^2 + \\ &\sum_{n=1}^N \exp \left[\frac{i}{2} n \Delta k_z (\sigma_z^1 + \sigma_z^2) z \right] \left[A_N^1(n) \sigma_x^1 + A_{N,z}^1(n) \sigma_z^1 + A_N^2(n) \sigma_x^2 + A_{N,z}^2(n) \sigma_z^2 \right] \\ &\exp \left[\frac{-i}{2} n \Delta k_z (\sigma_z^1 + \sigma_z^2) z \right]. \end{aligned} \quad (5.23)$$

For a train of RF pulses of nutation angles $\omega_y^1(n)$ and $\omega_y^2(n)$ all with the same phase, the n th transverse and longitudinal Fourier series coefficient after N th pulses, may be determined from the previous coefficients by the recursion relationships

$$\begin{aligned} A_N^i(n) &= A_{N-1}^i(n-1) \cos^2(\omega_y^i(n)\tau/2) - A_{N-1}^i(-n-1) \sin^2(\omega_y^i(n)\tau) \\ &\quad - A_{N-1,z}^i(|n|) \sin(\omega_y^i(n)\tau) \left(\frac{\epsilon_n}{2} \right) \\ A_{N,z}^i(n) &= \left[A_{N-1}^i(n-1) + A_{N-1}^i(-n-1) \right] \frac{\sin(\omega_y^i(n)\tau)}{\epsilon_n} \\ &\quad + A_{N-1,z}^i(n) \cos(\omega_y^i(n)\tau) \end{aligned} \quad (5.24)$$

where $\epsilon_n = 1 + \delta_n$. Initial conditions have to satisfy that $A_{0,z}^i(n) = \delta_n$ and that all $A_0^i(n) = 0$. The appropriate choice of the nutation angles enable us to construct arbitrary density matrix.

5.2.2 Collision

The choice of the particular components of the unitary collision operator determines the form of the macroscopic effective field theory and values of its transport coefficients. The same collision operator for the diffusion equation has been chosen:

$$\hat{C} = \exp \left[-i \frac{\pi}{8} \left(\sigma_x^1 \sigma_x^2 + \sigma_y^1 \sigma_y^2 + \sigma_z^1 \sigma_z^2 \right) \right]. \quad (5.25)$$

We already learn that a RF pulse does not shift the k value of each component, indicating the information between the neighbors cannot be manipulated using RF pulses and scalar evolution. Therefore, the local quantum collision gate can be accomplished

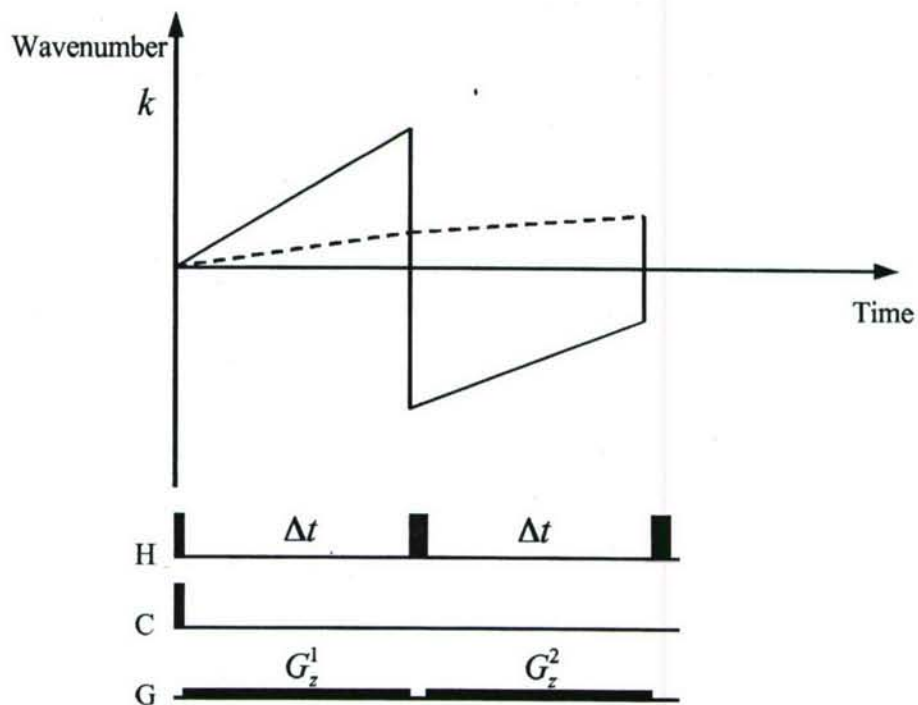


Figure 5-1: **One step in the initialization** One period of the sequence used in the initialization and corresponding changes of k values in the k -space are presented. The solid line, in the k space diagram, illustrates the shift of the wave number for the hydrogen spin while the time iterates forwards. The dash line gives the movement of k value for the carbon. At the end of the sequence, the wave numbers of the characteristic Fourier components of both spins are incremented by the same amount. Below the plot, the pulse sequence is demonstrated.

by the same pulse sequence described in Chapter 3.

5.2.3 Measurement

The occupation numbers resulting from the collision are obtained by measuring the z -magnetization, corresponding to $n_i = \frac{1}{2}(1 + \sigma_z^i)$. Since only the σ_x^i and σ_y^i operators are directly observable, a $\pi/2$ pulse transformed the z -magnetization into x -magnetization.

The measurements are carried out in two separate experiments, where a SWAP gate is applied to bring the magnetization from carbon channel to the proton channel due to the higher signal-to-noise ratio in the proton channel.

During the process, a weak magnetic field gradient is applied to refocus the gradient Hamiltonians. It is easy to realize that the signal is only observable while the k value is around zero. Otherwise, the ensemble signal is averaged over across the sample. Note that a spatial map of spin density in the sample weighted in some fashion during the measurement. The corresponding modulation function for our finite and uniform sample is a sinc function. Instead of observing a sharp magnetization peak, the signal is specified by a sinc function. Hence, the readout gradient has to be weak enough to separate the overlap between two sinc functions induced by the spin density.

5.2.4 Streaming

The last step of the QLG algorithm, we shift the occupation numbers obtained in the previous step to its nearest neighbors. In the k -space, the streaming step can be easily created by the application of linear field gradients sandwiched with π pulses: $G_3(z)\Delta t \rightarrow [\pi]_x^H \rightarrow G_4(z)\Delta t \rightarrow [\pi]_x^H$, where $G_3(z)$, $G_4(z)$ are the gradient strength and Δt is the duration. This sequence illustrates a single propagation where the occupation probability on the first qubit at site $n\Delta k$ moves to site $(n-1)\Delta k$, while the occupation number on the second spin advances to site $(n+1)\Delta k$. The shift of

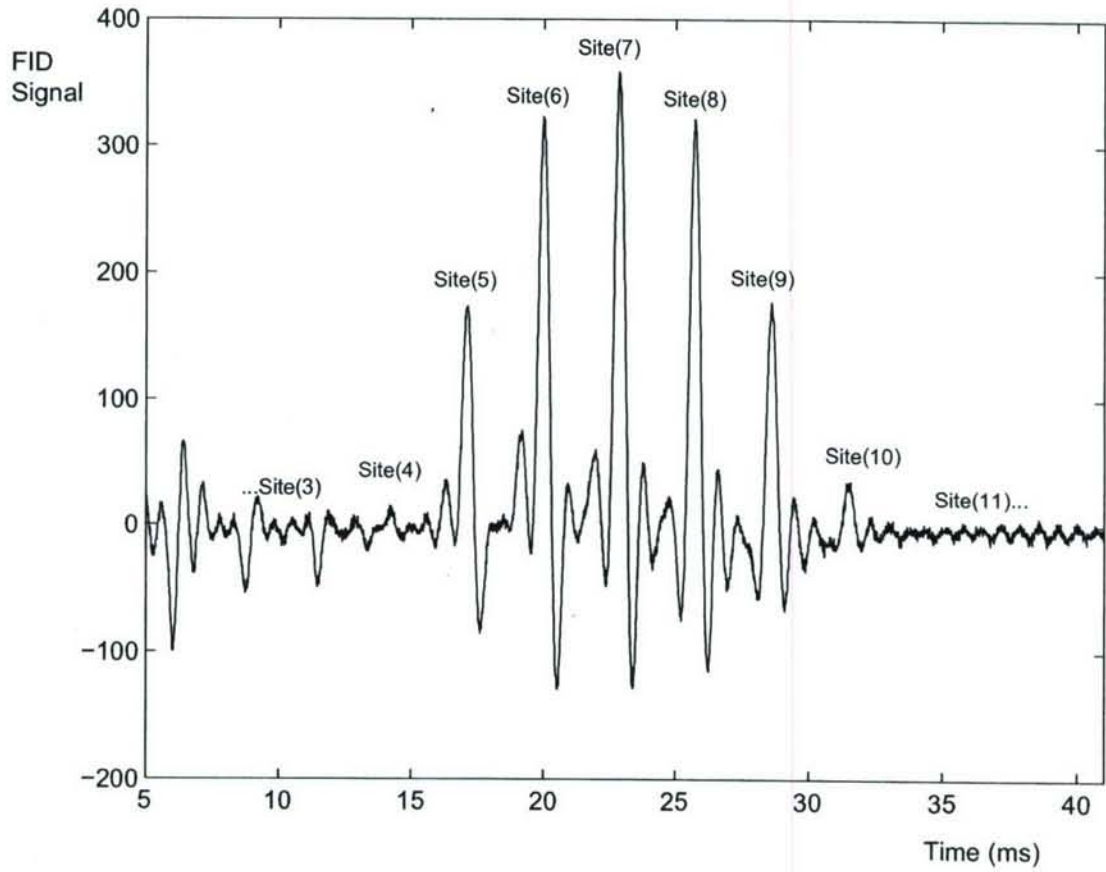


Figure 5-2: **Readout** Measurement on the hydrogen spin is illustrated here. The magnetization peaks are related to the occupation numbers at each lattice site by $n_i = \frac{1}{2}(1 + \sigma_z^i)$. The observed spectrum is imposed by a sinc function.

the k values should satisfy the following equation,

$$-(\Delta k_z^{1'} - \Delta k_z^1) = \Delta k_z^2 + \Delta k_z^{2'} = \Delta k. \quad (5.26)$$

Hence, the relation between two field gradients can be derived by

$$\frac{G_3(z)}{G_4(z)} = \frac{\gamma_H + \gamma_C}{\gamma_H - \gamma_C}. \quad (5.27)$$

Choose an identical time period Δt as in the lattice initialization step resulting in $G_3(z) = G_2(z)$ and $G_4(z) = G_1(z)$.

5.3 Conclusion and Discussion

The experimental mass densities are plotted in Fig. 5-3 with the exact analytical solutions. Four successive time steps of the quantum algorithm were implemented on 16 two-qubit sites.

Here, we demonstrate a single streaming step accomplished by the linear magnetic field gradient. Notice that contiguously applying the collision step and streaming step doesn't lead us to the numerical solution for the diffusion equation. However, it can be used to implement some type-I quantum lattice gas algorithms.

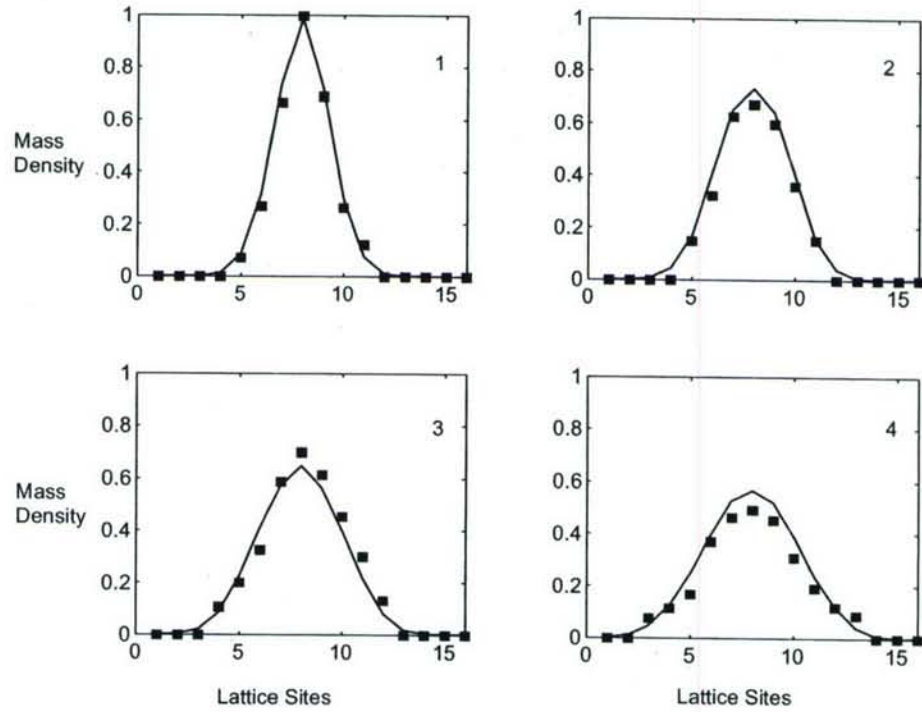


Figure 5-3: **k-space experimental data versus analytical solutions** The experimental data (dots) are plotted together with analytical solutions (solid lines) for four time steps on 16 two-qubit sites.

Chapter 6

Type-I Quantum Lattice Gas Algorithms

The difficulty of constructing, controlling and maintaining coherence in a single complicated quantum device makes an array of simple devices with fixed interactions particularly attractive from the point of view of quantum computation. In this paradigm, a quantum computer is a quantum cellular automata (QCA): the state of each simple device in the array depends on the states of the cells in some local neighborhood at the previous time-step. QCA, therefore, provide a valuable test-bed for investigating both potential quantum computer architectures and algorithms. The study of QCA is probably originated with the interesting work of Grossing and Zeilinger [40, 41, 42]. However, their models are approximately quantum mechanical because they are not linear and unitary even though the probability is preserve. The first homogeneous quantum cellular automata was introduced by Meyer [8]. He also defined one particle quantum lattice gas algorithm which simulates one-dimensional Dirac equation. Boghosian and Taylor [43, 44, 45] and separately Succi [46, 47] have defined QLG models for the Schroedinger equation in D dimensions.

The QLG algorithms may be simulated on a quantum computer with realizable substantial speedup over classical hardware. Watrous [48] showed that any partitioned

¹This section was extracted from an unpublished paper. This research is cooperated with Carlos Perez, University of Waterloo, Canada.

quantum cellular automata can be simulated by a quantum Turing machine. The first special quantum processor designed to directly realize quantum cellular automata is suggested by Seth Lloyd. Preliminary experimental designs have been proposed for ion traps, optical lattices and endohedral fullerenes on silicon [49, 50, 51].

Liquid state NMR has been proved to be an ideal way to explore many aspects of quantum computing and QIP. The success of NMR quantum computations means that large arrays of few entangled qubit quantum computers are already available now. We propose a QLG algorithm here and a potential design to implement the algorithm by nuclear magnetic resonance. A simple ring model has been chosen as the first test.

6.1 Quantum lattice gas algorithms

Usually, a random walk is simulated by selecting one particle in the system and transporting it at random upwards and downwards, provided that the destination site is empty. At each site z of the lattice, instead of only registering the position of the particle, one also tracks down the directions by associating two binary values $n_1(z, t)$ and $n_2(z, t)$. These quantities present occupation numbers indicating whether or not a upward- or downward-moving particle is entering site z at time t , respectively. The random motion is obtained by shuffling the two directions of motion at each lattice site and at each time step. A upward-moving particle, entering site z at time $t + \Delta t$, must be the one with probability p moving in the same direction at the site $z - \Delta z$ at time t , and with probability $1 - p$, it may be the one at the same site pointing downwards at site $z + \Delta z$ and time t . Therefore, the random walk rule can be expressed by a transition matrix,

$$A = \begin{pmatrix} p & 1 - p \\ 1 - p & p \end{pmatrix}. \quad (6.1)$$

The quantum lattice gas algorithms are the generalizations of classical lattice gas algorithms, introducing quantum mechanical features into the lattice. One may consider to replace a classical cell by a quantum state and the binary values associated

with each cell are denoted by complex values then [8]. The occupation numbers n_1 and n_2 map to the probability amplitudes $\psi_{z,\alpha}$ and $\psi_{z,\alpha'}$ of the position z , respectively. The single time step evolution is the composition of propagation and collision as described:

$$\begin{aligned} \sum \psi_{z,\alpha} |z, \alpha\rangle &\xrightarrow{\text{propagation}} \sum \psi_{z,\alpha} |z + \alpha, \alpha\rangle \\ &\xrightarrow{\text{collision}} \sum S_{\alpha,\alpha'} \psi_{z,\alpha} |z, \alpha'\rangle. \end{aligned} \quad (6.2)$$

where z is the current position of the particle and α indicates the directions. Then two

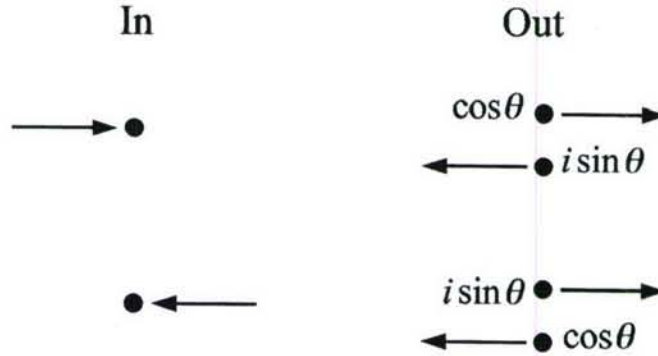


Figure 6-1: **Collision rules for 1D QLG algorithm** The collisions of the simplest one dimensional QLG algorithm. A single particle of mass $\tan \theta$ at a site has an amplitude to be scattered $i \sin \theta$.

directions of motions are shuffled in the collision step: the amplitudes and directions are changed by a uniform update rule $S_{\alpha,\alpha'}$ for all the sites. The collision operator

can be written as

$$S_{\alpha,\alpha'} = \begin{pmatrix} \cos \theta & i \sin \theta \\ i \sin \theta & \cos \theta \end{pmatrix}. \quad (6.3)$$

Then the particle propagates to the neighboring cell $|x + \alpha, \alpha\rangle$ associated with direction α or $|x - \alpha', \alpha'\rangle$ pointing to α' at time $t + \Delta t$. The evolution of the dynamic is given by repeating the actions of the update rules.

This algorithm described above requires a register of size $\log N$ where N is the number of lattice points. However, the above algorithm for a random walk of one particle does not generalize very nicely to k particles. It does not suffice to simply randomly shift the position of each particle, since if we are to admit any exclusion principle, then a particle cannot move to certain positions if those positions are already at maximum capacity. Say, if each position allows for only one particle, a particle can move there only if the site is empty. This requires one to check the current position of each other particles when updating the position of a particular particle. This approach requires $O(k \log N)$ bits of memory, and $O(k^2 \log N)$ for each update step. We will refer to this algorithm as a register approach, since it keeps the positions of each particle in different registers.

Here we propose a different generalization of classical lattice gas algorithm similar to the partitioned cellular automata mentioned by Morgolus [53], in which each lattice site is denoted by a single qubit. The dynamic of this system is easier to understand intuitively by taking the following picture. Two qubits are associated with one lattice site: qubits $\Psi(z, u, t)$ and $\Psi(z, d, t)$ represent the presence of a particle in the lattice point z at time t moving up or down, respectively. The update rule then consists of partitioning the lattice into a tiling set of contiguous pairs at each time step, such that the even and odd time step tilling overlap, depicted in Fig. 6-2. The values of each pair are then swapped with some probability amplitude. As long as the update operator u for each pair is unitary, so is the evolution of the whole lattice. The

Partitioned Cellular Automata

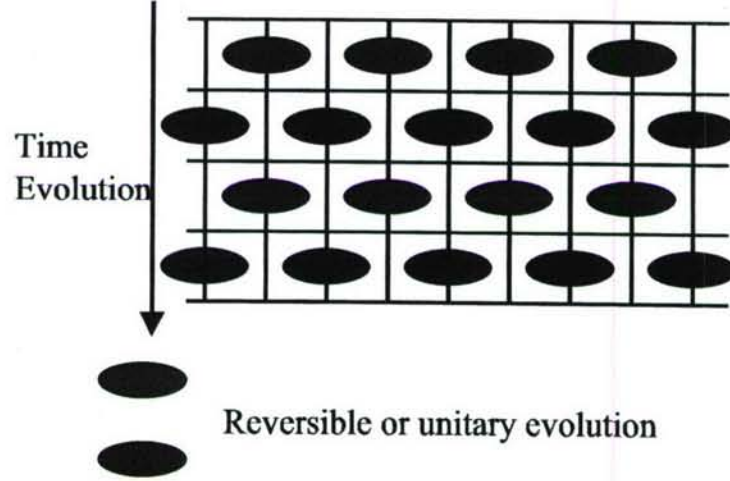


Figure 6-2: **Partitioned cellular automata** Each square represents a cell, and each oval is a unitary operator acting on two lattice cells. On odd/even steps the pairing is exchanged.

operator is defined as

$$u = \hat{C} = \begin{pmatrix} 1 & 0 & 0 & 0 \\ 0 & \frac{1+i}{2} & \frac{1-i}{2} & 0 \\ 0 & \frac{1-i}{2} & \frac{1+i}{2} & 0 \\ 0 & 0 & 0 & 1 \end{pmatrix}, \quad (6.4)$$

commonly called the *square-root-of-swap* gate. The system is evolved by repeated application of the unitary operators u . Suppose a system of an even number N of qubits, indicating $N/2$ lattice sites. Rewrite the gates in the odd and even time step as $U_{odd} = u^{\otimes N/2}$ and $U_{even} = 1 \otimes u^{\otimes N/2-2} \otimes 1$. Under the evolution $U = U_{even}U_{odd}$ we

have that:

$$\begin{aligned}\Psi(z, u, t + \Delta t) &= \frac{1+i}{2}\Psi(z - \Delta z, d, t) + \frac{1-i}{2}\Psi(z + \Delta z, u, t) \\ \Psi(z, d, t + \Delta t) &= \frac{1-i}{2}\Psi(z - \Delta z, d, t) + \frac{1+i}{2}\Psi(z + \Delta z, u, t).\end{aligned}\tag{6.5}$$

Taking $\Psi(z, t) = \Psi(z, u, t) + \Psi(z, d, t)$ we can calculate the continuous limit using the Chapman-Enskog method [53]. We get that the evolution limits to

$$\frac{\partial}{\partial t}\Psi(z, t) = \frac{i}{2}\frac{\partial^2}{\partial z^2}\Psi(z, t),\tag{6.6}$$

which is exactly the Hamiltonian for a freely moving particle in one dimension.

In the automata defined above, we assume that all (randomized) swaps between contiguous cells are done in parallel in one time step. Hence, this approach requires $O(N)$ bits of memory and requires $O(1)$ time for each update step. This is particularly good if we take $k = \Omega(N)$, i.e. the number of particles is in the order of lattice points, which is generally expected in a lattice gas. This performance gain is, of course, assuming that a cellular automata is a realizable architecture, i.e. it is in fact possible to perform all the updates of a time step in parallel.

6.2 Chain Architectures

It has been suggested by Seth Lloyd [4, 5] that above algorithms can be implemented on a chain of repeated quantum spins. Consider a one dimensional chain of spin $1/2$ systems, e.g. a polymer, with three different *species*, i.e. $ABCABC\dots$. The transition between the ground state and excited state of any quantum unit can be driven by applying a pulse at the resonant frequency. If A , B and C have distinct resonant frequencies, then they can be addressed independently. Consider only the nearest-neighbor interaction given by some (arbitrary) Hamiltonian H_{AB} , H_{BC} , H_{CA} . The effect of the interaction Hamiltonians is to shift the energy levels of each quantum unit corresponding to its neighbors. Hence, the resonant frequency ω_A takes distin-

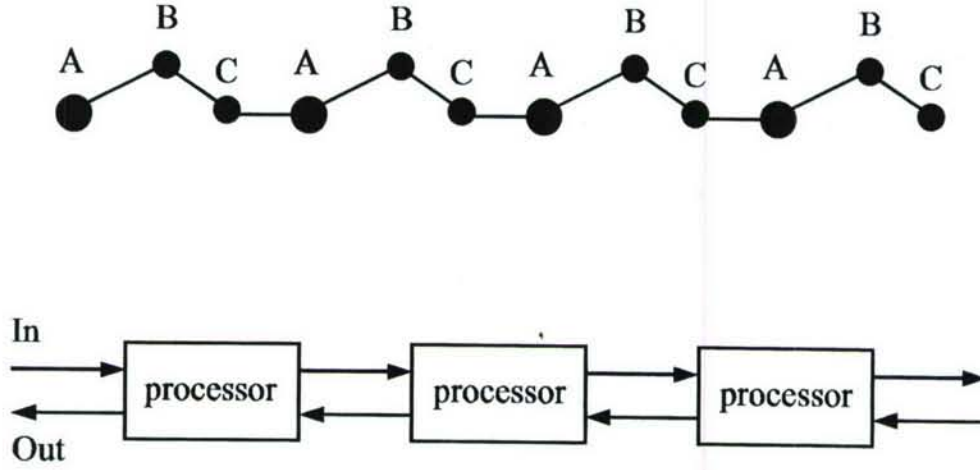


Figure 6-3: **Spin chain architectures** One-dimensional array of quantum units ($ABCABC\dots$), such as nuclear spins in a polymer, is depicted here. A series of spins ABC can be treated as a quantum information processor. Sequence of resonant pulses allow one to load information and unload results at the end of an array. Each processor has the same circuit and they can process information and exchange it with the nearest neighbors.

guishable values ω_{00}^A , ω_{01}^A , ω_{10}^A , ω_{11}^A , depending on whether it's C and B neighbors are in the states 0 and 0, 0 and 1, 1 and 0, or 1 and 1. If these are all different, then transitions on species A spins can be done selectively depending on the value of its neighbors. For example, by applying a π pulse with frequency ω_{00}^A all species A lattice points whose both neighbors are in the state 0 will be flipped. It is also possible to apply any two qubit gates on all pairs A, B or C, A or B, C . Though originally proposed with three distinguishable qubit species, the model can easily work with more species [52]. These single qubit operations and two qubit gates can supply the logical operations and can be wired together to give any desired logic gate.

Input of information and readout of the results are through the end unit of the array which can be controlled independently because it has only one neighbor. One can load arbitrary information onto the end of the array and exchange the information with its neighbor. As a result, any sequence of desired information can be loaded onto A , B and C by continuing uploading at the end unit and swapping between different units.

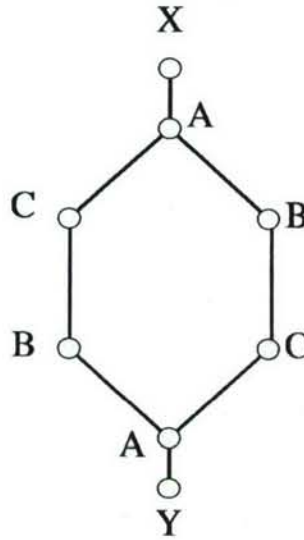


Figure 6-4: **The ring model** This model shows a chain of 6 qubits. Two loading qubits are presented by X and Y respectively. All the qubits with the same labels share the same resonant frequencies.

6.3 NMR Simulations

6.3.1 Spin System

A ring model, illustrated in Fig. 6-4, has been selected for the first study depending on the following four assumptions. (1) The ring is composed of two pairs of three distinguishable qubits ABC with qubits X and Y attached to A , served as loading

qubits. (2) Qubits A , B , C have the same Zeeman interaction with the applied magnetic field, but associated with different chemical shifts. The chemical shifts for qubit A , B and C are set to be $0Hz$, $4kHz$ and $8kHz$ respectively. (3) Only the nearest neighbor interactions have been taken into account and the scalar coupling constant is $50Hz$ altogether between ABC spins. The internal Hamiltonian of these spins, therefore, is

$$H_{internal} = -\frac{1}{2} \sum_{i=A}^C \omega_i \sigma_z^i + \frac{\pi J}{2} (\sigma_z^A \sigma_z^B + \sigma_z^B \sigma_z^C + \sigma_z^C \sigma_z^A) \quad (6.7)$$

where ω_i represent the chemical shifts of the spins and J are scalar coupling constants. (4) Loading qubits are several-hundred megahertz off-resonance and are not affected by any pulses applied to the ABC spins.

Unlike the labeled chloroform sample, the resonant frequencies are not widely separated, so that a RF pulse on resonance with one carbon spin will rotate all. Usually, a low-power RF pulse can be used to obtain selective operation on each qubit here. However, the selective pulses have disadvantage that low power implies long duration. This not only introduces errors due to relaxation, or decoherence, but also allows significant evolution under the action of the internal Hamiltonian. In the past, this evolution was rarely of concern because there was little importance placed on implementing a particular operation. Here, we use an alternative method with strongly modulating pulses to implement precisely the desired operations[31]. This allows us to use high-power pulses that strongly modulate the system's dynamics. These gates, shown in Table 6.3.1, allow arbitrary rotations of each spin, while refocusing the internal evolution.

6.3.2 Logic Gates

Information is initially stored in X and Y and a series of unitary transformations $\{U\}$ brings the information to other qubits. This set of unitary operators is essentially a series of two-qubit SWAP gates between adjacent qubits. A single two-qubit SWAP

Pulse	Time (μs)	Max. Power (kHz)	Discrete Fidelity
π_x^A	226.24	5.18	0.9989
π_x^B	267.35	4.87	0.9985
π_x^C	267.35	4.87	0.9985
$\frac{\pi}{2}_x^{AB}$	355.12	5.25	0.9983
π_x^{AB}	338.19	11.36	0.9973
π_x^{BC}	459	4.95	0.9977
π_x^{AC}	302.57	13.33	0.9985

Table 6.1: **Summary of the relevant characteristics for the set of transformations required for the implementation of QCA.** The three columns list the pulse duration (in μs), maximum power (in kHz), and the fidelity of simulated pulse.

gate for qubit A, B is

$$\begin{aligned}
U_{swap}^{AB} = & \exp \left[i \frac{\pi}{4} (\sigma_x^A + \sigma_x^B) \right] \exp \left[-i \frac{\pi}{4} \sigma_z^A \sigma_z^B \right] \exp \left[-i \frac{\pi}{4} (\sigma_x^A + \sigma_x^B) \right] \\
& \exp \left[-i \frac{\pi}{4} \sigma_z^A \sigma_z^B \right] \\
& \exp \left[-i \frac{\pi}{4} (\sigma_y^A + \sigma_y^B) \right] \exp \left[-i \frac{\pi}{4} \sigma_z^A \sigma_z^B \right] \exp \left[i \frac{\pi}{4} (\sigma_y^A + \sigma_y^B) \right].
\end{aligned} \tag{6.8}$$

where the exponential terms proportional to $\sigma_z^A \sigma_z^B$ represent the internal Hamiltonian evolutions. Notice that the third spin C is also evolving under the internal Hamiltonian while applying a two-qubit operator. π pulses are applied to modulate the internal interaction terms, resulting in averaging the interaction with qubit C . The choice of this molecule is particular convenient because the scalar coupling constants are identical. Here, we demonstrate a scheme for implementing the operator in Fig. 6-5. Hence, the interaction term $\sigma_z^A \sigma_z^B$ can be recast as

$$\begin{aligned}
\exp \left[-i \frac{\pi}{4} \sigma_z^A \sigma_z^B \right] = & \exp \left[-i \frac{\pi}{16} (\sigma_z^A \sigma_z^B + \sigma_z^A \sigma_z^C + \sigma_z^B \sigma_z^C) \right] \exp \left[-i \frac{\pi}{2} \sigma_z^C \right] \\
& \exp \left[-i \frac{\pi}{16} (\sigma_z^A \sigma_z^B + \sigma_z^A \sigma_z^C + \sigma_z^B \sigma_z^C) \right] \exp \left[-i \frac{\pi}{2} (\sigma_x^A + \sigma_x^B) \right] \\
& \exp \left[-i \frac{\pi}{16} (\sigma_z^A \sigma_z^B + \sigma_z^A \sigma_z^C + \sigma_z^B \sigma_z^C) \right] \exp \left[i \frac{\pi}{2} \sigma_z^C \right] \\
& \exp \left[-i \frac{\pi}{16} (\sigma_z^A \sigma_z^B + \sigma_z^A \sigma_z^C + \sigma_z^B \sigma_z^C) \right] \exp \left[i \frac{\pi}{2} (\sigma_x^A + \sigma_x^B) \right].
\end{aligned} \tag{6.9}$$

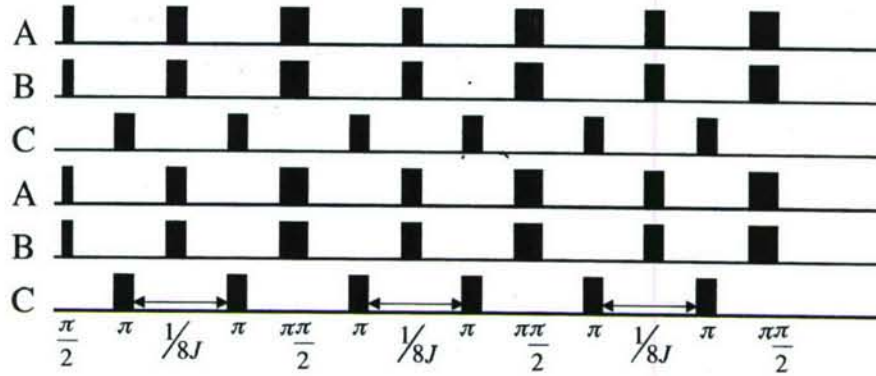


Figure 6-5: **The two-qubit SWAP gate** Here demonstrates the pulse sequence of the SWAP gate on two qubits and untouched the third spin. To refocus the scalar interactions between pair AC and BC , a π pulse has been performed on pair AB and separate the delay period to half. Two π pulses are performed on qubit C in the a quarter and three quarter of the delay respectively.

In summary, the usage of strong modulating pulses in conjunction with the selective evolution in 6.9 gives us the desired unitary operations to shift the information. The gate fidelities of these operators are listed in Table 6.3.2.

6.3.3 Methodology

One way to implement our QLG algorithm on a ABC chain is to map every 2 cells of the QCA lattice to three spins of the chains. For instance, only using A and B spins here results in a lattice of 4 cells. A single step of implementation of our QCA can be performed as following:

1. performing the update rule \hat{C}_{AB} on pairs AB on odd iterations
2. exchanging the information on qubits BC

Gates	Gates Fidelity
U_{AB}^{swap}	0.9556
U_{BC}^{swap}	0.9443
\hat{C}_{AB}	0.9605
\hat{C}_{CA}	0.9582

Table 6.2: **Summary of the gates fidelities.** The two columns list the unitary operators, and the gate fidelity of them .

3. applying the same update rule on CA with \hat{C}_{CA}
4. then swapping BC again.

These operations are repeated until the mass density has evolved for the desired number of time steps.

Equation 6.4 shows the unitary operator used to update in each time step. These unitary matrix can be implemented by a similar manner described for the SWAP gates. Table 6.3.2 gives the simulated fidelities for \hat{C}_{AB} and \hat{C}_{CA} .

Using the SWAP operators and the update unitary operators, we can translate QCA to experimental tasks as shown in Fig. 6-6. The lattice initialization step makes use of both the strong modulating pulses and the internal Hamiltonian to generate the desired unitary operation and shift the information. The repeated application of the update rules is accomplished by a similar way. The measurement is the reversed step of the lattice initialization.

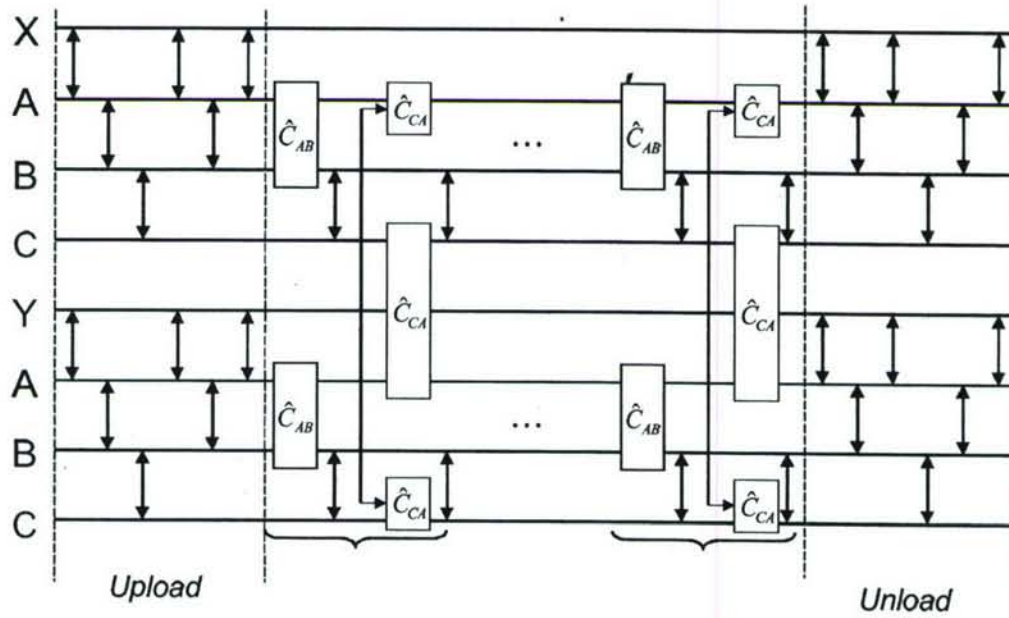


Figure 6-6: **One step QLG algorithm** The NMR implementation consists of three main section, each corresponding to the prescribed QCA step. The horizontal lines in the diagram correspond to RF pluses applied to each qubit respectively. In the encoding section, the initial magnetization is recorded on loading qubits before transferred to the other qubits. The unitary operator on pair AB and swap gate between BC follow the encoding. In the next step, the unitary operator on pair CA are applied, followed by swap gate between BC again.

Appendix A

Quantum Simulation using NMR

In 1982, Feynman recognized that a quantum system could efficiently be simulated by a computer based on the principle of quantum mechanics rather than classical mechanics [3]. This is perhaps one of the most important short term applications of QIP. An efficient quantum simulator will also enable new approaches to the study of multibody dynamics and provide a testbed for understanding decoherence. NMR has provided a valuable experimental testbed for quantum simulations. Here, We will briefly review some experiments other than the implementation of the quantum lattice gas algorithms.

A general scheme of simulating one system by another is expressed in Fig. A-1. The goal is to simulate the evolution of a quantum system S using a physical system P . The physical system is related to the simulated system via an invertible map ϕ , which creates the correspondence of states and the system S is mapped to $V = \phi U \phi^{-1}$. After the evolution of the physical system from state p to p_T , The inverse map brings it back to the final state $s(T)$ of the simulated system.

The first explicit experimental NMR realization of such a scheme was the simulation of a truncated quantum harmonic oscillator (QHO) [54]. The states of the truncated QHO were mapped onto a two-qubit system as follows

$$|n = 0\rangle \leftrightarrow |0\rangle|0\rangle \equiv |00\rangle$$

$$|n = 1\rangle \leftrightarrow |0\rangle|1\rangle \equiv |01\rangle$$

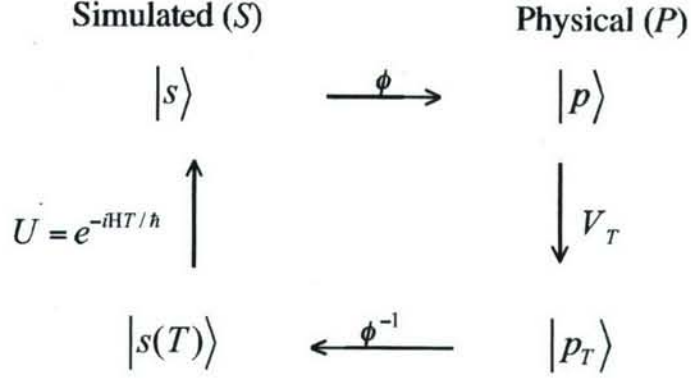


Figure A-1: **Quantum simulation scheme** Correspondence between the simulated and physical system. The initial state s evolves to $s(T)$ under the propagator U . This process is related to the evolution of state p in the physical system by an invertible map ϕ .

$$\begin{aligned}
|n=2\rangle &\leftrightarrow |1\rangle|0\rangle \equiv |10\rangle \\
|n=3\rangle &\leftrightarrow |1\rangle|1\rangle \equiv |11\rangle
\end{aligned} \tag{A.1}$$

The propagator of the truncated QHO

$$U = \exp \left[-i \left(\frac{1}{2} |0\rangle\langle 0| + \frac{3}{2} |1\rangle\langle 1| + \frac{5}{2} |2\rangle\langle 2| + \frac{7}{2} |3\rangle\langle 3| \right) \right] \tag{A.2}$$

(Ω is the oscillator frequency) was mapped onto the following propagator of a two-spin system

$$V_T = \exp \left[i(2I_z^2(1 - I_z^1) - 2)\Omega T \right]. \tag{A.3}$$

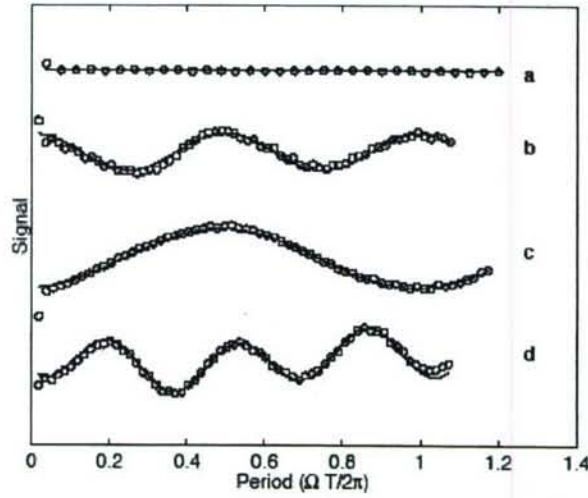


Figure A-2: **Truncated quantum harmonic oscillator** NMR signals demonstrate a quantum simulation of truncated harmonic oscillator. The solid lines are fits to theoretical expectations. Evolution of the different initial states are shown: (a) evolution of $|0\rangle$ with no oscillation (b) evolution of $|0\rangle + i|2\rangle$, showing 2Ω oscillations (c) evolution of $|0\rangle + |1\rangle + |2\rangle + |3\rangle$, showing Ω oscillation and (d) 3Ω oscillations.

Implementing this propagator on the 2-spin system simulates the truncated QHO as shown in Fig. A-2.

Quantum simulation however is not restricted to unitary dynamics. It is sometimes possible to engineer the noise in a system to control the decoherence behavior and simulate non-unitary dynamics of the system [55]. Simple models of decoherence have been shown using a controlled quantum environment in order to gain further understanding about decoherence mechanisms.

In one model [56], the environment is taken to be a large number of spins coupled to a single system spin so that the total Hamiltonian can be expressed as

$$\mathcal{H} = \omega_1 I_z^1 + \sum_{k=2}^N \omega_k I_z^k + 2\pi \sum_{k=2}^N J_{1k} I_z^1 I_z^k \quad (\text{A.4})$$

corresponding to the system, the environment, and the coupling between the system and the environment, respectively. The number of spins in a typical QIP NMR molecule is small, which makes the decoherence arising from the few system-environment

couplings rather ineffective, as the recurrence time due to a small environment is relatively short. This can be circumvented by using a second classical environment which interacts with a smaller quantum environment (see Fig. A-3 for an illustration of the model) [57].

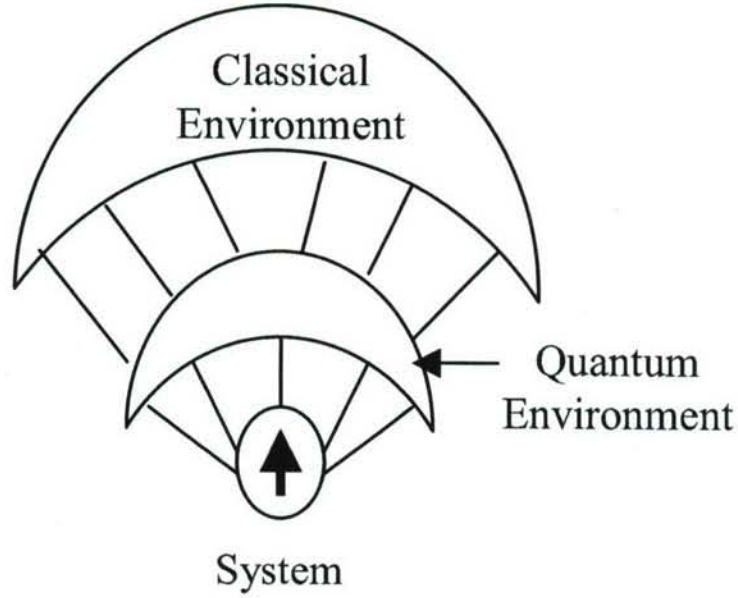


Figure A-3: **Demonstration of system and environment** Basic model for the system, local quantum and classical environment.

In this model, following the evolution of the system and the small quantum environment, a random phase kick was applied to the quantum environment. This has the effect of scrambling the system phase information stored in the environment during the coupling interaction and therefore emulates the loss of memory. When the kick angles are averaged over small angles, the decay induced by the kicks is exponential and the rate is linear in the number of the kicks. As the kick angles are completely randomized over the interval from 0 to 2π , a Zeno type effect is observed. Fig. A-4 shows the dependence of the decay rate on the kick frequency: the decay rate initially increases to reach a maximum and then decreases, thereby illustrating the motional narrowing or decoupling limit. This NMR-inspired model thus provides implementation of controlled decoherence yielding both non-exponential and exponential decays (with some control over the decay rates), and can be extended to investigate other

noise processes.

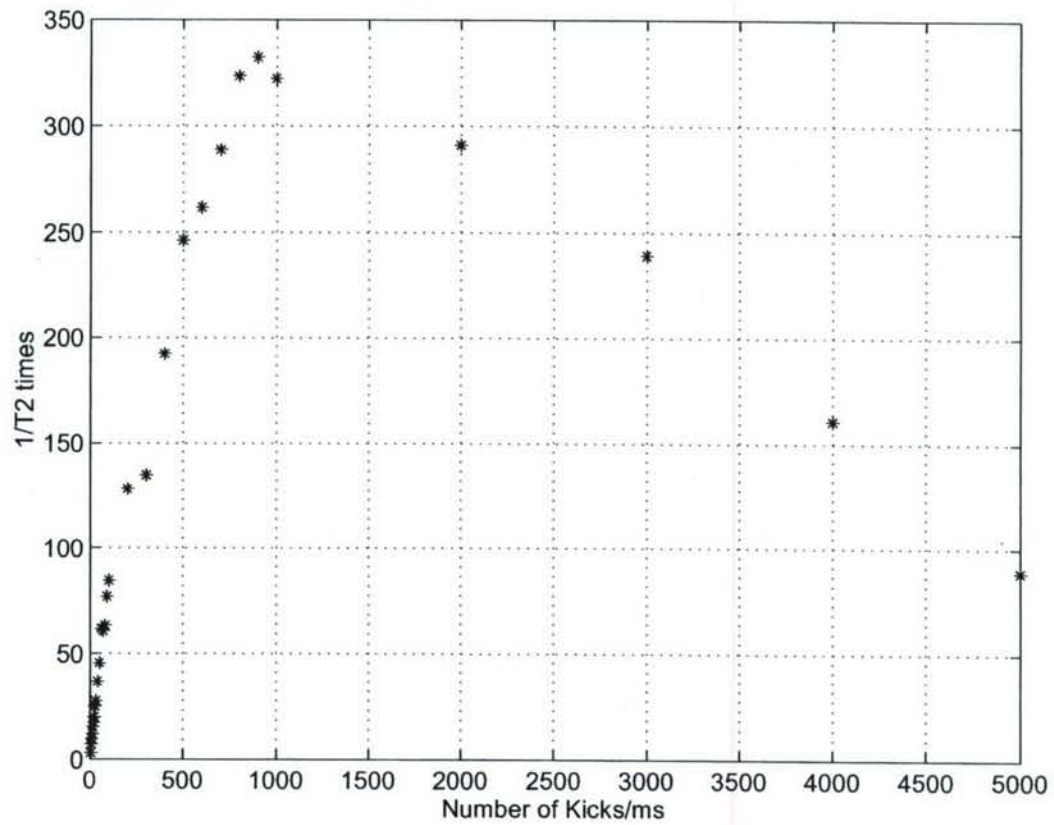


Figure A-4: **Decay rate** Simulation showing the dependence of the decay rate on the kick rate, and the onset of the decoupling limit. Beyond 900 *kicks/ms* the decay rate decreases.

Bibliography

- [1] M. A. Nielsen and I. L. Chuang. *Quantum Computation and Quantum Information*. Cambridge University Press, Cambridge, UK, 2000.
- [2] P. W. Shor. Polynomial-time algorithms for prime factorization and discrete logarithms on a quantum computer. *Siam. J. Comput.*, 26:1484-1509, 1997.
- [3] R. Feynman. Simulating physics with computers. *International Journal of Theoretical Physics*, 21(6-7):467-488, 1982.
- [4] S. Lloyd. A potentially realizable quantum computer. *Science*, 261:1569-1571, 1993
- [5] S. Lloyd. Universal quantum simulators. *Science*, 273:1073-1078, 1996.
- [6] C. Zalka. Efficient simulation of quantum systems by quantum computers. *Progress of Physics*, 46:877-879, 1998.
- [7] S. Wiesner. Simulations of many-body quantum systems by a quantum computer. quant-ph/9603028.
- [8] D. A. Meyer. From quantum cellular automata to quantum lattice gases. *Journal of Statistical Physics*, 85:551-574, 1996.
- [9] D. A. Meyer. On the absence of homogeneous scalar unitary cellular automata. *Physics Letter A*, 223:337-340, 1996.
- [10] D. A. Meyer. Quantum mechanics of lattice gas automata: One-particle plane waves and potentials. *Physical Review E*, 55:5261-5269, 1997.

- [11] J. Yepez. Type-ii quantum computers. *International Journal of Modern Physics C*, 12:1273-84, 2001.
- [12] A. N. Emerton, P. V. Coveney, and B. M. Boghosian. Lattice-gas simulations of domain growth, saturation, and self-assembly in immiscible fluids and microemulsions. *Physical Review E*, 55:708-720, 1997.
- [13] S. Chen, G. D. Doolen, K. Eggert, D. Grunau, and E. Y. Loh. Local lattice-gas model for immiscible fluids. *Physical Review A*, 43:7053-7056, 1991.
- [14] C. Appert and S. Zaleski. Lattice gas with a liquid-gas transition. *Physical Review Letters*, 64:1-4, 1990.
- [15] D.H. Rothman and S. Zaleski. Lattice-gas models of phase separation: interfaces, phase transitions, and multiphase flow. *Reviews of Modern Physics*, 66:1417-1479, 1994.
- [16] B. Chopard, and M. Droz. Cellular automata. Cambridge University Press, Cambridge, UK, 1998.
- [17] D. A. Wolf-Gladrow. Lattice-gas cellular automata and lattice boltzmann models. Springer-Verlag, Berlin, Heidelberg, 2000.
- [18] J. Yepez. Quantum lattice-gas model for the diffusion equation. *International Journal of Modern Physics C*, 12:1285-1303, 2001.
- [19] J. Yepez. Quantum lattice-gas model for burger's equation. *Journal of Statistical Physics*, 107:203-224, 2002.
- [20] J. Yepez. Quantum lattice-gas algorithm for mhd. In preparation.
- [21] R. R. Ernst, G. Bodenhausen, and A. Wokaun. *Principles of Nuclear Magnetic Resonance in One and Two Dimensions*. Oxford University Press, Oxford, 1994.

- [22] D. G. Cory, A. F. Fahmy, and T. F. Havel. Ensemble quantum computing by nuclear magnetic resonance spectroscopy. *Proceedings of the National Academy of Science*, 94:1634-1639, 1997.
- [23] N. A. Gershenfeld and I. L. Chuang. Bulk spin-resonance quantum computation. *Science*, 275:350-356, 1997.
- [24] M. Pravia, E. Fortunato, Y. Weinstein, M. D. Price, G. Teklemariam, R. J. Nelson, Y. Sharf, S. Somaroo, C. H. Tseng, T. F. Havel, and D. G. Cory. Observations of quantum dynamics by solution-state n. m. r. spectroscopy. *Concepts in Magnetic Resonance*, 11:225-238, 1999.
- [25] A. N. Garroway, P.K. Grannell, and P. Mansfield. Image formation in n. m. r. by a selective irradiative process. *Journal of Physics C*, 7:457-462, 1974.
- [26] T. F. Havel, Y. Sharf, L. Viola, and D. G. Cory. Hadamard products of product operators and the design of gradient-diffusion experiments for simulating decoherence by NMR spectroscopy. *Physics Letter A*, 280:282, 2001.
- [27] E. Knill, R. Laflamme, R. Martinez, and C. H. Tseng. An algorithmic benchmark for quantum information processing. *Nature*, 404:368-370, 2000.
- [28] L. M. K. Vandersypen, M. Steffen, G. Breyta, C. S. Yannoni, R. Cleve, and I. L. Chuang. Experimental realization of an order-finding algorithm with an NMR quantum computer. *Physical Review Letter*, 85:5452-5455, 2000.
- [29] L. M. K. Vandersypen, M. Steffen, G. Breyta, C. S. Yannoni, M. H. Sherwood, and I. L. Chuang. Experimental realization of Shor's quantum factoring algorithm using nuclear magnetic resonance. *Nature*, 414:883-887, 2001.
- [30] A. Sodickson and D.G. Cory. A generalized k -space formalism for treating the spatial aspects of a variety of n. m. r. experiments. *Progress in Nuclear Magnetic Resonance Spectroscopy*, 33:77-108, 1998.

- [31] E. M. Fortunato, M. A. Pravia, N. Boulant, G. Teklemariam, T. F. Havel, and D. G. Cory. Design of strongly modulating pulses to implement precise effective Hamiltonians for quantum information processing. *Journal of Chemical Physics*, 116:7599-7606, 2002
- [32] P. J. Love, B. M. Boghosian and D. A. Meyer. Lattice-gas and lattice-Boltzman methods from the perspective of quantum computation. in preparation.
- [33] M. D. Price, T. F. Havel, and D. G. Cory. Nuclear magnetic resonance spectroscopy: an experimentally accessible paradigm for quantum computing. *Physica D*, 120:82-101, 1998.
- [34] J.A. Jones and E. Knill. Efficient refocussing of one spin and two spin interactions for n. m. r. quantum computing. *Journal of Magnetic Resonance*, 141:322-325, 1999.
- [35] J.A. Jones. N. m. r. quantum computing. *Progress in Nuclear Magnetic Resonance Spectroscopy*, 38:325-360, 2001.
- [36] H. K. Cummins, and J. Jones. Use of composite rotation to correct systematic errors in nmr quantum computation. *New Journal Physics* 2:1-2, 2000.
- [37] J. Jones. arXiv E-print quant-ph/0301019, 2003.
- [38] M. A. Pravia, N. Boulant, J. Emerson, A. Farid, E. M. Fortunato, T. F. Havel, R. Martinez, D. G. Cory. Robust control of quantum information. *Journal of Chemical Physics*, 119:9993-10001, 2003.
- [39] N. Boulant, J. Emerson, T. F. Havel, D. G. Cory and S. Furuta. Incoherent noise and quantum information processing. *Journal of Chemical Physics*, 121:2955-2961, 2004.
- [40] G. Grossing, and A. Zeilinger. Quantum cellular automata. *Complex Systems*, 2:197-208, 1988.

- [41] S. Fussy, G. Grossing, H. Schwabl, and A. Scrinzi. Nonlocal computation in quantum cellular automata *Physical Review A*, 48:3470-3477, 1993.
- [42] G. Grossing, and A. Zeilinger. Structures in quantum cellular automata *Physica A*, 151:366-370, 1988.
- [43] B. M. Boghosian, and W. Taylor. Quantum lattice-gas models for the many-body Schrodinger equation. *International Journal of Modern Physics C*, 8:705-716, 1997.
- [44] B. M. Boghosian, and W. Taylor. Quantum lattice-gas model for the many-particle Schrodinger equation in d dimensions. *Physical Review E*, 57:54-66, 1998.
- [45] B. M. Boghosian, and W. Taylor. Simulating quantum mechanics on a quantum computer. *Physica D*, 120:30-42, 1998.
- [46] S. Succi. Numerical solution of the Schrodinger equation using discrete kinetic theory. *Physical Review E*, 53:1969-1965, 1996.
- [47] S. Succi, and R. Benzi. Lattice Boltzmann equation from quantum mechanics. *Physica D*, 69:327-332, 1993.
- [48] J. Watrous. *Proceedings of the 36th annual meeting on the foundations of computer science*, 528-537, 1995.
- [49] B. C. Travaglione, and G. J. Milburn. Implementing the quantum random walk. *Physical Review A*, 65:032310, 2002.
- [50] W. Dur, R. Raussendorf, V. M. Kendon, and H. J. Briegel. Quantum walks in optical lattices. *Physical Review A*, 66:052319, 2002.
- [51] J. Twamley. Quantum-cellular-automata quantum computing with endohedral fullerenes. *Physical Review A*, 67:052318, 2003.
- [52] S. C. Benjamin, and N. F. Johnson. Cellular structures for computation in the quantum regime. *Physical Review A*, 60:4334-4337, 1999.

- [53] T. Toffoli, and N. H. Margolus. *Cellular Automata Machines*. The MIT Press, Cambridge, Massachusetts, 1987.
- [54] S. Somaroo, C.-H. Tseng, T.F. Havel, R. Laflamme, and D.G. Cory. Quantum simulations on a quantum computer. *Physical Review Letters*, 82:5381-5384, 1999.
- [55] D. Bacon, A. M. Childs, I. L. Chuang, J. Kempe, D. W. Leung, and X. L. Zhou. Universal simulation of Markovian quantum dynamics. *Physical Review A*, 64:062302, 2001.
- [56] W. H. Zurek. Environment-induced superselection rules. *Physical Review D*, 26:1862, 1982.
- [57] G. Teklemariam, E. M. Fortumato, C. C. Lopez, J. Emerson, J. P. Paz, T. F. Havel, and D. G. Cory. Method for modeling decoherence on a quantum-information processor. *Physical Review A*, 67:062312, 2003.

Investigations on Resource-limited Quantum Control Through NMR Pulses

by

Karen Lee

Submitted to the Department of Electrical Engineering and Computer
Science

in partial fulfillment of the requirements for the degree of

Master of Science in Electrical Engineering and Computer Science

at the

MASSACHUSETTS INSTITUTE OF TECHNOLOGY

June 2006

© Massachusetts Institute of Technology 2006. All rights reserved.

Author

Department of Electrical Engineering and Computer Science

May 19, 2006

Certified by

David Cory

Professor of Nuclear Science and Engineering

Thesis Supervisor

Accepted by

Arthur C. Smith

Chairman, Department Committee on Graduate Theses

Investigations on Resource-limited Quantum Control Through NMR Pulses

by

Karen Lee

Submitted to the Department of Electrical Engineering and Computer Science
on May 19, 2006, in partial fulfillment of the
requirements for the degree of
Master of Science in Electrical Engineering and Computer Science

Abstract

Universal high fidelity coherent control over large Hilbert spaces is essential for quantum information processing to become a useful tool in science, engineering, communications and computation. The development of methods for coherent control are however still in their infancy. In particular, very little is known about the efficiency of quantum control subject to limitations in resources such as drive power, drive bandwidth and system decoherence. Here we report the results of numerical simulations to investigate the influence of limited resources. We introduce the curvature of fidelity as a measure of robustness. We apply these ideas to strongly modulating NMR pulse sequences and study the effects of increasing resources on the fidelity and curvature.

Thesis Supervisor: David Cory

Title: Professor of Nuclear Science and Engineering

Acknowledgments

First of all, I would like express my most sincere gratitude to my thesis supervisor, Professor David Cory, for his insightful guidance and mentorship. Besides the actual knowledge that I've picked up, I have learned a great deal about how to be a scientist from him. My most heart-felt thanks also goes to Professor Terry Orlando for being a great academic advisor and a wonderful housemaster. Terry and Ann have made MIT a most welcoming place for this new graduate student.

I would like to thank all of my colleagues in the Cory group, in particular Paola and Jonathan, whom I bombarded constantly with questions in the last year and a half. Great thanks to Cecilia for being a great officemate and wonderful friend, full of insight in issues both work-related and non-work-related. Also thanks to Ben, Michael, Jamie, Anatoly, Sid, Sekhar and Tim for their patient help at various times. Thanks Cecilia and Ben for all the (fondue) parties!

I would like to thank all my friends, whether in my department, in my dorm, or other long-time friends for their support, help, and all the good times and jokes.

I would like to thank all my friends in the Hong Kong Student Bible Study for their priceless fellowship and spiritual, emotional support and their help in so many other ways.

I cannot thank more my wonderful parents and family, for their committed and loving support through the years. Without their tender care I would not be who I am today.

Most importantly, I would like to thank God, my Father in Heaven, who has blessed me with everything that I have and all that I am today, and for the opportunity of being educated at this great institute.

Contents

1	Introduction	13
1.1	Quantum vs Classical Behavior?	13
1.1.1	Quantum States	14
1.1.2	Observables	14
1.1.3	Quantum Measurements	15
1.1.4	Unitary Quantum Dynamics	17
1.1.5	Density Operator Formalism	18
1.1.6	Decoherence	19
1.2	Optimal Control Theory applied to Quantum Systems	22
2	Quantum Control in the NMR context	23
2.1	Spin, Magnetic Moment and Angular Momentum	24
2.2	Nuclear spin and resonance	26
2.3	The Bloch model and the single-pulse NMR experiment	27
3	Methodology	29
3.1	Strongly Modulating Pulses as an efficient implementation of unitary transformations	29
3.2	Control Curvature: a measure of robustness of control	36
4	Results and Analysis	39
4.1	Fidelity vs Curvature	39
4.2	The effect of varying coupling strength between spins	52

4.3 Expanding available resources	53
5 Conclusions	57

List of Figures

- 4-1 Scatter plot of pulse fidelity verses curvature with respect to fractional changes in total time, $t = t_1 + t_2$, of the pulse. Each blue diamond corresponds to a U_{12} pulse and each circle corresponds to a U_1 pulse. C_t for the non-selective rotation U_{12} are in the range $[10, 10^4]$, whereas values for the selective rotation U_1 lie mostly in the range $[10^5, 10^8]$. This indicates that the selective pulses are less robust to variations in the durations of applied RF pulses. 40
- 4-2 Scatter plot of fidelity vs the curvature with respect to the average power $\omega_{ave} = \frac{\omega_1 t_1 + \omega_2 t_2}{t_1 + t_2}$. C_{aP} for the non-selective rotation U_{12} are in the range $[10, 10^4]$, whereas values for the selective rotation U_1 lie mostly in the range $[10^3, 10^8]$. This again indicates that the selective pulses are less robust to variations in pulse parameters: this time the strength of applied RF fields. For average power, all the three selective U_1 pulses with highest fidelities have very low C_{aP} , which means that they are very good pulses with respect to both fidelity and robustness to RF power. 41

- 4-3 Scatter plot of fidelity vs the curvature with respect to the maximum power $\omega_{max} = \max\{\omega_1, \omega_2\}$ is expected to be similar to that of the average power. C_{maxP} for the non-selective rotation U_{12} are mostly in the range $[1, 10^3]$, whereas values for the selective rotation U_1 lie mostly in the range $[10^4, 10^7]$. These values are smaller, and within a narrower range than the average power. The reason is likely that the influence of higher power period is more dominant, and is thus less vulnerable to variations. 42
- 4-4 The C_f for the non-selective rotation U_{12} are mostly in the range $[10^{-1}, 10^3]$, whereas values for the selective rotation U_1 lie mostly in the range $[10^4, 10^7]$. This is consistent with the results about the other parameters. Pulse sequences β and ϵ are both robust with respect to variations in frequency bandwidth. However, pulse α , which has the highest fidelity, has the largest C_f and hence the worst robustness. . . 43
- 4-5 The C_ϕ for the non-selective rotation U_{12} are mostly in the range $[10^{-6}, 10^6]$, whereas values for the selective rotation U_1 lie mostly in the range $[10^2, 10^8]$. This is consistent with the results about the other parameters. All the three highest fidelity U_1 pulses have the lowest C_ϕ values and are thus both robust with respect to variations in ϕ 44
- 4-6 This is a plot of fidelity versus curvature with respect to fractional changes in the duration of the second period, t_2 for two given pulses—one selective and one non-selective. The fidelity of the non-selective is higher than that of the selective pulse, and by inspection, the curvature is lower, showing more robust behavior. 45
- 4-7 This is a plot of fidelity versus curvature with respect to fractional changes in the RF frequency of the first period, f_1 for two given pulses—one selective and one non-selective. Again, the fidelity is higher and the pulse is more robust for the non-selective case. 46

4-8	This is a plot of fidelity versus curvature with respect to fractional changes in the phase of the first period, ϕ_1 for two given pulses-one selective and one non-selective. Again, the fidelity is higher and the pulse is more robust for the non-selective case.	47
4-9	The trajectory of non-selective pulse a is shown. The red and blue arrows show the motion of the spin A and spin B on the Bloch's respectively. The motions of both spins during the two periods are very direct.	48
4-10	The trajectory of non-selective pulse b is shown. As with non-selective pulse a, the motions of both spins during the two periods are very direct.	48
4-11	The trajectory of selective pulse a is shown. The motions of both spins from the initial to final state during the two periods are still very direct.	49
4-12	The trajectory of selective pulse b is shown. Spin B moves to negative z during the first period and returns to positive z during the second, thus we have used resources to generate unnecessary rotation.	49
4-13	The mean curvature is calculated using C_t , C_{aP} , C_f and C_{ph}	50
4-14	The mean curvature is calculated using C_t , C_{maxP} , C_f and C_{ph}	51
4-15	The mean curvature is calculated using C_t , C_{aP} , C_f and C_{ph}	51
4-16	The mean curvature is calculated using C_t , C_{maxP} , C_f and C_{ph}	52
4-17	As expected, the fidelity decreases monotonically as we increase coupling strength. When the chemical shift difference is set to 0, $f = 0.720$. The trend indicates an asymptotic value that the fidelity approaches for each of 2-period and 3-period pulses.	54
4-18	The result is indeed what we predicted, that fidelity increases as the number of periods allowed. In the limit of the number of period going to infinity, we will expect to achieve perfect fidelity in universal control as has been shown by Khaneja without regards to limitations in resources. (ref 76)	55

Chapter 1

Introduction

Since the advent of Quantum Mechanics at the beginning of the last century, scientists have dreamed of controlling the behavior of systems at the atomic or molecular scale. To this day, very little of that dream has been realized to different extents, but recent advances in the theoretical work and experimental realizations of quantum control have generated much excitement in the scientific community recently. Its important applications include the control of chemical reaction selectivity and of molecular motion [22], excitation of specified molecular states [6, 16], molecular structure determination by means of nuclear and electron magnetic resonance spectroscopy as well as microwave and optical spectroscopy [23], laser cooling [7], and quantum information [3], have significant implications to the future technologies.

1.1 Quantum vs Classical Behavior?

Quantum mechanics has only been postulated less than a century ago, and yet there has been no experiment that falsified its predictions. A natural question is, if quantum mechanics indeed governs the behavior of the physical universe, why does it take so long for us to discover it? What makes a system ‘quantum’? The answer is that non-classical, i.e. quantum behavior can only be observed under special laboratory conditions. Quantum behavior arises when a relative small physical system (with only a few dynamical degrees of freedom) can be well isolated from environmental

disturbances and dissipative couplings. This may be achieved by cooling down an experimental setup to temperatures on the order of a few mK. Quantum mechanics is believed to be a correct microscopic theory of non-relativistic physics, but the reduced dynamics of subsystems nearly always corresponds closely to models that fall within the domain of classical mechanics. Hence strongly non-classical behavior can only be observed in a system on timescales short compared to those that characterize its couplings to its environment[15].

1.1.1 Quantum States

A state is a complete description of a physical system. In quantum mechanics, a state of a closed system is represented by a ray in a Hilbert space, whose dimensionality is specified according to the physical system under consideration. A ray is an equivalence class of vectors that differ by a non-zero multiplicative scalar. We choose a representative of the class to have unit norm

$$\langle\psi|\psi\rangle = 1$$

which, for a state in a finite-dimensional Hilbert space expressed as a linear combination of orthonormal basis states $|\psi\rangle = \sum_{a'} c_{a'} |a'\rangle$ is $\sum_{a'} |c_{a'}|^2 = 1$, and for a state in an infinite-dimensional Hilbert space, for example, the position of a particle, $|\alpha\rangle = \int c_x |x\rangle dx$, then $\int |c_x|^2 dx = 1$.

We can represent the joint state of several smaller systems using by the tensor-products of the rays. For example, if we have 2 two-level systems A and B, $|\psi\rangle_A = (a_1 a_2)^+$ and $|\psi\rangle_B = (b_1 b_2)^+$, we can write

$$\begin{aligned} |\psi\rangle &= |\psi\rangle_A \otimes |\psi\rangle_B \\ &= (a_1 b_1 \quad a_1 b_2 \quad a_2 b_1 \quad a_2 b_2)^+ \end{aligned}$$

1.1.2 Observables

An observable is a property of a physical system that can in principle be measured. In quantum mechanics, each observable has a corresponding Hermitian operator. An

operator is a linear map taking a vector (representing a state) to another vector.

$$A : |\psi\rangle \rightarrow A|\psi\rangle, A(a|\psi\rangle + b|\psi\rangle) = aA|\psi\rangle + bA|\psi\rangle$$

The Hermitian conjugate of the operator is defined by $\langle\phi|A\psi\rangle = \langle A^+\phi|\psi\rangle$ for all vectors $|\phi\rangle, |\psi\rangle$. A is a Hermitian operator if $A = A^+$.

A Hermitian operator in a Hilbert space H has real eigenvalues, and its eigenvectors form a complete orthonormal basis in H . We can express a Hermitian operator A as

$$A = \sum_n a_n P_n$$

where a_n is an eigenvalue of A , P_n is the projection operator onto the subspace of eigenvectors with eigenvalue a_n . It can be shown that the eigenvalues A_n are purely real and that the P_n 's satisfy

$$P_n P_m = \delta_{n,m} P_n$$

$$P_n^+ = P_n = |n\rangle\langle n|$$

1.1.3 Quantum Measurements

Quoting from Dirac, 'A measurement always causes the system to jump into an eigenstate of the dynamical variable that is being measured.' [19] In classical dynamics, if we measure the position of a particle along a line, we obtain the value of the x-coordinate without affecting its position. However, measurements usually change the state of a quantum system. Before the measurement of an observable is made, the system is assumed to be a coherent superposition of the eigenstates:

$$|\alpha\rangle = \sum_{a'} c_{a'} |a'\rangle = \sum_{a'} |a'\rangle \langle a'|\alpha\rangle$$

When a measurement is performed, the system is 'thrown into' one of the eigentstates, for example, $|a'\rangle$. Therefore, unless the system was already in an eigenstate of the observable being measured prior to the measurement, the state of the system is always

changed. This is a postulate of quantum mechanics and cannot be proven. We do not know which eigenstate would result after the measurement, but the probability of obtaining a certain value is given by

$$P(a') = |c_{a'}|^2 = |\langle a' | \alpha \rangle|^2$$

Moreover, thus the quantum system remains in that particular eigenstate immediately after the measurement. Repeated measurements therefore yield the same result.

In order to determine this probability empirically, we need to consider a great number of measurements performed on a pure ensemble, i.e. a collection of system all identically prepared in state $|\alpha\rangle$ and estimate the probability from the frequency of occurrence of various results.

We define the expectation value of A taken with respect to state $|\alpha\rangle$ as

$$\langle A \rangle = \langle \alpha | A | \alpha \rangle$$

since

$$\begin{aligned} \langle A \rangle &= \sum_{a'} \sum_{a''} \langle \alpha | a'' \rangle \langle a'' | A | a' \rangle \langle a' | \alpha \rangle \\ &= \sum_{a'} a' |\langle a' | \alpha \rangle|^2 \end{aligned}$$

agrees with the classical notion of 'average' measured value.

The commutator of two operators A and B are defined to be

$$[A, B] = AB - BA$$

Since A and B are operators and not scalars, the commutator may not be zero. If we have two observables A and B , they will have the same eigenstates if and only if $[A, B] = 0$. In other words, after a measurement of A on a system, a measurement of B will change the state of the system by throwing it into one of the eigenstates of B . Therefore, only when A and B are compatible observables, i.e., $[A, B] = 0$, will a

second measurement of A following the measurement of B give the same answer as the first A measurement. It can be shown that for any state we have the following inequality:

$$\langle(\Delta A)^2\rangle\langle(\Delta B)^2\rangle \geq \frac{1}{4}|\langle[A, B]\rangle|^2$$

The above is known as the Uncertain Relation and tells us that in general, there is a limit to how precise our measurements of incompatible observables can be made.

1.1.4 Unitary Quantum Dynamics

The dynamics of any quantum system is governed by the Schrödinger equation, which is given by

$$i\hbar \frac{d|\psi(t)\rangle}{dt} = H(t)|\psi(t)\rangle$$

where \hbar is Planck's constant, and H , the Hamiltonian, is a linear Hermitian operator that describes the total energy of the system. When the Hamiltonian is time-independent, the information on the state of the system is captured in the wavefunction

$$|\psi(t)\rangle = e^{-\frac{iHt}{\hbar}}|\psi(0)\rangle.$$

We see that $U(t) = e^{-\frac{iHt}{\hbar}}$ is a unitary operator since H is Hermitian. In general,

$$|\psi(t)\rangle = U(t)|\psi(0)\rangle$$

Factoring out $|\psi(0)\rangle$ on both sides, we obtain

$$i\hbar \dot{U} = H(t)U$$

and the propagator is given by

$$U(t, t_0) = T e^{-\frac{i}{\hbar} \int_{t_0}^t dt' H(t')}$$

where T is the Dyson time-ordering operator.

The expectation value of a time-independent observable A is

$$\frac{d\langle A \rangle}{dt} = \frac{1}{i\hbar} [A, H]$$

1.1.5 Density Operator Formalism

In general, we do not have a pure ensemble, but instead, we have a mixed ensemble in which every system has a random state. Suppose we make a measurement on a mixed ensemble of some observable A . [19] The ensemble average of A is given by

$$\begin{aligned} [A] &= \sum_i p_i \langle \alpha_i | A | \alpha_i \rangle \\ &= \sum_i \sum_{a'} p_i |\langle a' | \alpha_i \rangle|^2 a' \end{aligned}$$

where $|a'\rangle$ is an eigenstate of A . The above can be rewritten using a more general basis, $|b'\rangle$:

$$\begin{aligned} [A] &= \sum_i p_i \sum_{b'} \sum_{b''} \langle \alpha_i | b' \rangle \langle b' | A | b'' \rangle \langle b'' | \alpha_i \rangle \\ &= \sum_{b'} \sum_{b''} \left(\sum_i p_i \langle b'' | \alpha_i \rangle \langle \alpha_i | b' \rangle \right) \langle b' | A | b'' \rangle \\ &= \sum_{b'} \sum_{b''} \langle b'' | \rho | b' \rangle \langle b' | A | b'' \rangle \\ &= \text{Tr}(\rho A) \end{aligned}$$

We define the density operator

$$\rho = \sum_i p_i |\alpha_i\rangle \langle \alpha_i|$$

where $\sum_i p_i = 1$ and $p_i \geq 0$. It is a generalization of a ray to represent the state of a mixed ensemble. The density operator of a pure state is just $|\psi\rangle \langle \psi|$ since all but one of the p_i 's are zero.

The density operator is Hermitian, positive and:

$$\text{Tr}(\rho) = 1$$

In general,

$$\text{Tr}(\rho^2) \leq 1$$

Note that $\text{Tr}(\rho^2) = 1$ if and only if ρ is a pure state. As with the ray representation of a pure state, tensor products of density matrices represent the density matrix of the extended system.

1.1.6 Decoherence

We can describe the dynamics of an open quantum system as arising from an interaction between the system of interest and an environment, which together form a closed quantum system. [24]

$$\begin{aligned}\rho_{out} = \mathcal{E}(\rho_{in}) &= \text{Tr}_{env}[U(\rho_{in} \otimes \rho_{env})U^\dagger] \\ &= \sum_k \langle e_k | U(\rho_{in} \otimes \rho_{env})U^\dagger | e_k \rangle \\ &= \sum_k A_k \rho_{in} A_k^\dagger\end{aligned}$$

where U is a unitary evolution on the joint Hilbert space of the system and the environment, and \otimes represents a Kronecker product. In the second line we have assumed that the environment is initially in a pure and separable state $\rho_{env} = |e_0\rangle\langle e_0|$ and the $|e_k\rangle$'s form an orthonormal basis for the environment.

The operators $\{A_k\} = \langle e_k | U | e_0 \rangle$ are known as the operation elements of the quantum operation, or superoperator, \mathcal{E} . From the unitarity of U , the operation elements satisfy the completeness relation

$$\sum_k A_k A_k^\dagger = 1$$

The linear map \mathcal{E} satisfies the following:

1. It preserves Hermiticity: $\rho_{out}^\dagger = \sum_k A_k \rho_{in}^\dagger A_k^\dagger = \rho_{out}$
2. It is trace-preserving: $\text{tr}(\rho_{out}) = \sum_k \text{Tr}(\rho_{in} A_k^\dagger A_k) = 1 = \text{Tr}(\rho_{in})$
3. It is completely-positive: $\langle \psi | \rho_{out} | \psi \rangle = \sum_k (\langle \psi | A_k) \rho_{in} (A_k^\dagger | \psi \rangle)$

Since

$$\mathcal{E}(\rho_{in}) = \sum_k \text{Tr}(A_k \rho_{in} A_k^+) \frac{A_k \rho_{in} A_k^+}{\text{Tr}(A_k \rho_{in} A_k^+)}$$

The above is true of the Kraus operator-sum representation but may not be true for superoperators in general. The action of the quantum operation is equivalent to taking the state ρ and taking it to the state $\frac{A_k \rho_{in} A_k^+}{\text{Tr}(A_k \rho_{in} A_k^+)}$ with probability $\text{Tr}(A_k \rho_{in} A_k^+)$ and can be interpreted as doing a measurement in the computational basis of the environment basis. Note that unitary evolution of system alone is the special case in which there is only one term in the operator sum.

Quantum decoherence, which is the process by which quantum systems in complex environments exhibit classical behavior, can be understood by the operator-sum formalism or this ‘tracing over the degrees of freedom’ of the environment. Decoherence occurs when a system interacts with its environment in such a way that different parts of its wavefunction can no longer interfere with each other by invalidating the superposition principle. In the Copenhagen interpretation of quantum mechanics, decoherence is responsible for the appearance of wavefunction collapse. The off-diagonal entries of the system density matrix represent the quantum correlations or phase relationships in a coherent superposition, and when a system decoheres or dephases, these entries decay in a specific basis. The application of quantum mechanics to information processing has changed the nature of interest in the study of decoherence. Decoherence used to be just the solution to the interpretation of measurement. In quantum information processing, it is the major problem to be combated since it destroys the ‘quantumness’ of quantum information. The time-scales of decoherence varies from system to system.

Due to a distribution of external experimental parameters, the system undergoes non-unitary behavior as with decoherence, which is known as decoherence. This is known as incoherence. It can be described by the operator-sum formalism, but since the spread of these parameters is often continuous, we present the corresponding form

as follows:

$$\rho_{out} = \int p(\mathbf{r})(U(\mathbf{r})\rho_{in}U^\dagger(\mathbf{r}))d\mathbf{r}$$

An alternative way to express the above [5] is

$$|\rho_{out}\rangle = S|\rho_{in}\rangle$$

where $|\rho\rangle$ is the columnized density matrix, \bar{U} is the complex conjugate of U and $p(\mathbf{r})$ is a classical probability function. The input state $|\rho_{in}\rangle$ is thus transformed into the output state ρ_{out} by the superoperator

$$S = \int p(\mathbf{r})\bar{U}(\mathbf{r}) \otimes U(\mathbf{r})d\mathbf{r}$$

Here, $p(\mathbf{r})$ is a classical probability distribution and we can understand it in the context of the original operation elements as $A_k = \sqrt{p_k}U_k$. We therefore see that decoherent and incoherent processes are the same mathematically, except that the operation elements on a decoherent process are not functions of external parameters. The distinction is therefore practical and depends on the correlation time of the variation of experimental parameters. If the latter is larger than the typical modulation frequency, the process falls into the class of incoherent noise. While correcting for decoherent errors, we need to utilize the full power of quantum error-correction, but incoherent errors can in principle be refocussed and thus can often be reduced by careful design of the time dependence of control fields. This is possible since the operators underlying the incoherence are assumed to be time independent over the length of the expectation value measurement. Common approaches for instance in NMR include composite and adiabatic pulses [2] .

Removing the restriction that the operation elements arise from a unitary on the overall Hilbert space, the completeness relation does not have to be specified, but the following still holds

$$\sum_k A_k A_k^\dagger \leq 1$$

This corresponds to processes in which extra information about the processes is obtained by measurement.

1.2 Optimal Control Theory applied to Quantum Systems

One of the main goals for theoretical research in quantum control will be further to integrate what is known from the physics of open quantum systems with core engineering methodologies. Much progress in the field has been made both experimentally and theoretical. In particular, optimal control theory (OCT) has been applied to analyze quantum systems in small Hilbert spaces in order to find upper bounds of control performance as well as derive control sequences to approach these bounds [15, 8, 9, 11]. OCT-based algorithms have also been developed to search for control sequences in NMR applications to maximize coherence transfer in given time for both uncoupled and coupled spin systems and have shown promising results for use in an ensemble of quantum systems with parameter variations, both in the presence of absence of relaxation [14, 10, 12]. Quantum filtering equations, which are stochastic differential equations (SDE's) describing the evolution of density matrices under weak measurements have also been developed and verified in some systems [20, 21]. Assuming controllability and the absence of decoherence, it has been shown that the extrema of fidelity of quantum control correspond to either perfect control or no control [18]. In other words, the control landscape of the same dimensions have the same structure and as we search for fidelity maxima, there are no 'traps' of inferior solutions of 'false maxima'. In other words, in the absence of relaxation and with unrestrictions amount of resources, every control is perfect [17]. We also know that a universal set of quantum gates can be constructed in an n -spin Hilbert space from one-qubit and two-qubit operations [13].

Chapter 2

Quantum Control in the NMR context

We will discuss how unitary control is achieved in Nuclear Magnetic Resonance (NMR) spectroscopy. An introduction to NMR spectroscopy is therefore worthwhile and will be the subject of this chapter.

In 1946, Purcell and Bloch observed the magnetic induction of nuclear spins. This opened up a new field of research leading to important applications such as molecular structure determination, the study of fluids flows in system and magnetic resonance imaging (MRI) for medical diagnostics. Recently, NMR has been proposed to implement quantum information processing devices. NMR is a physical phenomenon based up the magnetic property of an atom's nucleus. All nuclei that contain odd numbers of nucleons and some that contain even numbers of nucleons have an intrinsic magnetic moment. The most often-used isotopes are hydrogen-1 and carbon-13. NMR studies a magnetic nucleus by aligning it with a very powerful external magnetic field and perturbing the nuclear spin state using a usually oscillating electromagnetic field. The response to this perturbing field allows us to detect a time-domain signal known as the free induction decay (FID), which is the data we obtain in nuclear magnetic resonance spectroscopy and magnetic resonance imaging. Before we go into the details of NMR spectroscopy, we shall introduce a quantum mechanical concept with no classical counterpart: spin angular momentum.

2.1 Spin, Magnetic Moment and Angular Momentum

Classically, the angular momentum of a particle about some origin is

$$\mathbf{L} = \mathbf{r} \times \mathbf{p}$$

where \mathbf{r} is the position of the particle and \mathbf{p} is the linear momentum of the particle. Classical angular momentum generates mechanical rotations about the origin. Defining angular momentum as the generator of rotations, we find in quantum mechanics that there exists spin angular momentum, which does not depend on the position or linear momentum of the particle, but is an intrinsic property of particles. This degree of freedom was clearly shown by Stern and Gerlach in 1920 [19]. A beam of silver atoms were sent through a magnetic field and a continuum of vertical positions of screen was expected. However, they witnessed that all particles were deflected either up or down by the same amount and postulated that there must be a quantized angular momentum associated with the nucleus.

Nuclear spin angular momentum is a quantum phenomenon with no classical counterpart. It is a vector quantity that can be specified along the (x, y, z) directions by (I_x, I_y, I_z) . I_k is the generator of rotation about the k th axis. The fundamental commutation relations of angular momentum are as follows:

$$[I_i, I_j] = i\hbar\epsilon_{ijk}I_k$$

where ϵ_{ijk} is the Levi-Civita symbol, a completely antisymmetric tensor.

The lowest number of dimensions in which the angular momentum commutation relation is realized is $N=2$, corresponding to spin- $\frac{1}{2}$ systems. The operators are defined

by

$$\begin{aligned} I_x &= \frac{\hbar}{2} \{ |+\rangle\langle -| + |- \rangle\langle +| \} \\ I_y &= \frac{i\hbar}{2} \{ -|+\rangle\langle -| + |- \rangle\langle +| \} \\ I_z &= \frac{\hbar}{2} \{ |+\rangle\langle -| - |- \rangle\langle +| \} \end{aligned}$$

The above spin operators have matrix representations $I_k = \frac{\hbar}{2}\sigma_k$, where σ_k are the Pauli matrices

$$\begin{aligned} \sigma_x &= \begin{pmatrix} 0 & 1 \\ 1 & 0 \end{pmatrix} \\ \sigma_y &= \begin{pmatrix} 0 & -i \\ i & 0 \end{pmatrix} \\ \sigma_z &= \begin{pmatrix} 1 & 0 \\ 0 & -1 \end{pmatrix} \end{aligned}$$

When we measure the spin along the x, y or z axis, we obtain one of the eigenstates of the operator corresponding to the axis we measure along.

Defining

$$I \cdot \hat{n} = n_x I_x + n_y I_y + n_z I_z$$

we can write a rotation operator

$$R(\hat{n}, \phi) = e^{\frac{-iI \cdot \hat{n}}{\hbar} \phi}$$

Let $i, j, k \in x, y, z$. Expanding $R(\hat{n}, \phi)$ is a Taylor series and using the commutation relations,

$$e^{\frac{-iI_i}{\hbar}} I_j e^{\frac{iI_i}{\hbar}} = I_j \cos \phi + \epsilon_{ijk} I_k \sin \phi$$

2.2 Nuclear spin and resonance

The Hamiltonian of a spin in a magnetic field along the positive z direction is

$$H = -\frac{e}{m_e c} \mathbf{S} \cdot \mathbf{B} = -\gamma B \mathbf{I}_z = \omega \mathbf{I}_z$$

where

$$\omega = \frac{|e|B}{m_e c} = -\gamma B$$

The frequency ω is the Larmor frequency of precession and we shall discuss it again in the next section. We know from the non-zero commutators of the I_j 's that only one of the three components of \mathbf{I} can be specified. The value of the z component of \mathbf{I} is given by

$$I_z = \hbar m$$

where $m \in \{-I, -I+1, \dots, I-1, I\}$. A nucleus with spin I has $2I+1$ possible values of I_z as specified by the magnetic quantum number m . [4] We can detect the presence of these energy levels by observing transitions between them. This is achieved in NMR by irradiating the sample with an electromagnetic radiation, the details of which will be described in the next section.

The time-evolution operator based on our Hamiltonian is

$$U(t, 0) = e^{\frac{-iHt}{\hbar}} = e^{\frac{-iI_z \omega t}{\hbar}}$$

We can show that

$$\begin{aligned}\langle S_x(t) \rangle &= \langle S_x(0) \rangle \cos(\omega t) - \langle S_y(0) \rangle \sin(\omega t) \\ \langle S_y(t) \rangle &= \langle S_y(0) \rangle \cos(\omega t) + \langle S_x(0) \rangle \sin(\omega t) \\ \langle S_z(t) \rangle &= \langle S_z(0) \rangle\end{aligned}$$

The above equations describe the spin-precession of the nuclear spin of an atom

corresponding to the classical Bloch model.

2.3 The Bloch model and the single-pulse NMR experiment

Classically, the rate of change of angular momentum is equal to the torque on the system.

$$\frac{d\mathbf{L}}{dt} = \boldsymbol{\mu} \times \mathbf{B}$$

where $\boldsymbol{\mu}$ is the magnetic moment. Letting γ be the gyromagnetic ratio of the particle, $\boldsymbol{\mu}$ is given by

$$\boldsymbol{\mu} = \gamma \mathbf{L}$$

Therefore, we see that

$$\frac{d\mathbf{L}}{dt} = -\gamma \mathbf{B} \times \mathbf{L} = \boldsymbol{\omega} \times \mathbf{L}$$

where $\boldsymbol{\omega} = -\gamma \mathbf{B}$ is the Larmor frequency. In the case of a static field B_0 along the z-axis, we see that, surprisingly, the energy difference between the levels is exactly equal to the classical Larmor frequency of precession.

The coupling between energy levels to stimulate an observable response is commonly produced by an alternating magnetic field applied perpendicular to the static field.

$$H_{rf} = -\gamma \hbar B_1 (I_x \cos(\omega_{rf} t + \phi) + I_y \sin(\omega_{rf} t + \phi))$$

To see the effect of this oscillating field on the bulk magnetization, which is proportional to the magnetic moment, we can make a change of coordinates to a frame rotating with respect to the fixed axis with angular frequency ω_{rf} and obtain

$$\frac{d\mathbf{M}(\mathbf{t})}{dt} = \mathbf{M}(\mathbf{t}) \times (\gamma\mathbf{B}(\mathbf{t}) + \omega_{rf})$$

The effect field is therefore

$$\mathbf{B}_{\text{eff}} = \mathbf{B}(\mathbf{t}) + \frac{\omega}{\gamma}$$

For $B(t) = B_0\hat{z}$ and $\omega_{rf} = -\gamma B_0$, the magnetization

$$\frac{d\mathbf{M}_r(t)}{dt} = \mathbf{M}_r(t) \times \gamma\mathbf{B}_r(t)$$

and the magnetic field in the rotating frame is

$$\mathbf{B}_r = B_1\cos\phi\hat{\mathbf{x}} + B_1\sin\phi\hat{\mathbf{y}} + (\omega_0 - \omega_{rf})\hat{\mathbf{z}}$$

When $\omega_0 = \omega_{rf}$, B_r lies entirely on the transverse plane and the radiation is said to be applied on-resonance. Without losing generality, if we set $\phi = 0$, the bulk magnetization M_r precesses around the x-axis at the angular frequency $\omega_1 = -\gamma B_1$.

Chapter 3

Methodology

3.1 Strongly Modulating Pulses as an efficient implementation of unitary transformations

In the standard model of quantum computing, an algorithm can be expressed as a series of unitary transformations on the quantum states. We would like to have a quantum system with a Hamiltonian that contains a sufficient set of externally controlled parameters to allow for the generation of a universal set of gates, such that any arbitrary unitary can be achieved. The task of control is to find a time-dependent sequence of values of these control parameters to generate each particular unitary to the precision required for fault-tolerance. A metric of a gate's performance should describe how closely our solution implements the desired unitary operation. Two such useful metrics are the state correlation and gate fidelity. The correlation measures the closeness between our simulated or experimentally obtained output state, ρ_{out} , and the desired output state ρ_{ideal} resulting from a particular input state ρ_{in} through evolution of different propagators, where

$$\rho_{ideal} = U_{ideal}\rho_{in}U_{ideal}^+$$

In order to describe the fidelity and correlation measures we must first explore the complex dynamics that the physical system undergoes. We will use liquid state NMR as a model physical implementation. In liquid-state NMR, the homonuclear internal Hamiltonian for a molecule containing N spin- $\frac{1}{2}$ nuclei is

$$H_{int} = \sum_{k=1}^N \omega_k \mathbf{I}_z^k + 2\pi \sum_{j>k}^N \sum_{k=1}^N J_{kj} \mathbf{I}^k \cdot \mathbf{I}^j,$$

where ω_k represents the chemical shift frequency of the k th spin, J_{kj} is the coupling constant between the spins k and j and \mathbf{I}^k denotes the k th spin's angular momentum operator. The first term, the nuclear Zeeman interaction, dominates the internal Hamiltonian. The mapping between the physical spin system and the qubits is to take the eigenstates of the Zeeman interaction as the computational basis states. the scalar coupling slightly mixes the states.

The control sequences consist of a time ordered series of intervals during which a simple RF field is applied. The external Hamiltonian of the time dependent RF field is

$$H_{ext}(t) = \sum_{k=1}^N e^{-i(\omega_{rf}(t)t+\phi(t))\mathbf{I}_z^k} (-\omega_1(t)\mathbf{I}_x^k) e^{i(\omega_{rf}(t)t+\phi(t))\mathbf{I}_z^k}$$

where ω_{rf} is the transmitter's angular frequency, $\phi(t)$ the phase, the ω_1 the power. Control sequences of this form have the advantages of being simple to simulate (by moving into the interaction frame of H_{ext} during each interval) and of being straightforward to experimentally implement. For complex propagators in large Hilbert spaces they are inefficient to find and alternative schemes based on OCT may be preferred. For the study reported here we are interested in only small Hilbert spaces and SMP suffice. We expect the conclusions to be true also for OCT methods since the control limitations reflect the structure of the underlying Hamiltonians. Note also that the combination of H_{int} and $H_{ext}(t)$ is sufficient to provide universal control unless there are accidental symmetries in H_{int} (such as $\omega_k = \omega_{k'}$, where $k \neq k'$). This universality has been well described and demonstrated in the literature and it is easily seen that the commutator of H_{int} and $H_{ext}(t)$ span the entire Hilbert space. Given that we have universality we will focus our attention on control sequences in

the class of strongly modulating pulses (SMP) [5]. These have been shown to provide compact high fidelity coherent control even in the presence of incoherence. (ref).

Excluding decoherence, the evolution generated by several periods of RF pulses with different parameters is

$$U_{gate} = \prod_{m=1}^M U_z^{-1}(f_m, \tau_m) \exp[-iH_{eff}^m(\omega_{rf,m}, f_m, \phi_m)\tau_m],$$

where $U_z^{-1}(f_m, \tau_m)$ executes the rotating-frame transformation of the m th period and H_{eff} is the effective, time-independent Hamiltonian in the new frame of reference. [4]

However, due to decoherence and incoherence, the actual evolution on the system is non-unitary and is instead given in terms of the Kraus operators A_k .

$$\rho_{out} = \sum_k A_k \rho_{in} A_k^\dagger$$

where

$$\sum_k A_k A_k^\dagger \leq 1$$

The primary sources of incoherence in our system are the spatial variation in the power of the RF frequency ω_1 , and the spatial variation in the Zeeman frequency, ω_0 . Since the power of the RF field (in frequency units), ω_1 , is in practice a function of position in the spectrometer due to RF field variations in space within the sample, we actually have

$$\rho_{out} = \int p(\mathbf{r}) U(\mathbf{r}) \rho_{in} U^\dagger(\mathbf{r}) d\mathbf{r}$$

and

$$|\rho_{out}\rangle = \int p(\mathbf{r}) \overline{U(\mathbf{r})} \otimes U(\mathbf{r}) d\mathbf{r} |\rho_{in}\rangle$$

where $|\rho\rangle$ is the columnized density matrix, \overline{U} is the complex conjugate of U and \otimes is the Kronecker product of the matrices. The input state $|\rho_{in}\rangle$ is thus transformed into the output state ρ_{out} by the superoperator

$$S = \int p(\mathbf{r}) \overline{U(\mathbf{r})} \otimes U(\mathbf{r}) d\mathbf{r}$$

Note that the superoperator is also capable of characterizing decoherence. Similar processes may be used to characterize the spatial variation in the Zeeman interaction.

Experimental imperfections are characterized by a spatially or temporally ‘incoherent variation’ in the system’s Hamiltonian. Experimental reality presents an important set of challenges to achieving precise control over quantum systems. Spatially incoherent errors have been a recurring topic of interest in the field of NMR, where they arise as inhomogeneities in the static and radio-frequency (RF) fields involved. The spatially incoherent evolution caused by the inhomogeneities dephases the spins in the NMR ensemble, attenuating and rotating the final state away from the desired state. The main difference between incoherent errors and decoherent errors lie in the fact that incoherent errors can in principle be refocused, while decoherence represents information lost to the environment or to inaccessible degrees of freedom.

The state correlation is the normalized overlap between two quantum states and quantifies how similar they are. It is a function of ρ_{in} , U_{ideal} and the experimental output state ρ_{out} and is given by

$$C(\rho_{ideal}, \rho_{out}) = \frac{\text{Tr}(\rho_{ideal} \rho_{out})}{\sqrt{\text{Tr}(\rho_{ideal}^2) \text{Tr}(\rho_{out}^2)}}$$

Due to non-unitary operations, there is a loss of information. We insert an attenuation factor to obtain the attenuated correlation, which includes the loss of purity during the evolution.

$$\begin{aligned} C_A(\rho_{ideal}, \rho_{out}) &= C(\rho_{ideal}, \rho_{out}) \sqrt{\frac{\text{Tr}(\rho_{out}^2)}{\text{Tr}(\rho_{in}^2)}} \\ &= \frac{\text{Tr}(\rho_{ideal} \rho_{out})}{\sqrt{\text{Tr}(\rho_{ideal}^2) \text{Tr}(\rho_{in}^2)}} \end{aligned}$$

The gate fidelity F is a measure of the precision of the operation

$$F = \overline{C_A(\rho_{ideal}, \rho_{out})}$$

where the overline notation $\overline{C_A}$ represents the average attenuated correlation over a complete basis of orthonormal Hermitian matrices ρ_j . In the case of incoherent processes, it is often convenient to use the equivalent expression for F directly in terms of U_{ideal} and the Kraus operators $\{A_k\}$,

$$F = \|\text{Tr}(U_{ideal}^+ A_k)\|^2 \frac{1}{N^2}$$

where $N = 2^n$ and n being the number of qubits.

With these backgrounds in mind, we pose the following questions:

1. How do we quantify the robustness of a given control sequence? Do we need additional resources to engineer robustness into our quantum control systems?
2. We are limited by available resources, for instance, finite power, bandwidth, and decoherence. Taking resources into account, can we generate any effective Hamiltonian we desire with arbitrary fidelity?

Quantum Control Theory has yet to develop to the level to answer such questions in complete generality analytically beyond $SU(2)$, and we therefore rely on numerical simulations to shed light on these issues.

Here we take the simplest non-trivial system and one that has been well studied experimentally. Consider the following real system: the two coupled proton spins of dibromothiophene. The Hamiltonian of the system is given by

$$H_{int} = \Delta\omega(\mathbf{I}_z^A - \mathbf{I}_z^B) + 2\pi J\mathbf{I}^A \cdot \mathbf{I}^A$$

where $\Delta\omega = 2\pi 65\text{Hz}$, $J = 5.75\text{Hz}$. There are many possible operators in the 2-spin Hilbert space of the dibromothiophene molecule. However, much can be learned by

focussing on the implementation of the following two operators U_1 and U_{12} , where

$$U_1 = e^{\frac{-i\pi}{2}\mathbf{I}_x^A}$$

and

$$U_{12} = e^{\frac{-i\pi}{2}(\mathbf{I}_x^A + \mathbf{I}_x^B)}$$

Here, U_1 is a selective $\frac{\pi}{2}$ rotation of spin A about the x-axis; spin B is left unchanged. In contrast, U_{12} is a non-selective transformation and rotates both spins A and B by $\frac{\pi}{2}$ about the x-axis. We choose these for their computation importance and since the conditional gates can be constructed from these and periods of free evolution under the internal Hamiltonian.

For these simple pulses and in this small Hilbert space it is sufficient to achieve high fidelity to have SMP of only 2 time intervals. We search the space of the 8 parameters for a 2 period pulse to achieve U_1 and U_{12} . First, a random number in a typical range for each parameter is generated. For U_1 , the range for t_1 and t_2 was $[0, 1\text{ms}]$; the range for f_1 and f_2 was $[0, 60\text{kHz}]$; the range for ω_1 and ω_2 was $[0, 1\text{MHz}]$ and the range for ϕ_1 and ϕ_2 was $[0, 2\pi]$. These 8 parameters are then fed into a search function that is aimed at maximizing the fidelity of the unitary propagator U_{real} in implementing the desired operation U_{ideal} , given by

$$F(U_{ideal}, U_{real}) = \text{Tr}(U_{ideal}^+ U_{real})$$

The fidelity F measures how closely U_{real} , the unitary propagator on the system generated by the 2-period RF magnetic pulse implements U_{ideal} . For a given desired operation U_{ideal} , the search function used is a non-derivative method set to minimize the cost $g(x) = 1 - F(U_{ideal}, U_{real}(x))$ over the vector x , where $U_{real}(x)$ is the unitary propagator that results from the RF pulse with parameters x . For our 2-period case, x would be an 8 by 1 vector containing the time durations, RF frequencies, magnetic field strengths and the initial phases for the two pulses. It is a member of the family

of coordinate descent methods, more specifically, the Nelder-Mead simplex search method. This direct search method is particularly convenient since the analytic form of the fidelity F is unknown. For a function to be optimized with respect to n parameters, the algorithm randomly generates $n+1$ convex points, $x_0, x_1, x_2, \dots, x_n$ and goes through iterations until F converges.

At each iteration, we start with a simplex of $n+1$ points and end up with another simplex. Let x_{min} and x_{max} denote the best and worst vertices of the simplex, that is,

$$g(x_{min}) = \min_{i=0,1,2,\dots,n} g(x^i)$$

$$g(x_{max}) = \max_{i=0,1,2,\dots,n} g(x^i)$$

Let \hat{x} denote the centroid of the face of the simplex formed by all vertices by x_{max} .

$$\hat{x} = \frac{1}{n} (-x_{max} + \sum_{i=0}^n x^i)$$

The iteration replaces the worst vertex x_{max} by a better one. A typical iteration consists of the following steps [1]:

1. Step 1: Reflection step

Compute the reflection point

$$x_{ref} = 2\hat{x} - x_{max}$$

Then compute x_{new} to replace x_{max} according to three cases:

- (a) x_{ref} has minimum cost: If $g(x_{min}) > g(x_{ref})$, go to Step 2.
- (b) x_{ref} has intermediate cost: If $\max\{g(x^i) | x^i \neq x_{max}\} > g(x_{ref}) \geq g(x_{min})$, go to Step 3.
- (c) x_{ref} has maximum cost: If $g(x_{ref}) \geq \max\{g(x^i) | x^i \neq x_{max}\}$, go to Step 4.

2. Step 2: Attempt Expansion Compute

$$x_{exp} = 2x_{ref} - \hat{x}$$

The new point x_{new} is given by

$$x_{new} = \begin{cases} x_{exp}, & \text{if } g(x_{exp}) < g(x_{ref}), \\ x_{ref} & \text{otherwise} \end{cases}$$

3. Step 3: Use Reflection Use the Reflection point as the new coordinate.

$$x_{new} = x_{ref}$$

4. Step 4: Perform Contraction Define

$$x_{new} = \begin{cases} \frac{1}{2}(x_{max} + \hat{x}), & \text{if } g(x_{exp}) < g(x_{ref}), \\ \frac{1}{2}(x_{ref} + \hat{x}) & \text{otherwise} \end{cases}$$

and form the new simplex by replacing x_{max} with x_{new} .

Using the above algorithm, 25 pulses for U_1 and 33 pulses for U_{12} at fidelity maxima were generated for the real system. We will next discuss the characterization of robustness of these pulses.

3.2 Control Curvature: a measure of robustness of control

It has been our experience in implementing control schemes in larger Hilbert spaces that occasionally the experimental implementation fails to provide the expected fidelity. The reason for this rare event is unknown but we associate it with the effects of small errors in the control fields. There is imprecision in the control of RF magnetic fields strength, frequencies, phases and the duration for which these pulses are applied, as well as variations of field strength within the sample (lack of homogeneity). All of these factors mean that depending on how sensitive the fidelity of our pulse is with respect to variations of control parameters, the fidelity would suffer to different

extents. For example, pulse durations can be controlled to the order of 12.5ns; on top of that, since we are driving a high Q RF circuit, transient effects may decrease the precision. Phases can be controlled well to the order of 0.01 degrees, while frequencies can be controlled to 0.005Hz, but bandwidths for frequency changes are on the order of 3MHz. We therefore wish to have a measure to characterize the robustness of these control pulses. One such measure is the curvature C with respect to parameter a (e.g. one dimension of the vector x) below:

$$C_a = \left\| \frac{\partial^2 F}{\partial a^2} \right\|$$

The higher the value of C_a is, the more vulnerable the fidelity is with respect to changes in the parameter a . For the pulses we found, we calculate the curvature with respect to each of the 8 parameters using the finite difference method. For a being the i th coordinate of the x vector, the second derivative of the fidelity f is approximated by

$$\frac{\partial^2 F}{\partial a^2} = \frac{1}{\Delta x^2} (F(x^k + \Delta x e_i) + F(x^k - \Delta x e_i) - 2F(x^k))$$

Values of $F(x^k + n\Delta x e_i)$, where $n = 0, 1$ or -1 , are obtained by simulating the effective unitary propagator for the corresponding parameters and calculating the fidelity $F(U_{ideal}, U_{real}(x^k + n\Delta x e_i))$. The choice of the interval Δx is tricky, since pulses with different sensitivities would naturally require different values to give an accurate estimate. When Δx is too large, the approximation would be inaccurate. However, if we reduce it too much, the roundoff errors that occur when quantities of similar magnitude are subtracted gives a large relative error size in the gradient approximation. Our results were arrived at by trial and error and by ensuring that the curvature at neighboring points agree to 2 significant figures.

In order for fair comparison between parameters of different units (for example, seconds for time and radians/s for RF strength), we calculated the second derivative with respect to *fractional* changes in the parameters, so that C is unitless.

To more meaningfully explore the relationship between fidelity and curvature, we have integrated the the curvatures with respect to individual parameters such as t_1 and f_2 to form curvatures with respect to quantities representative of a class

of parameters such as time duration of the sequence and strength of RF power. We report such quantities for four classes of parameters, time, control field power, control field frequency and control field phase. The following quantities have been chosen:

1. Total time of the pulse sequence

$$t = t_1 + t_2$$

2. Average power (in frequency units)

$$\omega_{ave} = \frac{\omega_1 t_1 + \omega_2 t_2}{t_1 + t_2}$$

3. Maximum power

$$\omega_{max} = \max\{\omega_1, \omega_2\}$$

4. Frequency bandwidth

$$f = |f_1 - f_2|$$

The frequency bandwidth $f = |f_1 - f_2|$, measures the range of RF frequencies used to excite our system.

5. Phase bandwidth

$$\phi = |\phi_1 - \phi_2|$$

The phase bandwidth $\phi = |\phi_1 - \phi_2|$, measures the jump in the phase of the pulse between the two different time periods.

Chapter 4

Results and Analysis

4.1 Fidelity vs Curvature

Scatter plots of pulse sequence fidelity versus curvatures with respect to the parameters we have chosen are shown in Figures 4-1 through 4-5. We label sequences with the highest fidelity pulses in the diagrams. Sequence a , b and c correspond to the three modulation sequences with the highest fidelities.

The first thing we note from all the plots is that the fidelities for the non-selective U_{12} pulses are consistently higher than those for the selective U_1 pulses. The U_1 pulses also have a larger spread in fidelities. This was expected and illustrates an important point for controls to achieve different operators in the Hilbert space, namely, that different unitary operators will have implementations or controls of different performance.

The second thing we learn is that in all 5 plots, the selective pulses have, on average, higher curvatures with respect to the integrated parameter concerned, i.e., $C_a(U_1) > C_a(U_{12})$. These two results have important implications, that in order for us to achieve a certain fidelity and robustness, selective operators require more resources to implement than a non-selective operator due to the differences in tensor product structures.

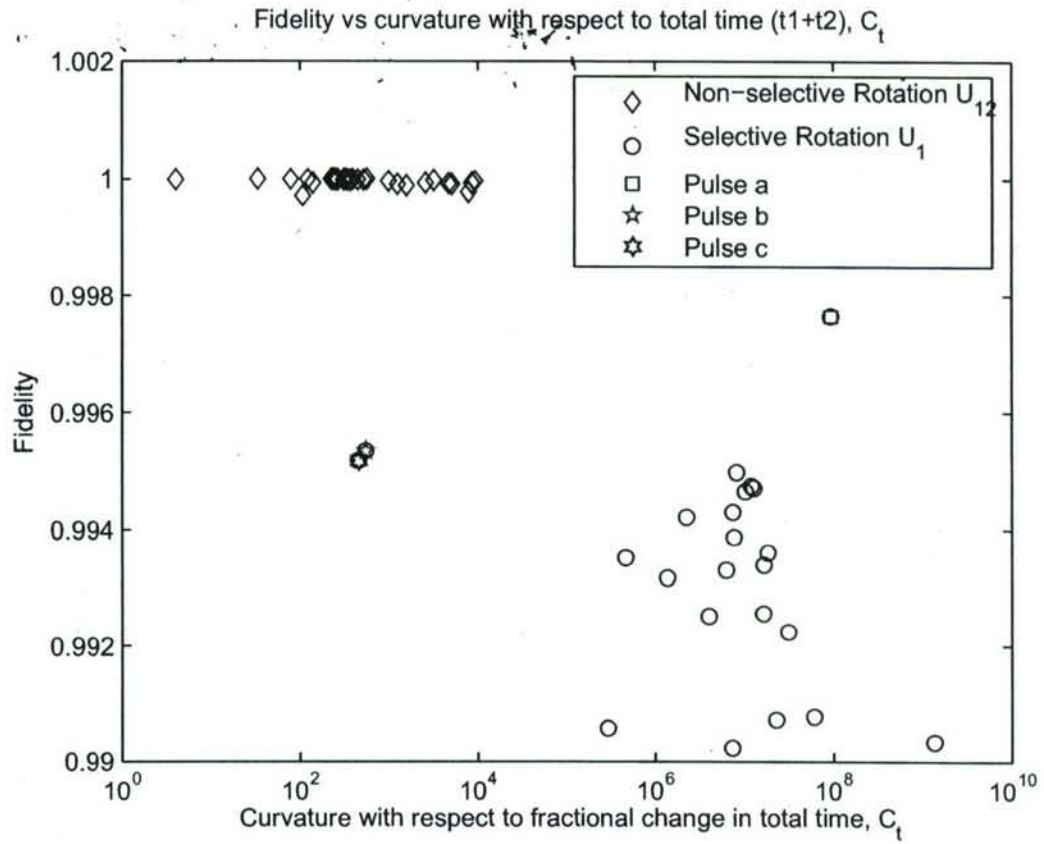


Figure 4-1: Scatter plot of pulse fidelity verses curvature with respect to fractional changes in total time, $t = t_1 + t_2$, of the pulse. Each blue diamond corresponds to a U_{12} pulse and each circle corresponds to a U_1 pulse. C_t for the non-selective rotation U_{12} are in the range $[10, 10^4]$, whereas values for the selective rotation U_1 lie mostly in the range $[10^5, 10^8]$. This indicates that the selective pulses are less robust to variations in the durations of applied RF pulses.

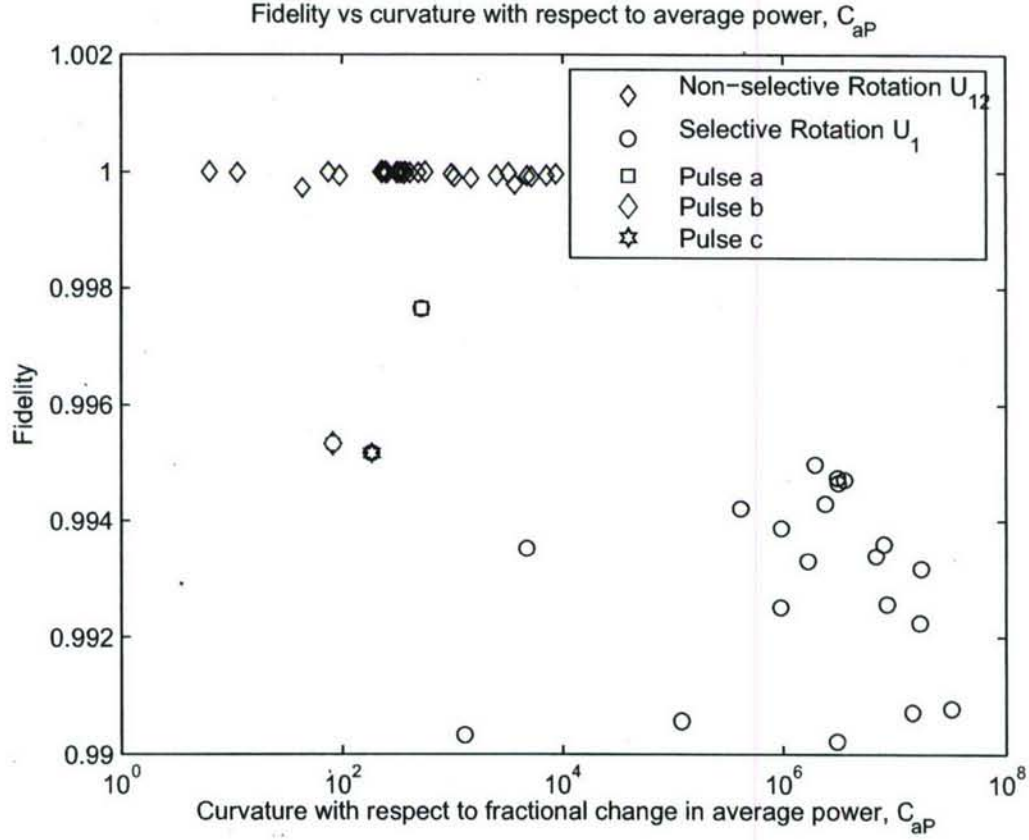


Figure 4-2: Scatter plot of fidelity vs the curvature with respect to the average power $\omega_{ave} = \frac{\omega_1 t_1 + \omega_2 t_2}{t_1 + t_2}$. C_{aP} for the non-selective rotation U_{12} are in the range $[10, 10^4]$, whereas values for the selective rotation U_1 lie mostly in the range $[10^3, 10^8]$. This again indicates that the selective pulses are less robust to variations in pulse parameters: this time the strength of applied RF fields. For average power, all the three selective U_1 pulses with highest fidelities have very low C_{aP} , which means that they are very good pulses with respect to both fidelity and robustness to RF power.

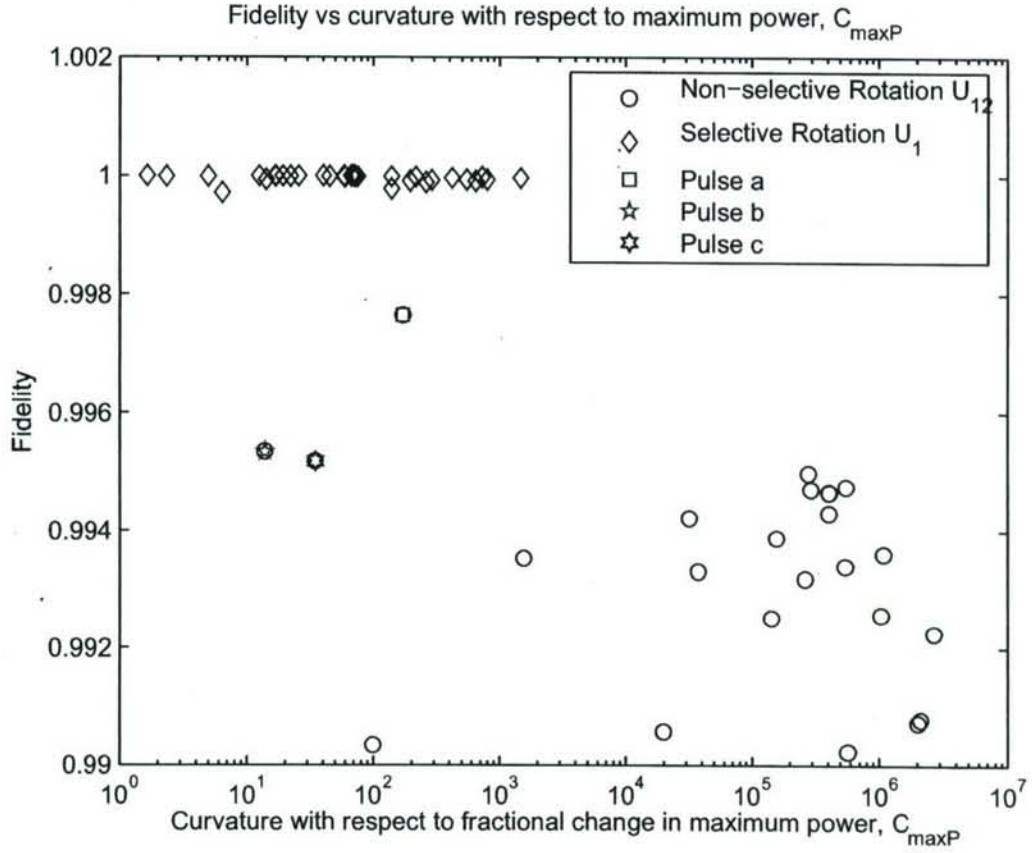


Figure 4-3: Scatter plot of fidelity vs the curvature with respect to the maximum power $\omega_{max} = \max\{\omega_1, \omega_2\}$ is expected to be similar to that of the average power. C_{maxP} for the non-selective rotation U_{12} are mostly in the range $[1, 10^3]$, whereas values for the selective rotation U_1 lie mostly in the range $[10^4, 10^7]$. These values are smaller, and within a narrower range than the average power. The reason is likely that the influence of higher power period is more dominant, and is thus less vulnerable to variations.

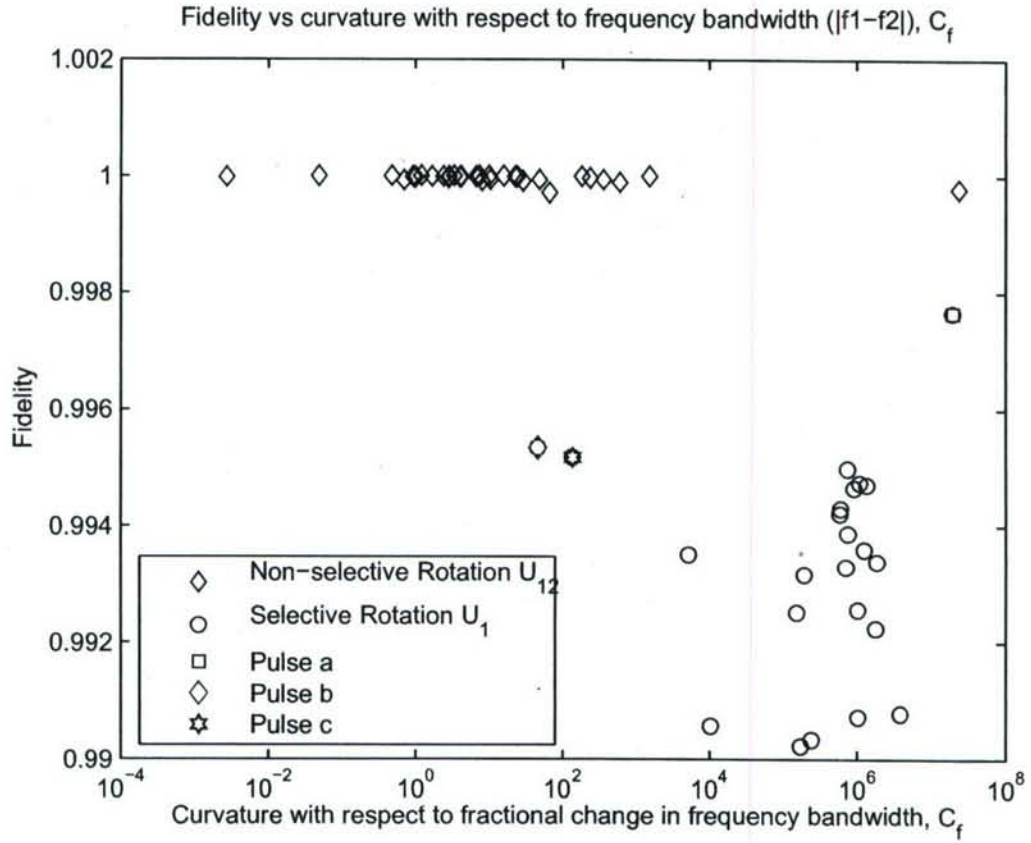


Figure 4-4: The C_f for the non-selective rotation U_{12} are mostly in the range $[10^{-1}, 10^3]$, whereas values for the selective rotation U_1 lie mostly in the range $[10^4, 10^7]$. This is consistent with the results about the other parameters. Pulse sequences β and ϵ are both robust with respect to variations in frequency bandwidth. However, pulse α , which has the highest fidelity, has the largest C_f and hence the worst robustness.

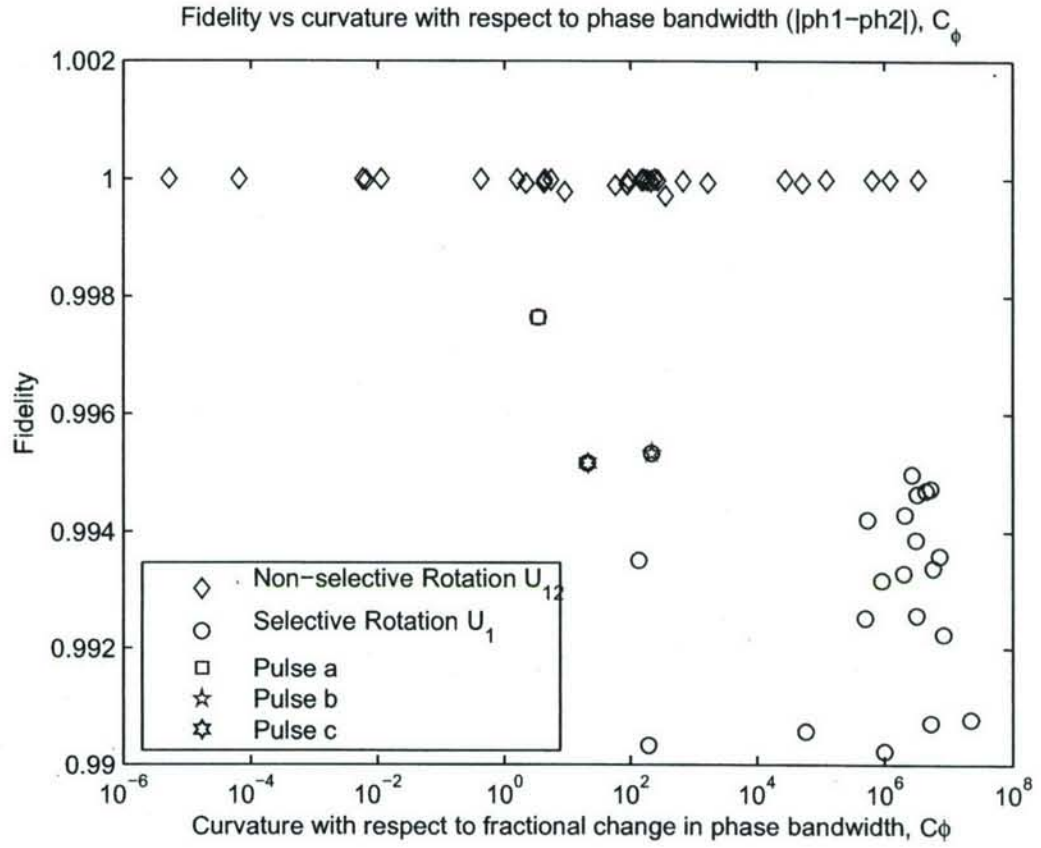


Figure 4-5: The C_ϕ for the non-selective rotation U_{12} are mostly in the range $[10^{-6}, 10^6]$, whereas values for the selective rotation U_1 lie mostly in the range $[10^2, 10^8]$. This is consistent with the results about the other parameters. All the three highest fidelity U_1 pulses have the lowest C_ϕ values and are thus both robust with respect to variations in ϕ .

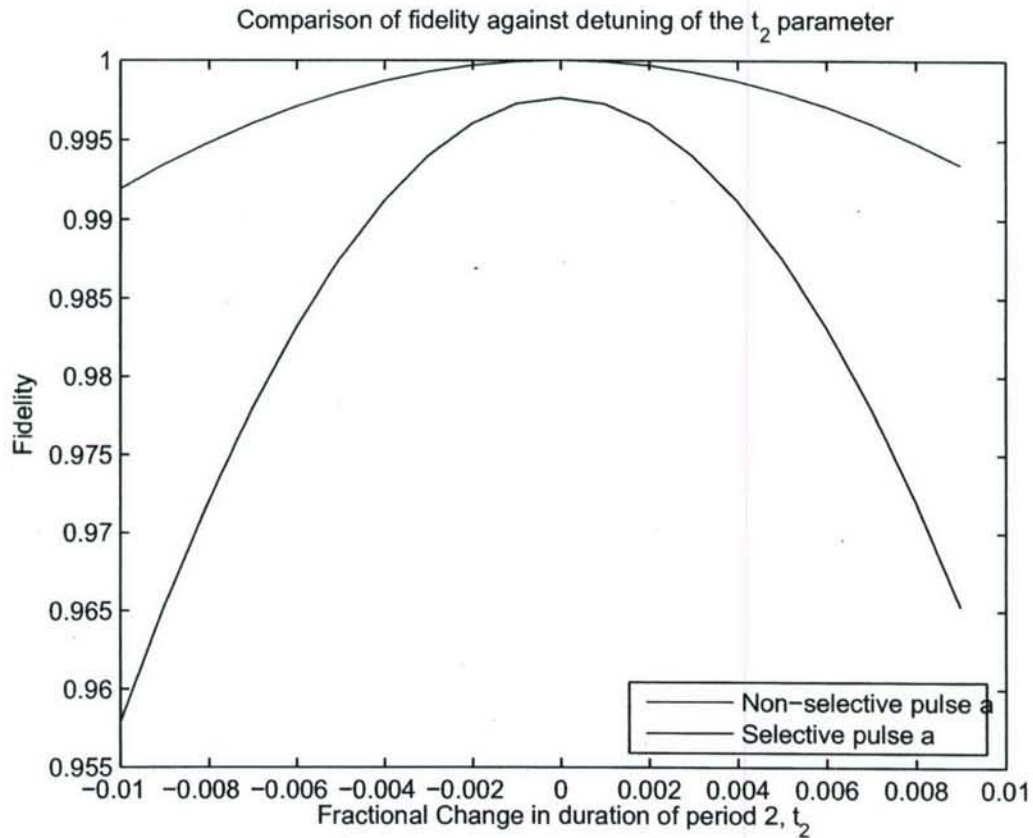


Figure 4-6: This is a plot of fidelity versus curvature with respect to fractional changes in the duration of the second period, t_2 for two given pulses-one selective and one non-selective. The fidelity of the non-selective is higher than that of the selective pulse, and by inspection, the curvature is lower, showing more robust behavior.

To further examine the truth of the above two points, we plot the behavior of fidelity versus detuning from a maximizing parameter value. Figures 4-6 and 4-7 show the comparison between the highest fidelity non-selective pulse sequence and the highest fidelity selective pulse sequence, labelled 'nonselective pulse a' and 'selective pulse a' in Figures 4-13 through 4-16. Figure 4-8 shows a comparison between another pair of pulse sequences labelled 'nonselective pulse b' and 'selective pulse b'.

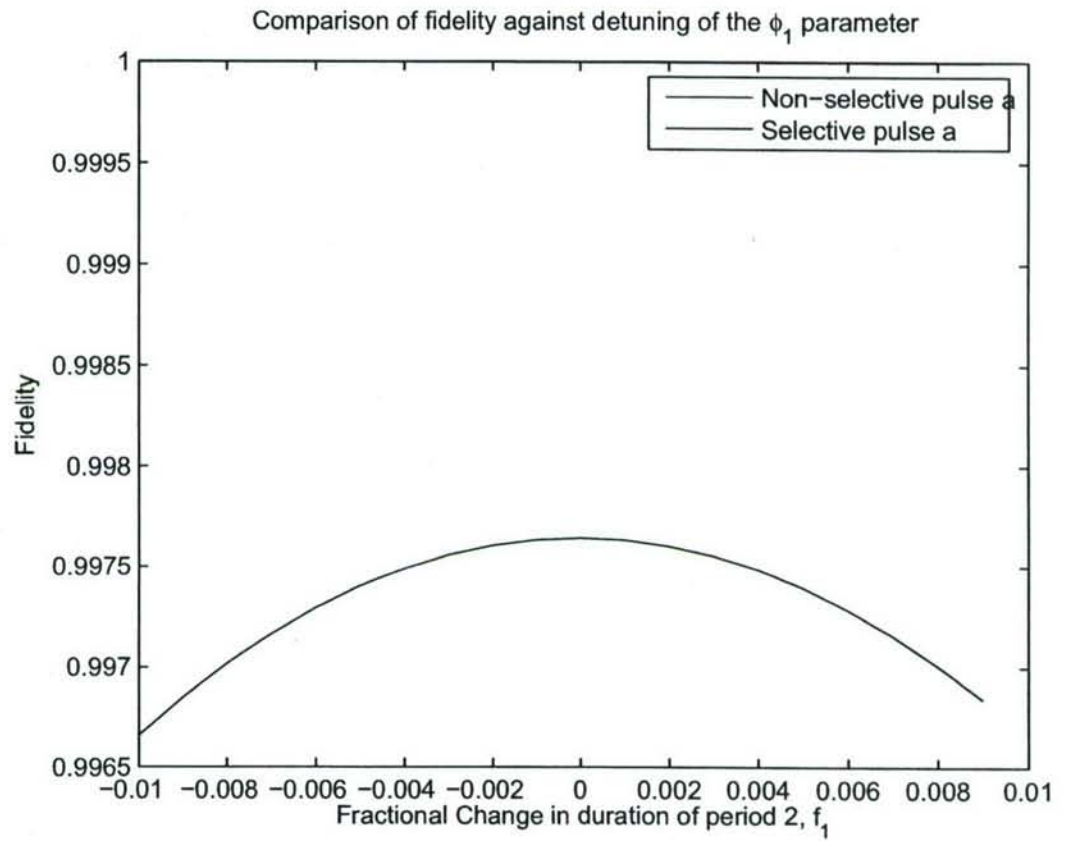


Figure 4-7: This is a plot of fidelity versus curvature with respect to fractional changes in the RF frequency of the first period, f_1 for two given pulses-one selective and one non-selective. Again, the fidelity is higher and the pulse is more robust for the non-selective case.

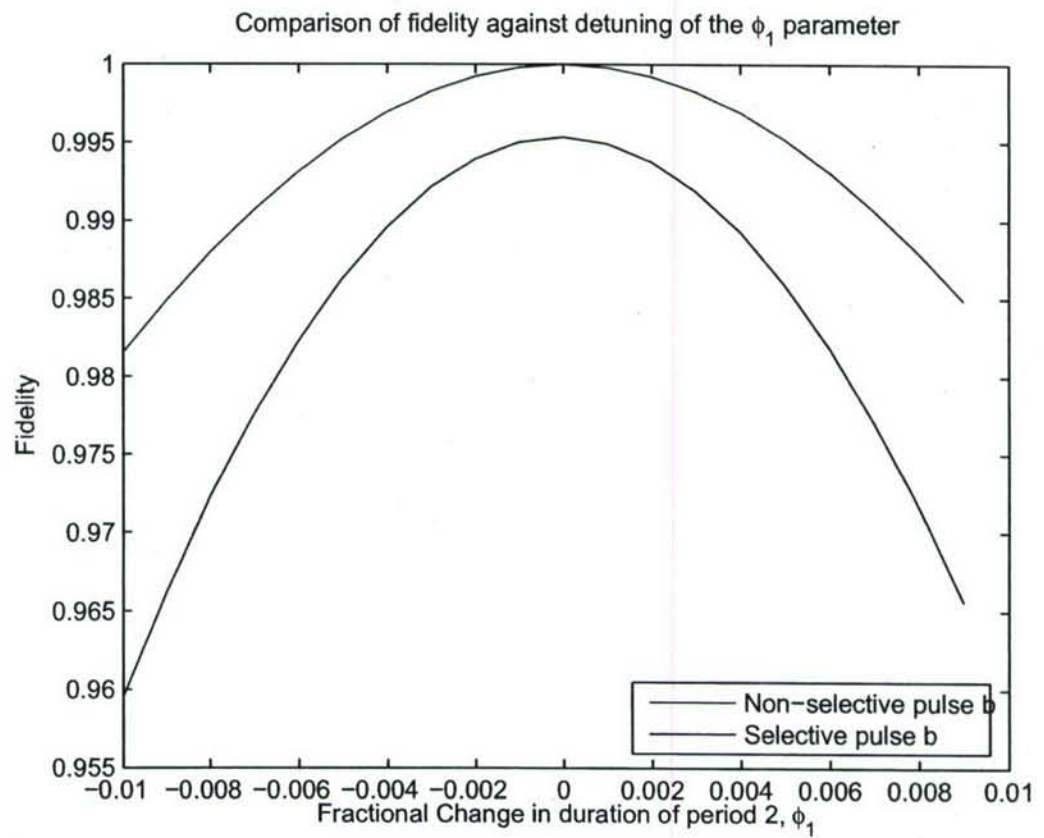


Figure 4-8: This is a plot of fidelity versus curvature with respect to fractional changes in the phase of the first period, ϕ_1 for two given pulses-one selective and one non-selective. Again, the fidelity is higher and the pulse is more robust for the non-selective case.

The following figures show the trajectories of the two periods of the four modulation sequences we considered. The red and blue arrows show the motion of the spin A and spin B on the Bloch's respectively. The final position of the spin A for U_1 is positive x, while spin B is to return to the equilibrium positive z eventually. From the trajectories it can be seen that there is motion of spin B along the Bloch sphere to a non-equilibrium point, which is unnecessary since we did not intend its state to be changed. Therefore, we would expect the selective operation U_1 to be less efficient, having a lower fidelity and higher curvature.

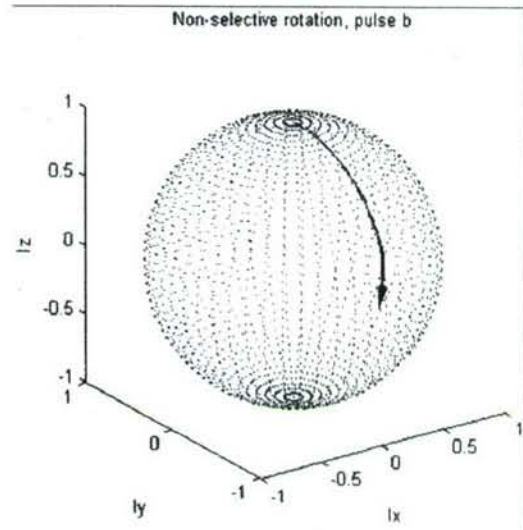
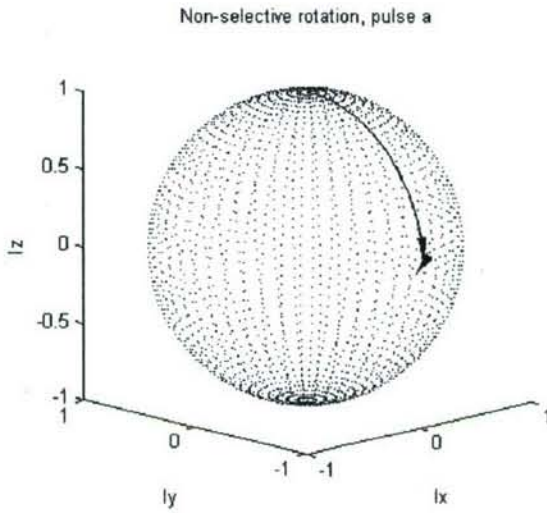


Figure 4-9: The trajectory of non-selective pulse a is shown. The red and blue arrows show the motion of the spin A and spin B on the Bloch's respectively. The motions of both spins during the two periods are very direct.

Figure 4-10: The trajectory of non-selective pulse b is shown. As with non-selective pulse a, the motions of both spins during the two periods are very direct.

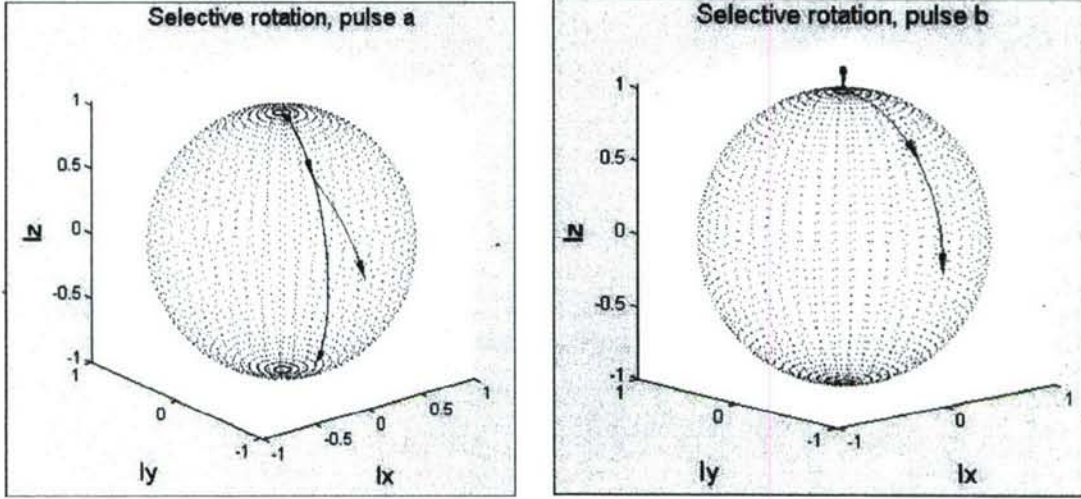


Figure 4-11: The trajectory of selective pulse a is shown. The motions of both spins from b is shown. Spin B moves to negative z during the initial to final state during the two periods the first period and returns to positive z during the second, thus we have used resources to generate unnecessary rotation.

We would like to have robust control sequences with high fidelity. Therefore, pulses at the top left corners of our plots are desirable. The pulse sequence with the highest fidelity are not the ones with the lowest curvature: there is a tradeoff between finding the pulse with the highest fidelity and lowest curvature C . However, there do exist reasonably good pulses with both good fidelities and lower C values.

From Figures 4-1 through 4-5, we have observed that any given pulse has very different sensitivities with respect to different parameters. For example, sequence α , the pulse with the best fidelity, has a high C_t value, but has very low values of C_{aP} , C_{maxP} and C_ϕ . This fact invites us to define a scaled measure of the overall robustness of a pulse. A natural way to achieve this is to have a weighted average of the different C_a values according to the degree of precision of control we have of that parameter. For example, in our case, due to limited RF field homogeneity in the spectrometer, we can control the RF field strength to an accuracy or homogeneity of only 10 – 15%, whereas all the other parameters can be controlled very precisely. Therefore, we can assign values to w_t , w_p , w_f and w_ϕ and define the mean curvature C as follows:

$$C = \sum_i w_i C_i \text{ where } i \in \{t, p, f, \phi\}$$

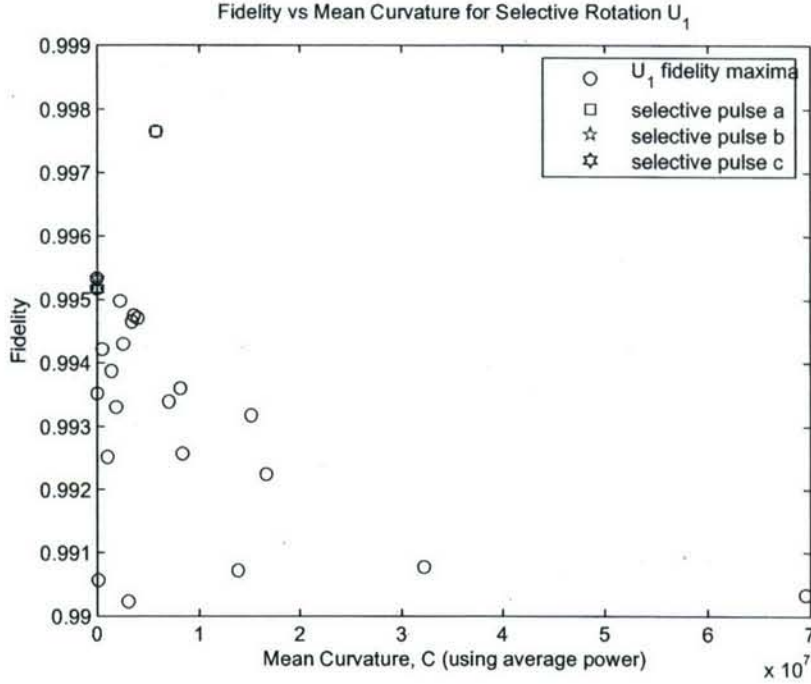


Figure 4-13: The mean curvature is calculated using C_t , C_{aP} , C_f and C_{ph} .

As an example, I will assign $w_t = 0.05$, $w_p = 0.85$, $w_f = 0.05$ and $w_\phi = 0.05$ and integrate the results of the above plots. Figures 6 and 7 show results calculated using C_{aP} and C_{maxP} as a measure of robustness with respect to RF power respectively.

The Curvature C , as shown in the two plots, agree to a large extent with each other. With the above investigations, we see that the curvature C is a good measure to quantify the robustness of a sequence. Experimental characterization of various uncertainties can be used to assign these weights to scale different C_a and combine them to form the Curvature to measure the robustness of a control sequence. Although we focus on NMR RF pulses, this can be straightwardly extended to other means of quantum control as well. Including the Curvature C into a cost that puts a penalty on a sequence that is long in time and high in power, and rewards high fidelity, would greatly improve the quality of our solutions in practice.

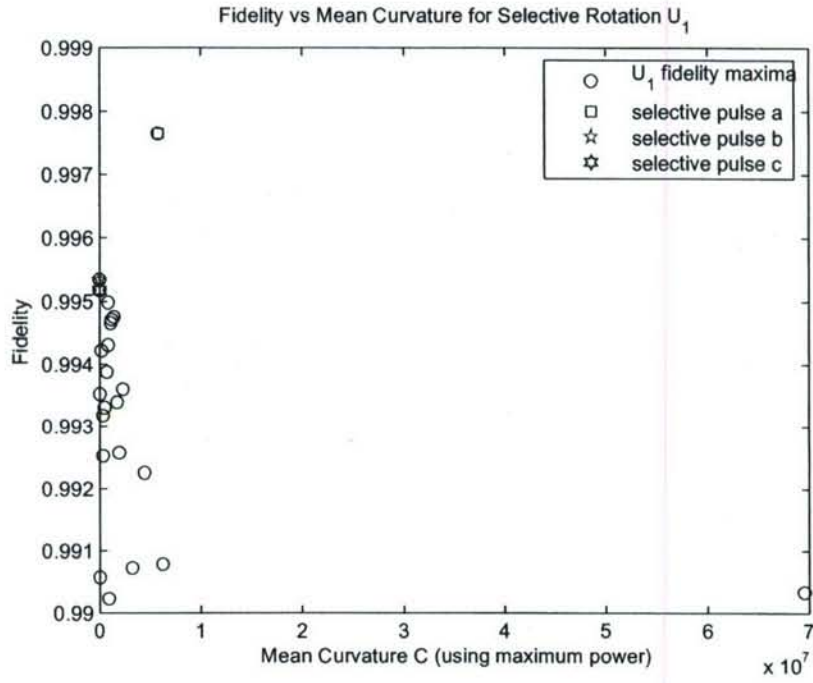


Figure 4-14: The mean curvature is calculated using C_t , C_{maxP} , C_f and C_{ph} .

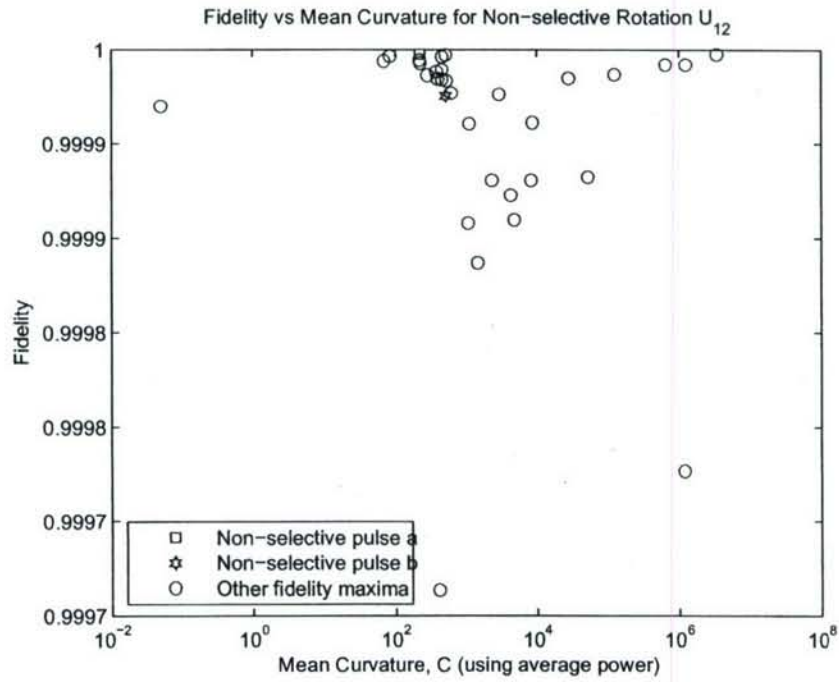


Figure 4-15: The mean curvature is calculated using C_t , C_{aP} , C_f and C_{ph} .

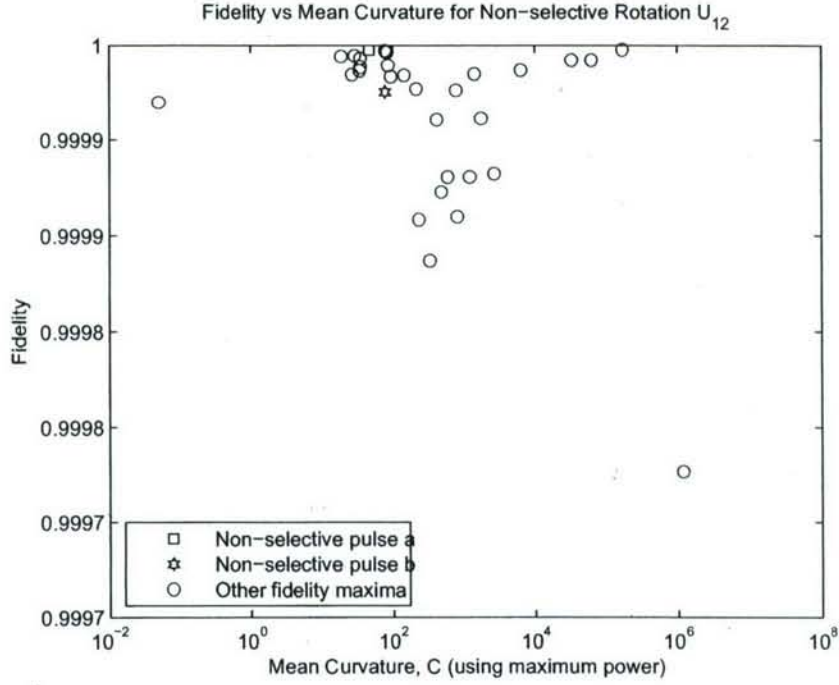


Figure 4-16: The mean curvature is calculated using C_t , C_{maxP} , C_f and C_{ph} .

4.2 The effect of varying coupling strength between spins

Our next investigation is to vary the parameters of the real system and observe differences in fidelity of pulses found. Given the form of our internal Hamiltonian

$$H_{int} = \left(\frac{\omega_A + \omega_B}{2} \right) (\mathbf{I}_z^A + \mathbf{I}_z^B) + \left(\frac{\omega_A - \omega_B}{2} \right) (\mathbf{I}_z^A - \mathbf{I}_z^B) + 2\pi J \mathbf{I}^A \cdot \mathbf{I}^B,$$

if $\Delta\omega \neq 0$, then we have universal control over $SU(4)$, but if $\Delta\omega = 0$, then the system collapses into a spin-1 and a spin-0 subspace. The RF field does not break this symmetry, so without adding another qubit, or spin- $\frac{1}{2}$ particle, we cannot achieve universal control. Therefore, as long as there is some chemical shift difference, we can achieve an ideal selective rotation, if we don't take resources into account. Now we study the behavior when our resources (in this case, number of periods in the control sequence) are limited. The use of number of periods scales roughly linearly with time duration of the pulse sequence. The chemical shift difference $\Delta\omega$ was varied to give

specified values of the coupling strength $S = \frac{2\pi J}{\Delta\omega}$. It is expected that the fidelity would decrease with increasing coupling strength. This is because as the chemical shift difference decreases, it takes more time to selectively address the spins. When $\Delta\omega$ vanishes, two spins are no longer distinguishable, and by symmetry it is impossible to achieve selective rotation. More rigorously, let U be transformation between the Zeeman basis and the eigenbasis, i.e.

$$U = \begin{pmatrix} 1 & 0 & 0 & 0 \\ 0 & \frac{1}{\sqrt{2}} & 0 & \frac{1}{\sqrt{2}} \\ 0 & \frac{1}{\sqrt{2}} & 0 & -\frac{1}{\sqrt{2}} \\ 0 & 0 & 1 & 0 \end{pmatrix}$$

$$U^\dagger \sigma_x U = \frac{1}{\sqrt{2}} \begin{pmatrix} 0 & 1 & 0 & -1 \\ 1 & 0 & 1 & 0 \\ 0 & 1 & 0 & 1 \\ -1 & 0 & 1 & 0 \end{pmatrix}$$

$U^\dagger \sigma_x U$ is not a member of the direct sum space, and thus it is impossible for us to achieve this selective operation when there is no chemical shift difference. By this, we can deduce that the higher the coupling strength between the two spins, the closer we get to this limit of the direct sum space, and thus the harder it is to achieve this addressability. Given the same number of allowed periods, we expect a monotonically decreasing fidelity as we increase the coupling strength S . However, the functional form or rate of the decay is not known.

4.3 Expanding available resources

With the form of pulse sequences we utilize here, a good measure of resources is the number of periods allowed in the control. As the number of periods increases, we expect the average fidelity of the selective operation to increase. For example, let P2 be the 2-period pulse with parameters $\{t_1, \omega_1, f_1, \phi_1; t_2, \omega_2, f_2, \phi_2\}$ and P3 be the 3-period pulse with parameters $\{t_a, \omega_a, f_a, \phi_a; t_b, \omega_b, f_b, \phi_b; t_c, \omega_c, f_c, \phi_c\}$. If we set the

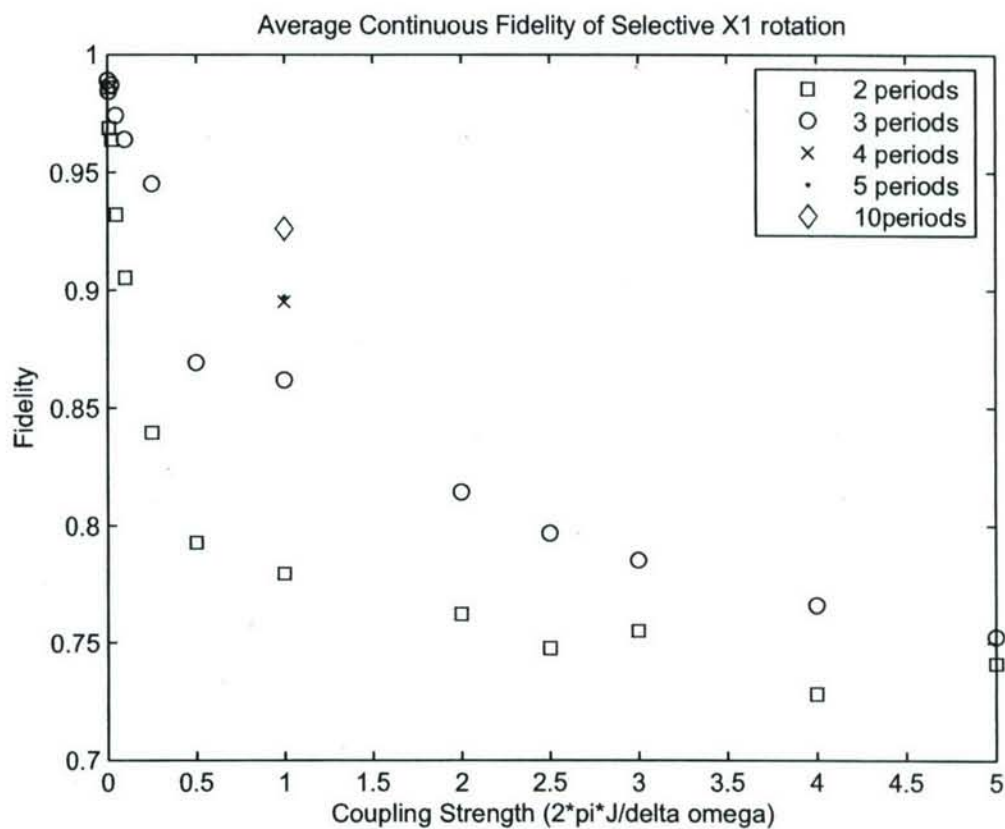


Figure 4-17: As expected, the fidelity decreases monotonically as we increase coupling strength. When the chemical shift difference is set to 0, $f = 0.720$. The trend indicates an asymptotic value that the fidelity approaches for each of 2-period and 3-period pulses.

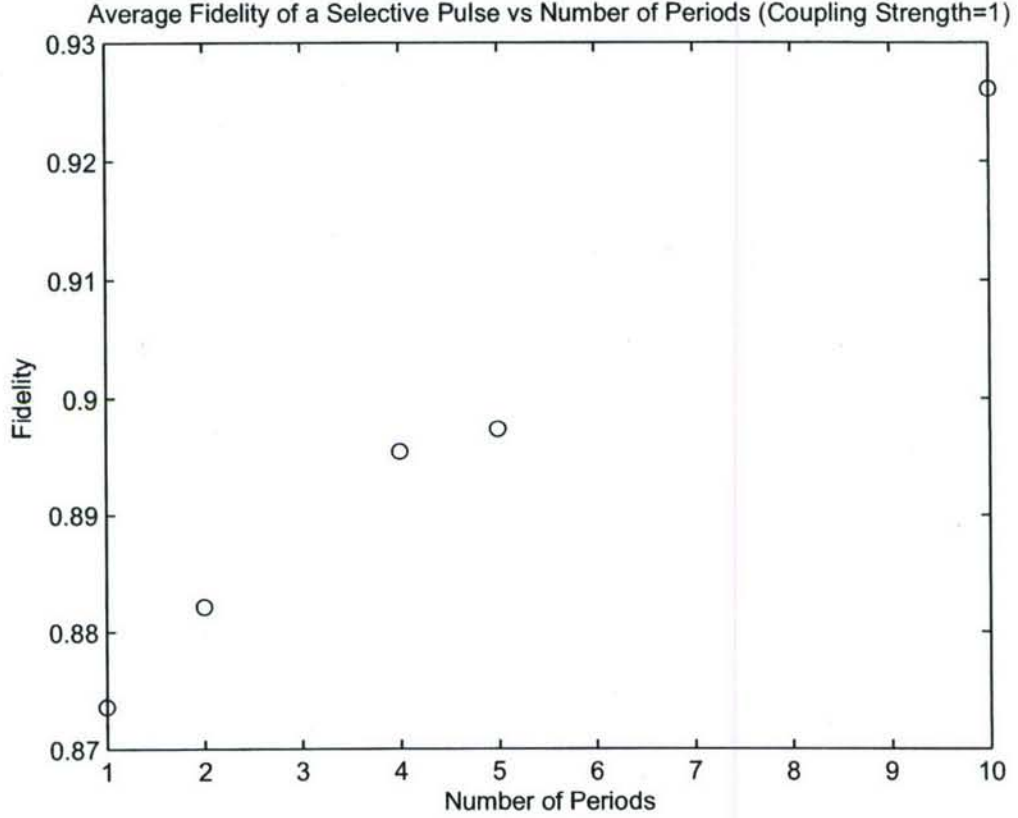


Figure 4-18: The result is indeed what we predicted, that fidelity increases as the number of periods allowed. In the limit of the number of period going to infinity, we will expect to achieve perfect fidelity in universal control as has been shown by Khaneja without regards to limitations in resources. (ref 76)

parameters of P3 such that $t_1 = t_a + t_b$, $f_1 = f_a = f_b$, $\omega_1 = \omega_a = \omega_b$, and $\phi_1 = \phi_a = \phi_b$, then P2 is actually the same as P3. Therefore, we see that an n -period pulse can do as least as well as an m -period pulse for $m < n$. We expect the n -period pulse would do better because we have more flexibility on the control of the pulse shape, like we have more 'knobs to turn' in lab. Extending our discussions in the above section, since there is universality and controllability in a system of n coupled spin- $\frac{1}{2}$ particles with non-zero chemical shift difference, if we allow more resources in our control, we would expect an improvement in the fidelity.

From our numerical results, we can answer the second question we posed: we would like to address: taking resources into account, can we generate any effective

Hamiltonian we desire with perfect fidelity? The answer is no as long as we don't have an infinite amount of resources. However, in the limit of an infinite amount of resources, we are reduced to the previously studied cases, where perfect control can be achieved. Our discussion on resources can be generalized to for instance, RF power and frequency bandwidth in NMR and laser power and linewidth in optical control.

Chapter 5

Conclusions

We have numerically explored some aspects of coherent control in the presence of limited resources. As expected, the amount of available resources is important. We find that resources can be used to improve fidelity and robustness. We suggest that a local curvature may be a useful parameter for robustness. Finally we briefly looked at the additional resources needed when the addressability is reduced.

This work is the beginning of an exploration into the effects of non-ideal control to fidelity of control. There are many more issues that we have not yet studied. Some of the future directions we see are for instance analytic work on the effects of limited RF frequency bandwidth on control on $SU(2)$ and $SU(4)$. For example, in $SU(4)$, what is the analytic expression for the ideal pulse sequences to achieve U_1 and U_1^2 , and the average Hamiltonian resulting from these pulse sequences. How are the fidelities and curvatures degraded as we limit the available resources to implement these sequences? As the coupling of between the two spins increase, how do decreased resources impact the fidelity and curvature of selective and non-selective operations?

Another area of relevant possible research is a comparison between different approaches of control sequence search methods. The two main different types are Strongly Modulating Pulses (SMP, based on simplex search)[5] and search methods based on OCT, such as the Gradient Ascent Algorithm (GRAPE)[12]. The former optimizes for the time duration, RF power and frequency and incorporates simulations of system dynamics into the calculation of fidelity, and minimizes a cost which

is aimed at maximizing the fidelity and penalizing very high RF powers and very long pulse sequences. It increases the number of periods of the sequence if a certain criterion on a cost is not yet met and repeats the process. The latter is based on OCT and fixes the total duration and number of piecewise constant intervals of the pulse and just calculates the forward propagated initial density matrix and the back-propagated target state. It would be interesting to look into how effectively the latter strongly modulates the dynamics of systems, especially if the systems have strong couplings, since the simulations of the actual dynamics are not carried out.

Bibliography

- [1] D.P. Bertsekas. *Nonlinear Programming*. Athena Scientific, 1995.
- [2] N. Boulant, J. Emerson, T. Havel, D.G. Cory, and S. Furuta. Incoherent noise and quantum information processing. *J. Chem. Phys.*, 121:2955, 2004.
- [3] D.G. Cory, A.F. Fahmy, and T.F. Havel. Ensemble quantum computing by nmr spectroscopy. *Proc. of the Nat. Academy of Science, USA*, 94:1634–1639, 1997.
- [4] R.R. Ernst. *Principles of Nuclear Magnetic Resonance in One and Two Dimensions*. Oxford University Press, 1990.
- [5] E.M. Fortunato, M.A. Pravia, N. Boulant, G. Teklemariam, T.F. Havel, and D.G. Cory. Design of strongly modulating pulses to implement precise effective hamiltonians for quantum information processing. *J. Chem. Phys.*, 116(17):7599–7606, 2002.
- [6] R.S. Judson and H. Rabitz. Teaching lasers to control molecules. *Phys. Rev. Lett.*, 68(10):1500–1503, 1992.
- [7] M. Kasevich and S. Chu. Laser cooling below a photon recoil with three-level atoms. *Phys. Rev. Lett.*, 69:1741–1744, 1992.
- [8] N. Khaneja, R.W. Brockett, and S.J. Glaser. Time optimal control of spin systems. *Phys. Rev. A*, 63(3):032308, 2001.
- [9] N. Khaneja, S.J. Glaser, and R.W. Brockett. Sub-riemannian geometry and optimal control of three spin systems. *Int. J. Robust Nonlinear Control*, 65(3):032301, 2002.

- [10] N. Khaneja, S. Li, C. Kehlet, B. Luy, and S.J. Glaser. Broadband relaxation optimized polarization transfer in magnetic resonance. *Proc. of the Nat. Academy of Sciences USA 2004*, 101:14742–14747, 2004.
- [11] N. Khaneja, B. Luy, and S.J. Glaser. Boundary of quantum evolution under decoherence. *Proc. of the Nat. Academy of Sciences USA 2003*, 100:13162–13166, 2003.
- [12] N. Khaneja, T. Reiss, C. Kehlet, T. Schulte-Herbrüggen, and S.J. Glaser. Optimal control of coupled spin dynamics: design of nmr pulse sequences by gradient ascent algorithms. *J. Mag. Res.*, 172:296–305, 2005.
- [13] Navin Khaneja and Steffen J. Glaser. Cartan decomposition of $su(2^n)$ and control of spin systems. *Chemical Physics*, 267:11–23, 2001.
- [14] Navin Khaneja, T Reiss, B Luy, and Steffen J. Glaser. Optimal control of spin dynamics in the presence of relaxation. *Journal of Magnetic Resonance*, 162:311–319, 2003.
- [15] H. Mabuchi and N. Khaneja. Principles and applications of control in quantum systems. *Int. J. Robust Nonlinear Control*, 15:647–667, 2005.
- [16] H. Rabitz. Shaped laser pulses as reagents. *Science*, 299:525–527, 2003.
- [17] H. Rabitz. Controlling quantum phenomena: why does it appear easy to achieve? *J. Modern Optics*, 51(16-18):2469–2475, 2004.
- [18] H. Rabitz, M.M. Hsieh, and C.M. Rosenthal. Quantum optimally controlled transition landscapes. *Science*, 303:1998–2001, 1992.
- [19] J.J. Sakurai. *Modern Quantum Mechanics*. Addison-Wesley, 1993.
- [20] D.A. Steck, K. Jacobs, H. Mabuchi, T. Bhattacharya, and S. Habib. Quantum feedback control of atomic motion in an optical cavity. *Phys. Rev. Lett.*, 92:223004, 2004.

- [21] J.K. Stockton, R. van Handel, and H. Mabuchi. Deterministic dicke-state preparation with continuous measurement and control. *Phys. Rev. A*, 70:022106, 2004.
- [22] D.J. Tannor and S.A. Rice. Control of selectivity of chemical reaction via control of wave packet evolution. *J. Chem. Phys.*, 83(10):5013–5018, 1985.
- [23] W.S. Warren, H. Rabitz, and M. Dahleh. Coherent control of quantum dynamics: the dream is alive. *Science*, 259:1581, 1993.
- [24] W.H. Zurek. Doherence and the transition from quantum to classical-revisited. *Los Alamos Science*, 27:2, 2001.

COHERENT CONTROL OF DIPOLAR COUPLED SPINS IN
LARGE HILBERT SPACES

by

SUDDHASATTWA SINHA

B.Sc.(Hons.) in Physics, Indian Institute of Technology, Kharagpur, India (2001)

Submitted to the Department of Nuclear Science and Engineering
in partial fulfillment of the requirements for the degree of

DOCTOR OF PHILOSOPHY

at the

MASSACHUSETTS INSTITUTE OF TECHNOLOGY

April 2006

© Massachusetts Institute of Technology 2006. All rights reserved.

Author _____
Department of Nuclear Science and Engineering
April 27, 2006

Certified by _____
David G. Cory
Professor
Thesis Supervisor

Read by _____
Terry P. Orlando
Professor
Thesis Reader

Read by _____
Seth Lloyd
Professor
Thesis Reader

Accepted by _____
Jeffery Coderre
Chairman, Department Committee on Graduate Students

COHERENT CONTROL OF DIPOLAR COUPLED SPINS IN LARGE HILBERT SPACES

by

SUDDHASATTWA SINHA

ABSTRACT

Controlling the dynamics of a dipolar-coupled spin system is critical to the development of solid-state spin-based quantum information processors. Such control remains challenging, as every spin is coupled to a large number of surrounding spins. In this thesis, we primarily focus on developing coherent control techniques for such large spin systems.

We start by experimentally simulating spin squeezing using a liquid-state NMR quantum information processor. We demonstrate that the precision of quantum control obtained using strongly modulating pulses was sufficient to reproduce the theoretically expected behavior of the spin observables and the associated entanglement measures among the underlying qubits.

We then investigate coherent control in a more complex solid-state spin system consisting of an ensemble of spin pairs. Using pulse amplitude modulation techniques, we decouple the weaker interactions between different pairs and extend the coherence lifetimes within the two-spin system. This is achieved without decoupling the stronger interaction between the two spins within a pair. We thus demonstrated that it is possible to restrict the evolution of a dipolar coupled spin network to a much smaller subspace of the system Hilbert space which allows us to significantly extend the phase coherence times for selected states.

Finally, we demonstrate the sensitivity of highly correlated multiple-quantum states to the presence of rare spin defects in a solid-state spin system. We design two multiple-pulse control sequences - one that suspends all spin interactions in the system including that of the defect spins, while the other selectively allows the defect spins to interact only with the abundant spins. By measuring the effective relaxation time of the rare spins, we demonstrate the efficiency of the two control sequences. Furthermore we observe that for small spin cluster sizes, the sensitivity of the highly correlated spin states to the spin defects depends on the coherence order of these correlated spin states. But beyond a certain cluster size, one observes a saturation effect as the higher coherence orders are no longer increasingly sensitive to the defect spin dynamics.

Thesis Supervisor: David G. Cory

Title: Professor

Acknowledgments

I would like to thank Professor David Cory for giving me the opportunity to work with him and guiding me for the past four years. His insight on every aspect of Nuclear Magnetic Resonance and Quantum Information Processing has been inspiring. I would also like to acknowledge Dr. Sekhar Ramanathan for his help and advice. He has been intimately involved in the each and every one of my research projects and has been extremely supportive all through out. His words of encouragement and compassion have especially helped me get through the past six months when things were not going well.

Among my group mates, first and foremost I would like to thank all my office mates – Paola (the fille fille), Jonathan (the bike shop garçon) and Nick (the garçon garçon). It was a lot of fun working with them over the past few years on various research projects and problem-sets. It was always a pleasure working with Joon (the probe garçon) trying to tune probes and run solid-state NMR experiments. I would also like to thank Jamie (the cool garçon), Michael (the dude garçon), Anatoly (the DNP garçon), Ben (the cake garçon), Dima (the Russian garçon) and Cecilia (the party fille). It had a wonderful experience spending time with them in the lab. I would also like to thank some of the people who had helped me get started during my first year at MIT including Evan, Marco, Grum, Yaakov and Dr. Timothy Havel and Dr. Joseph Emerson.

Outside the lab, I would like to thank all my friends in Ashdown. The list is too long to enumerate here. But their friendship has made my MIT experience even more rewarding. I have many fond memories of my years at MIT and I will cherish them for the rest of my life.

Finally, I would like to thank my family - my parents and my sister. It would be impossible for me to convey my gratitude to them in a few sentences. All I can say is: without their love and support I would not have seen this day.

In loving memory of Bapi (father):

His perseverance and dedication will always inspire me;

His encouragement and ideals will forever guide me;

His love and affection will never cease to comfort me.

CONTENTS

Abstract	3
Acknowledgments	5
Table of Contents	9
List of Figures	13
List of Tables	21
1 Introduction	23
2 Experimental Simulation of Spin Squeezing by NMR	27
2.1 Introduction	27
2.2 Simulation of spin squeezing in a multi-spin-1/2 system	28
2.3 The NMR implementation of squeezed spin states	32
2.4 Results of spin squeezing experiments	36
2.4.1 The spin-1 case	39
2.4.2 The spin-3/2 case	39

2.4.3	Behavior of entanglement measures	41
2.5	Conclusions	44
3	Selective coherence transfers in homonuclear dipolar coupled spin systems	47
3.1	Introduction	47
3.2	Theory of the modulation scheme	49
3.3	Experimental Results	52
3.4	Conclusions	55
4	Sensitivity of highly correlated multiple-spin states to the presence of rare spins	59
4.1	Introduction	59
4.1.1	Creation and detection of highly correlated multiple-quantum states	60
4.1.2	Decay of highly correlated multiple-spin states in CaF_2	63
4.1.3	Effect of rare spins on the decay of the multiple-spin states. .	65
4.1.4	Sensitivity the of highly correlated multiple-spin states to the presence of rare spins	70
4.2	Overview of average Hamiltonian theory	71
4.3	The C-48 time-suspension sequence	73
4.4	The design criteria for the new time-suspension and heteronuclear recoupling sequences	77
4.5	The properties of the TS-96 and the HR-96 sequences	82
4.6	Experimental Results	84

4.6.1	Effective T_2 relaxation times of ^{13}C spins under the TS-96 and the HR-96 sequences.	84
4.6.2	Sensitivity of ^1H multiple quantum coherence to the presence of ^{13}C spins	87
4.7	Conclusions and future work	90
A	Zeroth order average Hamiltonian calculations for the TS-96 and the HR-96 sequences	95

LIST OF FIGURES

- 2-1 (i) A coherent state spin- j vector with expectation values $[\langle J_x \rangle, \langle J_y \rangle, \langle J_z \rangle] = [1, 0, 0]$ may be visualized as a coherent superposition of angular momentum vectors on a cone about the x-axis, all with a projection of $j/2$ along that axis. (ii) After squeezing via the one-axis mechanism (see text), the cone representing the state of a spin-1 particle is elliptical, with its squeezed (minor) axis making an angle of $\pm\pi/4$ with the y, z-axes. (iii) In the maximally squeezed state of a spin-1 particle the cone has been folded into a nearly degenerate ruled surface. 29
- 2-2 The molecular structure of 2,3-dibromo-thiophene is shown on the left, with the two hydrogen atoms used for the spin-1 simulations numbered as in the main text. The coupling strength J between them and the chemical shift of the first compared to the second are also shown. The diagram on the right shows the pulse sequence used to implement spin squeezing for a given parameter k , where $f(k) \equiv k/(2\pi J)$, narrow rectangles indicate $\pi/2$ y-rotations, the broad rectangles y-rotations by π , and the rectangles point downwards for pulses effecting rotations by the negatives of these angles. 34

- 2-3 The molecular structure alanine is shown on the left, with the three carbon-13 atoms used for the experiments numbered as in the text. The numbers next to the dashed lines are the corresponding coupling constants (in Hz), while the numbers next to the carbons are their chemical shifts relative to the third (in Hz). On the top right is a schematic diagram of the pulse sequence used, where the horizontal striping indicates an y-pulse, vertical striping an x-pulse, the narrower pulses induce rotations by $\pi/2$, and the wider ones by π (or the negatives thereof if the pulse is below the spin's line). The grey boxes indicate one of the two "modules" show on the bottom right, which allow a $I_z^m I_z^n$ evolution by the angle (k or $\pi/2$) shown on the bottom of the pulse sequence diagram while refocussing the chemical shifts and the coupling between the pairs not contained in the grey box. The functions which relate the delay time to the squeezing parameter k is given by $f_{mn}(k) \equiv k/(4\pi J^{mn})$ for $[m, n] = [1, 2], [2, 3]$ 35
- 2-4 (i) The real part of the experimental density matrix representing the initial pseudo-pure state $|00\rangle$ for the spin-1 experiments. (ii) The real part of the experimental density matrix representing the maximally squeezed state of the effective spin-1 particle. 38
- 2-5 (i) The real part of the experimental density matrix representing the initial pseudo-pure state $|000\rangle$ for the spin-3/2 experiments. (ii) The real part of the density matrix when the squeezing parameter $k = \pi/2$, at which point a GHZ state is obtained [28]. 38
- 2-6 Plots of the theoretically expected uncertainties as a function of the squeezing parameter k (in degrees) for spin-1 (solid lines), along with the fits (dashed lines) to the uncertainties computed from the experimental density matrices (+ or *). (i) Plots of $\langle \Delta J_y \rangle$ (lower curves), and $\langle \Delta J_z \rangle$ with k (upper curves). (ii) Plot of $|\langle J_x \rangle|$ (no fits shown). . . 40

2-7	Plots of the theoretically expected uncertainties as a function of the squeezing parameter k (in degrees) for spin-3/2 (solid lines), along with fits (dashed lines) to the uncertainties computed from the experimental density matrices (+ or *). (i) Plots of $\langle \Delta \mathbf{J}_y \rangle$ (lower curves) and $\langle \Delta \mathbf{J}_z \rangle$ (upper curves). (ii) Plot of $ \langle \mathbf{J}_x \rangle $	42
2-8	Plots of the entanglement of formation (i) and concurrence (ii) with the squeezing parameter k (in degrees) for spin-1. The solid lines are the theoretically expected curves, while the dashed lines interpolate linearly between the values computed from the experimental density matrices (*) obtained via tomography.	43
2-9	Plots of the Meyer's metric or average entanglement after tracing down to a single qubit (i) and concurrence after tracing down to any pair of qubits (ii) with the squeezing parameter k (in degrees) for spin-3/2. The solid lines are the theoretically expected curves, while the dashed lines are a fifth-order polynomial fit to the values computed from the experimental density matrices (*) obtained via tomography.	44
3-1	Two pairs of strongly coupled spin- $\frac{1}{2}$ systems with each pair decomposed into its singlet and triplet manifolds (in the rotating frame). The triplet manifolds are weakly coupled to each other while the singlet manifolds do not interact.	51
3-2	(a) The proton spectrum of a single crystal of gypsum in the [010] orientation (Pake doublet). The splitting between the peaks corresponds to $3\omega_D^S/2\pi = 44.4$ KHz. Each peak is broadened due to weak dipolar coupling to the other water molecules. Therefore, $3\omega_D^w/2\pi \sim 16.4$ KHz (b) The line narrowing observed under the modulation sequence with RF amplitude $\omega_1 = 3\omega_D^S/4$. (c) Evolution of the collective single spin $\sum_i \sigma_x^i$ terms under the modulation sequence.	54

- 3-3 (a) pulse sequence used to read out the $\sigma_x^1 + \sigma_x^2$ terms. Following the modulation pulse, a $\pi/2$ pulse is applied to rotate the σ_x terms to σ_z . During the 150 μs interval (much shorter than T_1) all terms other than the σ_z decay. A $\pi/2$ pulse is then used to monitor σ_z . (b) pulse sequence used to read out the $\sigma_y^1\sigma_z^2 + \sigma_z^1\sigma_y^2$ term. Following the modulation two back to back $\pi/2$ pulses act as a double quantum filter to suppress the single spin σ_x terms. A four step phase cycle is necessary to implement the filter. 55
- 3-4 The solid line shows the $\sigma_x^1 + \sigma_x^2$ and the dashed line shows the $\sigma_z^1\sigma_y^2 + \sigma_y^1\sigma_z^2$ terms. (a) Under the dipolar Hamiltonian evolution, the above terms evolve into unobservable higher order spin correlations within 100 μs . (b) Under the modulation sequence, the terms oscillate 90 deg out-of-phase with each other for up to 360 μs without any significant attenuation in amplitude. In this case the RF amplitude $\omega_1 = 3\omega_D^S/4$. 56
- 3-5 The solid line shows the $\sigma_x^1 + \sigma_x^2$ and the dashed line shows the $\sigma_z^1\sigma_y^2 + \sigma_y^1\sigma_z^2$ terms. Under the modulation sequence, the terms oscillate 90 deg out-of-phase with each other. The RF amplitude ω_1 is varied from $2\omega_D^S/4$ to $7\omega_D^S/4$ in steps of $\omega_D^S/4$. When the value of ω_1 is no longer in the optimum range, the amplitude of the signal is significantly attenuated. 57
- 4-1 Energy level diagram of a N spin- $\frac{1}{2}$ system. The eigenvalue of \hat{I}_z can take any value from $\frac{N}{2}$ to $-\frac{N}{2}$. The number of levels for each allowed eigenvalue is $\binom{N}{m+\frac{N}{2}}$. Thus the number of allowed single-quantum transitions increase exponentially with N and are thus unresolvable in large spin-systems. 61

4-2	The basic form of a multiple-quantum NMR experiment [63] - (i) Preparation: Creating the highly correlated multiple-quantum states. (ii) Evolution: Evolving these states under any desired Hamiltonian. (iii) Mixing: Transforming the higher order coherences to observable single-spin single quantum coherences. (iv) Detection: Measuring the observable single-spin single quantum magnetization	62
4-3	Effective decay times of various coherence orders due to the action of the secular dipolar Hamiltonian. Highly correlated spin- ^{19}F states in CaF_2 are created by exciting the thermal spin- ^{19}F state using the DQ Hamiltonian. The effective decay times of the coherences for the various excitation times (τ_1) are plotted.	64
4-4	Effective decay times of various coherence orders of the the highly correlated spin- ^{19}F states in CaF_2 . In this case, the secular dipolar Hamiltonian is suppressed using a multiple-pulse C-48 sequence. The effective decay times of the coherences for the various excitation times (τ_1) under the DQ Hamiltonian are plotted.	65
4-5	The model system (on the right), consists of one \mathbf{S} spin (labeled as \mathbf{S}_1) interacting with an abundant number of \mathbf{I} spins. The C-48 sequence averages out the homonuclear interaction between the \mathbf{I} spins during τ_2 . During this time interval (τ_2), \mathbf{S}_1 is correlated with the multiple-quantum spin- \mathbf{I} states present in $\rho(\tau_1)$. But if the \mathbf{S}_1 spin state remains constant during τ_2 , the heteronuclear interaction is also averaged out under the action of the C-48 sequence. Thus \mathbf{S}_1 is <i>no longer correlated</i> to the spin- \mathbf{I} states at the end of τ_2 . However if \mathbf{S}_1 flips at any point during this interval, it will <i>remain correlated</i> with the spin- \mathbf{I} states even at the end of τ_2	67

4-6	The model system (on the right), consists of one S spin (labeled as S ₁) interacting with an abundant number of I spins and a few neighboring S spins. We assume that these S spins interact <i>only</i> with the S ₁ spin. The homonuclear interaction between the I spins is averaged out during τ_2 using the C-48 sequence. The Hamiltonians $H_D^{IS_1}$ and $H_D^{SS_1}$ do not commute. Thus the multiple-quantum spin I states present in $\rho(\tau_1)$ evolve under their action during τ_2	68
4-7	Sketch of the experiments designed to detect rare spins (S) using the highly correlated multiple-spin states of the abundant spins (I) as a 'probe'. It involves contrasting the effect of the two control sequences (in (a) and (b)) on the intensity of the multiple quantum coherence of these correlated spin I states.	71
4-8	The schematic diagram of the three-pulse sequences used to design the C-48 sequence, where the horizontal striping indicates an y-pulse, vertical striping an x-pulse. All the pulses induce rotations by $\pi/2$. (or the negatives thereof if the pulses are below the bold reference lines) .	75
4-9	The schematic diagram of the three-pulse sequences used to design the C-48 sequence, where the horizontal striping indicates an y-pulse, vertical striping an x-pulse. All the pulses induce rotations by $\pi/2$. (or the negatives thereof if the pulses are below the bold reference lines) .	76
4-10	(a) The first sub-cycle (n=1) of the time-suspension (TS-96) sequence: I -(<i>Aa</i>), S -(<i>aE</i>). The sequence is made up of 16 such sub-cycles. The horizontal striping indicates an y-pulse, vertical striping an x-pulse. All the pulses induce rotations by $\pi/2$. (or the negatives thereof if the pulses are below the bold reference lines).	80

- 4-11 (a) The first sub-cycle ($n=1$) of the heteronuclear recoupling (HR-96) sequence: **I**-(*Aa*), **S**-(*bE*). The sequence is made up of 16 such sub-cycles. The horizontal striping indicates an *y*-pulse, vertical striping an *x*-pulse. All the pulses induce rotations by $\pi/2$. (or the negatives thereof if the pulses are below the bold reference lines). 81
- 4-12 The schematic of the experiment that measures the effective T_2 of the ^{13}C in adamantane under (a) TS-96 sequence and (b) HR-96 sequence. Before applying the two sequences, we use a $\pi/2$ pulse to flip the ^{13}C spins on to the transverse plane. The ^{13}C magnetization is measured while decoupling the ^1H spins. 84
- 4-13 The ^{13}C signal intensity plotted after every 96- pulse cycle of the the TS-96 (\square) and the HR-96 (\diamond) sequences. The cycle time period of 1728 μs 85
- 4-14 The ^{13}C signal intensity plotted after every 6 pulse sub-cycle of the (a) TS-96 and (b) HR-96 sequences. The sampling rate in both cases is 108 μs . The points marked by \square in (a) and \diamond in (b) indicate the signal intensity after the full 96-pulse sequence. The system was evolved up to 4 cycles of the 96-pulse sequences with a cycle time period of 1728 μs . 86
- 4-15 The schematic of the experiment that creates ^1H multiple quantum coherences in adamantane. The 16 pulse sequence in the shaded box is used to generate the effective DQ Hamiltonian. The smaller spacing between the pulses is given by Δ while the larger spacing is given by the sum of 2Δ and the $\pi/2$ pulse length. Thus the cycle time of the sequence is $t_c = 24(\Delta + \pi/2 \text{ pulse length})$. The vertical striping indicates an *x*-pulse. All the pulses induce rotations by $\pi/2$. (or the negatives thereof if the pulses are below the bold reference lines) . . . 87
- 4-16 The ^1H multiple quantum coherence in adamantane. The system was evolved under the DQ Hamiltonian for a period of 604.8 μs 88

4-17	Coherence order distribution after evolution under the TS-96 (solid line), two back-to-back C-48 (dashed line) and the HR-96 (dotted line) sequences. The cycle time was 1.4ms for all three sequences. Thus, the time period of evolution (τ_2) were 1.4 ms (for the top figure) and 2.8 ms (for the bottom figure).	89
4-18	The net difference in signal intensity for the various coherence orders after one cycle of the TS-96 and HR-96 sequences.	90

LIST OF TABLES

2.1	The representation of a spin-1 by two spin-1/2 particles	30
2.2	Coupled representation ($ j, m\rangle$) of the basis states spanned by three spin-1/2 particles	30
2.3	Theoretical and experimental spin expectation values and uncertainties of the maximally squeezed spin-1 states	39
2.4	Theoretical and experimental spin expectation values and uncertainties of the maximally squeezed spin-3/2 states	41
4.1	The average Hamiltonian for various time-suspension sequences . . .	73
4.2	Composition of the sub-cycles of the TS-96 and HR-96 sequences . .	79
4.3	The average Hamiltonian properties of the TS-96 and the HR-96 sequence taking into account finite pulse width effects	82
4.4	Sub-cycles at which the various interactions average to zero for the TS-96 and the HR-96 sequences <i>without</i> taking into account finite pulse width effects	83
4.5	Sub-cycles at which the various interactions average to zero for the TS-96 and the HR-96 sequences taking into account finite pulse width effects	83

A.1	The 0^{th} order heteronuclear average Hamiltonian values for the TS-96 (top) and the HR-96 (bottom) sequences	95
A.2	The 0^{th} order heteronuclear average Hamiltonian values for the TS-96 sequence	96
A.3	The 0^{th} order heteronuclear average Hamiltonian values for the HR-96 sequence	96
A.4	The 0^{th} order spin-I homonuclear average Hamiltonian values for the C-48 sequence	97
A.5	The 0^{th} order spin-S homonuclear average Hamiltonian values for the TS-96 sequence	98
A.6	The 0^{th} order spin-S homonuclear average Hamiltonian values for the HR-96 sequence	99

CHAPTER 1

INTRODUCTION

Quantum information processors (QIPs) derive their power from the quantum parallelism due to the superposition of quantum states. An n -qubit quantum information processor forms a superposition of 2^n states, with each state being equivalent to a n -bit classical processor. Peter Shor, Lov Grover and other scientists have harnessed this massive power to devise quantum algorithms like the factorization and the quantum database search algorithm. Compared to their classical counterpart, a QIP provides a more efficient platform to solve certain problems. Physical realization of a QIP requires precise quantum control of a physical system while protecting the system from decoherence effects induced by noise in the environment. Coupled with the fact that, as we push Moore's law to its limit with nano-scale devices - a regime where nature follows the laws of quantum physics, development of quantum control techniques assumes added importance.

Various schemes have been proposed for the experimental realization of QIPs including ion traps [1], cavity QEDs [2] and SQUIDs [3]. But the experimental implementation of a QIP based on liquid-state Nuclear Magnetic Resonance (NMR) technology has been the most successful till date [4, 5]. Existing coherent control NMR techniques have been adopted to manipulate up to 10 qubits while new techniques have been developed to account for incoherent and decoherent noise. These advances have enabled researchers to experimentally implement some of the quantum algorithms. However

this implementation scheme has its limitations - the non-scalability of the initial state (known as the pseudo-pure state) preparation, large ratio of the gate time over the decoherence time, among others. The method of addressing qubits using chemical shifts becomes increasingly cumbersome as the complexity of the molecules increase with the number of qubits. This severely limits the maximum number of qubits that can be manipulated using this technology.

Solid-state spin-based NMR QIP has been proposed as the next generation processor. The ability to create higher thermal polarization using existing solid-state NMR techniques, the stronger dipolar couplings and the longer spin-lattice relaxation times partially address the issues of scalability, faster quantum gates and higher decoherence times respectively. Using gradient fields to address spins in solid samples removes some of the limitations one faces while addressing a large number of qubits in its liquid-state counterpart. To simulate a QIP, various solid-state system designs have been suggested - single crystals of deuterated molecules with dilute concentration of suitably labeled ones [6], phosphorous atoms in a silicon grid at a low temperature [7], endohedral fullerenes on a silicon surface [8], among others.

In any implementation of a solid-state spin-based NMR QIP, an underlying challenge is the coherent control of spins in large Hilbert spaces. Unlike liquid samples where all intramolecular interactions are averaged out due to molecular motions, in a rigid-solid lattice all nuclear spins strongly interact with each other. Thus the solid-state spin system spans a much larger Hilbert space. The control of spin dynamics in such large Hilbert spaces is essential for the application of quantum gates - a key step in the implementation of quantum algorithms. Experimental investigation of these multi-spin dynamics have been carried out using multiple-quantum coherence [9, 10, 11, 12] and spin diffusion [13, 14] techniques. In this thesis, we primarily focus on developing new coherent control techniques for such large spin systems.

We start by experimentally simulating spin squeezing using a liquid-state NMR QIP (chapter 2). This was done by identifying the energy levels within the symmetric subspace of a system of n spin-1/2 nuclei with the energy levels of the simulated

spin- $(n/2)$ system. The results obtained for our simulations of spin-1 and spin- $3/2$ systems are consistent with earlier theoretical studies of spin squeezing. We demonstrate that the precision of quantum control obtained using strongly modulating pulses [31] was sufficient to reproduce the theoretically expected behavior of the spin observables and the associated entanglement measures among the underlying qubits. Then we investigate coherent control in a more complex solid-state spin system consisting of an ensemble of spin pairs (chapter 3). Using pulse amplitude-modulation techniques, we decouple the weaker interactions between different pairs and extend the coherence lifetimes within the two-spin systems. This is achieved without decoupling the stronger interaction between the two spins within a pair. Finally, we demonstrate the sensitivity of highly correlated spin states to the presence of rare spin defects in a solid-state system (chapter 4). We show that the homonuclear dipolar interactions of the rare spins can cause decoherence effects in such correlated spin states even if these spins are decoupled from the correlated spin system. For our sensitivity measurements, we design two multiple-pulse control techniques (based on coherent averaging theory) - one that suspends all spin interactions in the system while the other selectively allows only the heteronuclear dipolar interaction between the rare spins and the correlated spin system. By measuring the effective relaxation time of the rare spins, we demonstrate the efficiency of the two control sequences. Furthermore, we observe that the sensitivity of the highly correlated spin states to defects depends on the coherence order of the correlated spin states. But beyond a certain cluster size, one observes a saturation effect in the sensitivity measurements as the higher coherence orders are not increasingly sensitive to the defect spin dynamics.

CHAPTER 2

EXPERIMENTAL SIMULATION OF SPIN SQUEEZING BY NMR

2.1 Introduction

The minimum uncertainty associated with complementary observables is given by the uncertainty relations. For example, the position and momentum fluctuations in a coherent state of the quantum harmonic oscillator are both equal to the quantum limit $\hbar/2$. States for which the fluctuations in one of these observables is less than the standard quantum limit of $\hbar/2$, while the fluctuations in the complementary observable increase so as to satisfy the uncertainty relation, are called “squeezed states” [17, 34]. Thus a squeezed state can be visualized as an ellipse of constant uncertainty in phase space.

Squeezed spin states have been defined using analogous criteria [19, 25, 36, 42, 43, 44, 45], and several experimental demonstrations of spin squeezing have been published. They include interaction of collection of atoms with squeezed radiation [15], the displacement of two optical lattices with respect to each other [37], and collisional interactions between the atoms in a Bose-Einstein condensate [19, 36, 38].

¹Parts of this chapter were extracted from the paper “Experimental simulation of spin squeezing by Nuclear Magnetic Resonance”, by S. Sinha, J. Emerson, N. Boulant, T. F. Havel and D. G. Cory, *Quantum Information Processing*, Vol. 2, No. 6, December 2003.

Spin squeezing by quantum non-demolition measurements has also been proposed [26].

A spin $1/2$ is always in a coherent state, but it is possible to squeeze the “effective” higher spin with $j = n/2$ that lives within the symmetric manifold of states in a system of $n > 1$ spins each with $j = 1/2$ [20, 33]. In this paper we describe experimental realizations of squeezed states of these simulated higher order spins on a liquid-state nuclear magnetic resonance (NMR) quantum information processor, using the method suggested by Kitagawa [25]. First, we review the properties of coherent spin states and Kitagawa’s method for creating squeezed spin states, along with the representation of a spin- j system for $j = 1$ and $3/2$ within the totally symmetric subspace of the Hilbert space of $2j$ spin- $1/2$ particles. We then describe the NMR implementation of the method and the measures used to access its overall precision, after which experimental results of squeezing are presented and the level of control attained is discussed. We end by verifying the relation between the degree of squeezing of the simulated spin- j system and the degree of pure state entanglement among the underlying spin- $1/2$ particles, as quantified by various well-established entanglement measures (cf. [18, 36, 37]).

2.2 Simulation of spin squeezing in a multi-spin- $1/2$ system

Throughout the remainder of this paper we will work with units such that $\hbar = 1$. Coherent spin states (CSS) may then be defined by the following properties: (i) The uncertainty relation for the total angular momentum operator J becomes saturated, i.e. $\Delta J_x \Delta J_y = \frac{1}{2} |\langle J_z \rangle|$, where (x, y, z) label the coordinate axes. (ii) The absolute expectation value of the spin in the direction of polarization, e.g. $|\langle J_z \rangle|$, is maximum and equal to j . (iii) The spin uncertainties are equally distributed in any two orthogonal directions in the plane normal to the direction of polarization,

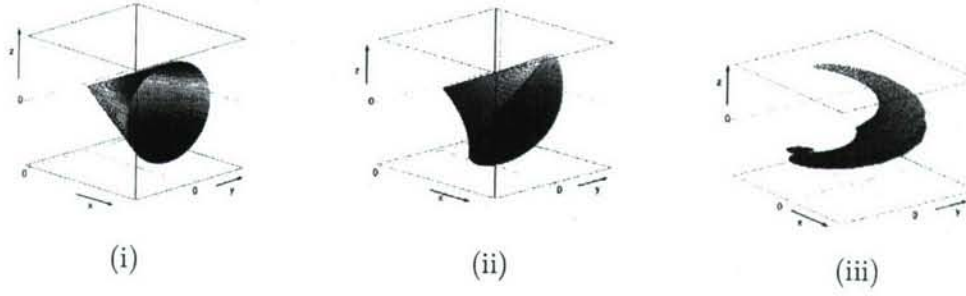


Figure 2-1: (i) A coherent state spin- j vector with expectation values $[\langle J_x \rangle, \langle J_y \rangle, \langle J_z \rangle] = [1, 0, 0]$ may be visualized as a coherent superposition of angular momentum vectors on a cone about the x-axis, all with a projection of $j/2$ along that axis. (ii) After squeezing via the one-axis mechanism (see text), the cone representing the state of a spin-1 particle is elliptical, with its squeezed (minor) axis making an angle of $\pm\pi/4$ with the y, z-axes. (iii) In the maximally squeezed state of a spin-1 particle the cone has been folded into a nearly degenerate ruled surface.

e.g. $\Delta J_x = \Delta J_y$. Kitagawa and Ueda [25] proposed that a spin state is squeezed if the minimum spin uncertainty in the (x, y)-plane is less than the standard quantum limit of $\sqrt{j/2}$. Since a squeezed spin state (SSS) is not related to a CSS by a simple rotation, the polarization of an SSS is less than maximum, e.g. $|\langle J_z \rangle| < j$.

To create a SSS, a “non-linear” operation must be applied, i.e. one that involves products or powers of the spin operators J_x , J_y & J_z in its Hamiltonian H . Kitagawa and Ueda proposed two methods for squeezing a CSS: (i) $H = J_z^2$ (the one-axis twisting mechanism), or (ii) $H = J_x J_y + J_y J_x$ (the two-axis twisting mechanism). The second Hamiltonian can be applied directly to any CSS to squeeze it, whereas the first requires that the CSS be rotated to the (x, y)-plane before the propagator $\exp(i k J_z^2)$ is used to squeeze it, where k is real number which we will call the squeezing parameter. Figure 2-1 illustrate the one-axis process for $j = 1$, in which case maximum squeezing in the (y, z)-plane is obtained when $k = \pi/2$. This one-axis method was used in the NMR experiments described below.

Table 2.1: The representation of a spin-1 by two spin-1/2 particles

Uncoupled Representation ($ m^1 m^2\rangle$)	Coupled Representation ($ j, m\rangle$)
$ 00\rangle = \uparrow\uparrow\rangle$	$ 1, 1\rangle = \uparrow\uparrow\rangle$
$ 01\rangle = \uparrow\downarrow\rangle$	$ 1, 0\rangle = \frac{1}{\sqrt{2}}[\uparrow\downarrow\rangle + \downarrow\uparrow\rangle]$
$ 10\rangle = \downarrow\uparrow\rangle$	$ 1, -1\rangle = \downarrow\downarrow\rangle$
$ 11\rangle = \downarrow\downarrow\rangle$	$ 0, 0\rangle = \frac{1}{\sqrt{2}}[\uparrow\downarrow\rangle - \downarrow\uparrow\rangle]$

Table 2.2: Coupled representation ($|j, m\rangle$) of the basis states spanned by three spin-1/2 particles

Spin-3/2 subspace basis	Spin-1/2 subspace basis
$ \frac{3}{2}, \frac{3}{2}\rangle = \uparrow\uparrow\uparrow\rangle$	$ \frac{1}{2}, \frac{1}{2}\rangle = \frac{1}{\sqrt{6}}[2 \uparrow\uparrow\downarrow\rangle - \uparrow\downarrow\uparrow\rangle - \downarrow\uparrow\uparrow\rangle]$
$ \frac{3}{2}, \frac{1}{2}\rangle = \frac{1}{\sqrt{3}}[\uparrow\uparrow\downarrow\rangle + \uparrow\downarrow\uparrow\rangle + \downarrow\uparrow\uparrow\rangle]$	$ \frac{1}{2}, -\frac{1}{2}\rangle = \frac{1}{\sqrt{6}}[\uparrow\downarrow\downarrow\rangle + \downarrow\uparrow\downarrow\rangle - 2 \downarrow\downarrow\uparrow\rangle]$
$ \frac{3}{2}, -\frac{1}{2}\rangle = \frac{1}{\sqrt{3}}[\downarrow\downarrow\uparrow\rangle + \uparrow\downarrow\downarrow\rangle + \downarrow\uparrow\downarrow\rangle]$	$ \frac{1}{2}, \frac{1}{2}\rangle = \frac{1}{\sqrt{2}}[\uparrow\downarrow\uparrow\rangle - \downarrow\uparrow\uparrow\rangle]$
$ \frac{3}{2}, -\frac{3}{2}\rangle = \downarrow\downarrow\downarrow\rangle$	$ \frac{1}{2}, -\frac{1}{2}\rangle = \frac{1}{\sqrt{2}}[\uparrow\downarrow\downarrow\rangle - \downarrow\uparrow\downarrow\rangle]$

A system of two spin-1/2 particles has 4 basis states. In the coupled representation (in Table 2.1), the three symmetric states span a subspace that transforms under identical rotations of both spins like a single spin-1. Similarly, a system of three spin-1/2 particles has 8 basis states, which span a symmetric subspace that transforms like a single spin-3/2, as well as two spin-1/2 subspaces with lower symmetry. The four states listed on the left-hand column of Table 2.2 are the coupled representation of the spin-3/2 subspace.

From the uncoupled and coupled representations, we see that there is a linear mapping from the spin- j subspaces into the combined $2j$ spin-1/2 systems. These mappings induce the mappings between the spin- j operators and products of spin-1/2 operators (denoted here by $I_{\text{axis}}^{\text{spin}}$), which for $j = 1$ is simply

$$J_x = I_x^1 + I_x^2, \quad J_y = I_y^1 + I_y^2, \quad J_z = I_z^1 + I_z^2. \quad (2.1)$$

For $j = 3/2$, on the other hand, we obtain

$$\begin{aligned}
J_x &= I_x^1 I_x^2 I_x^3 \left(2 + \frac{2}{3}(I_x^1 I_x^2 + I_x^1 I_x^3 + I_x^2 I_x^3) - \frac{8}{3}(I^1 \cdot I^2 + I^1 \cdot I^3 + I^2 \cdot I^3) \right) \\
J_y &= I_y^1 I_y^2 I_y^3 \left(2 + \frac{2}{3}(I_y^1 I_y^2 + I_y^1 I_y^3 + I_y^2 I_y^3) - \frac{8}{3}(I^1 \cdot I^2 + I^1 \cdot I^3 + I^2 \cdot I^3) \right) \\
J_z &= I_z^1 I_z^2 I_z^3 \left(2 + \frac{2}{3}(I_z^1 I_z^2 + I_z^1 I_z^3 + I_z^2 I_z^3) - \frac{8}{3}(I^1 \cdot I^2 + I^1 \cdot I^3 + I^2 \cdot I^3) \right)
\end{aligned} \quad (2.2)$$

Given the apparent complexity of implementing these operations, it was decided instead to implement the far simpler analogues of Eq. (2.2), namely:

$$\tilde{J}_x = I_x^1 + I_x^2 + I_x^3, \quad \tilde{J}_y = I_y^1 + I_y^2 + I_y^3, \quad \tilde{J}_z = I_z^1 + I_z^2 + I_z^3. \quad (2.3)$$

It is easily shown that J_x , J_y , and J_z are contained within the algebra generated by \tilde{J}_x , \tilde{J}_y , and \tilde{J}_z , and that the latter satisfy the usual angular momentum commutation relations. In fact, since they have two extra pairs of identical eigenvalues $\pm 1/2$, they are the sum of the angular momentum operators for a spin-3/2 mixed with those for a pair of spin-1/2. As a result, it was not possible to squeeze the corresponding coherent states to the amount that would have been possible if a pure spin-3/2 representation had been used.

It is apparent that for $j = 1$, $\exp(-i k J_z^2)$ is an evolution $\exp(-i k 4 I_z^1 I_z^2)$ under the bilinear Hamiltonian associated with the scalar coupling interaction between spins in NMR, up to an overall phase factor. Thus the traceless part of the pseudopure state as a function of the squeezing parameter, and its spin-1 pure state equivalent, are

$$\begin{aligned}
e^{-i k 4 I_z^1 I_z^2} \left(\frac{1}{2} I_x^1 + \frac{1}{2} I_x^2 + I_x^1 I_x^2 \right) e^{i k 4 I_z^1 I_z^2} &= \cos(k) \left(\frac{1}{2} I_x^1 + \frac{1}{2} I_x^2 + I_x^1 I_x^2 \right) - \sin(k) (I_y^1 I_z^2 + I_z^1 I_y^2) \\
\Leftrightarrow e^{-i k J_z^2} \frac{1}{2} (J_x + J_x^2) e^{i k J_z^2} &= \cos(k) \frac{1}{2} J_x + \frac{1}{2} J_x^2 - i \sin(k) \frac{1}{2} [J_x, J_z^2], \quad (2.4)
\end{aligned}$$

where $[,]$ is the commutator.

For $j = 3/2$, on the other hand, we find that

$$\begin{aligned} J_z^2 &= \frac{5}{8}I_8 + \frac{1}{6}(\mathbf{I}^1 \cdot \mathbf{I}^2 + \mathbf{I}^1 \cdot \mathbf{I}^3 + \mathbf{I}^2 \cdot \mathbf{I}^3) + 2(I_z^1 I_z^2 + I_z^1 I_z^3 + I_z^2 I_z^3), \\ &= \tilde{J}_z^2 + \frac{1}{6}(\mathbf{I}^1 \cdot \mathbf{I}^2 + \mathbf{I}^1 \cdot \mathbf{I}^3 + \mathbf{I}^2 \cdot \mathbf{I}^3 - \frac{3}{4}I_8). \end{aligned} \quad (2.5)$$

It follows that $\exp(-ikJ_z^2)$ is, to a fairly good approximation, the same as three equal scalar coupling evolutions up to phase, and the (pure) state as a function of the squeezing parameter becomes

$$\begin{aligned} &e^{-ik4(I_z^1 I_z^2 + I_z^1 I_z^3 + I_z^2 I_z^3)} \frac{1}{2}(I_8 + 2I_x^1) \frac{1}{2}(I_8 + 2I_x^2) \frac{1}{2}(I_8 + 2I_x^3) e^{ik4(I_z^1 I_z^2 + I_z^1 I_z^3 + I_z^2 I_z^3)} \\ &= \frac{1}{2}(I_8 + I_x^1(I_8 - 4I_z^2 I_z^3) + \cos(2k)I_x^1(I_8 + 4I_z^2 I_z^3) - \sin(2k)I_y^1(I_z^2 + I_z^3)) \dots \\ &\quad \frac{1}{2}(I_8 + I_x^2(I_8 - 4I_z^1 I_z^3) + \cos(2k)I_x^2(I_8 + 4I_z^1 I_z^3) - \sin(2k)I_y^2(I_z^1 + I_z^3)) \dots \quad (2.6) \\ &\quad \frac{1}{2}(I_8 + I_x^3(I_8 - 4I_z^1 I_z^2) + \cos(2k)I_x^3(I_8 + 4I_z^1 I_z^2) - \sin(2k)I_y^3(I_z^1 + I_z^2)) \\ &\leftrightarrow \frac{1}{16}(e^{-ik/4}(18 - J_z^2) + e^{-ik9/4}(2 - J_z^2)) \dots \\ &\quad \frac{1}{48}(-3I_8 - 2J_x + 12J_x^2 + 8J_x^3) \frac{1}{16}(e^{ik/4}(18 - J_z^2) + e^{ik9/4}(2 - J_z^2)), \end{aligned}$$

where in the last line we have expanded both the exponential $\exp(-ikJ_z^2)$ and the initial coherent state along x in terms of angular momentum operators. Finally, the CSS $|0\rangle$ is, for both values of j , the same as the Zeeman ground state $|\uparrow\uparrow\rangle$ or $|\uparrow\uparrow\uparrow\rangle$ in the uncoupled representation.

2.3 The NMR implementation of squeezed spin states

The implementation of spin squeezing was carried out on a liquid-state NMR quantum information processor, using the two spin-1/2 hydrogen nuclei of 2,3-dibromothiophene (see Fig. 2-2) to represent the spin-1 system, while the spin-3/2 system was represented using the three carbon atoms of a ^{13}C -labeled sample of alanine

(see Fig. 2-3). Both the experiments were carried out on a Bruker AVANCE-400 spectrometer in a field of ca. 9.4 Tesla. In the case of the two-spin experiment, frequency-selective pulses were used to rotate single spins, and hard π -pulses to refocus unwanted chemical shifts. To compensate for pulse imperfections, composite pulses were employed instead of the standard π -pulse [35]. In the three-spin experiment, strongly modulating pulses were used to more accurately perform the desired unitary operations [21, 31]. Unlike low-power “soft” pulses, these pulses average out unwanted evolution, are shorter in time and hence also reduce relaxation effects.

The $I_z^1 I_z^2$ operator used to squeeze the spin-1 system was implemented using π -pulses to refocus the Zeeman evolution of the spins while allowing the scalar coupling between them to evolve, in the standard fashion [22]. Because the coupling between spins 1 and 3 of the alanine system is so small ($J^{13} = -1.29$ Hz), the coupling between them was generated out of the much stronger 1, 2 and 2, 3 couplings [41]. The sum of the three scalar coupling terms of the form $I_z^\ell I_z^m$ was taken as an approximation to J_z^2 in the spin-3/2, as described in Eq. (2.5). As usual in NMR quantum information processing [23, 27], pseudo-pure states were used to represent the dynamics of pure states. These were obtained using spatial averaging techniques based on magnetic field gradients [32, 39].

Even though the decoherence times in liquid-state NMR are long, the intrinsic decoherence rates of the spins still impose limits on the accuracy of the experimental results. The T_2 relaxation rates in 2,3-dibromo-thiophene were 3.2 s^{-1} for both of the hydrogen spins, while in alanine these rates were 0.55, 0.42 and 0.80 s^{-1} for the C^1 , C^2 and C^3 spins, respectively. The products of the shortest of these decoherence times, multiplied by the weakest coupling constant used, were better than 15 for both 2,3-dibromo-thiophene and alanine, which allows about 30 c-NOT gates before decoherence begins to seriously degrade the quality of the results. The amount of time needed for the longest experiments reported here was only about one third of this.

The accuracy of the experiments is further affected by systematic errors like imperfect calibration of the pulses, off-resonance effects and RF inhomogeneity [22]. The effects

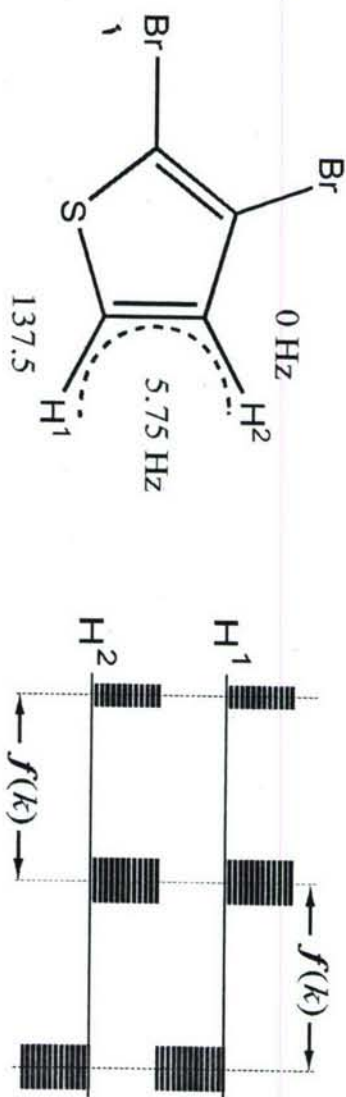


Figure 2-2: The molecular structure of 2,3-dibromo-thiophene is shown on the left, with the two hydrogen atoms used for the spin 1 simulations numbered as in the main text. The coupling strength J between them and the chemical shift of the first compared to the second are also shown. The diagram on the right shows the pulse sequence used to implement spin squeezing for a given parameter k , where $f(k) \equiv k/(2\pi J)$, narrow rectangles indicate $\pi/2$ y -rotations, the broad rectangles y -rotations by π , and the rectangles point downwards for pulses effecting rotations by the negatives of these angles.

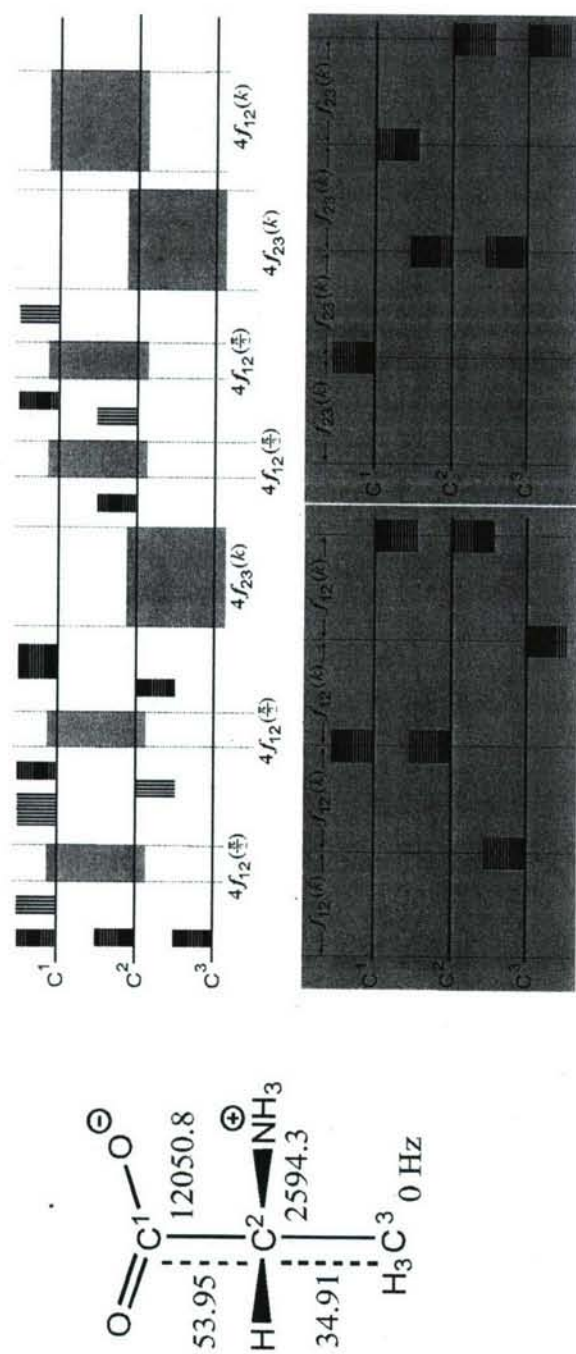


Figure 2-3: The molecular structure alanine is shown on the left, with the three carbon-13 atoms used for the experiments numbered as in the text. The numbers next to the dashed lines are the corresponding coupling constants (in Hz), while the numbers next to the carbons are their chemical shifts relative to the third (in Hz). On the top right is a schematic diagram of the pulse sequence used, where the horizontal striping indicates an x-pulse, vertical striping indicates a y-pulse, the narrower pulses indicate rotations by $\pi/2$, and the wider ones by π (or the negatives thereof if the pulse is below the spin's line). The grey boxes indicate one of the two "modules" show on the bottom right, which allow a $I_z^m I_z^n$ evolution by the angle (k or $\pi/2$) shown on the bottom of the pulse sequence diagram while refocussing the chemical shifts and the coupling between the pairs not contained in the grey box. The functions which relate the delay time to the squeezing parameter k is given by $f_{mn}(k) \equiv k/(4\pi J^{mn})$ for $[m, n] = [1, 2], [2, 3]$.

of these errors may be seen in the density matrices of the final states, which in turn were determined by full state tomography [30]. Although plots of these density matrices (see Figs. 2-4 and 2-5) provide a visual overview of the results, a more quantitative summary of the overall accuracy may be obtained by calculating the correlation between the theoretically expected and experimentally determined density matrices ρ_{the} and ρ_{fin} , respectively. This is defined as

$$C = \frac{\text{tr}(\rho_{\text{fin}}\rho_{\text{the}})}{\sqrt{\text{tr}(\rho_{\text{fin}}\rho_{\text{fin}})\text{tr}(\rho_{\text{the}}\rho_{\text{the}})}}. \quad (2.7)$$

To also include an estimate of the precision of the experiment, the amount of signal (or polarization) lost during the experiment must also be taken into account. This leads to a metric called the attenuated correlation [21], namely

$$C_{\text{att}} = C \frac{\sqrt{\text{tr}(\rho_{\text{fin}}\rho_{\text{fin}})}}{\sqrt{\text{tr}(\rho_{\text{ini}}\rho_{\text{ini}})}} = \frac{\text{tr}(\rho_{\text{fin}}\rho_{\text{the}})}{\sqrt{\text{tr}(\rho_{\text{ini}}\rho_{\text{ini}})\text{tr}(\rho_{\text{the}}\rho_{\text{the}})}}. \quad (2.8)$$

The theoretically expected density matrix ρ_{the} was obtained by applying the intended unitary transformation U_{the} to the initial pseudo-pure state ρ_{ini} , as determined by state tomography.

2.4 Results of spin squeezing experiments

Using state tomography [30], the $2j$ spin-1/2 density matrices ρ_{exp} were reconstructed following squeezed state preparation for various values of the squeezing parameter $k = 0, \dots, \pi$. The expectation values and uncertainties along the basis axes were then calculated directly from these density matrices and the J_μ (or approximate \tilde{J}_μ matrices given in Eqs. (2.1) and (2.3)), as follows:

$$\begin{aligned} \langle J_\mu \rangle &= \text{tr}(J_\mu \rho_{\text{exp}}); \\ \langle \Delta J_\mu \rangle &= \sqrt{\text{tr}(J_\mu^2 \rho_{\text{exp}}) - (\text{tr}(J_\mu \rho_{\text{exp}}))^2}. \end{aligned} \quad (2.9)$$

where $\mu = x, y, z$.

The correlation for the spin-1 pseudo-pure density matrix (see Fig. 2-4(i)) was 0.99. For the density matrix corresponding to the maximally squeezed ($k = \pi/2$) spin-1 state, the correlation and the attenuated correlation were 0.99 and 0.98 respectively. The correlation for the spin-3/2 pseudo-pure state density matrix (see Fig. 2-5(i)) was 0.98, while the correlation and the attenuated correlation of the maximally squeezed spin-3/2 state were 0.84 and 0.80, respectively.

Since the squeezing operator conserves the total angular momentum, the combined $2j$ spin-1/2 system should stay in the spin- j subspace during the course of the experiment. However, due to decoherence and other errors in the implementation there is some “leakage” out of the effective spin- j subspace. To quantify the accuracy with which we have been able to simulate the spin- j system, we computed the best pseudo-pure-state approximation to mixed-state density matrix ρ_{exp} , by taking the eigenvector $|\psi_{\text{max}}\rangle$ associated with the largest eigenvalue of ρ_{exp} . The probability of leakage was then obtained from the definition

$$Pr_{\text{leak}} = 1 - \sum_{m=-j}^j |\langle j, m | \psi_{\text{max}} \rangle|^2, \quad (2.10)$$

where $|j, m\rangle$ are the basis states of spin- j subspace. This probability of leakage, averaged over all the experiments performed, was $(0.02 \pm 0.02)\%$ for the spin-1 simulations and $(7.67 \pm 3.20)\%$ for the spin-3/2. The substantially larger leakage in the latter case was due to the fact that the protons were not decoupled from the carbons during the carbon scalar coupling evolution delays, in order to avoid the possibility of carbon-proton nuclear Overhauser effects.

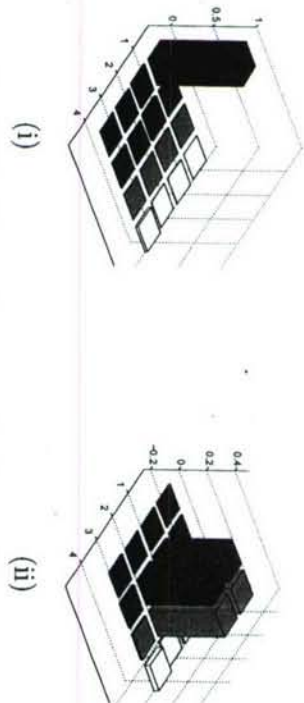


Figure 2-4: (i) The real part of the experimental density matrix representing the initial pseudo-pure state $|00\rangle$ for the spin 1 experiments.
(ii) The real part of the experimental density matrix representing the maximally squeezed state of the effective spin 1 particle.

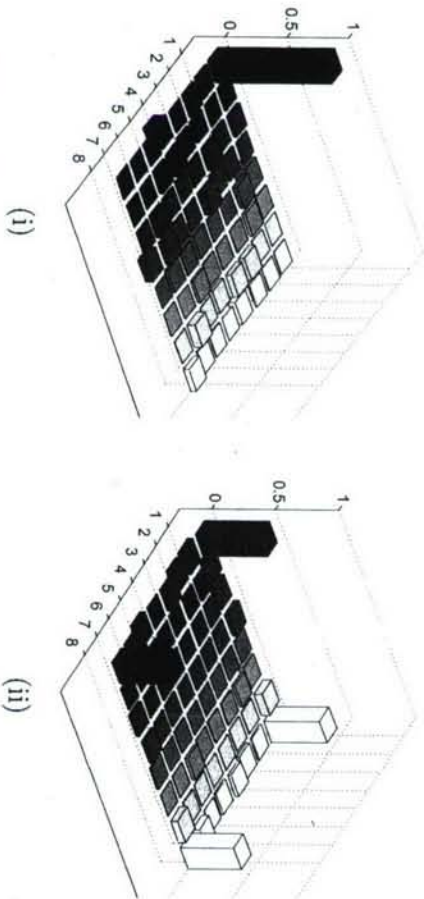


Figure 2-5: (i) The real part of the experimental density matrix representing the initial pseudo-pure state $|000\rangle$ for the spin $3/2$ experiments.
(ii) The real part of the density matrix when the squeezing parameter $k = \pi/2$, at which point a GHZ state is obtained [28].

2.4.1 The spin-1 case

The initial pseudo-pure state corresponds to a coherent state of the embedded spin-1 subspace. It remains in a coherent spin state after a $\frac{\pi}{2}$ rotation to the x-axis and accordingly, state tomography at this point reveals that $\langle \mathbf{J}_x \rangle$ is nearly equal to 1 while the spin uncertainties in the y and z-directions are nearly equal to $1/\sqrt{2}$. After applying the non-linear interaction for a period of $2f(k) = k/(\pi J)$, the spin-1 expectation values in all directions are all close to 0, consistent with a maximally entangled state (see Table 2.3). The uncertainty is now maximum in the x-direction, while the uncertainties in the y and z-directions are still nearly equal to $1/\sqrt{2}$ because the principle axes of the squeezed ellipsoid are at $\pi/4$ to the y and z axes (see Fig. 2-1(iii)). To make the squeezing more readily apparent, it was convenient to follow the squeezing step by a $\pi/4$ x-pulse so that the uncertainty along the z-axis becomes 1. The experimental and theoretical data for this maximally squeezed and rotated state are given in Table 2.3.

Table 2.3: Theoretical and experimental spin expectation values and uncertainties of the maximally squeezed spin-1 states

	$\langle \mathbf{J}_x \rangle$	$\langle \mathbf{J}_y \rangle$	$\langle \mathbf{J}_z \rangle$	$\langle \Delta \mathbf{J}_x \rangle$	$\langle \Delta \mathbf{J}_y \rangle$	$\langle \Delta \mathbf{J}_z \rangle$
Theory	0.00	0.00	0.00	1.00	0.00	1.00
Experiment	0.00	-0.02	0.00	0.97	0.21	0.98

The variation of $|\langle J_x \rangle|$, ΔJ_y and ΔJ_z for different values of k is plotted in Fig. 2-6. The corresponding values of $|\langle J_y \rangle|$ and $|\langle J_z \rangle|$ are close to zero implying that the spin system is polarized along x direction for all values of the squeezing parameter k .

2.4.2 The spin-3/2 case

After the initial $\pi/2$ rotation to the x-axis, state tomography showed that the spin-3/2 angular momentum vector pointed in the x-direction with $\langle \mathbf{J}_x \rangle \approx 1.5$, and uncertainties in the y and z-directions nearly equal to their theoretical values of $\sqrt{3}/2$.

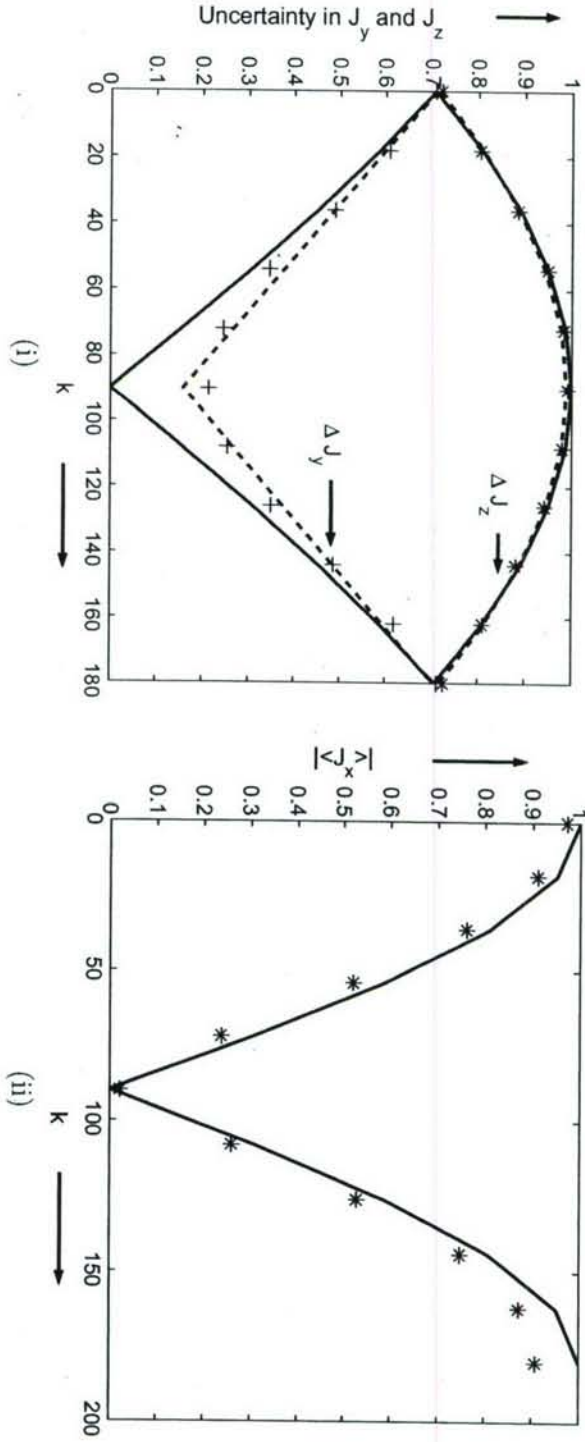


Figure 2-6: Plots of the theoretically expected uncertainties as a function of the squeezing parameter k (in degrees) for spin 1 (solid lines), along with the fits (dashed lines) to the uncertainties computed from the experimental density matrices ($+$ or $*$). (i) Plots of $\langle \Delta J_y \rangle$ (lower curves), and $\langle \Delta J_z \rangle$ with k (upper curves). (ii) Plot of $|\langle J_x \rangle|$ (no fits shown).

Table 2.4: Theoretical and experimental spin expectation values and uncertainties of the maximally squeezed spin-3/2 states

	$\langle \mathbf{J}_x \rangle$	$\langle \mathbf{J}_y \rangle$	$\langle \mathbf{J}_z \rangle$	$\langle \Delta \mathbf{J}_x \rangle$	$\langle \Delta \mathbf{J}_y \rangle$	$\langle \Delta \mathbf{J}_z \rangle$
Theory	1.00	0.00	0.00	0.87	0.50	1.32
Experiment	0.82	0.05	-0.13	0.92	0.53	1.36

Application of the non-linear interaction for a given k created some apparent entanglement in the system, as indicated by the fact that $\langle \mathbf{J}_x \rangle$ was reduced to about 1 while $\langle \mathbf{J}_y \rangle$ and $\langle \mathbf{J}_z \rangle$ remained zero. The uncertainty in the x-direction also increased from 0 to $\sqrt{3}/2$. To orient the axes of the squeezed uncertainty ellipsoid along the y and z-directions, the results of state tomography were rotated about the x-axis (on a computer, since unlike the spin-1 case the rotation angle needed depends on the value of k [25]). The experimental and theoretical data for the maximally squeezed state are shown in Table 2.4, while the variation of $|\langle \mathbf{J}_x \rangle|$, ΔJ_y and ΔJ_z for different values of k is plotted in Fig. 2-7. As in the spin-1 case, the corresponding values of $|\langle \mathbf{J}_y \rangle|$ and $|\langle \mathbf{J}_z \rangle|$ are close to zero, implying that the spin system is polarized along x-direction for all values of the squeezing parameter k , as desired.

2.4.3 Behavior of entanglement measures

The probability of leakage measurements described above (see Eq. (2.10)) show that the best pseudo-pure-state approximation to the final mixed-state density matrix quite accurately describes the spin- j system. Thus this pseudo-pure state may be used to study the entanglement of the constituent spin-1/2 particles by well-understood pure-state entanglement criteria. The criteria used here are the entanglement of formation [16] (or, for bipartite pure states, the von Neumann entropy of the partial trace over either subsystem), and the concurrence [24, 46] of (the partial trace onto any) pair of qubits. The purpose of this discussion is not to uncover any new features of entanglement in these simple systems, but rather to use the compatibility of the experimental results with the well-known behavior of these entanglement measures as

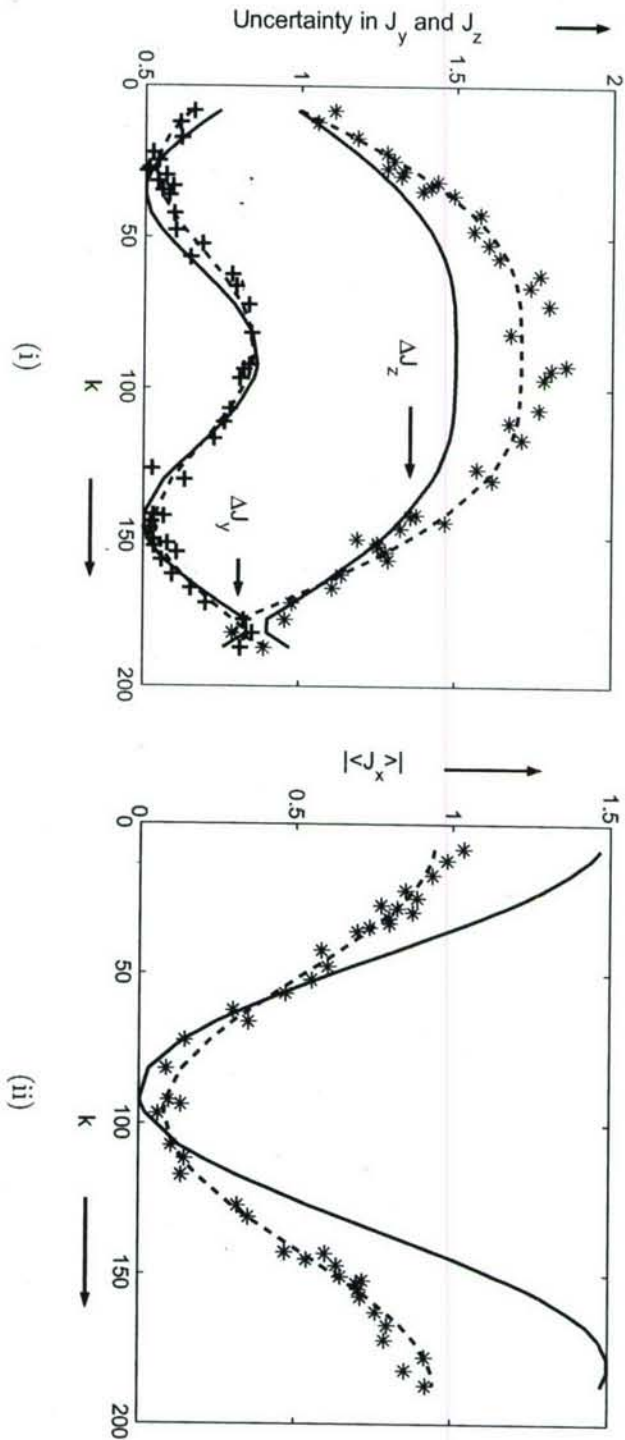


Figure 2-7: Plots of the theoretically expected uncertainties as a function of the squeezing parameter k (in degrees) for spin $3/2$ (solid lines), along with fits (dashed lines) to the uncertainties computed from the experimental density matrices (+ or *). (i) Plots of $\langle \Delta J_y \rangle$ (lower curves) and $\langle \Delta J_z \rangle$ (upper curves). (ii) Plot of $|\langle J_x \rangle|$.

a benchmark for the precision of control obtained. In addition, these entanglement measures were computed without taking into account the very large identity component that is always present in liquid-state NMR, and hence should be regarded as measures of the “pseudo-entanglement” associated with the pseudo-pure states used for the experiments.

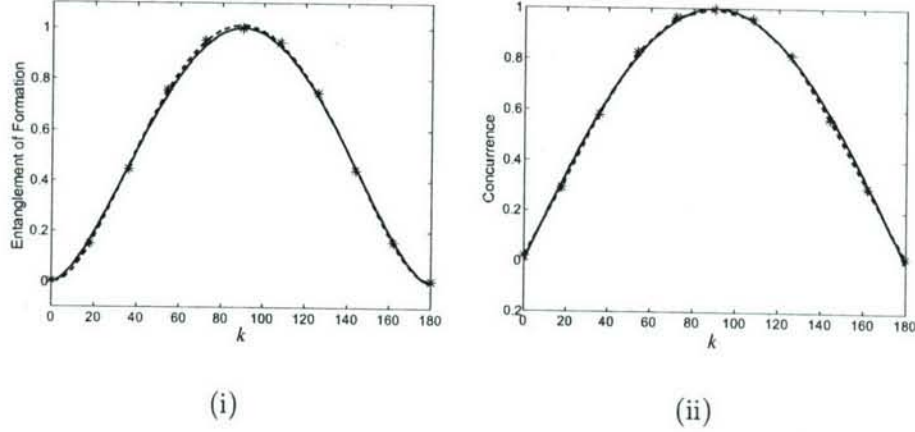


Figure 2-8: Plots of the entanglement of formation (i) and concurrence (ii) with the squeezing parameter k (in degrees) for spin-1. The solid lines are the theoretically expected curves, while the dashed lines interpolate linearly between the values computed from the experimental density matrices (*) obtained via tomography.

Figure 2-8 shows plots of the theoretically expected and experimentally observed entanglement measures as a function of the squeezing parameter k for the spin-1 experiments. It is immediately apparent that the theory and experiments agree extremely well with respect to either entanglement measure, in accord with the fact that the concurrence and entanglement of formation are monotonically related for two qubits. The maximally squeezed state ($k = 90^\circ$) is observed to correspond to the maximally entangled state, as theory predicts it should in a representation by Dicke states [40].

Figure 2-9 shows the analogous pair of plots for the spin-3/2 experiments, where the interpolation is now done using a fifth-order polynomial fit to the data (dashed lines). In this case three different entanglements of formation are obtained, depending on

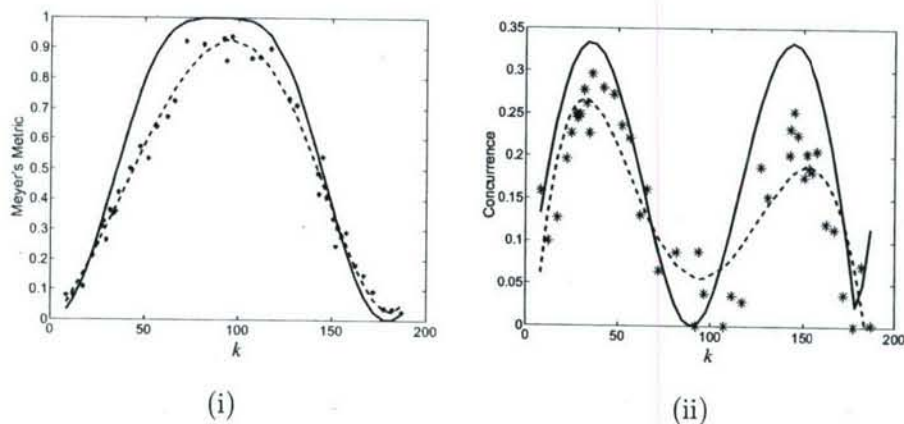


Figure 2-9: Plots of the Meyer's metric or average entanglement after tracing down to a single qubit (i) and concurrence after tracing down to any pair of qubits (ii) with the squeezing parameter k (in degrees) for spin-3/2. The solid lines are the theoretically expected curves, while the dashed lines are a fifth-order polynomial fit to the values computed from the experimental density matrices (*) obtained via tomography.

which pair of qubits is traced over in order to obtain the reduced density matrix, and their average, also known as the Meyer's entanglement metric[29], is plotted for simplicity. According to this metric, the maximum entanglement again occurs at $k = 90^\circ$ and corresponds to a Greenberger-Horne-Zeilinger state, which is however not a maximally squeezed state. The maximally squeezed state now occurs instead at $k = 34.7^\circ$ and again at $180 - 34.7 = 155.3^\circ$, and corresponds to the maximum concurrence of the reduced density matrix obtained by tracing over any one qubit (which is attained by a W -state). The correspondence between theory and experiment in this case is noticeably lower than in the spin-1 experiments, primarily because of leakage from the carbons used as qubits into the alpha and methyl protons during the experiment.

2.5 Conclusions

We have demonstrated the use of liquid-state NMR to simulate squeezed states of the effective spin-1 and 3/2 subsystem contained in a two and three-qubit system, respectively. We have further shown that the precision of quantum control obtained was sufficient to reproduce the theoretically expected behavior of the spin-1 and 3/2

observables as well as the associated entanglement measures among the underlying qubits. The results are a further demonstration of the utility of pseudo-pure states [23], and the power of strongly modulating pulses [31], for the development and validation of quantum control methods. The dynamics of the coherences among the fiducial states that were confirmed by complete tomography are fully in accord with these proposals, even though the highly mixed states used in our experiments were, of course, separable at all times. It is interesting to observe, however, that even when the identity component of the density matrix is fully taken into account the uncertainties in the x and y directions were unequal, i.e. the actual mixed states created could be regarded as (very slightly) “squeezed”.

It should also be pointed out that the interpretation of the higher spin states as “squeezed” or not depends on how the higher spin states are mapped into the symmetric subspace of the multi-spin- $1/2$ system. We discussed earlier, for example, how the mapping used here for the spin- $3/2$ experiments actually gave the sum of a spin- $3/2$ with a spin- $1/2$ pair, limiting the degree of squeezing attainable. Even when the mathematical representation is strictly correct, however, the physical properties of the squeezed states can be rather different. For instance, if we were to replace the Dicke states $|\uparrow\uparrow\rangle$ and $|\downarrow\downarrow\rangle$ in Table 2.1 by the Bell states $1/\sqrt{2}(|\uparrow\uparrow\rangle \pm |\downarrow\downarrow\rangle)$, the maximally squeezed state of the simulated spin-1 would correspond to the unentangled basis state $|00\rangle$ of the two-qubit system in which it is contained. Such a representation may be a bit unnatural, since rotations of the qubits no longer correspond to rotations of the higher spin, but should still be kept in mind when discussing the relations between entanglement in multi-qubit systems and the squeezing of the effective higher spins therein [18, 25].

CHAPTER 3

SELECTIVE COHERENCE TRANSFERS IN HOMONUCLEAR DIPOLAR COUPLED SPIN SYSTEMS

3.1 Introduction

Nuclear spins feature prominently in most proposals for solid state quantum information processors. They have the advantage of a simple and well defined energy level structure and they are normally well isolated from other degrees of freedom. The challenge of using nuclear spins in solids is to obtain control over the multi-spin dynamics. In a dielectric solid, the dominant interaction between the spins is the magnetic dipolar coupling. Since the strength of the coupling between two spins is inversely proportional to the cube of the distance between them, a single spin is coupled to a large number of surrounding spins, and not just its immediate neighbors. Therefore every desired gate is embedded in a complex, multi-body space and the dynamics have so far proven to be intractable. Controlling the evolution of a dipolar coupled spin system has long been an important goal in solid state NMR, particularly for spectroscopic studies. For example, the dipolar coupling has been effectively

²Parts of this chapter were extracted from the paper “Selective coherence transfers in homonuclear dipolar coupled spin systems”, by C. Ramanathan, S. Sinha, J. Baugh, T. F. Havel and D. G. Cory, *Physical Review A*, Vol. 71, 020303(R), February 2005.

turned off using techniques such as spinning the sample rapidly at the magic angle ($\theta_m = \cos^{-1}(1/\sqrt{3})$) and a variety of multiple pulse techniques, which average the spatial and spin tensors of the coupling respectively, as well as a combination of these [50, 51].

A very useful element of control would be to map the physical dipolar Hamiltonian of the spin system onto an effective interaction that has the form of only nearest neighbor couplings. This would significantly simplify the implementation of accurate two-qubit operations in a many-qubit solid state spin-based quantum processor [6, 47, 48, 8]. This restricted evolution is also necessary to avoid cross-talk between adjacent solid state quantum information processors in ensemble quantum computation [4, 5]. Without such control the gate fidelities achievable within a given processor element will be degraded due to leakage to other members of the ensemble. Nearest neighbor mapping would also allow quantum simulations of many-body systems such as the Ising, XY or Heisenberg Hamiltonians in 1, 2 or 3 dimensions. The mapping envisioned here would have significant applications beyond quantum information processing. For example, a nearest neighbor interaction could allow a more accurate determination of distances in NMR structural studies, and could be used to perform sequential polarization transfers, such as along the backbone of a protein.

Here we report the first step towards the experimental realization of such a scheme for the special case of an ensemble of spin pairs, where the dipolar coupling between the spins within a pair is significantly larger than the coupling between spins on neighboring pairs. We are able to extend the phase memory of the spin pairs by decoupling the pairs from each other, without decoupling the interaction between spins within a pair. The control sequence consists of a simple amplitude modulated RF field, with the modulation frequency set to the desired dipolar coupling strength.

3.2 Theory of the modulation scheme

Our model system is an assembly of identical spin pairs with (strong) dipolar coupling ω_D^S and weaker couplings between spins on different pairs. In a strong external magnetic field aligned along \hat{z} the truncated secular dipolar Hamiltonian for this system is given by

$$H_d = \frac{\hbar}{4} \sum_i \omega_D^S h_{12}^{ii} + \frac{\hbar}{4} \sum_{\alpha, \beta=1}^2 \sum_{i \neq j} \omega_D^{ij\alpha\beta} h_{\alpha\beta}^{ij} \quad (3.1)$$

where $h_{\alpha\beta}^{ij} = 2\sigma_{zi}^\alpha \sigma_{zj}^\beta - \sigma_{xi}^\alpha \sigma_{xj}^\beta - \sigma_{yi}^\alpha \sigma_{yj}^\beta$, and $\omega_D^{ij\alpha\beta}$ is the coupling between spin- α on pair i and spin- β on pair j .

The goal is to introduce a modulated RF field such that the effective Hamiltonian is restricted to just the isolated spin pairs (the first term in Eq. 3.1). Our solution may be understood by viewing the RF field in the interaction frame of this coupling. In the fully symmetric case the state $\sigma_x^1 + \sigma_x^2$ evolves as $(\sigma_x^1 + \sigma_x^2) \cos\left(\frac{3\omega_D^S}{2}t\right) + (\sigma_y^1 \sigma_z^2 + \sigma_z^1 \sigma_y^2) \sin\left(\frac{3\omega_D^S}{2}t\right)$, so we chose a RF that has an amplitude modulation frequency $\omega_m = 3\omega_D^S/2$ and is given (in the lab frame) by

$$H_{\text{mod}}(t) = \frac{\hbar\omega_1}{2} \cos\left(\frac{3\omega_D^S}{2}t\right) \times e^{i(\omega_0 t/2) \sum_i \sigma_z^i} \left(\sum_i \sigma_x^i \right) e^{-i(\omega_0 t/2) \sum_i \sigma_z^i} \quad (3.2)$$

where ω_0 is the Larmor frequency of the spins. The cosine amplitude modulation produces frequency sidebands at $\omega_0 \pm 3\omega_D^S/2$. Amplitude modulated pulses have previously been used in NMR for simultaneously irradiating multiple transitions in quadrupolar spin systems [49] to create multiple quantum coherences in the regime where the RF power is significantly smaller than the strength of the quadrupolar coupling.

We illustrate a simple physical picture of the averaging process using a 3-spin case. Consider the Hamiltonian (in the rotating frame) of a three-spin system, in which

spins 1 and 2 are strongly coupled and spin 3 is weakly coupled to spins 1 and 2 ($\omega_D^S \gg \omega_D^w$), under the RF modulation

$$H = \frac{\hbar\omega_D^S}{4}h_{12} + \frac{\hbar\omega_D^w}{4}(h_{13} + h_{23}) + \frac{\hbar\omega_1}{2} \cos\left(\frac{3\omega_D^S}{2}t\right) (\sigma_x^1 + \sigma_x^2 + \sigma_x^3) . \quad (3.3)$$

The time-dependent Hamiltonian in the interaction frame of the (1,2) pair interaction is given by

$$\tilde{H}(t) = e^{-i(\omega_D^S t)h_{12}/4} \left(H - \frac{\hbar\omega_D^S}{4}h_{12} \right) e^{+i(\omega_D^S t)h_{12}/4} \quad (3.4)$$

The zeroth order average Hamiltonian [51] of this interaction frame Hamiltonian over a period $\tau = 4\pi/3\omega_D^S$ is

$$\bar{H}^{(0)} = \frac{\hbar\omega_D^w}{2} (\sigma_z^1\sigma_z^3 + \sigma_z^2\sigma_z^3) + \frac{\hbar\omega_1}{4} (\sigma_x^1 + \sigma_x^2) . \quad (3.5)$$

The system can then be transformed into a second interaction frame via

$$U' = \exp\left(\frac{i\omega_1 t}{4} (\sigma_x^1 + \sigma_x^2)\right) . \quad (3.6)$$

Now, in this second averaging frame of $\bar{H}^{(0)}$ (Eq. 3.6), the first term, i.e. the residual dipolar couplings to spin 3, averages to zero over a cycle $\tau' = 4\pi/\omega_1$. Hence the second averaging of the couplings to spin 3 is efficient when $\omega_1 \gg 4\omega_D^w$, and the effective total system dynamics are generated by the (1,2) dipolar coupling (the Hamiltonian of the first frame transformation). This picture provides the motivation for our approach, but the overall dynamics are more complicated than that suggested by the zeroth-order average shown above. If ω_D^S is not significantly stronger than ω_1 , the higher order terms of the Magnus expansion become more important. In addition, if the strength of the 1-3 and 2-3 couplings are different, additional two and three body terms appear in the Hamiltonian.

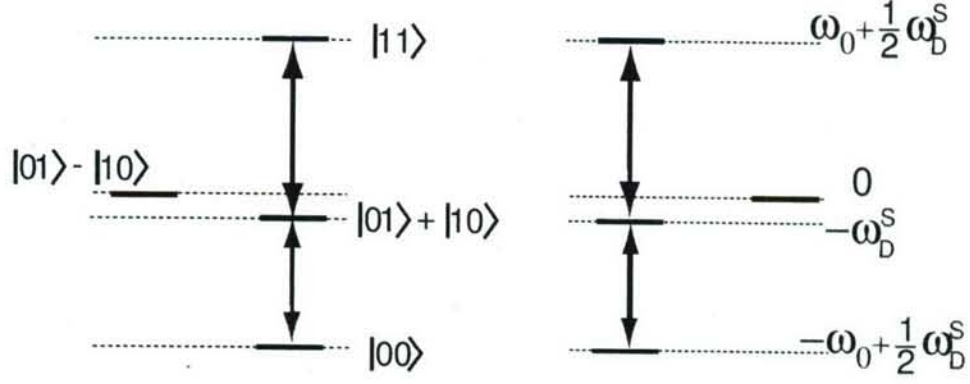


Figure 3-1: Two pairs of strongly coupled spin- $\frac{1}{2}$ systems with each pair decomposed into its singlet and triplet manifolds (in the rotating frame). The triplet manifolds are weakly coupled to each other while the singlet manifolds do not interact.

Further insight may be obtained by considering the energy level structure of an isolated dipole-coupled pair of spin-1/2 nuclei. This has four energy levels, with three triplet levels corresponding to a composite $I = 1$ system and a non-magnetic singlet with $I = 0$ [?]. A weakly coupled set of spin pairs will largely preserve this structure, but transitions between the singlet and triplet will no longer be forbidden due to the coupling between spins on different pairs. Let ω_D^w represent the average strength of the weaker couplings. Figure 1 illustrates how the spin pairs are decoupled from each other under the amplitude modulated (AM) RF irradiation. If $\omega_m = 3\omega_D^S/2$, the AM irradiation simultaneously drives transitions $|00\rangle \leftrightarrow |01\rangle + |10\rangle$ and $|01\rangle + |10\rangle \leftrightarrow |11\rangle$ of the triplet manifold. The rate at which these transitions are driven depend on the strength of the modulation field, ω_1 . If $\omega_1 \gg \omega_D^w$, the two triplet manifolds are decoupled from each other and the pairs are isolated from each other. However, if the RF power is increased further such that $\omega_1 \geq \omega_D^S$, the triplet sub-space structure gets destroyed as the strong coupling between the spins within the pair is decoupled.

Thus, our scheme works in the regime where $\omega_m = 3\omega_D^S/2$ and $\omega_D^S \gg \omega_1 \gg \omega_D^w$. Not surprisingly these are exactly the same conditions as obtained in the previous section. Intuitively, the RF modulation allows us to move into an interaction frame that is moving with the magnetization of the dipole coupled spin pair. The experiment bears some similarities to the spin-1 decoupling experiments originally proposed by Pines and coworkers [53, 54]. In fact they suggest that their method could be used to decouple a heteronuclear spin from a pair of identical spins. However, the scheme

presented here goes further, and permits a coherent evolution of the isolated spin pair while decoupling the pairs from each other.

It is also useful to move into the interaction frame of the RF modulation. The zeroth-order average Hamiltonian [81] of an isolated spin pair in the interaction frame of the RF modulation is

$$\begin{aligned} \bar{H}_d^{(0)} = & -\frac{\hbar}{8}\omega_D^S (2\sigma_x^1\sigma_x^2 - \sigma_y^1\sigma_y^2 - \sigma_z^1\sigma_z^2) + \\ & \frac{3\hbar}{8}\omega_D^S J_0 \left(\frac{4\omega_1}{\omega_D^S} \right) (\sigma_z^1\sigma_z^2 - \sigma_y^1\sigma_y^2) . \end{aligned} \quad (3.7)$$

where the average has again been performed over one period of the amplitude modulation ($t = 2\pi/\omega_m = 4\pi/3\omega_D^S$). Starting from the equilibrium state where the spins are along the external magnetic field, a collective $\pi/2$ rotation of the spins places a spin pair in the initial state $\sigma_x^1 + \sigma_x^2$. This state commutes with the first term of the interaction Hamiltonian shown above, and the effective evolution is only due to the second term $\sigma_z^1\sigma_z^2 - \sigma_y^1\sigma_y^2$. The set of operators, $(\sigma_x^1 + \sigma_x^2, \sigma_z^1\sigma_z^2 + \sigma_y^1\sigma_y^2, \sigma_z^1\sigma_z^2 - \sigma_y^1\sigma_y^2)$ form a subalgebra under the commutator that is isomorphic to the Cartesian subalgebra $(\sigma_x, \sigma_y, \sigma_z)$. Thus the strongly coupled spins oscillate between the single spin state $\sigma_x^1 + \sigma_x^2$ and the two spin state $\sigma_z^1\sigma_z^2 + \sigma_y^1\sigma_y^2$. If the first term of the Hamiltonian in Eq. 3.7 were absent, this scheme would map onto a nearest neighbor interaction, and as long as the initial state of the spin pairs was within this subspace, leakage out of the subspace would be substantially suppressed. However, in the current scheme, the initial state should be both within the subspace and commute with the first term of Eq. 3.7. For an ensemble of spin pairs, only the collective σ_x state satisfies these conditions.

3.3 Experimental Results

Gypsum ($\text{CaSO}_4 \cdot 2 \text{H}_2\text{O}$) was taken as a prototypical system for a weakly interacting ensemble of identical spin pairs. The protons in the waters of crystallization comprise

the strongly coupled spins. The coupling between protons on different water molecules is significantly smaller than that between protons in the same molecule. A unit cell of gypsum has four water molecules, with two pairs in two inequivalent sites. When the external magnetic field is applied along the [010] orientation, the dipolar splitting at the inequivalent water sites coincide and a Pake doublet is observed (see Fig. 3-2) in a one-pulse experiment [56]. In this orientation the strong dipolar coupling between protons in the water molecule is $\omega_D^S/2\pi = 14.8$ kHz, and the mean coupling between protons on different water molecules is $\omega_D^w/2\pi = 5.5$ kHz.

The experiments were carried out at room temperature at 7.1 T (^1H 300 MHz) using a Bruker Avance spectrometer on a 1 mm³ single crystal of gypsum in the [010] orientation. The length of the $\pi/2$ pulse used was 1.67 μs . The experiment was repeated as the duration of the AM RF was varied from 100 μs to 2.9 ms with an increment of 5.5 μs . The signal was Fourier transformed with respect to the length of the modulation pulse to yield the spectrum shown in Fig. 3-2(b). Fig. 3-2(c) shows the observed $\sum_i \sigma_x^i$ terms plotted against the length of the modulation pulse [57]. A dramatic narrowing of the spectral line is observed in the experiment. The effective T_2 of the spins under the modulation is 11.1 ms which corresponds to a linewidth of 29 Hz. This is a factor of 572 times smaller than the 16.6 kHz width of a single line of the Pake doublet.

In order to demonstrate that the spin pair continues to undergo a coherent evolution, we performed a second series of experiments to specifically filter out and separate the $\sigma_x^1 + \sigma_x^2$ and the $\sigma_y^1\sigma_z^2 + \sigma_z^1\sigma_y^2$ terms. The two experiments are shown in Figure 3-3. Figure 3-5(a) shows the coherence transfer under the dipolar Hamiltonian while Fig. 3-5(b) shows the coherence transfer under the action of the modulation sequence. Under the dipolar coupling the interactions with distant spins rapidly generate higher order spin correlations, and there is a strong damping of the oscillation between the single spin and the two-spin terms. However, under the modulation sequence this oscillation is seen to extend out significantly farther. Thus the observed line-narrowing is not a form of spin-locking of the single spin terms, as occurs under strong RF irradiation,

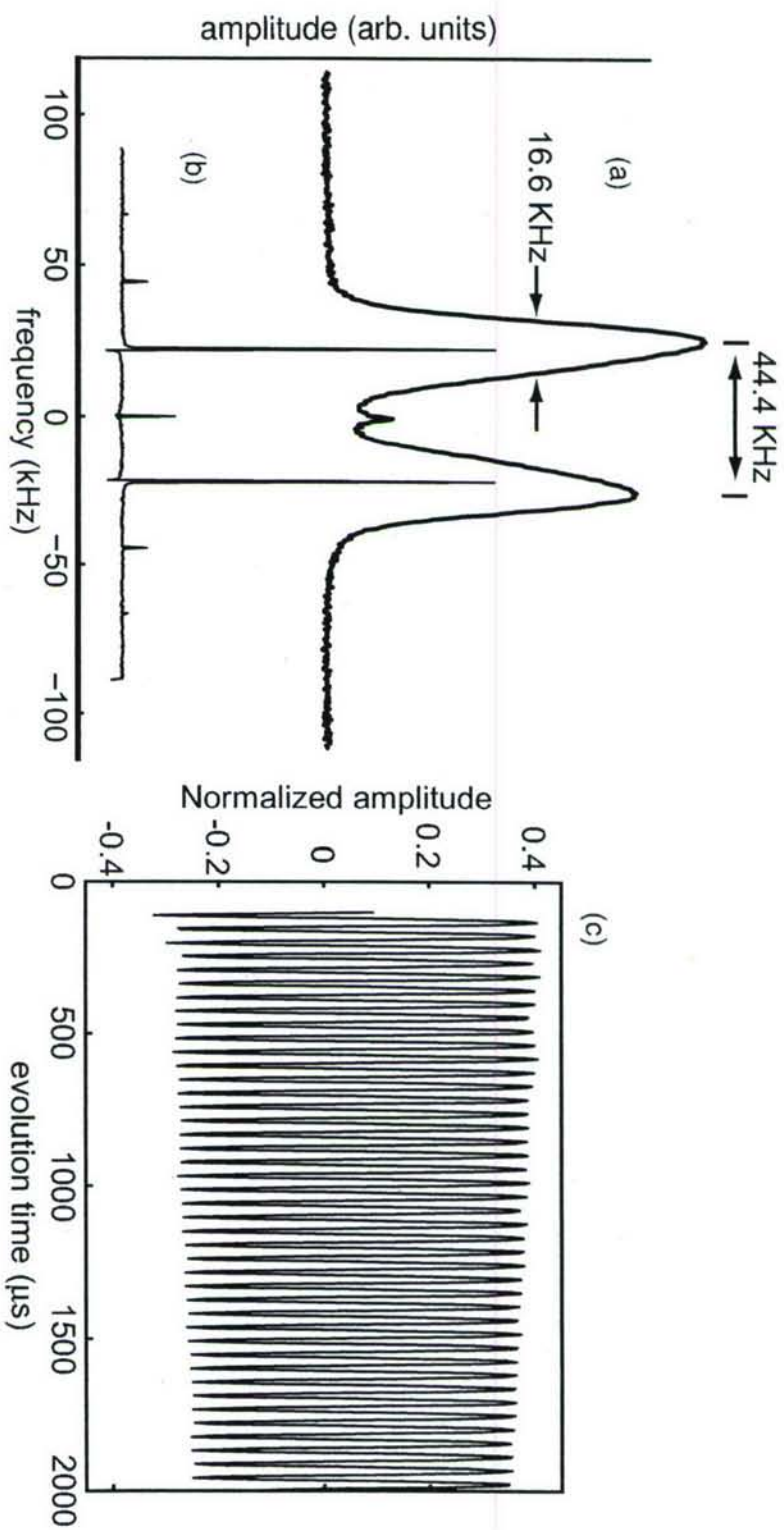


Figure 3-2: (a) The proton spectrum of a single crystal of gypsum in the [010] orientation (Pake doublet). The splitting between the peaks corresponds to $3\omega_D^S/2\pi = 44.4$ KHz. Each peak is broadened due to weak dipolar coupling to the other water molecules. Therefore, $3\omega_D^W/2\pi \sim 16.4$ KHz (b) The line narrowing observed under the modulation sequence with RF amplitude $\omega_1 = 3\omega_D^S/4$. (c) Evolution of the collective spin $\sum_i \sigma_z^i$ terms under the modulation sequence.

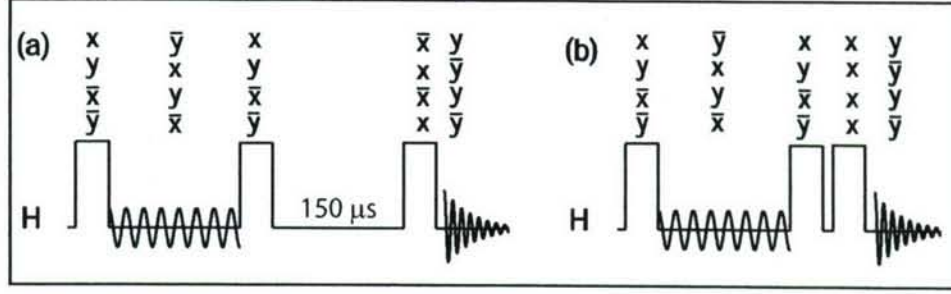


Figure 3-3: (a) pulse sequence used to read out the $\sigma_x^1 + \sigma_x^2$ terms. Following the modulation pulse, a $\pi/2$ pulse is applied to rotate the σ_x terms to σ_z . During the $150 \mu s$ interval (much shorter than T_1) all terms other than the σ_z decay. A $\pi/2$ pulse is then used to monitor σ_z . (b) pulse sequence used to read out the $\sigma_y^1 \sigma_z^2 + \sigma_z^1 \sigma_y^2$ term. Following the modulation two back to back $\pi/2$ pulses act as a double quantum filter to suppress the single spin σ_x terms. A four step phase cycle is necessary to implement the filter.

but is due to the selective decoupling of the weaker interactions between spins on different pairs.

3.4 Conclusions

In conclusion, we have demonstrated that it is possible to restrict the evolution of a dipolar coupled spin network to a much smaller subspace of the system Hilbert space. This restriction allows us to significantly extend the phase coherence times for selected states. The scheme developed works for a system consisting of an ensemble of spin pairs, where the coupling between spins in the same pair is stronger than the coupling between spins on different pairs.

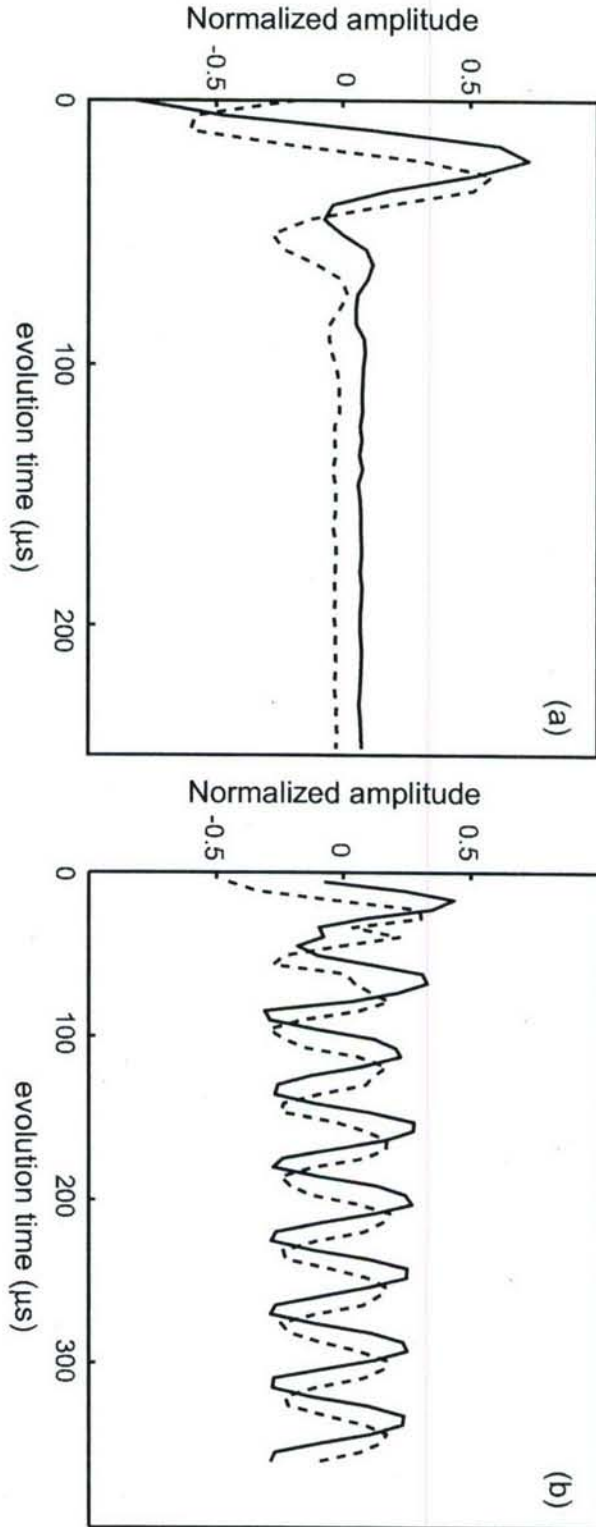


Figure 3-4: The solid line shows the $\sigma_x^1 + \sigma_x^2$ and the dashed line shows the $\sigma_z^1 \sigma_y^2 + \sigma_y^1 \sigma_z^2$ terms. (a) Under the dipolar Hamiltonian evolution, the above terms evolve into unobservable higher order spin correlations within 100 μs . (b) Under the modulation sequence, the terms oscillate 90 deg out-of-phase with each other for up to 360 μs without any significant attenuation in amplitude. In this case the RF amplitude $\omega_1 = 3\omega_D^S/4$.

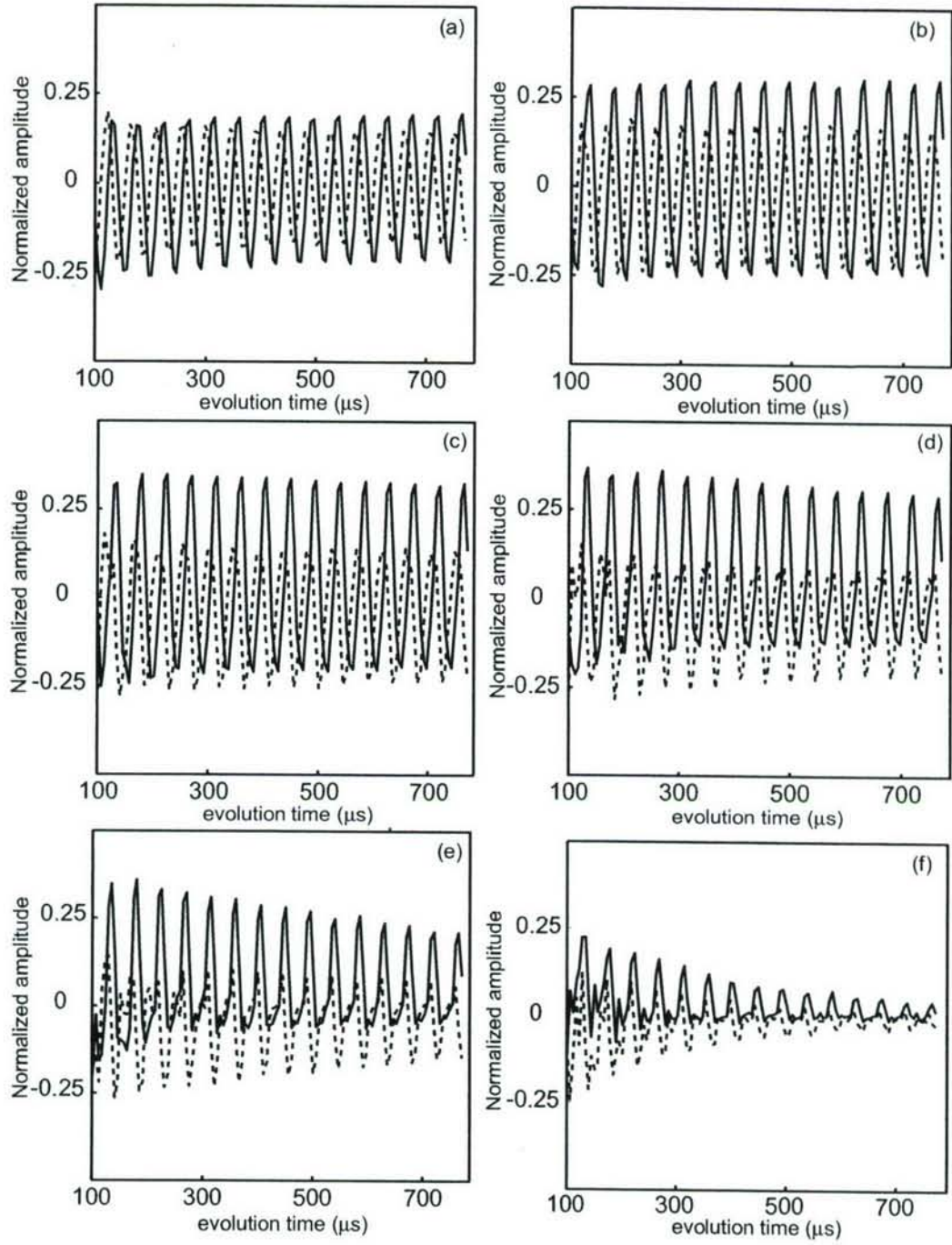


Figure 3-5: The solid line shows the $\sigma_x^1 + \sigma_x^2$ and the dashed line shows the $\sigma_z^1 \sigma_y^2 + \sigma_y^1 \sigma_z^2$ terms. Under the modulation sequence, the terms oscillate 90 deg out-of-phase with each other. The RF amplitude ω_1 is varied from $2\omega_D^S/4$ to $7\omega_D^S/4$ in steps of $\omega_D^S/4$. When the value of ω_1 is no longer in the optimum range, the amplitude of the signal is significantly attenuated.

CHAPTER 4

SENSITIVITY OF HIGHLY CORRELATED MULTIPLE-SPIN STATES TO THE PRESENCE OF RARE SPINS

4.1 Introduction

Solid-state spin-based NMR QIPs are a useful test-bed for the coherent control of modest Hilbert spaces. Using existing solid-state NMR techniques, one can study the dynamics and control of many-spin states. Here we explore our ability to control many spins in the presence of small number of spin defects. In the following subsection, we give a brief overview of the solid-state NMR techniques used to create and detect these many-spin states.

All the spins in a rigid spin lattice strongly interact with one another through their dipolar fields. In high magnetic fields and following a $\pi/2$ pulse, the evolution of the spin system is dominated by the secular dipolar Hamiltonian. This interaction creates highly correlated multiple-spin states causing the measured signal (Free Induction Decay - FID) to decay. The observable magnetization in NMR (as measured by the FID) comprises of the single-spin single quantum states. These single-spin single quantum states are transformed into unobservable multiple-spin single quantum states under the action of the dipolar Hamiltonian. By encoding the higher order

coherences of the multiple-spin states in a non-commuting basis of the secular dipolar Hamiltonian, Cho *et al.* [9] have studied the growth of these coherent multiple spin correlations during the FID. Solid-state NMR provides a ideal test-bed to investigate not only the growth of these large, correlated quantum states but also the dynamics and control of such states.

4.1.1 Creation and detection of highly correlated multiple-quantum states

In a strong magnetic field, $(B_0\hat{z})$, a N-spin $\frac{1}{2}$ system has 2^N stationary states. These states can be classified according to the magnetic quantum number M_z .

$$m = \sum_j m_{zj} = (N_{+\frac{1}{2}} - N_{-\frac{1}{2}})/2 \quad (4.1)$$

where m_{zj} is the eigenvalue of the j^{th} spin in the system. m_{zj} can take the values of either $\pm\frac{1}{2}$. $N_{+\frac{1}{2}}$ and $N_{-\frac{1}{2}}$ are the number of spins pointing up and down respectively. The energy eigenvalue corresponding to m is $E_z = -\gamma\hbar B_0 m$. In the case of non-degenerate states, there are on the order of 2^{2N-1} possible transitions between any two energy levels. The difference in the M_z values between the two levels is known as the coherence number.

When the state of the spin system is expressed in its eigenbasis as a density matrix, the presence of a non-zero matrix element $\langle z_i | \rho | z_j \rangle$ indicates the presence of a n -quantum coherence where $n = m(z_j) - m(z_i)$ (the difference between the magnetic quantum numbers of the two basis states z_i and z_j). This in turn indicates the presence of a superposition of the basis states z_i and z_j in the state of the spin system.

In theory, one can create multiple-quantum states by exciting the thermal equilibrium spin state $(\rho(0))$ using the double quantum (DQ) Hamiltonian given by:

$$H_{DQ}^{II} = \sum_{j < k} D_{jk}^{II} \{ \hat{I}_j^+ \hat{I}_k^+ + \hat{I}_j^- \hat{I}_k^- \} \quad (4.2)$$

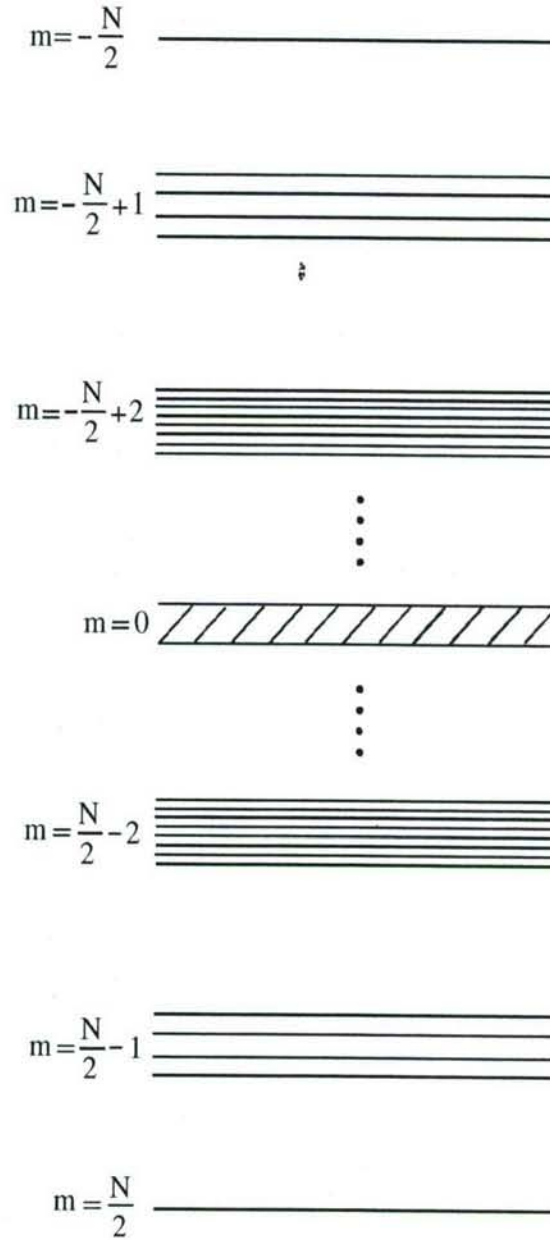


Figure 4-1: Energy level diagram of a N spin- $\frac{1}{2}$ system. The eigenvalue of \hat{I}_z can take any value from $\frac{N}{2}$ to $-\frac{N}{2}$. The number of levels for each allowed eigenvalue is $\binom{N}{m+\frac{N}{2}}$. Thus the number of allowed single-quantum transitions increase exponentially with N and are thus unresolvable in large spin-systems.

Though this particular form of spin interaction is not provided by nature, it can be engineered using standard multiple-pulse cycles based on coherent averaging techniques [58]. These multiple-pulse cycles implement an effective DQ Hamiltonian ($\overline{H_{DQ}^{II}}$) over the period of the pulse cycles.

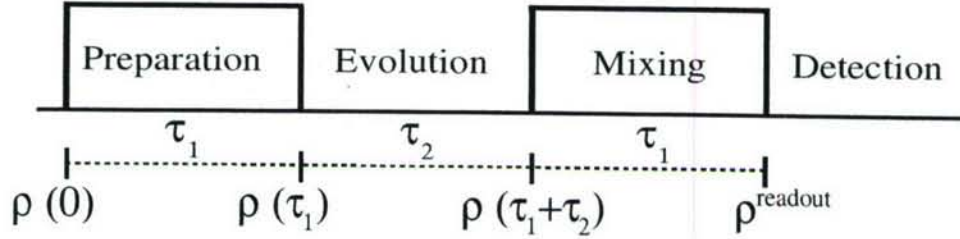


Figure 4-2: The basic form of a multiple-quantum NMR experiment [63] - (i) Preparation: Creating the highly correlated multiple-quantum states. (ii) Evolution: Evolving these states under any desired Hamiltonian. (iii) Mixing: Transforming the higher order coherences to observable single-spin single quantum coherences. (iv) Detection: Measuring the observable single-spin single quantum magnetization

A basic multiple-quantum NMR experiment is shown in Fig. 4-2. The DQ Hamiltonian is effective during τ_1 and creates highly correlated multiple-spin states in the preparation stage. These states give rise to a distribution of higher order coherences, which are encoded as phase factors (ϕ) using a collective rotation about the z-axis ($\sum_j \hat{I}_{jz}$).

$$\rho(\tau_1) = e^{-i\phi \sum_j \hat{I}_{jz}} e^{-i\overline{H_{DQ}^{II}} \tau_1} \rho(0) e^{i\overline{H_{DQ}^{II}} \tau_1} e^{i\phi \sum_j \hat{I}_{jz}} \quad (4.3)$$

In the evolution stage during τ_2 , we evolve the system under any desired Hamiltonian. By time-reversing the DQ Hamiltonian evolution in the mixing stage, higher order coherences are transformed to observable single-spin single quantum terms.

$$\rho^{readout} = e^{i\overline{H_{DQ}^{II}} \tau_1} \rho(\tau_1 + \tau_2) e^{-i\overline{H_{DQ}^{II}} \tau_1} \quad (4.4)$$

$$S(t) = Tr\left\{\left(\sum_j \hat{I}_j^+\right) \rho^{readout}\right\} \quad (4.5)$$

To extract the coherence order distribution in $\rho(\tau_1 + \tau_2)$, the signal ($S(t)$) observed in the detection stage is Fourier transformed with respect to ϕ .

Several pulse sequences have been developed to create and detect multiple-quantum coherences [59, 60, 61]. However, time-reversal schemes during preparation and detection are most widely used since they enhance the intensity of the multiple-quantum NMR experiments by refocusing the dipolar interaction [62, 63, 64].

While the advent of a n -quantum coherence in the coherence order distribution guarantees the creation of a n -spin state, it does not arise solely from such a spin state. Thus the distribution of the sizes of the highly correlated spin clusters for various excitation times under the DQ Hamiltonian is not known. However, as the excitation time period - τ_1 increases, higher order spin coherences emerge, indicating an increase in the effective size of these spin clusters. Even without precise knowledge of the size of the spin cluster, one can gain some insight on the many-spin dynamics by manipulating the existing multiple-quantum techniques. These techniques have been used extensively to study many body spin dynamics in dipolar coupled solids [65, 66, 67, 68]. It has also been used to probe spatial relationships between spins in large macromolecules, determine the size of spin clusters and in spin counting experiments [59, 60, 69, 70].

4.1.2 Decay of highly correlated multiple-spin states in CaF_2

The cubic lattice of 100% abundant ^{19}F spin-1/2 nuclei (denoted as I in the rest of this section) in a single crystal of CaF_2 have been used to study the decay of highly correlated multiple-spin states. Cho *et al.* report the effective T_2 under the dipolar Hamiltonian and under a time-suspension (C-48) sequence. See Figs. 4-3 and 4-4. The measurement was repeated for various periods of preparation under the grade-raising operator (DQ Hamiltonian). For a given coherence number, larger preparation

³The experimental data on CaF_2 has been extracted with permission from the doctoral thesis "Exploring large coherent spin systems with solid-state NMR", by H. Cho, submitted to the Department of NSE, MIT, February 2005.

periods incorporate more spins leading to larger clusters of correlated spins. We see in the figures that for both the dipolar evolution and the time-suspension sequence, as the number of spins in the cluster increase, the variation in T_2 with coherence number vanishes. Also, we note that the T_2 grows more slowly with spin number than simple theory predicts.

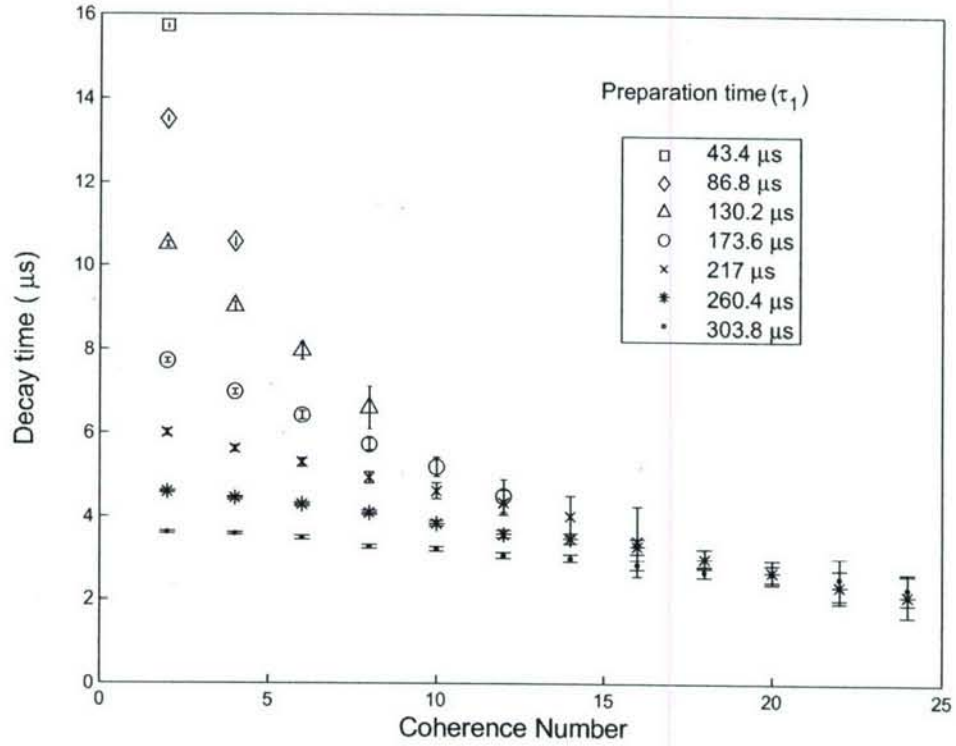


Figure 4-3: Effective decay times of various coherence orders due to the action of the secular dipolar Hamiltonian. Highly correlated spin- ^{19}F states in CaF_2 are created by exciting the thermal spin- ^{19}F state using the DQ Hamiltonian. The effective decay times of the coherences for the various excitation times (τ_1) are plotted.

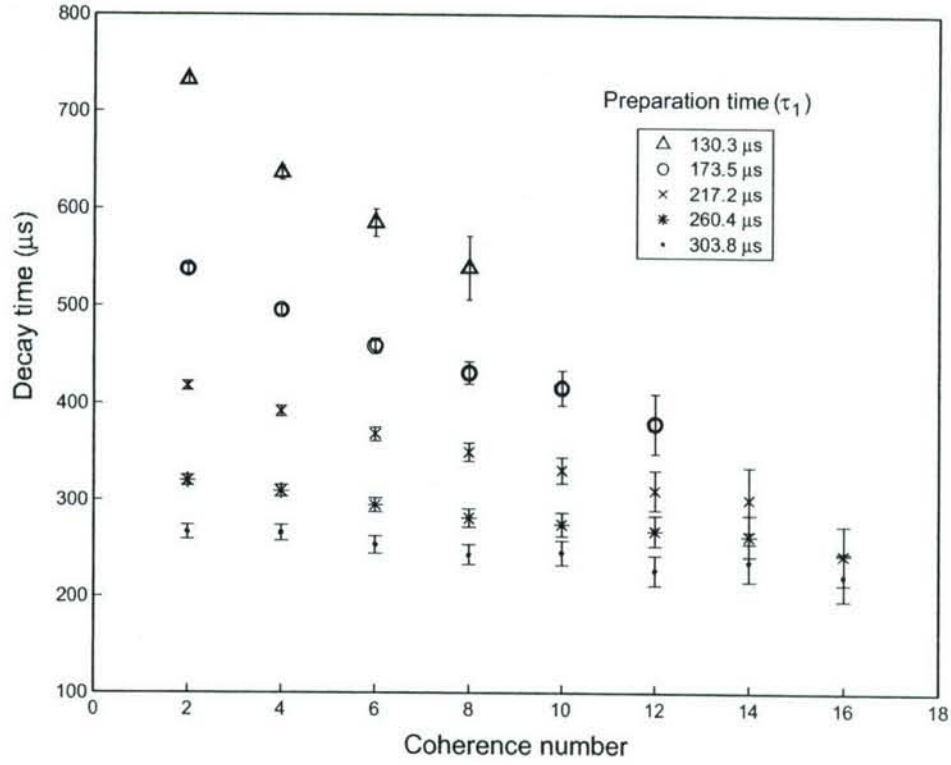


Figure 4-4: Effective decay times of various coherence orders of the the highly correlated spin- ^{19}F states in CaF_2 . In this case, the secular dipolar Hamiltonian is suppressed using a multiple-pulse C-48 sequence. The effective decay times of the coherences for the various excitation times (τ_1) under the DQ Hamiltonian are plotted.

4.1.3 Effect of rare spins on the decay of the multiple-spin states.

To understand this decay behavior, we take a closer look at the spin-system on which these experiments were carried out. In a CaF_2 single crystal, a spin-7/2 isotope of ^{43}Ca is present in low (0.13%) concentrations. Thus in addition to the homonuclear ^{19}F (H_D^{II}) dipolar spin interactions, the internal Hamiltonian of the spin system includes the heteronuclear ^{19}F - ^{43}Ca (H_D^{IS}) and the homonuclear ^{43}Ca (H_D^{SS}) dipolar spin interactions. Denoting this rare spin species as **S**, the initial equilibrium thermal

spin state and the on-resonance internal Hamiltonian are given by:

$$\begin{aligned}
\rho(0) &= \sum_j I_{jz} + \sum_k S_{kz} \\
H_{int} &= H_D^{II} + H_D^{SS} + H_D^{IS} \\
&= H_D^{II} + \sum_{j < k} D_{jk}^{SS} \{ \hat{S}_{jz} \hat{S}_{kz} - \frac{1}{4} (\hat{S}_j^+ \hat{S}_k^- + \hat{S}_j^- \hat{S}_k^+) \} + \sum_{j \in I, k \in S} D_{jk}^{IS} \hat{I}_{jz} \hat{S}_{kz}
\end{aligned} \tag{4.6}$$

The multiple-pulse sequence that creates the effective DQ interaction averages out the heteronuclear interaction (H_D^{IS}) to the 0^{th} order approximation. The efficiency with which the H_D^{SS} and H_D^{IS} interactions are suppressed during this excitation period (τ_1) affect the initial coherence order distribution of the created multiple-quantum spin-**I** states. However, the inefficiencies of the multiple-quantum creation process should not affect their subsequent decay which is the focus our discussion.

The C-48 sequence while averaging out the spin-**I** dipolar interaction, also averages out the heteronuclear interaction. Since $\overline{H_D^{IS}} \sim 0$, we would expect that the presence of **S** spins in the system will have no effect on the multiple-quantum spin-**I** states. If we could instantaneously ‘switch-off’ the dipolar coupling between the **I** and the **S** spins, our naive expectation would indeed hold true. However, this heteronuclear interaction is *not zero* at any given time point during the C-48 sequence. It *averages to zero* over the total cycle time of C-48 sequence. Thus we should not neglect the presence of **S** spins in the system.

To get a more intuitive understanding, we consider a model spin system comprising of a single **S** spin (labeled as **S**₁) and an abundant number of **I** spins with a internal Hamiltonian given by

$$H_{int} = H_D^{II} + H_D^{IS_1} = H_D^{II} + \sum_j D_{j1}^{IS_1} \hat{I}_{jz} \hat{S}_{1z} \tag{4.7}$$

Applying the DQ Hamiltonian on the equilibrium thermal spin state, we create our initial multiple-quantum spin-**I** states. The corresponding density matrix $\rho(\tau_1)$ is

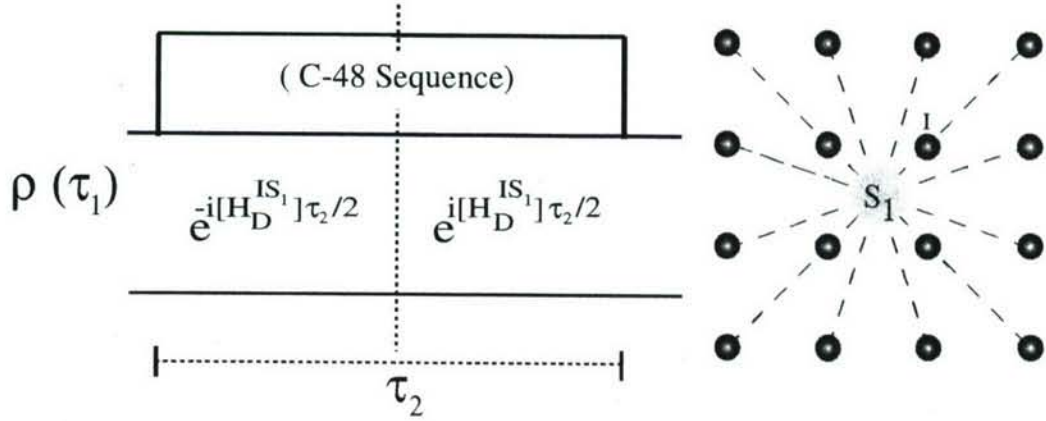


Figure 4-5: The model system (on the right), consists of one S spin (labeled as S_1) interacting with an abundant number of I spins. The C-48 sequence averages out the homonuclear interaction between the I spins during τ_2 . During this time interval (τ_2), S_1 is correlated with the multiple-quantum spin- I states present in $\rho(\tau_1)$. But if the S_1 spin state remains constant during τ_2 , the heteronuclear interaction is also averaged out under the action of the C-48 sequence. Thus S_1 is *no longer correlated* to the spin- I states at the end of τ_2 . However if S_1 flips at any point during this interval, it will *remain correlated* with the spin- I states even at the end of τ_2 .

allowed to evolve under the C-48 sequence over a time period τ_2 .

$$\rho^I(\tau_1) = \text{Tr}_{S_1}[e^{-i\overline{H}_{DQ}^I} \rho(0) e^{i\overline{H}_{DQ}^I} \tau_1] \quad (4.8)$$

$$\rho^I(\tau_1 + \tau_2) = \text{Tr}_{S_1}[U^{-IS_1}(\frac{\tau_2}{2})U^{IS_1}(\frac{\tau_2}{2})\rho(\tau_1)U^{\dagger IS_1}(\frac{\tau_2}{2})U^{\dagger -IS_1}(\frac{\tau_2}{2})] = \rho^I(\tau_1) \quad (4.9)$$

Since the C-48 sequence averages out the $H_D^{IS_1}$ interaction, the density matrix (obtained following a partial trace of the S_1 spin) $\rho^I(\tau_1 + \tau_2)$ undergoes zero net evolution over the period τ_2 (as shown in Eq. 4.9). Now if the S_1 spin flips in the middle of τ_2 , the density matrix (obtained after tracing out S_1) is no longer preserved.

$$\begin{aligned} \rho^I(\tau_1 + \tau_2) &= \text{Tr}_{S_1}[U^{-IS_1}(\frac{\tau_2}{2})U^{S_1}(\frac{\pi}{\omega})U^{IS_1}(\frac{\tau_2}{2})\rho(\tau_1)U^{\dagger IS_1}(\frac{\tau_2}{2})U^{\dagger S_1}(\frac{\pi}{\omega})U^{\dagger -IS_1}(\frac{\tau_2}{2})] \\ &\neq \rho^I(\tau_1) \end{aligned} \quad (4.10)$$

This holds true independent of when the spin flips during the course of the time

interval. See Fig. 4-5. In a solid-state spin system, energy conserving spin-flips can occur due to the flip-flop term of the homonuclear dipolar interaction.

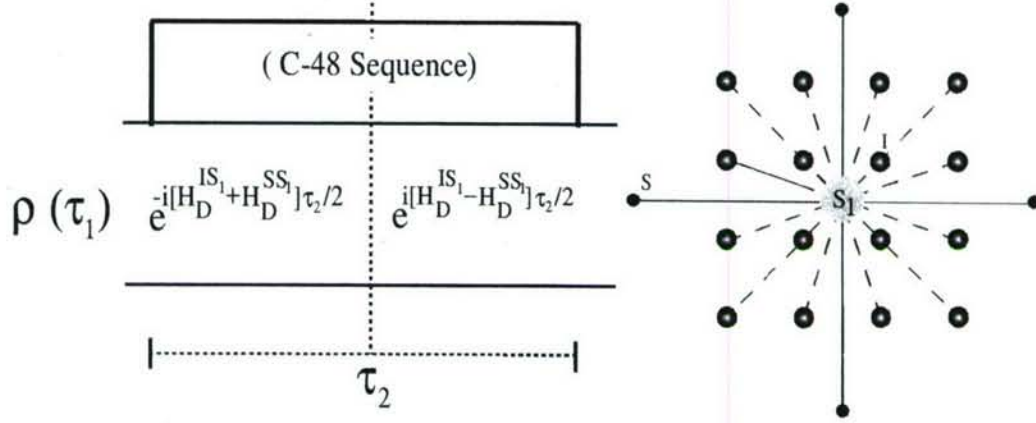


Figure 4-6: The model system (on the right), consists of one S spin (labeled as S_1) interacting with an abundant number of I spins and a few neighboring S spins. We assume that these S spins interact *only* with the S_1 spin. The homonuclear interaction between the I spins is averaged out during τ_2 using the C-48 sequence. The Hamiltonians $H_D^{IS_1}$ and $H_D^{SS_1}$ do not commute. Thus the multiple-quantum spin I states present in $\rho(\tau_1)$ evolve under their action during τ_2 .

To incorporate these spin-flip effects, we upgrade our model system to include a few neighboring S spins that interact with the S_1 spin. To simplify our arguments, we assume that these S spins do not interact with each other or with the I spins. These assumptions do not affect the conclusion we derive from the following arguments. The internal Hamiltonian of our model system is given by Eq. 4.11.

$$\begin{aligned}
 H_{int} &= H_D^{II} + H_D^{SS_1} + H_D^{IS_1} \\
 &= H_D^{II} + \sum_j D_{j1}^{SS_1} \{ \hat{S}_{jz} \hat{S}_{1z} - \frac{1}{4} (\hat{S}_j^+ \hat{S}_1^- + \hat{S}_j^- \hat{S}_1^+) \} + \sum_{j \in I} D_{j1}^{IS_1} \hat{I}_{jz} \hat{S}_{1z}
 \end{aligned} \tag{4.11}$$

Under the dipolar interaction $H_D^{SS_1}$, the total spin- S magnetization is conserved, not the state of the individual spin- S_1 . Therefore, the Hamiltonians $H_D^{SS_1}$ and $H_D^{IS_1}$ do not commute and the net evolution during the first half of τ_2 can no longer be

refocused during the second half. See Fig. 4-6.

$$\rho^I(\tau_1 + \tau_2) = \text{Tr}_{S_1}[U^{SS_1-IS_1}(\frac{\tau_2}{2})U^{SS_1+IS_1}(\frac{\tau_2}{2})\rho(\tau_1)U^{\dagger SS_1+IS_1}(\frac{\tau_2}{2})U^{\dagger SS_1-IS_1}(\frac{\tau_2}{2})] \neq \rho^I(\tau_1)$$

When the coherence order distribution of spin-**I** states is extracted from $\rho^I(\tau_1 + \tau_2)$, we will see a decay of the higher order coherences. Thus in this simple model, a single spin-**S** (**S**₁) interacting with neighboring **S** spins act as a spin defect for the highly correlated spin **I** states.

Going back to the coherence decay experiments under the secular dipolar Hamiltonian, neglecting arbitrary errors in experimental implementation, H_D^{II} and H_D^{IS} average to zero. However, the finite time period over which the heteronuclear decoupling takes place ensures that energy-conserving spin flips between neighboring **S** spins will lead to multiple-quantum spin-**I** transitions which are not refocused during the time-reversal of the DQ Hamiltonian - thus leading to a coherence order decay. Therefore, we need to refocus the homonuclear interaction (H_D^{SS}) since it facilitates these energy-conserving spin flips via the flip-flop component of its Hamiltonian. Moreover, the H_D^{IS} interaction needs to be averaged out on a time-scale which is fast with respect to the spin-**S** homonuclear dipolar coupling strength.

The C-48 sequence applied on the ¹⁹F spins suppresses only the homonuclear ¹⁹F interactions and the heteronuclear ¹⁹F-⁴³Ca interactions. Thus the ⁴³Ca spins act as centers of decoherence for the highly correlated multiple-spin states of the abundant ¹⁹F spins. We need to design new control sequences that address these rare spin homonuclear interactions and thus refocus the full internal Hamiltonian of the spin system. The decay rates of the highly correlated abundant spin states measured under this complete refocusing scenario will provide a more accurate measure of control of such states.

4.1.4 Sensitivity the of highly correlated multiple-spin states to the presence of rare spins

Quantifying the effect of these rare spins on the spin system dynamics is quite challenging - techniques that involve direct observation of these rare spins are experimentally unviable due to low S/N ratios. ‘Spy detection’ techniques [72] allows us to circumvent this problem by letting us take advantage of the higher bulk sensitivity (due to higher concentration) of the abundant spins in the system. This technique utilizes a particular spin species as a probe to monitor the behavior of a neighboring spin species. Spy techniques have been used to study spin diffusion in a single crystal of ferrocene. Ernst *et al.* proposed an indirect measurement of diffusion among the abundant spins (1H) using the rare spins (^{13}C) as a probe.

For our sensitivity measurements, we excite the abundant spins in the system using the DQ Hamiltonian. This creates highly correlated multiple-spin states while preserving thermal \hat{z} magnetization of the rare spins. We then isolate the effect of the rare spins on the dynamics of these abundant spin clusters. This involves designing a control sequence that selectively turns on the dipolar interaction between the rare spins and clusters of the abundant spins. Since all the spins (both abundant and rare) interact at all times through their dipolar couplings and chemical shifts, we must simultaneously suspend all the homonuclear spin interactions. To quantify a change in response, we also need a reference experiment against which we can measure this change. We design another control sequence, which in addition to suspending all the above interactions, turns off the interactions between the abundant spin clusters and the rare spins. We measure the relative intensities of the multiple quantum coherence of the abundant spins in both cases. Comparison of the intensities allow us to quantify the sensitivity of the abundant spin clusters to the rare spin defects. In the rest of this chapter, we refer to these two multiple-pulse control sequences as the heteronuclear recoupling (HR-96) sequence and the time-suspension (TS-96) sequence respectively. In the next section, we give a brief overview of average hamiltonian theory which was used to design these control sequences.

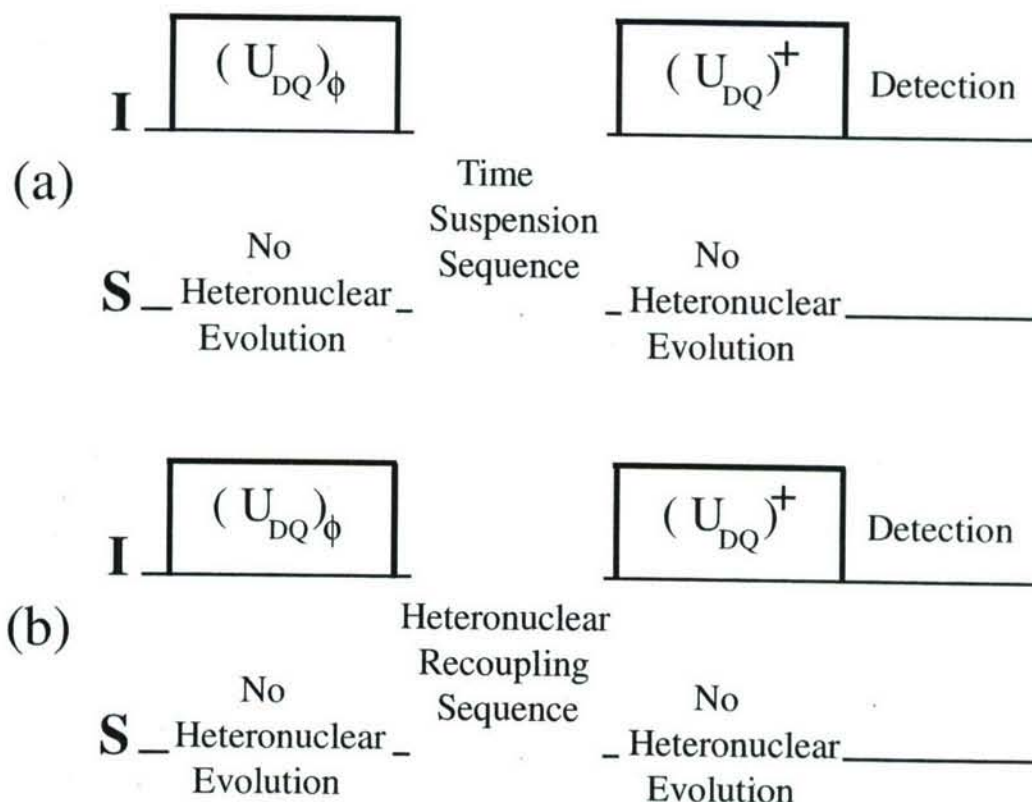


Figure 4-7: Sketch of the experiments designed to detect rare spins (**S**) using the highly correlated multiple-spin states of the abundant spins (**I**) as a 'probe'. It involves contrasting the effect of the two control sequences (in (a) and (b)) on the intensity of the multiple quantum coherence of these correlated spin **I** states.

4.2 Overview of average Hamiltonian theory

The concept of average hamiltonian theory has been used to design a wide range of pulse experiments. If a spin system is evolved under a periodic and cyclic sequence of RF pulses and delays (i.e., free evolution under the internal Hamiltonian), at periodic observation points it acts as if it was exposed to a time-independent average internal Hamiltonian. The time period between successive observations must however be much smaller then the spin lattice relaxation times. In between these observation times, the spin system passes through a complex array of states depending on the applied RF pulses. The average Hamiltonian defines the state of the system at successive

observation times also known as the cycle time (t_c) of the sequence. One of the important features of this theory is that it provides a simplified means of designing pulse sequences in solid state spin systems where calculations using density matrices are not possible.

If the sequence of RF pulses is cyclic ($U_{rf}(t_c) = \pm 1$), periodic ($H_{rf}(t) = H_{rf}(t + Nt_c)$), the average Hamiltonian \overline{H} is given by the Magnus expansion (written as Eq. 4.12). The 0^{th} order average Hamiltonian is given by Eq. 4.13 and the 1^{st} order average is given by Eq. 4.14.

$$\overline{H} = \overline{H^0} + \overline{H^1} + \overline{H^2} + \overline{H^3} + \dots \quad (4.12)$$

$$\overline{H^0} = \frac{1}{t_c} \int_0^{t_c} \tilde{H}_{int}(t) dt \quad (4.13)$$

$$\overline{H^1} = \frac{-i}{t_c} \int_{t_1}^{t_2} [\tilde{H}_{int}(t_1), \tilde{H}_{int}(t_2)] dt_1 dt_2 \quad (4.14)$$

where $\tilde{H}_{int}(t)$, also known as the toggling frame internal Hamiltonian, is given by

$$\tilde{H}_{int}(t) = U_{RF}^{-1} H_{int} U_{RF} \quad (4.15)$$

U_{RF} which is the unitary RF operator determined by the applied pulse sequence, is given by the Dyson time-ordering functional as expressed in Eq. 4.16. Each term U_i refers to the propagator corresponding to the i^{th} RF pulse of the pulse sequence.

$$U_{RF} = T e^{-i \int_0^{t_c} \tilde{H}_{RF}(t) dt} = \dots U_4 U_3 U_2 U_1 \quad (4.16)$$

Since the RF field is of finite strength, the evolution of the internal Hamiltonian during the duration of the pulse should be taken into account. The convergence of the series has been discussed by Maricq [73]. If the cycle time of the pulse sequence is short compared to the T_2 characterizing the homogenous broadening due to the interaction being averaged, the RF fields applied during experiments are strong enough that

calculation of the first two terms of the Magnus expansion (as given by Eqs. 4.13 and 4.14) provide a good approximation of the average Hamiltonian \overline{H} . Furthermore, designing the RF cycle to be symmetric gives the added advantage that all the odd order terms identically go to zero [74, 75]. This appealing property has been used repeatedly to design line narrowing sequences.

4.3 The C-48 time-suspension sequence

Time-suspension sequences have been widely used in NMR for purposes of imaging in solid-state samples [76, 77, 78]. Designing multiple-pulse cycles, that improve the line-narrowing efficiency by compensating for pulse errors while averaging out the dipolar spin interactions, has been the goal of NMR physicists since coherent averaging techniques were proposed [58, 75]. Other uses of time suspension sequences include the study of spin diffusion and molecular motion through relaxation experiments [79, 80].

Table 4.1: The average Hamiltonian for various time-suspension sequences

Average Hamiltonian terms	Second-averaged MREV-8	16 pulse cycle	24 pulse cycle
\overline{H}_D^0	0	0	0
\overline{H}_D^1	0	0	0
\overline{H}_D^2	$\neq 0$	$\neq 0$	0
\overline{H}_{DO}^1	0	0	$\neq 0$
\overline{H}_O^0	0	0	0

If a homonuclear spin system is off-resonance, the internal Hamiltonian can be written as $H_{int} = H_O + H_D$, where H_O and H_D are given by Eq. 4.17

$$\begin{aligned}
H_O &= \hbar \Delta \omega^I \sum_j I_{jz} \\
H_D &= \sum_{j < k} D_{jk}^{II} \{ \hat{I}_{jz} \hat{I}_{kz} - \frac{1}{4} (\hat{I}_j^+ \hat{I}_k^- + \hat{I}_j^- \hat{I}_k^+) \}
\end{aligned} \tag{4.17}$$

The WAHUA sequence, the second-averaged MREV-8 and other 16 and 24 pulse supercycles based on the MREV-8 sequence, average out some or all of these homo nuclear spin interactions with varying degrees of efficiency [81, 82]. The average internal Hamiltonians under these time-suspension sequences are listed in Table 4.1. By focussing on the state of the offset Hamiltonian in the toggling frame, Burum and Rhim used a simple notation to describe multiple-pulse cycles. For e.g., the toggling frame offset Hamiltonian during a solid-echo pulse pair cycle: $\tau - (\pi/2)_x - \tau - (\pi/2)_y - \tau$ can be written as $(I_z, -I_y, -I_x)$. Denoting the three orthogonal directions in the spin space as **a**, **b** and **c**, this solid-echo pulse sequence can be rewritten as (\overline{abc}) . Using this notation, the three time-suspension sequences can be written as follows:

- Second averaged MREV-8: $(\overline{abc})(\overline{cba})_p(\overline{abc})(\overline{cba})_p$.
- The 16-pulse cycle: $(\overline{abc})(\overline{cba})_p(\overline{abc})(\overline{cba})_p(\overline{abc})(\overline{cba})_p(\overline{abc})(\overline{cba})_p$
- The 24-pulse cycle: $(\overline{abc})(\overline{cba})_p(\overline{abc})(\overline{cba})_p(\overline{abc})(\overline{cba})_p(\overline{abc})(\overline{cba})_p(\overline{abc})(\overline{cba})_p(\overline{abc})(\overline{cba})_p$

where the sub-script p indicates that the RF pulse pair are phase toggled.

In [83], Cory *et al.* proposed a sequence that averaged the dipolar Hamiltonian and the dipolar-offset cross term to zero up to the 1st order. The C-48 sequence is made up of three-pulse sequences $-A, a, B, b, C, c, \dots H, h$. See Figs. 4-8 and 4-9. Various permutations and combinations of two of these three-pulse sequences lead to the formation of dipolar-decoupled π pulse cycles, e.g., $(Aa), (Bb), (Cc), (Dd), (Ee) \dots$ Eight of these dipolar-decoupled π pulse cycles are combined to form a ‘super cycle’ that averages out to zero all the terms in Table 4.1. The complete C-48 sequence can be written as: $(Aa)(Bb)(Cc)(Dd)(Ee)(Ff)(Gg)(Hh)$.

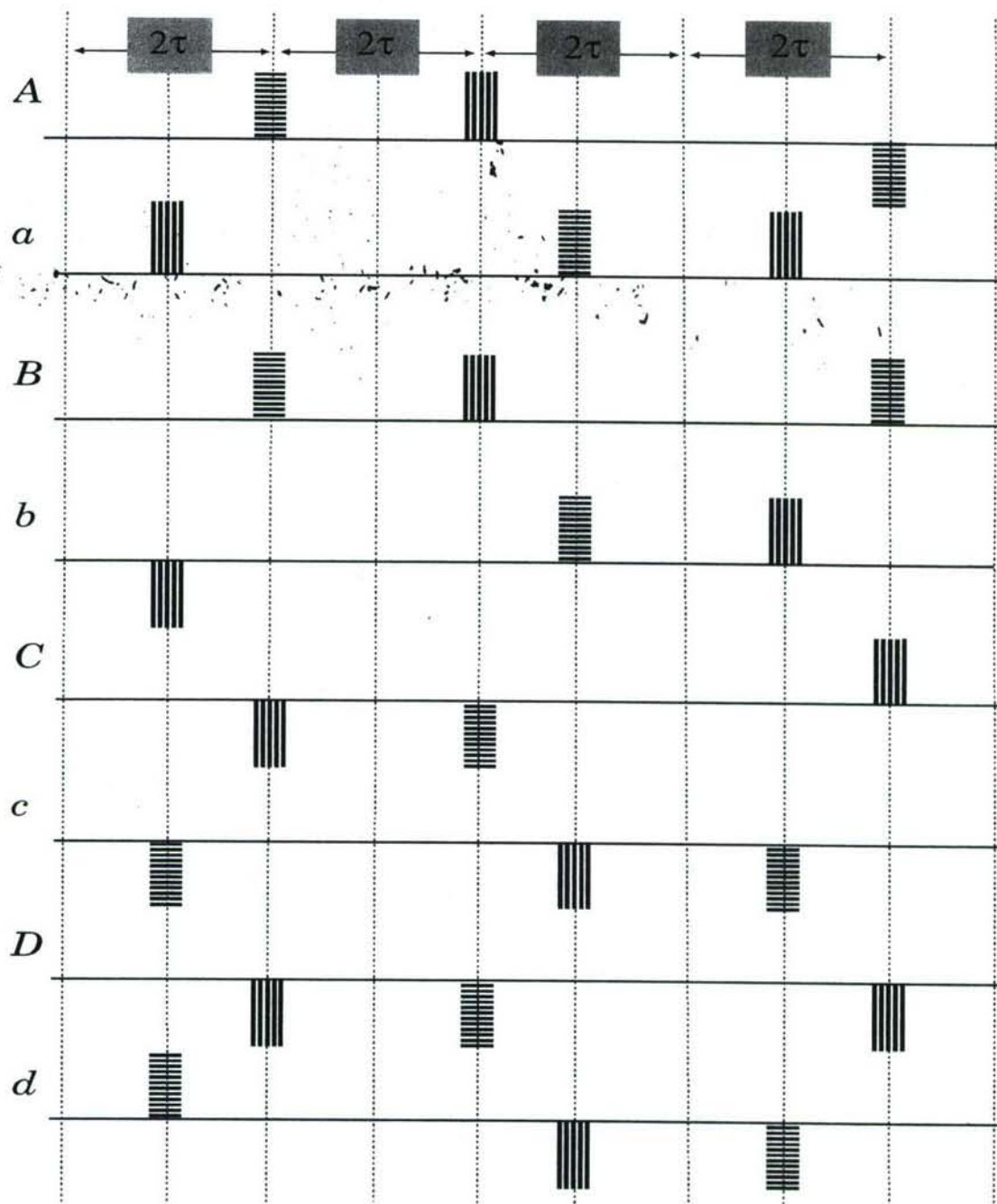


Figure 4-8: The schematic diagram of the three-pulse sequences used to design the C-48 sequence, where the horizontal striping indicates an y-pulse, vertical striping an x-pulse. All the pulses induce rotations by $\pi/2$. (or the negatives thereof if the pulses are below the bold reference lines)

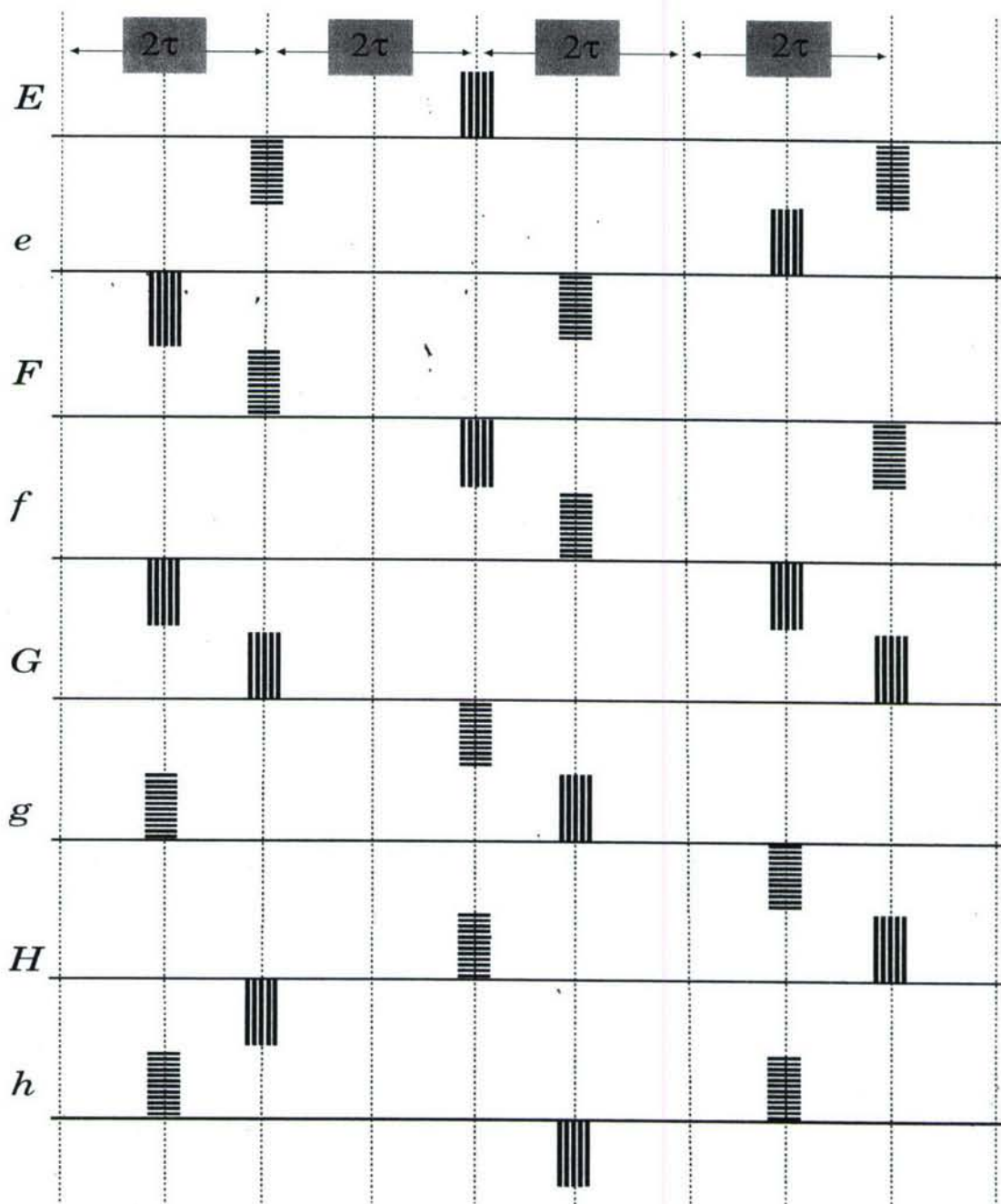


Figure 4-9: The schematic diagram of the three-pulse sequences used to design the C-48 sequence, where the horizontal striping indicates an y -pulse, vertical striping an x -pulse. All the pulses induce rotations by $\pi/2$. (or the negatives thereof if the pulses are below the bold reference lines)

4.4 The design criteria for the new time-suspension and heteronuclear recoupling sequences

In a heteronuclear spin system, the internal Hamiltonian is modified to include both the homonuclear as well as the heteronuclear spin interactions.

$$\begin{aligned}
 H_O &= \hbar\Delta\omega^I \sum_j I_{jz} + \hbar\Delta\omega^S \sum_k S_{kz} \\
 H_{int} &= H_D^{II} + H_D^{SS} + H_D^{IS} \\
 &= \sum_{j < k} D_{jk}^{II} \{ \hat{I}_{jz} \hat{I}_{kz} - \frac{1}{4} (\hat{I}_j^+ \hat{I}_k^- + \hat{I}_j^- \hat{I}_k^+) \} + \sum_{j < k} D_{jk}^{SS} \{ \hat{S}_{jz} \hat{S}_{kz} - \frac{1}{4} (\hat{S}_j^+ \hat{S}_k^- + \hat{S}_j^- \hat{S}_k^+) \} \\
 &\quad + \sum_{j \in I, k \in S} D_{jk}^{IS} \{ \hat{I}_{jz} \hat{S}_{kz} \}
 \end{aligned} \tag{4.18}$$

D_{jk}^{IS} is the heteronuclear dipolar coupling constant between the j^{th} spin-I and the k^{th} spin-S. The homonuclear dipolar constants for the j^{th} and k^{th} spins of spin-I (or spin-S) is defined by D_{jk}^{II} (or D_{jk}^{SS} respectively). In general, the dipolar constant can be defined as

$$D_{jk}^{\alpha\beta} = \frac{\gamma_\alpha \gamma_\beta \hbar^2}{r_{jk}^3} (1 - 3\cos^2\theta_{jk}) \tag{4.19}$$

where γ_α and γ_β are the gyromagnetic ratios, \vec{r}_{jk} is the distance between j^{th} spin- α and k^{th} spin- β , and θ_{jk} is the angle between the external magnetic field and the internuclear vector \vec{r}_{jk} .

In designing the new time-suspension sequence, the objective was to average out all the homonuclear and heteronuclear interactions as expressed in Eq. 4.18. Note that if the C-48 sequence is applied to one of nuclear spin species, for e.g. spin-I, the S spins will evolve under the spin-S offset and dipolar terms (the 2nd term of H_O and H_D respectively in Eq. 4.18). However, since the spin-I offset term goes to zero to the 0th order, the heteronuclear dipolar interaction between the I and S spins (i.e., the 3rd term of H_D in Eq. 4.18) also goes to zero. Applying the C-48 sequence to

both **I** and **S** spins will average out all the homonuclear interactions. However, it will lead to a resultant heteronuclear strong coupling (**I.S**) interaction.

The dipolar spin interactions have varying strengths. We assume that for our model system, the average strength of the dipolar spin interactions (in descending order) can be written as: $D^{II} \gg D^{IS} \gg D^{SS}$. Note that for many typical solid-state samples, these are the correct assumptions. Since the spin-**I** average homonuclear dipolar interaction is the strongest, it needs to be averaged out faster than the other interactions. Using the three-pulse sequences – A, a, B, \dots, h (shown in Figs. 4-8 and 4-9) as building blocks, we construct two 96-pulse sequences for the **S** spins. The multiple-pulse cycles of the TS-96 and HR-96 sequences average out the spin-**S** dipolar and offset interactions. At the same time, the multiple-pulse cycle of the HR-96 sequence selectively reintroduces the heteronuclear dipolar interaction. To average out the spin-**I** dipolar and offset interactions, we apply two back-to-back C-48 sequences to the **I** spins. Both pulse sequences consist of 16 six-pulse sub-cycles. Each six-pulse sub-cycle averages the homonuclear dipolar Hamiltonian (for both **I** and **S** spins) to zero. The details of the composition are written in Table 4.2. In the case of the TS-96 sequence, the complete averaging out of all interactions require 16 sub-cycles (96 pulses). The RF sequence applied during sub-cycles 9:16 is the same as that applied during sub-cycles 1:8 *except* that all 48 pulses in the first eight sub-cycles are phase shifted by π . For e.g. in Table 4.2, \bar{a} denotes a pulse-sequence in which the three applied RF pulses of the pulse-sequence a are phase shifted by π . In the case of the HR-96 sequence, all undesired interactions are averaged out at the end of sub-cycle number 8 i.e., after every 48 pulses. Thus in sub-cycles 9:16, the sequence applied in sub-cycle 1:8 is repeated. This was done to ensure that both sequences had the same cycle time.

Table 4.2: Composition of the sub-cycles of the TS-96 and HR-96 sequences

Sub-cycles numbers n	TS-96		HR-96	
	I	S	I	S
1	<i>Aa</i>	<i>aE</i>	<i>Aa</i>	<i>bE</i>
2	<i>Bb</i>	<i>fB</i>	<i>Bb</i>	<i>fA</i>
3	<i>Cc</i>	<i>dG</i>	<i>Cc</i>	<i>dG</i>
4	<i>Dd</i>	<i>hD</i>	<i>Dd</i>	<i>hC</i>
5	<i>Ee</i>	<i>bF</i>	<i>Ee</i>	<i>aF</i>
6	<i>Ff</i>	<i>eA</i>	<i>Ff</i>	<i>eB</i>
7	<i>Gg</i>	<i>cH</i>	<i>Gg</i>	<i>cH</i>
8	<i>Hh</i>	<i>gC</i>	<i>Hh</i>	<i>gD</i>
9	<i>Aa</i>	\overline{aE}	<i>Aa</i>	<i>bE</i>
10	<i>Bb</i>	\overline{fB}	<i>Bb</i>	<i>fA</i>
11	<i>Cc</i>	\overline{dG}	<i>Cc</i>	<i>dG</i>
12	<i>Dd</i>	\overline{hD}	<i>Dd</i>	<i>hC</i>
13	<i>Ee</i>	\overline{bF}	<i>Ee</i>	<i>aF</i>
14	<i>Ff</i>	\overline{eA}	<i>Ff</i>	<i>eB</i>
15	<i>Gg</i>	\overline{cH}	<i>Gg</i>	<i>cH</i>
16	<i>Hh</i>	\overline{gC}	<i>Hh</i>	<i>gD</i>

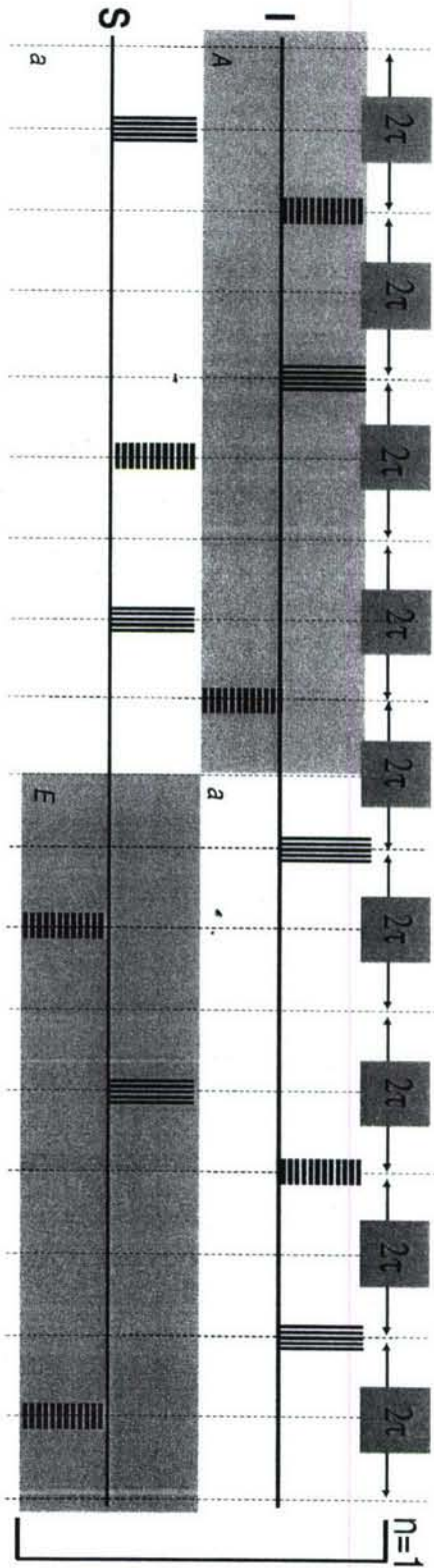


Figure 4-10: (a) The first sub-cycle ($n=1$) of the time-suspension (TS-96) sequence: **I**-(**Aa**), **S**-(**aE**). The sequence is made up of 16 such sub-cycles. The horizontal striping indicates an y-pulse, vertical striping an x-pulse. All the pulses induce rotations by $\pi/2$. (or the negatives thereof if the pulses are below the bold reference lines).

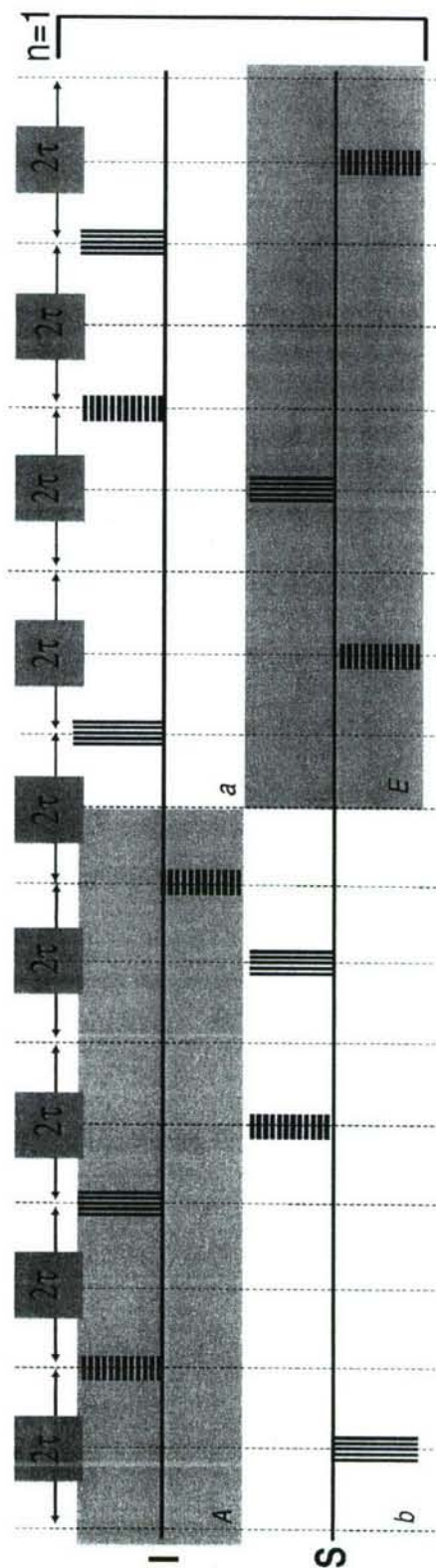


Figure 4-11: (a) The first sub-cycle ($n=1$) of the heteronuclear recoupling (HR-96) sequence: **I**-(**Aa**), **S**-(**bE**). The sequence is made up of 16 such sub-cycles. The horizontal striping indicates an x-pulse, vertical striping an x-pulse. All the pulses induce rotations by $\pi/2$. (or the negatives thereof if the pulses are below the bold reference lines).

4.5 The properties of the TS-96 and the HR-96 sequences

The average Hamiltonian properties of TS-96 and HR-96 are listed in Table 4.3. The HR-96 sequence scales down the heteronuclear interaction by a factor of $\frac{2}{9}$. For detailed calculation of the average Hamiltonian terms, please refer to the Appendix. As mentioned before, average Hamiltonian theory allows one to follow the complex

Table 4.3: The average Hamiltonian properties of the TS-96 and the HR-96 sequence taking into account finite pulse width effects

Terms of Average Hamiltonian	TS-96	HR-96
$\overline{H}_D^1(\text{between I spins})$	0	0
$\overline{H}_D^1(\text{between S spins})$	0	0
$\overline{H}_D^1(\text{between I and S spins})$	0	$\frac{2}{9}$
$\overline{H}_O^0(\text{for I spins})$	0	0
$\overline{H}_O^0(\text{for S spins})$	0	0

path that the spin system takes when multiple pulse sequences are applied. In other words, one can calculate the rate at which the various product operators that span the interaction space average out over the whole duration of the sequence. This is especially useful considering that some of the interactions are much stronger than the others. Ideally, one would like to average out all the interactions as quickly as possible. However, considering the complexity of the problem, our approach has been to preferentially average out all the stronger interactions faster than the weaker ones. In Table 4.4 we show the rate at which the various interactions average to zero without taking into account the finite strength of the applied RF pulses. In Table 4.5 we show the same taking into account these finite pulse width effects. Note that all undesired interactions average out within 8 sub-cycles for both sequences in the 0th order approximation. However for the TS-96 sequence, we require 16 sub-cycles to average out some of the undesired interactions to the 1st order approximation.

Table 4.4: Sub-cycles at which the various interactions average to zero for the TS-96 and the HR-96 sequences *without* taking into account finite pulse width effects

Terms of the Average Hamiltonian	Number of sub-cycles	
	TS-96	HR-96
$\overline{H}_D^0(\text{between I spins})$	1	1
$\overline{H}_D^0(\text{between S spins})$	1	1
$\overline{H}_D^0(\text{between I and S spins})$	8	—
$\overline{H}_O^0(\text{for I spins})$	8	8
$\overline{H}_O^0(\text{for S spins})$	8	8

Table 4.5: Sub-cycles at which the various interactions average to zero for the TS-96 and the HR-96 sequences taking into account finite pulse width effects

Terms of the Average Hamiltonian	Sub-cycle number of the TS-96	Sub-cycle number of the HR-96
$\overline{H}_D^0(\text{between I spins})$	1	1
$\overline{H}_D^0(\text{between S spins})$	8	2
$\overline{H}_D^0(\text{between I and S spins})$	8	—
$\overline{H}_D^1(\text{between I spins})$	2	2
$\overline{H}_D^1(\text{between S spins})$	16	4
$\overline{H}_D^1(\text{between I and S spins})$	16	—
$\overline{H}_O^0(\text{for I spins})$	8	8
$\overline{H}_O^0(\text{for S spins})$	8	8

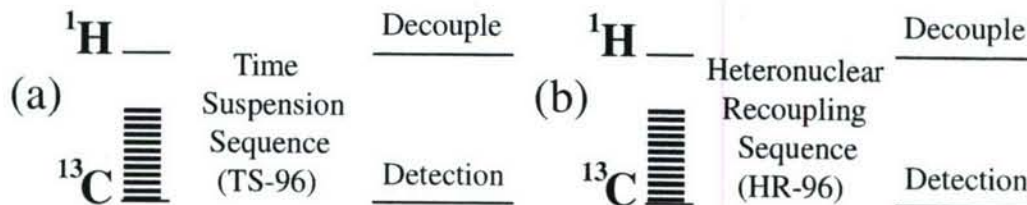


Figure 4-12: The schematic of the experiment that measures the effective T_2 of the ^{13}C in adamantane under (a) TS-96 sequence and (b) HR-96 sequence. Before applying the two sequences, we use a $\pi/2$ pulse to flip the ^{13}C spins on to the transverse plane. The ^{13}C magnetization is measured while decoupling the ^1H spins.

4.6 Experimental Results

Adamantane ($\text{C}_{10}\text{H}_{16}$) was taken as a prototypical system with an ensemble of abundant (^1H spins) and rare spins (the natural abundance ^{13}C spins). Adamantane undergoes rapid molecular reorientation above 160K [84]. This rapid isotropic molecular rotation averages all the intramolecular magnetic interactions to zero [84, 85]. The largest interaction in the spin system is the intermolecular homonuclear ^1H dipolar coupling which leads to a static proton line-width of 13,800 Hz (full-width at half maximum). The average ^{13}C dipolar coupling strength is approximately 50Hz [86] while the ^{13}C - ^1H hetero nuclear coupling was measured to be 500Hz [87]. The T_1 relaxation times for ^1H and ^{13}C spins are approximately 0.5 s and 30s respectively. The experiments were carried out at room temperature at 9.4 T (^1H 400 MHz) using a Bruker Avance spectrometer on a 5 mm³ powdered sample of adamantane.

4.6.1 Effective T_2 relaxation times of ^{13}C spins under the TS-96 and the HR-96 sequences.

First we tested the efficiency of the the TS-96 and the HR-96 control sequences. We used their line narrowing capabilities as measure of their efficiency. As shown in section 1.4, the TS-96 sequence suspends all spin interactions. Thus the line narrowing efficiency of this sequence should be much superior than other time suspension sequences like the C-48 sequence. To compare the line-narrowing efficiencies of the

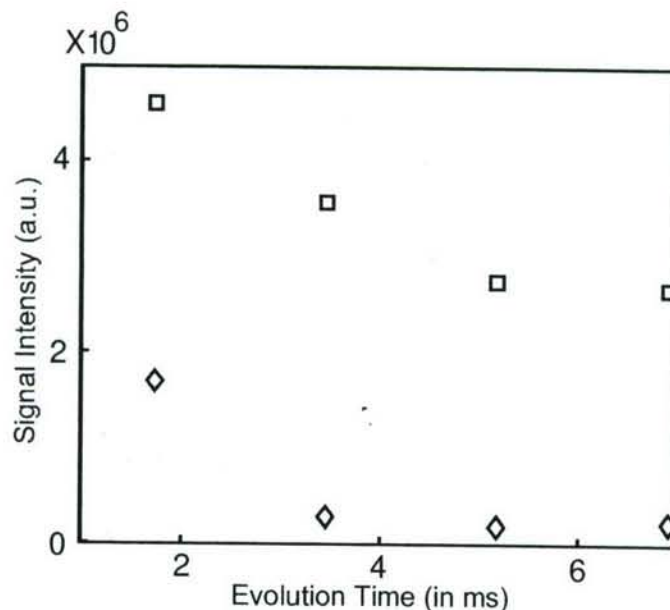


Figure 4-13: The ^{13}C signal intensity plotted after every 96- pulse cycle of the the TS-96 (\square) and the HR-96 (\diamond) sequences. The cycle time period of $1728\ \mu\text{s}$.

different sequences, we measure the effective T_2 of ^{13}C spins for each sequence.

As shown by the schematic in Fig. 4-12, we run a set of 2-D experiments which measures the ^{13}C magnetization after every 6 pulse sub-cycle of the 96 pulse sequence. To simulate a stroboscopic measurement, the amplitude of the 5th point of the free induction decay (FID) for each experiment is plotted. See Fig. 4-14. The $\pi/2$ pulse length for ^{13}C was $3.8\ \mu\text{s}$. The optimized ^1H $\pi/2$ pulse length was $4.8\ \mu\text{s}$. The spacing between two consecutive pulses was set at $6\ \mu\text{s}$ for both sequences leading to a 6 pulse sub-cycle time of $108\ \mu\text{s}$. The effective T_2 in the case of the TS-96 sequence and the HR-96 sequence were measured to be $4.02\ \text{ms}$ and $974\ \mu\text{s}$ respectively. Note that in the case of the TS-96 sequence, the signal intensity does not go to zero at longer evolution times due to a spin-locking effect. Thus the calculated linewidths in the two cases are $75\ \text{Hz}$ and $300\ \text{Hz}$ respectively. We also carried out a ^{13}C observe experiment with ^1H decoupling using the C-48 sequence (similar to the experiments outlined in Fig. 4-12). The effective T_2 was measured to be of the order of $1\ \text{ms}$. These results prove that for heteronuclear spin systems, the TS-96 sequence has more efficient line-narrowing capabilities as compared to the C-48 sequence.

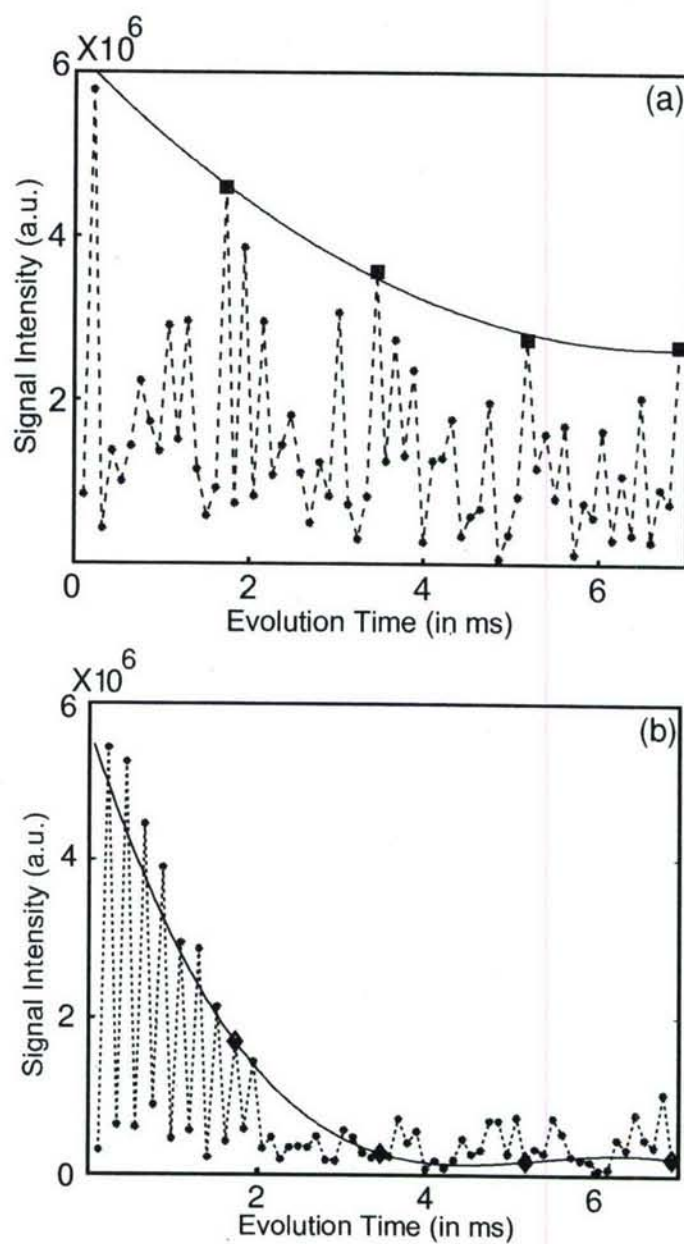


Figure 4-14: The ^{13}C signal intensity plotted after every 6 pulse sub-cycle of the (a) TS-96 and (b) HR-96 sequences. The sampling rate in both cases is $108 \mu\text{s}$. The points marked by \square in (a) and \diamond in (b) indicate the signal intensity after the full 96-pulse sequence. The system was evolved up to 4 cycles of the 96-pulse sequences with a cycle time period of $1728 \mu\text{s}$.

4.6.2 Sensitivity of ^1H multiple quantum coherence to the presence of ^{13}C spins

We create the ^1H multiple quantum coherence in adamantane by evolving the initial zeeman state ^1H spins under an average double quantum (DQ) Hamiltonian - $\overline{H_{DQ}^{II}}$. A collective rotation by ϕ about the z-axis is applied to this evolved state where ϕ is uniformly sampled out to a multiple of 2π . The resulting data is Fourier transformed with respect to ϕ to obtain the coherence number distribution. The evolution under $\overline{H_{DQ}^{II}}$ creates even order coherences in the z-basis. A 16-pulse DQ selective sequence – comprising of two cycles of 8 pulse sequences that compensate for pulse imperfections and resonance offsets, was used (See Fig. 4-15). To carry out the phase encoding, all the pulses in the 16 pulse experiment were phase-shifted by ϕ [10].

In Fig. 4-16, the maximum coherence encoded was ± 64 with $\Delta\phi=2\pi/128$. The phase incrementation was carried out to 4π . The ^{13}C $\pi/2$ pulse length was $3.8\ \mu\text{s}$. The optimized ^1H $\pi/2$ pulse length for the DQ selective sequence was $4.3\ \mu\text{s}$. The smallest delay between the pulses, Δ , was set to $2\ \mu\text{s}$, resulting in a cycle time of $151.2\ \mu\text{s}$.

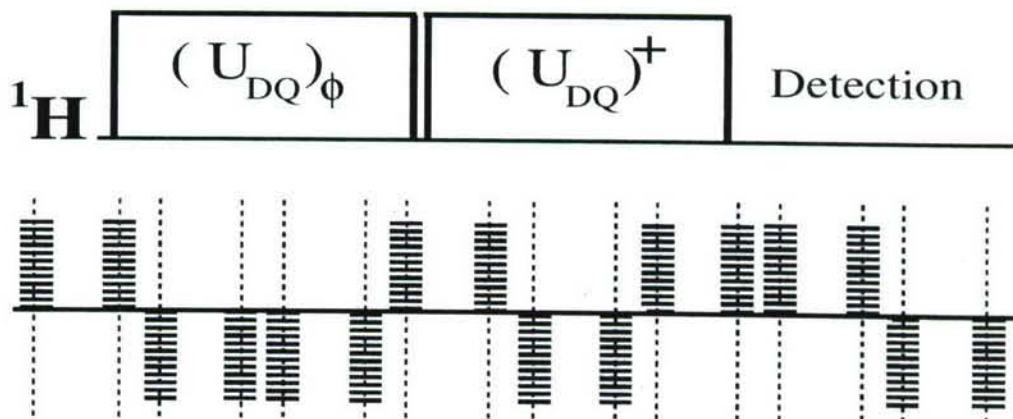


Figure 4-15: The schematic of the experiment that creates ^1H multiple quantum coherences in adamantane. The 16 pulse sequence in the shaded box is used to generate the effective DQ Hamiltonian. The smaller spacing between the pulses is given by Δ while the larger spacing is given by the sum of 2Δ and the $\pi/2$ pulse length. Thus the cycle time of the sequence is $t_c = 24(\Delta + \pi/2 \text{ pulse length})$. The vertical striping indicates an x-pulse. All the pulses induce rotations by $\pi/2$. (or the negatives thereof if the pulses are below the bold reference lines)

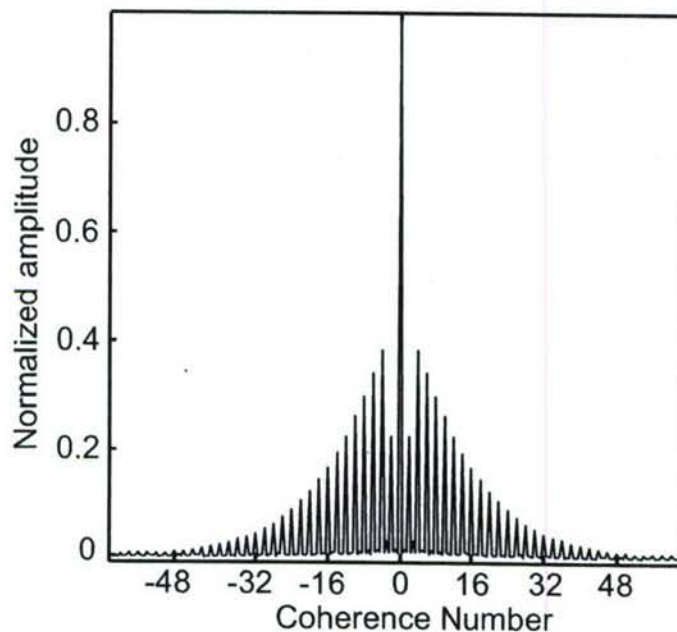


Figure 4-16: The ^1H multiple quantum coherence in adamantane. The system was evolved under the DQ Hamiltonian for a period of $604.8 \mu\text{s}$.

We then carry out the experiments outlined in Fig. 4-7. The cycle times of the TS-96 and the HR-96 sequences were set to 1.4 ms. At the end of one cycle of the TS-96 and HR-96 sequences, we can observe up to 32 coherences - though the magnitudes of the coherences in the case of the HR-96 sequence are substantially lower. See Fig. 4-17(a). At the end of two cycles, this difference becomes more pronounced. While in the case of TS-96 sequence we observe up to 24 coherences, we do not observe beyond 8 coherences for the HR-96 sequence. For sake of complete comparison, we applied two back-to-back C-48 sequence with the same total cycle time. For both one and two loops of this 96 pulse super-cycle of the C-48 sequence, the coherence intensities are slightly higher than those obtained for the HR-96 sequence. We compare the net change in intensity of the coherence orders after one loop of the TS-96 and the HR-96 sequences. We observe that as the coherence order increases, the net change in intensity also increases. Thus the sensitivity of the multiple-spin state to the presence of ^{13}C spins increase with the number of correlated ^1H spins in the multiple-spin state. We discuss our results in more details in the next section.

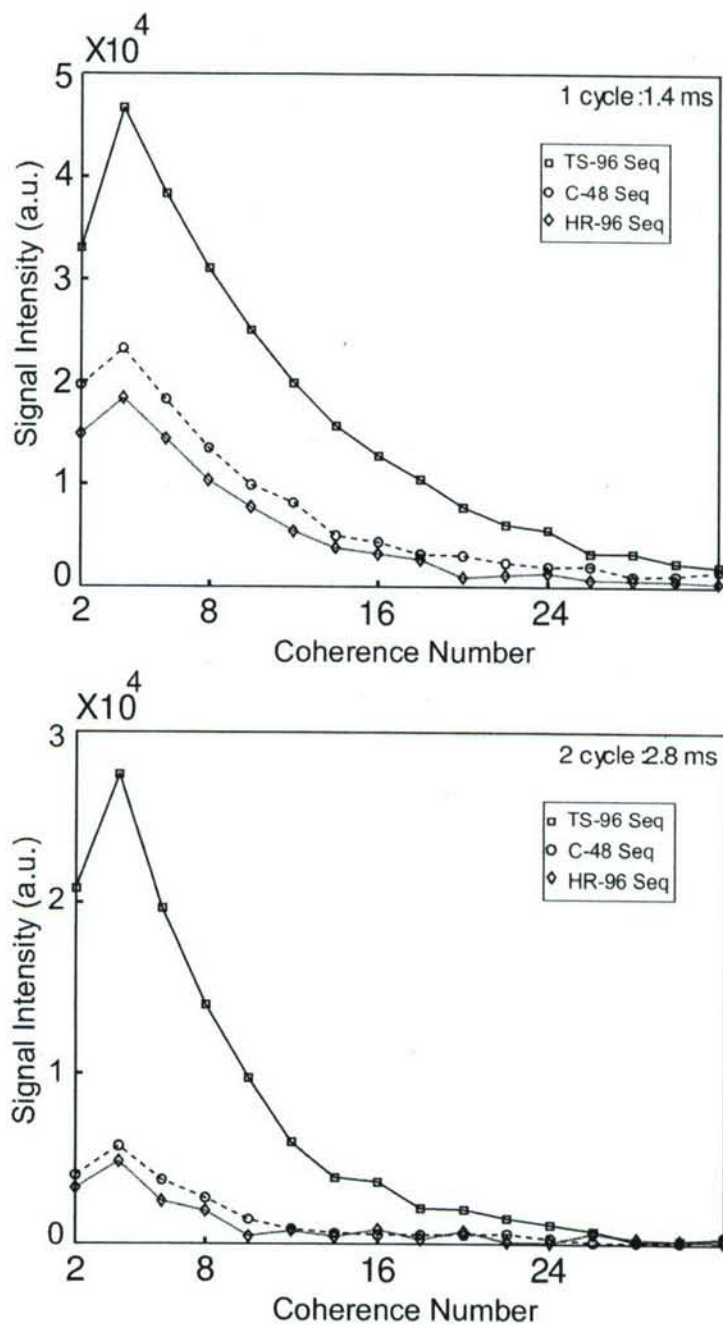


Figure 4-17: Coherence order distribution after evolution under the TS-96 (solid line), two back-to-back C-48 (dashed line) and the HR-96 (dotted line) sequences. The cycle time was 1.4ms for all three sequences. Thus, the time period of evolution (τ_2) were 1.4 ms (for the top figure) and 2.8 ms (for the bottom figure).

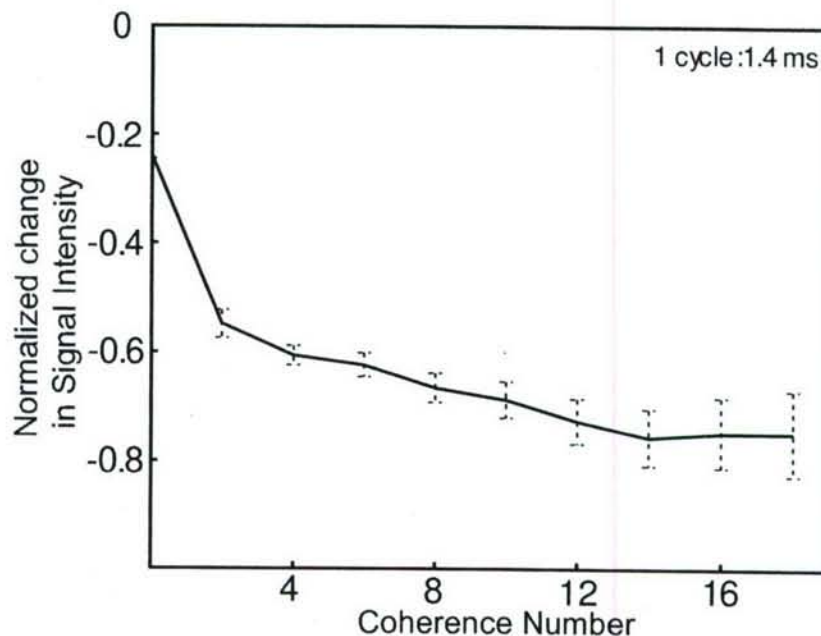


Figure 4-18: The net difference in signal intensity for the various coherence orders after one cycle of the TS-96 and HR-96 sequences.

4.7 Conclusions and future work

In this chapter, we made an attempt to understand the decay behavior of the highly correlated multiple-quantum spin- ^{19}F states observed in CaF_2 . We used adamantane as a test-bed to study the effect of the rare spins on the correlated multi-spin dynamics for a variety of reasons. Unlike the spin- $7/2$ ^{43}Ca spins, all the spins in adamantane are spin- $1/2$. Thus designing the multiple-pulse sequences were much simpler since we could ignore the quadrupolar spin interactions associated with a spin- $7/2$ system. Furthermore, the absence of intramolecular interactions, the weaker dipolar interactions and the low T_1 times are factors that contribute to the suitability of adamantane for these multiple-quantum experiments.

For our sensitivity measurements, we developed two multiple-pulse cycles - while the TS-96 sequence suppresses all the spin interactions in a heteronuclear system (comprising of two-spin species), the HR-96 sequence selectively reintroduces *only* the heteronuclear interaction between the spin species. Existing time-suspension se-

quences were designed to address interactions (chemical shift offsets and/or dipolar interactions) of a single-spin species in a spin system. Thus compared to these existing sequences, the TS-96 sequence has superior line-narrowing capabilities in such heteronuclear spin systems. Many solid-state spin systems that are studied in NMR comprise of two-spin species. Therefore this sequence could prove useful for line-narrowing experiments on similar systems.

The rate at which the various interactions average out should affect the line-narrowing capabilities (effective T_2 times) of the sequences. In adamantane, both the TS-96 and the HR-96 sequences average out the homonuclear spin- ^{13}C interactions in addition to the homonuclear spin- ^1H interactions. Comparing the rates at which these interactions are averaged out by the two sequences, we see that the homonuclear dipolar spin- ^{13}C interactions are averaged out 4 times faster by the former sequence. In spite of that, the measured effective T_2 for the spin- ^{13}C was 4 times higher for the TS-96 sequence (as seen in Fig. 4-13). This suggests that the effective T_2 is highly sensitive to the heteronuclear dipolar interaction. However, this effective T_2 is still considerably less than the T_1 . This could be due to the fact that this heteronuclear interaction is not being averaged out fast enough.

However compared to the C-48 sequence, the heteronuclear averaging capability of the TS-96 sequence is vastly superior. While the C-48 sequence averages out the heteronuclear interaction to the 0^{th} order without taking into account the finite pulse width effects, the TS-96 sequence averages out this interaction to the 1^{st} order while taking into account the finite pulse width effects. These factors partially contribute to the higher intensity of the coherence order distribution for the TS-96 sequence. This noticeable improvement in signal intensity for the TS-96 sequence over that of two back-to-back C-48 sequences can be seen in Fig. 4-17.

In CaF_2 , the measured coherence decay patterns were very similar under both cases - (i) evolution under the internal Hamiltonian and (ii) suppression of the spin- ^{19}F homonuclear and heteronuclear interactions. The decay behavior in the first case is primarily due to the fact that the multiple-quantum transitions under the action of the

^{19}F (secular) homonuclear dipolar Hamiltonian are not refocused to observable magnetization. To explain the decay behavior in the second case, we hypothesized that even though the ^{19}F - ^{43}Ca interaction is decoupled, the presence of rare ^{43}Ca spins give rise to decoherence effects. Due to the finite time period over which the heteronuclear interactions are averaged out, the ^{19}F spin clusters are correlated to neighboring ^{43}Ca spins at any instant during this decoupling period. The ^{43}Ca homonuclear interaction further increases the number of correlated ^{43}Ca spins in the cluster. These interactions are not refocused to observable magnetization leading to a decay in coherence orders. The decay data in both cases showed three broad features:

- As the size of spin correlations grew (with increasing coherence numbers and/or excitation periods under the DQ Hamiltonian), the decay rates became faster.
- As the excitation period under the DQ Hamiltonian increased, the decay times under different coherence orders became more uniform.
- The relative change (reduction) in the decay times decrease with increasing excitation times under the DQ Hamiltonian.

To test our hypothesis, we demonstrated the sensitivity of the highly correlated multiple-spin states of abundant spins (^1H) to the presence of rare spins (^{13}C) on our test-bed system. We used the multiple-pulse sequences to selectively create correlations between the ^{13}C spins and multiple-spin states of the ^1H spins. We observe that the sensitivity increases with increasing coherence order of the multiple-spin states for a given excitation period under the DQ Hamiltonian. As the coherence number increases, the number of the correlated ^1H spins (i.e., the spin cluster size) increase. Since the number of ^{13}C spins present in the cluster also increases with increasing cluster size, the highly-correlated states corresponding to the larger spin clusters are more sensitive to the presence of the ^{13}C spins (as seen in Fig. 4-18).

In light of the above experimental observations on adamantane, some ‘plausible’ explanations for the distinct features of the coherence decay data in CaF_2 are as follows:

We can envision each defect spin as introducing a phase error to the correlated spin states in its neighborhood. When the spin cluster size is small, there are very few defect spins within a cluster. All the spins in a correlated spin state see the same phase errors. Thus the rate of decoherence of the correlated states in the cluster depends on the coherence order of the states – the higher order coherences dephase faster than the lower order ones. However as the preparation time (τ_1) becomes longer, the size of the spin clusters increases and so does the number of defect spins in a cluster. Higher number of defects leads to a higher decoherence rate for the correlated spin states in the cluster. At the same time, the phase errors introduced by these numerous defect spins (at the site of any abundant spin) become increasingly uncorrelated. Thus the decay rate of the correlated states no longer strongly depends on the coherence number of these states. It depends on the spin number i.e., the number of spins in the cluster [88]. At short preparation times, the ^{19}F spin cluster size is small and there are few ^{43}Ca spins in a cluster. The decay rates strongly depend on the coherence number of the correlated spin states. An analogous behavior is experimentally observed for ^1H spin correlations and the defect ^{13}C spins in adamantane as seen in Fig. 4-18. For the preparation time of 1.4ms, while the lower order coherences mostly comprise of small spin clusters, the higher order spin coherences (≥ 14) comprise of only large spin clusters and thus see more defect spins. Therefore one observes a flattening of the curve for these higher coherence orders (in Fig. 4-18) suggesting that the increasingly uncorrelated phase errors lead to a saturation of decay rates beyond a certain cluster size. It would be interesting to see how the sensitivity of the correlated states varies with coherence order for various preparation times.

In any multiple-pulse experiment, RF inhomogeneity, phase transients and finite RF pulse widths can contribute to errors in the experimental data. To negate the finite pulse width effects, we took them into consideration for our average Hamiltonian calculations for the multiple-pulse cycles. Many of the the higher order terms of the average Hamiltonian are scaled by (a power of) the RF pulse strength. Thus the shorter the RF pulse, lower will be the effect of these interaction (error) terms

on the spin dynamics. All the above factors can lead to errors in the experimental implementation. At the same time, we made certain assumptions which if disregarded can lead to modifications in our initial analysis. We assumed that the inefficiencies of the multiple-quantum state creation process do not affect their subsequent decay. However, it can be shown that imperfect DQ Hamiltonian refocusing can contribute to a coherence order decay.

To conclude, our work provide some insight on the complex dynamics of highly correlated spin states in the presence of spin defects. In the process, we have also developed two multiple-pulse sequences which may have wider applications in NMR. As future work, we can further our study on the control of many spins in the presence of defect spins. One interesting control experiment is to evolve the highly correlated spin-system selectively under a heteronuclear interaction and then time-reverse the evolution. Thus by selectively correlating and then un-correlating the defect spins from the abundant spin system using multiple-pulse techniques, we can further investigate our ability of coherently controlling the defect spin interactions. We can also carry out the above sensitivity measurements on CaF_2 . It might be hard to predict the performance the TS-96 and the HR-96 sequences since they were designed for spin-1/2 systems. However working in the spin- $\pm 1/2$ manifold of the spin-7/2 ^{43}Ca spin system, it would be interesting to see the results.

APPENDIX A

ZEROth ORDER AVERAGE HAMILTONIAN CALCULATIONS FOR THE TS-96 AND THE HR-96 SEQUENCES

The zeroth order average Hamiltonian terms are scaled by a factor which is equal to the inverse of the cycle time ($t_c = 288\tau$) of the sequences.

Table A.1: The 0th order heteronuclear average Hamiltonian values for the TS-96 (top) and the HR-96 (bottom) sequences

Sub-cycles numbers	TS-96		0 th order average Hamiltonian
	I	S	
1 – 2	(Aa)(Bb)	(aE)(fB)	$(-8\tau - \frac{8}{\omega_{rf}} + \frac{2\pi}{\omega_{rf}})\mathbf{I}_z\mathbf{S}_z$
3 – 4	(Cc)(Dd)	(dG)(hD)	$(12\tau + \frac{12}{\omega_{rf}} - \frac{3\pi}{\omega_{rf}})\mathbf{I}_z\mathbf{S}_z$
5 – 6	(Ee)(Ff)	(bF)(eA)	$(-8\tau - \frac{8}{\omega_{rf}} + \frac{2\pi}{\omega_{rf}})\mathbf{I}_z\mathbf{S}_z$
7 – 8	(Gg)(Hh)	(cH)(gC)	$(12\tau + \frac{12}{\omega_{rf}} - \frac{3\pi}{\omega_{rf}})\mathbf{I}_z\mathbf{S}_z$

Sub-cycles numbers	HR-96		0 th order average Hamiltonian
	I	S	
1 – 2	(Aa)(Bb)	(bE)(fA)	$(16\tau + \frac{16}{\omega_{rf}} - \frac{4\pi}{\omega_{rf}})\mathbf{I}_z\mathbf{S}_z$
3 – 4	(Cc)(Dd)	(dG)(hC)	$(16\tau + \frac{16}{\omega_{rf}} - \frac{4\pi}{\omega_{rf}})\mathbf{I}_z\mathbf{S}_z$
5 – 6	(Ee)(Ff)	(aF)(eB)	$(16\tau + \frac{16}{\omega_{rf}} - \frac{4\pi}{\omega_{rf}})\mathbf{I}_z\mathbf{S}_z$
7 – 8	(Gg)(Hh)	(cH)(gD)	$(16\tau + \frac{16}{\omega_{rf}} - \frac{4\pi}{\omega_{rf}})\mathbf{I}_z\mathbf{S}_z$

Table A.2: The 0^{th} order heteronuclear average Hamiltonian values for the TS-96 sequence

Sub-cycles number n	TS-96		0^{th} order Average Hamiltonian
	I	S	
1 – 4	$(Aa)(Bb)(Cc)(Dd)$	$(aE)(fB)(dG)(hD)$	$(4\tau + \frac{4}{\omega_{rf}} - \frac{\pi}{\omega_f})\mathbf{I}_z\mathbf{S}_z$
4 – 8	$(Ee)(Ff)(Gg)(Hh)$	$(bF)(eA)(cH)(gC)$	$(4\tau + \frac{4}{\omega_{rf}} - \frac{\pi}{\omega_f})\mathbf{I}_z\mathbf{S}_z$

Sub-cycles number n	TS-96		0^{th} order Average Hamiltonian
	I	S	
1 – 8	$(Aa)(Bb)(Cc)(Dd)(Ee)(Ff)(Gg)(Hh)$	$(aE)(fB)(dG)(hD)(bF)(eA)(cH)(gC)$	0

Table A.3: The 0^{th} order heteronuclear average Hamiltonian values for the HR-96 sequence

Sub-cycles number n	HR-96		0^{th} order Average Hamiltonian
	I	S	
1 – 4	$(Aa)(Bb)(Cc)(Dd)$	$(bE)(fA)(dG)(hC)$	$(32\tau + \frac{32}{\omega_{rf}} - \frac{8\pi}{\omega_f})\mathbf{I}_z\mathbf{S}_z$
4 – 8	$(Ee)(Ff)(Gg)(Hh)$	$(aF)(eB)(cH)(gD)$	$(32\tau + \frac{32}{\omega_{rf}} - \frac{8\pi}{\omega_f})\mathbf{I}_z\mathbf{S}_z$

Sub-cycles number n	HR-96		0^{th} order Average Hamiltonian
	I	S	
1 – 8	$(Aa)(Bb)(Cc)(Dd)(Ee)(Ff)(Gg)(Hh)$	$(bE)(fA)(dG)(hC)(aF)(eB)(cH)(gD)$	$(64\tau + \frac{64}{\omega_{rf}} - \frac{16\pi}{\omega_f})\mathbf{I}_z\mathbf{S}_z$

Table A.4: The 0th order spin-I homonuclear average Hamiltonian values for the C-48 sequence

Sub-cycles numbers	C-48	0 th order Average Hamiltonian	
		Chemical Shift Term	Dipolar Term
1 – 2	(Aa)(Bb)	$(2\tau + \frac{4}{\omega_{rf}} - \frac{\pi}{\omega_{rf}})\mathbf{I}_x + (-2\tau - \frac{4}{\omega_{rf}} + \frac{\pi}{\omega_{rf}})\mathbf{I}_y + (2\tau + \frac{4}{\omega_{rf}} - \frac{\pi}{\omega_{rf}})\mathbf{I}_z$	0
3 – 4	(Cc)(Dd)	$(-2\tau - \frac{4}{\omega_{rf}} + \frac{\pi}{\omega_{rf}})\mathbf{I}_x + (2\tau + \frac{4}{\omega_{rf}} - \frac{\pi}{\omega_{rf}})\mathbf{I}_y + (2\tau + \frac{4}{\omega_{rf}} - \frac{\pi}{\omega_{rf}})\mathbf{I}_z$	0
5 – 6	(Ee)(Ff)	$(-2\tau - \frac{4}{\omega_{rf}} + \frac{\pi}{\omega_{rf}})\mathbf{I}_x + (2\tau + \frac{4}{\omega_{rf}} - \frac{\pi}{\omega_{rf}})\mathbf{I}_y + (-2\tau - \frac{4}{\omega_{rf}} + \frac{\pi}{\omega_{rf}})\mathbf{I}_z$	0
7 – 8	(Gg)(Hh)	$(2\tau + \frac{4}{\omega_{rf}} - \frac{\pi}{\omega_{rf}})\mathbf{I}_x + (-2\tau - \frac{4}{\omega_{rf}} + \frac{\pi}{\omega_{rf}})\mathbf{I}_y + (-2\tau - \frac{4}{\omega_{rf}} + \frac{\pi}{\omega_{rf}})\mathbf{I}_z$	0

Sub-cycles numbers	C-48	0 th order Average Hamiltonian	
		Chemical Shift Term	Dipolar Term
1 – 4	(Aa)(Bb)(Cc)(Dd)	$(4\tau + \frac{8}{\omega_{rf}} - \frac{2\pi}{\omega_{rf}})\mathbf{I}_x + (-4\tau - \frac{8}{\omega_{rf}} + \frac{2\pi}{\omega_{rf}})\mathbf{I}_y + (4\tau + \frac{8}{\omega_{rf}} - \frac{2\pi}{\omega_{rf}})\mathbf{I}_z$	0
4 – 8	(Ee)(Ff)(Gg)(Hh)	$(-4\tau - \frac{8}{\omega_{rf}} + \frac{2\pi}{\omega_{rf}})\mathbf{I}_x + (4\tau + \frac{8}{\omega_{rf}} - \frac{2\pi}{\omega_{rf}})\mathbf{I}_y + (-4\tau - \frac{8}{\omega_{rf}} + \frac{2\pi}{\omega_{rf}})\mathbf{I}_z$	0

Sub-cycles numbers	C-48	0 th order Average Hamiltonian	
		Chemical Shift Term	Dipolar Term
1 – 4	(Aa)(Bb)(Cc)(Dd)(Ee)(Ff)(Gg)(Hh)	0	0

Table A.5: The 0^{th} order spin-**S** homonuclear average Hamiltonian values for the TS-96 sequence

Sub-cycles numbers	TS-96	0^{th} order Average Hamiltonian		
		Chemical Shift Term	Dipolar Term	
1 – 2	$(aE)(fB)$	$(2\tau + \frac{4}{\omega_{rf}} - \frac{\pi}{\omega_{rf}})\mathbf{S}_x + (2\tau + \frac{4}{\omega_{rf}} - \frac{\pi}{\omega_{rf}})\mathbf{S}_y + (2\tau)\mathbf{S}_z$	$(\frac{3}{\omega_{rf}})(\mathbf{S}_x\mathbf{S}_z + \mathbf{S}_z\mathbf{S}_x + \mathbf{S}_y\mathbf{S}_z + \mathbf{S}_z\mathbf{S}_y)$	
3 – 4	$(dG)(hD)$	$(2\tau + \frac{4}{\omega_{rf}} - \frac{\pi}{\omega_{rf}})\mathbf{S}_x + (-2\tau - \frac{4}{\omega_{rf}} + \frac{\pi}{\omega_{rf}})\mathbf{S}_y + (\frac{2}{\omega_{rf}} - \frac{\pi}{2\omega_{rf}})\mathbf{S}_z$	$(-\frac{3}{\omega_{rf}})(\mathbf{S}_x\mathbf{S}_z + \mathbf{S}_z\mathbf{S}_x)$	
5 – 6	$(bF)(eA)$	$(-2\tau - \frac{4}{\omega_{rf}} + \frac{\pi}{\omega_{rf}})\mathbf{S}_x + (-2\tau - \frac{4}{\omega_{rf}} + \frac{\pi}{\omega_{rf}})\mathbf{S}_y + (6\tau + \frac{8}{\omega_{rf}} - \frac{2\pi}{\omega_{rf}})\mathbf{S}_z$	$(-\frac{3}{\omega_{rf}})(\mathbf{S}_x\mathbf{S}_z + \mathbf{S}_z\mathbf{S}_x + \mathbf{S}_y\mathbf{S}_z + \mathbf{S}_z\mathbf{S}_y)$	
7 – 8	$(cH)(gC)$	$(-2\tau - \frac{4}{\omega_{rf}} + \frac{\pi}{\omega_{rf}})\mathbf{S}_x + (2\tau + \frac{4}{\omega_{rf}} - \frac{\pi}{\omega_{rf}})\mathbf{S}_y + (-4\tau - \frac{6}{\omega_{rf}} + \frac{3\pi}{2\omega_{rf}})\mathbf{S}_z$	$(\frac{3}{\omega_{rf}})(\mathbf{S}_x\mathbf{S}_z + \mathbf{S}_z\mathbf{S}_x)$	

Sub-cycles numbers	TS-96	0^{th} order Average Hamiltonian	
		Chemical Shift Term	Dipolar Term
1 – 4	$(aE)(fB)(dG)(hD)$	$(4\tau + \frac{8}{\omega_{rf}} - \frac{2\pi}{\omega_{rf}})\mathbf{S}_x + (2\tau + \frac{2}{\omega_{rf}} - \frac{\pi}{2\omega_{rf}})\mathbf{S}_z$	$(\frac{3}{\omega_{rf}})(\mathbf{S}_y\mathbf{S}_z + \mathbf{S}_z\mathbf{S}_y)$
5 – 8	$(bF)(eA)(cH)(gD)$	$(-4\tau - \frac{8}{\omega_{rf}} + \frac{2\pi}{\omega_{rf}})\mathbf{S}_x + (2\tau + \frac{2}{\omega_{rf}} - \frac{\pi}{2\omega_{rf}})\mathbf{S}_z$	$(-\frac{3}{\omega_{rf}})(\mathbf{S}_y\mathbf{S}_z + \mathbf{S}_z\mathbf{S}_y)$

Sub-cycles numbers	TS-96	0^{th} order Average Hamiltonian	
		Chemical Shift Term	Dipolar Term
1 – 8	$(aE)(fB)(dG)(hD)(bF)(eA)(cH)(gD)$	0	0

Table A.6: The 0th order spin-**S** homonuclear average Hamiltonian values for the HR-96 sequence

Sub-cycles numbers	HR-96	0 th order Average Hamiltonian	
		Chemical Shift Term	Dipolar Term
1 – 2	$(bE)(fA)$	$(-2\tau - \frac{4}{\omega_{rf}} + \frac{\pi}{\omega_{rf}})\mathbf{S}_x + (2\tau + \frac{4}{\omega_{rf}} - \frac{\pi}{\omega_{rf}})\mathbf{S}_y + (2\tau + \frac{4}{\omega_{rf}} - \frac{\pi}{\omega_{rf}})\mathbf{S}_z$	0
3 – 4	$(dG)(hC)$	$(2\tau + \frac{4}{\omega_{rf}} - \frac{\pi}{\omega_{rf}})\mathbf{S}_x + (-2\tau - \frac{4}{\omega_{rf}} + \frac{\pi}{\omega_{rf}})\mathbf{S}_y + (2\tau + \frac{4}{\omega_{rf}} - \frac{\pi}{\omega_{rf}})\mathbf{S}_z$	0
5 – 6	$(aF)(eB)$	$(2\tau + \frac{4}{\omega_{rf}} - \frac{\pi}{\omega_{rf}})\mathbf{S}_x + (-2\tau - \frac{4}{\omega_{rf}} + \frac{\pi}{\omega_{rf}})\mathbf{S}_y + (-2\tau - \frac{4}{\omega_{rf}} + \frac{2\pi}{\omega_{rf}})\mathbf{S}_z$	0
7 – 8	$(cH)(gD)$	$(-2\tau - \frac{4}{\omega_{rf}} + \frac{\pi}{\omega_{rf}})\mathbf{S}_x + (2\tau + \frac{4}{\omega_{rf}} - \frac{\pi}{\omega_{rf}})\mathbf{S}_y + (-2\tau - \frac{4}{\omega_{rf}} + \frac{\pi}{\omega_{rf}})\mathbf{S}_z$	0

Sub-cycles numbers	HR-96	0 th order Average Hamiltonian	
		Chemical Shift Term	Dipolar Term
1 – 4	$(bE)(fA)(dG)(hC)$	$(-4\tau - \frac{8}{\omega_{rf}} + \frac{2\pi}{\omega_{rf}})\mathbf{S}_x + (4\tau + \frac{8}{\omega_{rf}} - \frac{2\pi}{\omega_{rf}})\mathbf{S}_y + (4\tau + \frac{8}{\omega_{rf}} - \frac{2\pi}{\omega_{rf}})\mathbf{S}_z$	0
5 – 8	$(aF)(eB)(cH)(gD)$	$(4\tau + \frac{8}{\omega_{rf}} - \frac{2\pi}{\omega_{rf}})\mathbf{S}_x + (-4\tau - \frac{8}{\omega_{rf}} + \frac{2\pi}{\omega_{rf}})\mathbf{S}_y + (-4\tau - \frac{8}{\omega_{rf}} + \frac{2\pi}{\omega_{rf}})\mathbf{S}_z$	0

Sub-cycles numbers	HR-96	0 th order Average Hamiltonian	
		Chemical Shift Term	Dipolar Term
1 – 8	$(bE)(fA)(dG)(hC)(aF)(eB)(cH)(gD)$	0	0

BIBLIOGRAPHY

- [1] J. I. Cirac and P. Zoller. *Phys. Rev. Lett.*, **74**:4094, 1995.
- [2] P. Grangier and G. Reymond and N. Schlosser. *Fortschr. Phys*, **48**:859, 2000.
- [3] J. E. Mooij and T. P. Orlando and L. Levitov and L. Tian and C. H. VanderWal and S. Llyod. *Science*, **285**:1036, 1999.
- [4] D. G. Cory and A. F. Fahmy and T. F. Havel. *Proc. Nat. Acad. Sci. USA*, **94**:1634, 1997.
- [5] I. L. Chuang and N. A. Gershenfeld. *Science*, **275**:350, 1997.
- [6] D. G. Cory and R. Laflamme and E. Knill and L. Viola and T. F. Havel and N. Boulant and G. Boutis and E. Fortunato and S. Lloyd and R. Martinez. *Fortschr. Phys*, **48**:975, 2000.
- [7] B. E. Kane. *Nature*, **393**:133, 1998.
- [8] D. Suter and K. Lim. *Phys. Rev. A*, **65**:052309, 2002.
- [9] H. Cho and D. G. Cory and C. Ramanathan. *J. Chem. Phys.*, **118**:3686, 2003.
- [10] C. Ramanathan and H. Cho and P. Capperallo and G. S. Boutis and D. G. Cory. *Chem. Phys. Lett.*, **369**:311, 2003.
- [11] H. Cho and T. D. Ladd and J. Baugh and D. G. Cory and C. Ramanathan. *Phys. Rev. B*, **118**:3686, 2003.

- [12] H. G. Krojanski and D. Suter. *Phys. Rev. Lett.*, **93**:090501-1, 2004.
- [13] W. Zhang and D. G. Cory. *Phys. Rev. Lett.*, **80**:1324, 1998.
- [14] G. S. Boutis and D. Greenbaum and H. Cho and D. G. Cory and C. Ramanathan. *Phys. Rev. Lett.*, **92**:137201, 2004.
- [15] G. S. Agarwal and R. R. Puri. *Phys. Rev. A*, **41**:3782, 1990.
- [16] C. H. Bennett, D. P. DiVincenzo, J. A. Smolin, and W. K. Wootters. *Phys. Rev. A*, **54**:3824, 1996.
- [17] S. H. Chen and M. Kotlarchyk. *Interactions of photons and neutrons with matter*. World Scientific Publ., 1997.
- [18] A. R. Usha Devi, X. Wang, and B. C. Sanders. *Quantum Inform. Processing*, **2**:207, 2003.
- [19] L.-M. Duan, A. Sorensen, J. I. Chirac, and P. Zoller. *Phys. Rev. Lett.*, **85**:3991, 2000.
- [20] A. R. Edmonds. *Angular Momentum in Quantum Mechanics*. Princeton Univ. Press, 1974.
- [21] E. M. Fortunato, M. A. Pravia, N. Boulant, G. Teklemariam, T. F. Havel, and D. G. Cory. *J. Chem. Phys.*, **116**:7599, 2002.
- [22] R. Freeman. *Spin Choreography*. Oxford Univ. Press, 1998.
- [23] T. F. Havel, S. S. Somaroo, C.-H. Tseng, and D. G. Cory. In T. Beth and M. Grassl, editors, *Applicable Algebra in Engineering, Communications and Computing*, volume 10, pages 339–374, Berlin, 2000. Springer-Verlag.
- [24] S. Hill and W. K. Wootters. *Phys. Rev. Lett.*, **78**:5022, 1997.
- [25] M. Kitagawa and M. Ueda. *Phys. Rev. A*, **47**:5138, 1993.
- [26] A. Kuzmich, L. Mandel, and N. P. Bigelow. *Phys. Rev. Lett.*, **85**:1594, 2000.

- [27] R. Laflamme, E. Knill, D. G. Cory, E. M. Fortunato, T. F. Havel, C. Miquel, R. Martinez, C. Negrevergne, G. Ortiz, M. A. Pravia, Y. Sharf, S. Sinha, R. Somma, and L. Viola. *Los Alamos Science*, **27**:2, 2002.
- [28] R. Laflamme, E. Knill, W. H. Zurek, P. Catasti, and S. Marathan. *Phil. Trans. R. Soc. Lond. A*, **356**:1941, 1998.
- [29] D. A. Meyer and N. R. Wallach. *J. Math. Phys.*, **43**:4273, 2002.
- [30] M. A. Nielsen and I. L. Chuang. *Quantum Computation and Quantum Information*. Cambridge Univ. Press, 2000.
- [31] M. A. Pravia, N. Boulant, J. Emerson, A. Farid, E. M. Fortunato, T. F. Havel, R. Martinez, and D. G. Cory. *J. Chem. Phys.*, **119**:9993, 2003.
- [32] M. D. Price, T. F. Havel, and D. G. Cory. *Phys. D*, **120**:82, 1998.
- [33] M. E. Rose. *Elementary theory of Angular Momentum*. John Wiley & Sons, 1957. Reprinted by Dover Publ., 1995.
- [34] M. O. Scully. *Quantum Optics*. Cambridge Univ. Press, 1997.
- [35] A.J. Shaka and R. Freeman. *J. Magn. Reson.*, **55**:487, 1983.
- [36] A. Sorensen, L.-M. Duan, J. I. Cirac, and P. Zoller. *Nature*, **409**:63, 2001.
- [37] A. Sorensen and K. Molmer. *Phys. Rev. A*, **83**:2274, 1999.
- [38] A. Sorensen and K. Molmer. *Phys. Rev. Lett.*, **83**:2274, 1999.
- [39] G. Teklemariam, E. M. Fortunato, M. A. Pravia, T. F. Havel, and D. G. Cory. *Phys. Rev. Lett.*, **86**:5845, 2001.
- [40] Xiaoguang Wang and K. Molmer. *Eur. Phys. J. D*, **18**:385, 2002.
- [41] Y. S. Weinstein, M. A. Pravia, E. M. Fortunato, S. Lloyd, and D. G. Cory. *Phys. Rev. Lett.*, **86**:1889, 2001.

- [42] D. J. Wineland, J. J. Bollinger, W. M. Itano, and F.L. Moore. *Phys. Rev. A*, **46**:6797, 1992.
- [43] D. J. Wineland, J.J. Bollinger, W. M. Itano, and D. J. Heinzen. *Phys. Rev. A*, **50**:67, 1994.
- [44] K. Wodkiewicz. *J. Mod. Opt.*, **34**:941, 1987.
- [45] K. Wodkiewicz and J. Eberly. *J. Opt. Soc. Am. B*, **2**:458, 1985.
- [46] W. K. Wootters. *Phys. Rev. Lett.*, **80**:2245, 1998.
- [47] J. Wrachtrup and S. Y. Kilin and A. P. Nizovtsev. *Opt. Spectrosc+*, **91**:429, 2001.
- [48] T. D. Ladd and J. R. Goldman and F. Yamaguchi and Y. Yamamoto. *Phys. Rev. Lett.*, **89**:017901, 2002.
- [49] S. Vega and Y. Naor. *J. Chem. Phys.*, **75**:75, 1981.
- [50] M. Mehring. *High Resolution NMR Spectroscopy in Solids*. Springer-Verlag, Berlin, 1983.
- [51] U. Haeberlen. *High Resolution NMR in Solids*. Academic Press, New York, 1976.
- [52] A. Keller. *Adv. Magn. Reson.*, **12**:183, 1990.
- [53] A. Pines and D. J. Ruben and S. Vega and M. Mehring. *Phys. Rev. Lett.*, **36**:110, 1976.
- [54] A. Pines and S. Vega and M. Mehring. *Phys. Rev. B*, **18**:112, 1978.
- [55] J. Waugh and U. Haeberlen. *Phys. Rev.*, **175**:453, 1968.
- [56] G. Pake *J. Chem. Phys.*, **16**:327, 1948.

- [57] The signal was measured using a solid echo sequence. The amplitude of the 15th point on the acquired data was then either plotted against the duration of the RF modulation or Fourier transformed to yield a spectrum.
- [58] U. Haeberlen and J. S. Waugh. *Phys. Rev.*, **175**:453, 1968.
- [59] M. Munowitz and A. Pines. *Adv. Chem. Phys.*, **66**:1, 1987.
- [60] D. P. Weitekamp. *Adv. Magn. Reson.*, **11**:111, 1983.
- [61] G. Drobny. *Ann. Rev. Phys. Chem.*, **26**:451, 1985.
- [62] Y. S. Yen and A. Pines. *J. Chem. Phys.*, **78**:3579, 1982.
- [63] J. Baum and M. Munowitz and A. N. Garroway and A. Pines. *J. Chem. Phys.*, **83**:2015, 1985.
- [64] J. Baum and A. Pines. *J. Am. Chem. Soc.*, **108**:7447, 1986.
- [65] R. Tycko. *J. Magn. Reson.*, **139**:302, 1999.
- [66] M. Munowitz and A. Pines. *Science*, **233**:525, 1986.
- [67] S. Lacelle and S. J. Hwang and B. C. Gerstein. *J. Chem. Phys.*, **99**:8407, 1993.
- [68] E. B. Feldman and S. Lacelle. *J. Chem. Phys.*, **107**:7067, 1977.
- [69] S. Lacelle. *J. Magn. Reson.*, **16**:193, 1991.
- [70] D. A. Lathrop and E. S. Handy and K. K. Gleason. *J. Magn. Reson. Series A.*, **111**:161, 1994.
- [71] M. Munowitz and A. Pines and M. Mehring. *J. Chem. Phys.*, **86**:3172, 1987.
- [72] S. Zhang and B. H. Meier and R. R. Ernst. *Sol. Stat. Nucl. Magn. Reson.*, **1**:313, 1992.
- [73] M. Maricq *Phys. Rev. B*, **25**:6622, 1982.

- [74] C. H. Wang and J. D. Ramshaw. *Phys. Rev. B*, **6**:3253, 1972.
- [75] P. Mansfield and U. Haeberlen. *Z. Naturforsch*, **28**:1081, 1973.
- [76] P. Mansfield and P. K. Grannell. *Phys. Rev. B*, **12**:3618, 1975.
- [77] H. M. Cho and C. J. Lee and D. N. Shykind and D. P. Weitekamp. *Phys. Rev. Lett.*, **55**:1923, 1985.
- [78] D. G. Cory and J. B. Miller and R. Turner and A. N. Garroway. *Mol. Phys.*, **70**:331, 1990.
- [79] D. P. Weitekamp and J. R. Garbow and A. Pines. *J. Chem. Phys.*, **77**:2870, 1982.
- [80] P. Caravatti and L. Braunschweiler and R. R. Ernst. *Chem. Phys. Lett.*, **100**:305, 1983.
- [81] J. S. Waugh and L. M. Huber and U. Haeberlen. *Phys. Rev. Lett.*, **20**:180, 1968.
- [82] W. K. Rhim and D. D. Elleman and R. W. Vaughan. *J. Chem. Phys.*, **58**:1772, 1973.
- [83] D. G. Cory and J. B. Miller and A. N. Garroway. *J. Mag. Reson.*, **90**:205, 1990.
- [84] H. A. Resing. *Mol. Cryst. Liq. Cryst.*, **9**:101, 1969.
- [85] A. Pines and M. G. Gibby and J. S. Waugh. *J. Chem. Phys.*, **56**:1776, 1972.
- [86] A. N. Garroway. *J. Magn. Reson.*, **28**:365, 1977.
- [87] C. E. Bronniman and N. M. Szeverenyi and G. E. Maciel. *Mol. Phys.*, **70**:331, 1990.
- [88] A. Fedorov and L. Fedichkin. *J. Phys. Cond. Mat.*, **18**:3217, 2006.

Coherent Control of Quantum Information

by

Michael Kevin Henry, Jr.

Submitted to the Department of Nuclear Science and Engineering
in partial fulfillment of the requirements for the degree of

Doctor of Philosophy in Nuclear Science and Engineering

at the

MASSACHUSETTS INSTITUTE OF TECHNOLOGY

June 2007

© Massachusetts Institute of Technology 2007. All rights reserved.

Author
Department of Nuclear Science and Engineering
April 30, 2007

Certified by
David G. Cory
Professor
Thesis Supervisor

Read by
Alan Jasanoff
Assistant Professor

Accepted by
Jeffrey A. Coderre
Chairman, Department Committee on Graduate Students

Coherent Control of Quantum Information

by

Michael Kevin Henry, Jr.

Submitted to the Department of Nuclear Science and Engineering
on April 30, 2007, in partial fulfillment of the
requirements for the degree of
Doctor of Philosophy in Nuclear Science and Engineering

Abstract

Quantum computation requires the ability to efficiently control quantum information in the presence of noise. In this thesis, NMR quantum information processors (QIPs) are used to study noise processes that compromise coherent control, to develop useful techniques for detecting noise, and to explore effective noise-protection schemes.

A quantum simulation of the quantum sawtooth map in the perturbative parameter regime is used to study the effects of experimental noise on quantum localization, a highly sensitive quantum interference phenomenon that depends on the coherence of the localized state. Experimental data and numerical simulations show that the decoherent noise known to act on the system is relatively inconsequential in this implementation of the map, and that incoherent noise is the biggest challenge to implementing localization.

While many incoherent processes appear decoherent, there are important differences. The distribution functions underlying incoherent processes are either static or slowly varying and so the errors introduced by these distributions are refocusable. The influence of incoherent noise is further explored in an experimentally implemented entangling operation, where incoherence can be difficult to separate from decoherence. By studying the fidelity decay under the cyclic entangling map, the effects of incoherence are easily distinguished from decoherence in experimental data.

Decoherence free subspaces (DFSs) provide some of the most efficient schemes of avoiding decoherence from noise sources with underlying symmetries. To achieve an internal Hamiltonian structure that naturally fits a DFS encoding over a well-defined Hilbert space, we employ liquid crystal solvents to partially align a four-proton spin system, reintroducing the spin-spin dipolar couplings. In these experiments, enhanced coherent control is achieved by encoding logical qubits in a DFS. Robust control sequences enable high fidelity control in the DFS even when the system Hamiltonian is known with some uncertainty.

Thesis Supervisor: David G. Cory
Title: Professor

Acknowledgments

I would like to thank David Cory for giving me the opportunity to work with him and the Cory group, and for all of the advice and instruction David has given during my years as a graduate student. David's integrity, energy, wisdom and kindness have truly inspired me.

I am thankful to many research collaborators and friends who contributed to the work described in this thesis - Sekhar Ramanathan, Joseph Emerson, Jonathan Hodges, Paola Cappellaro, Nicolas Boulant, Yaakov Weinstein, Alexey Gorshkov, Tim Havel, Colm Ryan, Mike Ditty, and Rudy Martinez.

I would also like to thank other Cory group members whom I have had the pleasure of working with - Deborah Chen, Jennifer Choy, Matthew Davidson, Anatoly Dementyev, Louis Fernandes, Daniel Greenbaum, Kai Iamsumang, Benjamin Levi, Cecilia Lopez, T. S. Mahesh, Kota Murali, Dmitry Pushin, Suddha Sinha, and Sergio Valenzuela. Special thanks to Jamie Yang, Troy Borneman and Hyungjoon Cho for helping out with many successful helium fills.

I am especially thankful to my very good friends and co-members of Graduate Lunch Seminar - Jamie Yang, Leeland Ekstrom, Alex Ince-Cushman, and Jonathan Hodges. Memories of quizbowl and our weekly meetings at Sunny's will always be dear to me.

I would like to thank my friends and family at home in Texas and in Colorado for their support and encouragement. Words cannot express my gratitude for my loving wife Brook, whose endless patience, kindness, and encouragement have been my source of strength and happiness through graduate school. Finally, I am thankful to God my Creator for His grace through Christ and for a life of abundant blessing.

Dedicated to my wife Brook,

“... the only one I see.”

Contents

1	Introduction	17
1.1	Quantum information processors	18
1.2	Toward more qubits and larger systems	19
2	Localization in the quantum sawtooth map	21
2.1	The sawtooth map	23
2.2	Implementation details	26
2.3	Numerical simulation	32
2.4	Experimental results	36
2.5	Discussion	37
2.6	Conclusions	42
3	Signatures of incoherence	43
3.1	Identifying incoherence by fidelity decay	44
3.1.1	Decoherent noise	45
3.1.2	Incoherent noise	47
3.2	Experiment	49
3.3	Numerical simulation	51
3.4	Results and discussion	54
3.5	Conclusions	57
4	Liquid crystal solvent NMR QIPs	59
4.1	NMR with liquid crystal solvents	59
4.2	Dipolar coupling in a partially oriented system	62
4.3	Liquid crystal solvent NMR QIPs	65

5	Enhanced control by logical qubit encoding	71
5.1	System model	71
5.2	Experiment	74
5.3	Analysis	77
5.4	Conclusions	79
6	Future direction	81
6.1	Larger Hilbert spaces	81
6.2	Limited addressability	82
6.3	Complex dynamics	83
6.4	Conclusions	83
A	Fidelity of logical qubit control	87
A.1	Measures of control	87
A.2	Control in the logical subspace	89

List of Figures

2-1	The momentum distribution after 0, 5, 10, and 40 iterations of the classical and quantum sawtooth maps. The classical map is chaotic, which causes the distribution to diffusively broaden. The quantum map causes localization, and the breadth of the distribution is essentially static.	25
2-2	Quantum circuits for implementing the quantum sawtooth map: the quantum Fourier transform and a generalized diagonal unitary operator. These circuits enable a computationally efficient quantum simulation of the quantum sawtooth map.	27
2-3	A diagram of the tris(trimethylsilyl)silane-acetylene molecule used to simulate the quantum sawtooth map in a liquid state NMR QIP.	30
2-4	The hydrogen and carbon rf control fields versus time for the full quantum sawtooth map pulse sequence.	31
2-5	The nine point distribution of carbon rf powers measured in previous experiments and used to simulate the experimentally implemented control sequence for the quantum sawtooth map.	34
2-6	Momentum distributions for different regions of the ensemble generated by numerical simulations of the experiment which account for T1 and T2 decoherence. Each plot represents the momentum distribution resulting from a numerical simulation of the control sequence with a different carbon rf power. In experiments, the weighted average over the incoherence is observed. . . .	35
2-7	The momentum distribution observed in the experiment and in various numerical simulations of the experiment after zero through three iterations of the quantum sawtooth map.	36

2-8	The full width at half maximum (FWHM) of the momentum distribution after zero through four iterations of the sawtooth map in various implementations. The FWHM reveals that despite the noise affecting the QIP, the distribution mimics the ideal quantum behavior, and does not diffusively broaden as in the classical case.	38
2-9	The second moment of the momentum distribution determined from numerical simulations of the quantum sawtooth map experiment including the error models discussed in the text, compared to the ideal data and the experimental data. This plot demonstrates the relative importance of the individual noise mechanisms as they contribute to the experimentally observed delocalization process.	39
2-10	The magnitude of each element of the superoperators and most significant Kraus operators for numerical simulations of the quantum sawtooth map experiment, including different types of errors.	41
3-1	The quantum circuit for exploring incoherence in an entangling operation on a QIP. The circuit creates a maximally entangled GHZ state, to which $4n$ iterations of a two-qubit entangling operation are applied. The resulting entangled state is then converted to a computational basis state.	50
3-2	A diagram of the tris(trimethylsilyl)silane-acetylene molecule used to implement the quantum circuit in Fig. 3-1 in a liquid state NMR QIP.	51
3-3	The distribution of carbon rf powers measured in previous experiments and used in numerical simulations of the NMR implementation of the circuit in Fig. 3-1.	52
3-4	The fidelity decay from a numerical simulation of the experiment, where rf inhomogeneity is simulated using two different models. Comparison of the two plots shows that the fidelity decay recurrences are caused by incoherent noise.	53
3-5	The sum of the absolute value of the density matrix components measured in the experiment and in numerical simulations. This plot shows that incoherence in the entangling operation appears with distinct signatures in the experimental data.	55

3-6	The Fourier transform of each experimentally measured component of the density matrix, compared to numerical simulations of the experiment using two models of rf inhomogeneity discussed in the text. This plot shows that incoherence in the experimentally implemented entangling operation appears as high frequency components in the Fourier transform of a state fidelity measurement.	56
4-1	Illustration of the order properties of a nematic liquid crystal phase, showing orientational but not positional ordering. Solutes dissolved in a nematic liquid crystal adopt preferred orientations that restrict thermal rotation, causing nuclear spins within the molecule to retain non-zero dipolar interactions which are not present in an isotropic liquid.	60
4-2	600 MHz proton spectrum of o-chloronitrobenzene (CNB) partially oriented by the liquid crystal solvent ZLI-1132 showing suppression of the baseline signal caused by the solvent material. The baseline is suppressed by the Cory-48 pulse sequence, parameterized to refocus the dipolar couplings among solute protons but not among solvent protons.	61
4-3	Coordinate frames used in the expression of the order parameter, which determines the intramolecular nuclear spin dipolar coupling strengths.	63
4-4	600 MHz proton spectrum of benzene partially oriented by the liquid crystal solvent ZLI-1132.	65
4-5	Comparison of three regimes of NMR QIP, showing liquid crystal solvent NMR QIPs (LNQs) as a bridge between liquid and solid state implementations. LNQs provide a natural setting for addressing some of the important challenges in solid state NMR quantum information processing.	67
5-1	600 MHz proton spectrum of o-chloronitrobenzene (CNB) partially oriented by the liquid crystal solvent ZLI-1132. The inset was collected under the MREV-8 sequence, and shows the four protons uncoupled with chemical shifts scaled by the average Hamiltonian.	74

5-2	The procedure and experimental results of creating a Bell state over two logical qubits encoded in the four dipolar-coupled protons of the CNB molecule. The experimentally prepared logical input state has a correlation of 0.90 with the numerically simulated logical input state. The correlation for the Bell states is 0.84.	76
5-3	Correlation of the numerically simulated and experimentally measured density matrices for the logical input state and the logical Bell state. The correlations are averaged over a dispersion of simulated Hamiltonian parameters. As more couplings are varied, the correlations decrease only slightly since the pulse sequences were engineered to be robust to these variations, and the loss in correlation is most pronounced for the input state.	78
5-4	Fidelity of two-qubit entangling operation pulses numerically simulated under various conditions, comparing control of two logical qubits versus all pairs of spin qubits. The fidelity under each set of conditions is significantly better in the case of logical qubits than for any pair of spin qubits.	79
6-1	Diagram of the 4-hydroxyphenanthrene molecule which could be used as a 16 qubit heteronuclear LNQ.	82
6-2	NMR spectra for different regimes of Hamiltonians, showing addressable spins in the liquid state, resolved spin transitions in partially oriented systems, and many equivalent spins broadened by dipolar interactions in a solid.	84

List of Tables

2.1	Pulse sequence data for the quantum sawtooth map.	31
-----	---	----

Chapter 1

Introduction

Quantum systems have unique properties that are not observed in the classical, macroscopic world. Information stored in a quantum system - “quantum information” - has inherent manifestations of these unique properties and therefore has capabilities that are unparalleled in traditional computing devices. A quantum computer harnesses the computational power of quantum systems, exploiting coherent superposition states, entanglement, and other quantum resources, to achieve an advantage over classical computers in solving certain problems, such as factoring large numbers and searching unsorted lists [42, 95]. The feasibility of quantum computation relies on the possibility of quantum error encodings [96, 100], which enable arbitrarily precise quantum computation in the presence of noise [59].

In perhaps its most important function, a quantum computer can be programmed to simulate the dynamics of other quantum systems [36, 71]. Efficient quantum algorithms have been found for simulating a variety of complex quantum systems [1, 2, 40, 69, 93]. In this capacity, quantum computers could provide meaningful insight into the dynamics of large quantum systems which cannot be efficiently simulated on classical computers. In the second chapter of this thesis, an experimental implementation of one such algorithm [7] which efficiently simulates the dynamics of the quantum sawtooth map is presented.

The criteria [30] necessary for utilizing the full power of quantum computation have not currently been realized in any device. However, quantum information processors (QIPs) provide an experimentally accessible means for exploring coherent quantum control and for implementing quantum algorithms. This thesis describes a number of experiments performed with nuclear magnetic resonance (NMR) QIPs. The ideas explored in these ex-

periments have application in ongoing efforts to engineer precise coherent control in larger systems, toward a scalable quantum computer. The QIPs used here operate with a small number of quantum bits (qubits) in highly mixed states, and they are subject to significant noise.

1.1 Quantum information processors

Experimental implementations of quantum information processing have developed in a number of technologies including liquid state NMR, which allows precise coherent control of small networks of weakly coupled nuclear spins. Liquid state NMR experiments mimic pure state quantum dynamics by utilizing isomorphic pseudopure states [20, 41]. This approach has been used to successfully implement a variety of quantum information concepts including quantum error correction [11, 23], the Deutsch-Jozsa algorithm [50], the quantum Fourier transform [117], Shor's factoring algorithm [108], quantum process tomography [115], noiseless subsystems [38, 110], decoherence free subspaces [37, 49], various simulations of quantum dynamics [17, 98, 107, 116], and studies of quantum entanglement [9, 105] including experiments with up to twelve qubits [81].

A number of approaches have been developed for reducing the effects of noise in QIPs, advancing the state of the art in these devices. Strongly modulating pulses (SMPs) are numerically optimized rf control fields which implement precise, spin-selective control, averaging out all unwanted time evolution in the system while minimizing the effects of decoherence [37]. Gradient ascent pulse engineering (GRAPE) has also been used to design numerically optimized pulse sequences which implement precise unitary operators [54]. In addition, quantum error-correcting codes [96, 100], noiseless subsystems [58, 122], decoherence free subspaces [32, 70, 122], dynamical decoupling [109, 111–113], composite pulses [24, 68], and robust pulses [88], have all been developed for protecting quantum information against noise and decoherence. The noise protection scheme most appropriate for a given system is generally determined by the noise model, since each scheme is best suited for certain types of noise. In Chapter Three of this thesis, a discussion of incoherent noise is presented, along with a method for identifying its presence in a QIP, so that the appropriate noise protection scheme may be chosen.

1.2 Toward more qubits and larger systems

While liquid state NMR systems provide a useful testbed for quantum computation and continue to yield meaningful progress, they are fundamentally limited in their scalability - their potential to efficiently incorporate more qubits. As the number of qubits in a liquid state NMR QIP increases, the signal decreases exponentially [114]. Many of the proposed scalable approaches to nuclear spin-based quantum computing envision solid state implementations [21, 52, 55, 62, 94, 101]. Solids are composed of large networks of dipolar-coupled nuclear spins, and a principal challenge in these systems is controlling the multispin dynamics. While methods for coherent control of solid state nuclear spin systems have progressed [4, 5, 89], incorporating all the desired capabilities of a quantum computer remains a challenge.

Liquid crystal solvent NMR QIPs [72, 120] provide an intermediate ground between liquid and solid state implementations. Molecules dissolved in liquid crystalline material contain networks of dipolar-coupled spins that, to a good approximation, are uncoupled from their environment [34]. The network of spins is effectively limited to single molecules, and each spin in a molecule may have a unique resonance frequency, thus the multispin dynamics are more easily controlled than in solids. While liquid crystal solvent NMR QIPs are not scalable, they do present the possibility of modestly increasing the size of experimentally accessible Hilbert spaces, since interactions are mediated by strong long-range dipolar couplings and are not limited to bond-mediated scalar couplings as in liquids. Liquid crystals offer a more tractable setting for studying dipolar-coupled spin networks, while maintaining sufficient complexity to provide meaningful contributions to scalable systems.

The second section of this thesis has three parts: Chapter Four introduces fundamentals of liquid crystal solvent NMR QIPs, Chapter Five describes an implementation of two logical qubits using this technology, and Chapter Six suggests a future direction of these studies and how they might contribute to progress in the broader efforts of the quantum computing community.

Chapter 2

Localization in the quantum sawtooth map

The development of quantum computers promises a new approach for exploring quantum mechanics in complex systems. In the future, we hope to use quantum computation to emulate quantum behavior in Hilbert spaces that are larger than can be simulated on a classical computer. Today we have access to QIPs that are prototypes of quantum computers (QCs). These devices operate over small and limited Hilbert spaces, and with significant noise. However, even with these limitations they can be used to explore questions of quantum mechanics that start to reflect the power we expect of future QCs. Even when QIPs operate on highly mixed states, as is the case for liquid state NMR implementations, we can distill properties that are consistent with the desired quantum phenomena. Here we will explore one such example, localization under the quantum sawtooth map. Localization is a uniquely quantum phenomenon and thus a natural target of quantum computation.

Dynamical localization occurs in classically chaotic quantum maps, in which the quantum state initially diffuses at the classical rate due to repeated quasi-random perturbations, but then stabilizes to a fixed probability distribution and remains coherently localized under subsequent perturbations [16]. In the case of perturbative localization, the probability distribution is localized with no initial period of diffusion. In both cases, the exponentially peaked, static probability distribution distinctly contrasts with the classical, diffusive behavior. Efficient algorithms have been developed for simulating the dynamics of localization in the kicked rotator model [39], the quantum sawtooth map [7], and the kicked

Harper model [66] on a QIP. Although localization can in principle be observed in an ideal emulation using as few as three qubits [6], the sensitivity of this phenomenon to noise effects [6, 7, 65–67, 84, 99] poses a rigorous challenge in the task of creating and maintaining a localized state on a noisy QIP.

In our experiment, we explored localization on a small (3-qubit) QIP based on liquid state NMR [48]. The aim of the study was to implement the sawtooth map on our QIP, to do so in such a way that we observe properties of localization which are clearly distinct from the classical behavior, and to use this example emulation as a test of the precision of our implementation as well as to motivate the continued refinement of this implementation.

Since liquid state NMR QIP relies on a large spatially distributed ensemble of quantum systems, we have to be careful in selecting the measures that we use for observing localization. The errors in our implementation of the sawtooth map will vary over the ensemble due to the inhomogeneity of the rf control field. There will be regions of the ensemble where the fidelity of implementation of the sawtooth map is sufficient that we observe localization, while for other regions the errors will be large enough to prevent localization. In the experiment we observe the sum of these effects, and thus we expect to see a peak in the probability distribution in the basis of localization that is representative of those parts of the ensemble that are localized, accompanied by a background offset in the probability distribution in the basis of localization resulting from those parts of the ensemble that are not localized.

A description of the sawtooth map is given in Sec. 2.1, followed by an explanation of the experimental implementation of the map in Sec. 2.2. A discussion of the noise effects expected in the experiment are presented in Sec. 2.3, along with a discussion of their effects on the localization phenomenon. In Sec. 2.4 the experimental results are reported and shown to demonstrate properties which are consistent with localization. The results are further compared with numerical simulations of the experiment which show that the imperfections in the data are well accounted for by the error model identified in previous work [10, 88, 115]. Finally, in Sec. 2.5, numerical studies of the error model are applied to measure the relative degree of delocalization caused by the specific noise mechanisms.

2.1 The sawtooth map

The sawtooth map is a periodically kicked system with period T and kick strength k , whose classical dynamics are dictated by a single parameter $K = kT$. One iteration of the classical sawtooth map is compactly described by the equations

$$\begin{aligned}\bar{J} &= J + k(\Theta - \pi) \\ \bar{\Theta} &= \Theta + T\bar{J}\end{aligned}\tag{2.1}$$

where Θ is the angular position variable and J is the angular momentum variable. The cylindrical phase space, which results from the periodicity of the position variable ($0 \leq \Theta < 2\pi$), can be represented on a torus by truncating the momentum space to length $2\pi L/T$ and applying a periodic boundary condition. In the quantum regime, one iteration of the sawtooth map is represented by the unitary time evolution operator

$$U_{saw}(0, T) = \exp\left(-iT\hat{J}^2/2\right) \exp\left(ik(\hat{\Theta} - \pi)^2/2\right)\tag{2.2}$$

where \hat{J} and $\hat{\Theta}$ are conjugate action quantum mechanical operators. The state of the quantum system is represented by a density matrix $\hat{\rho}$ expressed in the momentum basis. A detailed description and insightful discussion of the sawtooth map can be found in reference [6].

In a simulation of the quantum sawtooth map on an n_q qubit quantum information processor, the momentum basis states of the emulated system are represented by $N = 2^{n_q}$ computational basis states, therefore $N = 2\pi L/T$. The momentum basis states are labeled by their eigenvalues $-N/2 \leq j < N/2$, such that $\hat{J}|j\rangle = j|j\rangle$. The position basis states $|\theta_m\rangle$ have eigenvalues $\theta_m = (2\pi m/N)$, such that $\hat{\Theta}|\theta_m\rangle = \theta_m|\theta_m\rangle$, where $0 \leq m < N$. The overlap between conjugate basis states is given by

$$\langle \theta_m | j \rangle = \frac{1}{\sqrt{N}} \exp\left[\frac{2\pi i m}{N} \left(j + \frac{N}{2}\right)\right]\tag{2.3}$$

Quantum localization. In the classical phase space, when $K < -4$ or $K > 0$, the sawtooth map induces chaotic motion, which is seen by considering a classical ensemble of trajectories, where each element of the ensemble has a fixed initial momentum ($J = 0$) and

a randomized initial position (Θ). The chaotic motion arises due to the presence of the term $k(\Theta - \pi)$ in Eq. 2.1, which gives a *kick* to the momentum at each iteration of the map. In chaotic parameter regimes, the strength of the sequence of kicks can be approximated as a quasi-random sequence, leading to diffusive broadening along the momentum dimension of the classical phase space, as shown in Fig. 2-1. As a result, the breadth of the distribution, as measured by its second moment, grows linearly with the number of map iterations, n , according to

$$\langle (\Delta J)^2 \rangle \approx Dn, \quad (2.4)$$

where $D \approx (\pi^2/3)k^2$ is the classical diffusion coefficient. As the map is iterated, momentum diffusion continues indefinitely, and the probability distribution approaches uniformity over the bounded toroidal phase space.

The quantum system demonstrates a strikingly different behavior. Like the classical map, the quantum sawtooth map initially causes diffusive broadening in the momentum basis according to the classical diffusion coefficient D . However, after $n^* \approx D$ iterations of the quantum map, diffusion is suppressed due to quantum interference, and for all subsequent iterations, the quantum state maintains roughly the same exponentially localized profile over the momentum basis. This surprising interference effect requires the coherence of the quantum state. The square root of the quantum standard deviation $\sqrt{\langle (\Delta \hat{J})^2 \rangle}$ represents the number of states that are significantly populated in the system, and is essentially static after n^* iterations, representing the onset of localization. Therefore, the localization length

$$l = \sqrt{\langle (\Delta \hat{J})^2 \rangle} = \sqrt{Dn^*} \quad (2.5)$$

serves as a useful parameter for characterizing a localized state. The inverse participation ratio (IPR) is another useful quantity for describing localized states [7]. However, the IPR of a localized state is approximately half of the localization length, and the IPR has a minimum value of 1. Therefore the IPR is not useful in the parameter regime discussed here, where $l < 2$.

The heuristic approximation $n^* \approx D \approx l$ [8] yields a theoretical prediction of the localization length based on the kick strength $l \approx (\pi^2/3)k^2$. Quantum localization occurs when the localization length is less than the total breadth of the phase space N . However, the degree to which a physical system becomes localized may be reduced by noise effects,

as this unique quantum phenomenon is quite sensitive to decoherence and other types of errors [65, 67, 84, 99]. This sensitivity poses a rigorous challenge when trying to create and maintain a localized state on a noisy QIP.

The implementation of the quantum sawtooth map reported here takes $L = 7$, $K = 1.5$, $N = 8$, which corresponds to the classically chaotic regime, with a diffusion coefficient of $D \approx (\pi^2/3)k^2 = 0.24$. The theoretical approximation that $n^* \approx D$ predicts that the system will be localized after one iteration of the map ($n^* < 1$). This effect is known as perturbative localization, where the system is localized without the initial diffusive behavior. The results of numerical simulations plotted in Fig. 2-1 confirm this prediction, as the breadth of the probability distribution is essentially static after a single iteration of the quantum map.

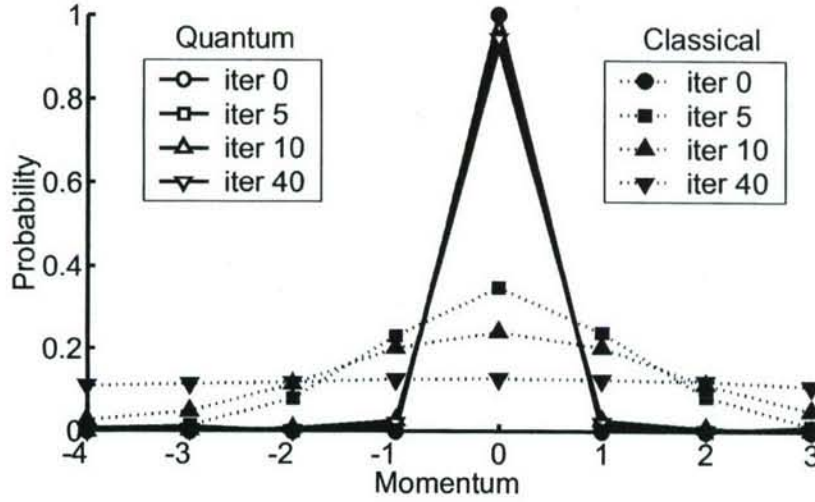


Figure 2-1: The momentum distribution after 0, 5, 10, and 40 iterations of the classical (red, filled markers) and quantum (blue, unfilled markers) sawtooth maps ($L = 7$, $K = 1.5$, $N = 8$). The classical distribution represents 20,000 realizations of the map, with initial momenta $j = 0$ and random initial positions uniformly distributed over the phase space. The initial quantum state is the $j = 0$ momentum eigenstate. In the quantum case, the momentum is discrete, and each data point represents the population of the indicated momentum state. In the classical case, the momentum is continuous, and each data point represents the probability of momentum being in the range of the indicated value $\pm 1/2$. The classical map is chaotic, which leads to the observed diffusive broadening. In the quantum map, since the localization length is less than 1, the state remains exponentially localized after a single iteration. The breadth of the momentum distribution is essentially static in the quantum case, and only the $j = 0$ momentum state is significantly populated.

2.2 Implementation details

An algorithm for the quantum sawtooth map can be generated by expressing the matrix elements of the map in the momentum basis:

$$\begin{aligned}
\langle j | U_{saw} | j' \rangle &= \sum_m \langle j | \exp(-iT\hat{J}^2/2) | \theta_m \rangle \langle \theta_m | \exp(ik(\hat{\Theta} - \pi)^2/2) | j' \rangle \\
&= \sum_m \exp(-iTj^2/2) \langle j | \theta_m \rangle \exp(ik(\theta_m - \pi)^2/2) \langle \theta_m | j' \rangle \\
&= \langle j | U_J U_{QFT}^{-1} U_{\Theta} U_{QFT} | j' \rangle
\end{aligned} \tag{2.6}$$

where U_{QFT} is the familiar Quantum Fourier Transform (QFT) which has the action of toggling between the position and momentum basis representations, and the diagonal free evolution and kick operators, U_J and U_{Θ} , are defined

$$\langle j | U_J | j' \rangle = \exp(-iTj^2/2) \langle j | j' \rangle \tag{2.7}$$

$$\langle \theta_m | U_{\Theta} | \theta'_m \rangle = \exp(ik(\theta_m - \pi)^2/2) \langle \theta_m | \theta'_m \rangle. \tag{2.8}$$

This form of the quantum sawtooth map ($U_{saw} = U_J U_{QFT}^{-1} U_{\Theta} U_{QFT}$) reveals the underlying structure of the map: After the system is initialized to a momentum basis state, the first operation in the quantum sawtooth map, the QFT, transforms the system to the position basis representation, where the diagonal kick operator U_{Θ} applies an impulse force. The inverse of the QFT is applied next, returning the system to the momentum basis representation, where the diagonal free evolution operator U_J is applied. These four steps ($U_{QFT}, U_{\Theta}, U_{QFT}^{-1}, U_J$) constitute a single iteration of the quantum sawtooth map. After iterating the map, the localized probability distribution corresponds to the diagonal elements of the density matrix, $W_j \equiv \langle j | \hat{\rho} | j \rangle$. Realizing that the only effect of the free evolution operator is to apply a phase to the coefficient of each momentum basis state, U_J can be neglected in the final iteration of the map, since a phase does not alter the measured probabilities in that basis.

Quantum circuits. A quantum circuit for the QFT is derived in [82] and shown in Fig. 2-2(b). Prior implementations and experimental analysis of the QFT are described in [115, 117]. Circuits for U_J and U_{Θ} are conveniently found in realizing that any diagonal

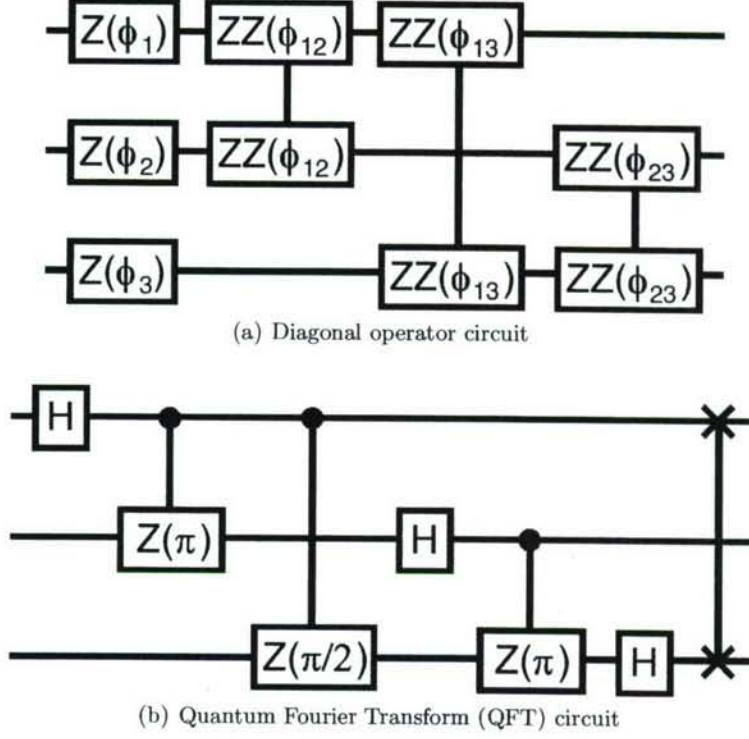


Figure 2-2: Quantum circuits for implementing the quantum sawtooth map. For both circuits, $Z(\chi)$ on qubit l indicates the Z-rotation, $\exp(-i\chi\sigma_z^l/2)$. $ZZ(\chi)$ on qubits l and k indicates the two-qubit operation $\exp(-i\chi\sigma_z^l\sigma_z^k)$. H indicates the Hadamard operator $(\sigma_x^l + \sigma_z^l)/\sqrt{2}$, and the two-qubit operation at the end of the QFT is the swap gate. (Top) The circuit for implementing any diagonal unitary operator. This circuit can be parameterized for either the diagonal free evolution operator U_J or the diagonal kick operator U_Θ using $\phi_l = 2^{l-1}(\alpha + 7\beta)$ and $\phi_{lk} = 2^{l+k-3}\beta$, where the α_J , α_Θ , β_J and β_Θ derived in the text. (Bottom) The QFT and its inverse are both used to implement the quantum sawtooth map.

operator can be decomposed into a series of single-qubit Z-rotations and two-qubit ZZ-interactions. The quantum sawtooth map is emulated by programming the gates in Fig. 2-2(a) to implement U_J and U_Θ . Parameterization of the circuit follows from a decomposition of the basis number operator $\hat{M} |m\rangle = m |m\rangle$, where $0 \leq m < N$, into a sum of products of spin operators

$$\hat{M} |m\rangle = \sum_{l=1}^{n_q} \left(\mathbb{1} - \sigma_z^l \right) 2^{l-2} |m\rangle, \quad (2.9)$$

where σ_z^l indicates the Pauli operator σ_z acting on the l^{th} qubit. For example $\sigma_z^{(l=n_q)} = \sigma_z \otimes 1 \otimes \dots \otimes 1$, and $\hat{M} |10 \dots 0\rangle = 2^{n_q} |10 \dots 0\rangle$.

In general,

$$\exp(-i\alpha\hat{M}) = \exp\left(-i\alpha \sum_{l=1}^{n_q} \left(\mathbb{1} - \sigma_z^l\right) 2^{l-1}\right) \quad (2.10)$$

$$\propto \exp\left(+i\alpha \sum_{l=1}^{n_q} \sigma_z^l 2^{l-1}\right) \quad (2.11)$$

$$\begin{aligned} \exp(-i\beta\hat{M}^2) &\propto \exp\left(+i\beta \left(\sum_{j=1}^{n_q} 2^{j-1}\right) \sum_{l=1}^{n_q} \sigma_z^l 2^{l-2}\right) \dots \\ &\exp\left(-i\beta \sum_{l < j}^{n_q} 2^{l+j-3} \sigma_z^l \sigma_z^j\right) \end{aligned} \quad (2.12)$$

where \propto indicates terms proportional to identity have been dropped since they have no observable effect on the quantum state. By identifying $\hat{\Theta} = 2\pi\hat{M}/N$, we can write the diagonal kick operator

$$U_\Theta = \exp\left(ik(\hat{\Theta} - \pi)^2/2\right) = \exp\left(\frac{ik}{2} \left(\frac{2\pi\hat{M}}{N} - \pi\right)^2\right) \quad (2.13)$$

$$\propto \exp\left(\frac{+i2k\pi^2}{N^2} (\hat{M}^2 - N\hat{M})\right) \quad (2.14)$$

$$\begin{aligned} &\propto \exp\left(+i \left(\alpha_\theta + \left(\sum_{j=1}^{n_q} 2^{j-1}\right) \beta_\theta\right) \sum_{l=1}^{n_q} \sigma_z^l 2^{l-1}\right) \dots \\ &\exp\left(-i\beta_\theta \sum_{l < j}^{n_q} 2^{l+j-3} \sigma_z^l \sigma_z^j\right) \end{aligned} \quad (2.15)$$

where we have defined

$$\alpha_\theta \equiv 2k\pi^2/N \quad (2.16)$$

$$\beta_\theta \equiv -2k\pi^2/N^2. \quad (2.17)$$

Equation 2.15 indicates that U_Θ is implemented by n_q single-qubit Z -rotations and $3n^2$ two-qubit ZZ -interactions. Each operation is parameterized by the values in the exponents of equation 2.15.

The parameters for implementing the diagonal free evolution operator can be found in a similar manner by recognizing that $\hat{J} = \hat{M} - N/2$, and therefore

$$U_J = \exp\left(-iT\hat{J}^2/2\right) = \exp\left(\frac{-iT}{2}\left(\hat{M} - \frac{N}{2}\right)^2\right) \quad (2.18)$$

$$\propto \exp\left(\frac{-iT}{2}\left(\hat{M}^2 - N\hat{M}\right)\right) \quad (2.19)$$

$$\propto \exp\left(+i\left(\alpha_J + \left(\sum_{j=1}^{n_q} 2^{j-1}\right)\beta_J\right)\sum_{l=1}^{n_q} \sigma_z^l 2^{l-2}\right) \dots$$

$$\exp\left(-i\beta_J \sum_{l < j}^{n_q} 2^{l+j-3} \sigma_z^l \sigma_z^j\right) \quad (2.20)$$

where we have defined

$$\alpha_J \equiv -TN/2 \equiv -\pi L \quad (2.21)$$

$$\beta_J \equiv T. \quad (2.22)$$

This circuit for the quantum sawtooth map is computationally efficient, in that the number of fundamental quantum gates required to implement the algorithm depends polynomially on the number of qubits [7].

NMR QIPs. In NMR quantum information processing, nuclear spins polarized by a strong external magnetic field serve as qubits. The molecule used in this experiment, diagrammed in Fig. 2-3, is tris(trimethylsilyl)silane-acetylene dissolved in deuterated chloroform. The carbon nuclei in the acetylene branch are carbon-13 enriched, and the methyl carbons are of natural isotopic abundance. The two carbon-13 nuclei and the hydrogen nucleus in the acetylene branch are used as qubits. The full internal Hamiltonian has the

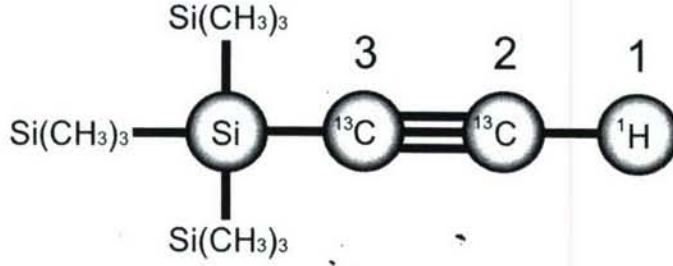


Figure 2-3: A diagram of the tris(trimethylsilyl)silane-acetylene molecule used to simulate the quantum sawtooth map in a liquid state NMR QIP. The hydrogen nucleus in the acetylene branch is labeled qubit 1 in the experiment; the two carbon-13 nuclei in the acetylene branch are labeled qubits 2 and 3.

form

$$\mathcal{H}_{int} = \sum_{i=1}^{n_q} \pi \nu_i \sigma_z^i + \sum_{j < k} \frac{\pi J_{jk}}{2} \sigma^j \cdot \sigma^k \quad (2.23)$$

where ν_i is the resonance frequency of the i^{th} spin, and J_{jk} is the frequency of scalar coupling between spins j and k . Note that J_{jk} is not related to the quantum operator \hat{J} . The hydrogen nucleus is labeled qubit number 1, making it the most significant bit in the computational state vector. The carbon qubits are labeled as indicated in Fig. 2-3. Experiments are performed in a 9.4 Tesla magnetic field, where the Carbon qubits are separated by 1.201 kHz. The scalar couplings are $J_{12} = 235.7$ Hz, $J_{23} = 132.6$ Hz, and $J_{13} = 42.9$ Hz. Because the spin system is in a highly mixed state at room temperature, the system was prepared in a pseudopure state [20] by the technique described in [104]. Three readout sequences were needed to measure the eight diagonal elements of the density matrix, which correspond to the distribution of momentum basis states.

Pulse sequences. The average gate fidelity [37] of each unitary control sequence was optimized over the full Hilbert space. The input state preparation pulse sequence, which is non-unitary, was optimized based on the state correlation [37] between the simulated input state $\hat{\rho}_{sim}$ and the ideal input state $\hat{\rho}_{ideal} = |100\rangle\langle 100|$. The average fidelity (or state correlation) of each implemented pulse sequence, as calculated by numerical simulation, is listed in Table 2.1. The NMR pulse sequence for one full iteration of the quantum sawtooth map is shown in Fig. 2-4.

Table 2.1: Pulse sequences designed for the quantum sawtooth map experiment. Fidelities are calculated by numerical simulations which account for rf inhomogeneity, neglecting decoherence effects.

Map	Duration (ms)	Fidelity
Input State Preparation	50	$Corr = 0.99$
QFT	6	0.99
QFT Inverse	6	0.99
J Diagonal	50	0.99
Θ Diagonal	20	0.99
Readout 1	0.01	1.00
Readout 2	62	0.98
Readout 3	72	0.98

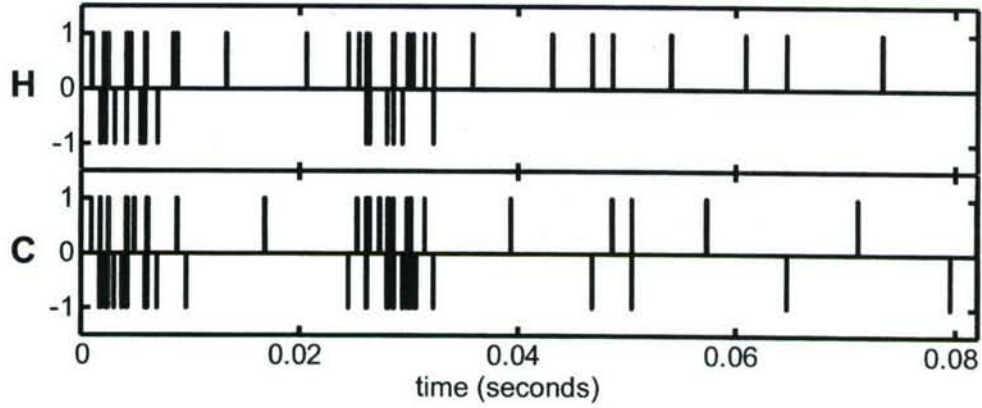


Figure 2-4: The hydrogen (H) and carbon (C) rf control fields versus time for the full quantum sawtooth map pulse sequence. Red versus blue pulses are 90 degrees out of phase; pulses above versus below the horizontal axis are 180 degrees out of phase. The nutation frequency of each hydrogen (carbon) pulse is 46.7 kHz (17.5 kHz).

2.3 Numerical simulation

Through numerical simulation of the experiment, it is possible to predict the behavior of the system under the optimized control sequence in the presence of various types of noise known to influence the QIP. Errors affecting the implementation of the quantum sawtooth map are conveniently classified in three categories [10,88,115] - coherent errors, decoherent errors, and incoherent errors - which can be generally used to categorize the errors affecting any QIP. Each type of error delocalizes the system in a different manner.

In the presence of coherent errors, the system evolves under a unitary process other than the ideal quantum sawtooth map. Due to their unitary nature, coherent errors are reversible. The coherent errors modeled in numerical simulations arise in the experiment due to strong coupling between the carbon qubits, as well as the action of the internal Hamiltonian during rf pulses. Coherent errors delocalize the system by introducing unitary transitions between momentum states.

Decoherent errors cause the individual members of the ensemble (and hence the observed ensemble average) to evolve in a non-unitary fashion. Decoherent evolution can be modeled as a coupling between the system and an external environment and can usually be represented by a completely positive linear map, expressed as an $N^2 \times N^2$ superoperator \hat{S} acting on a columnized $N^2 \times 1$ state vector $|\rho\rangle$, according to

$$|\rho_{out}\rangle = \hat{S} |\rho_{in}\rangle. \quad (2.24)$$

Decoherent errors are accounted for in numerical simulations by allowing the system to evolve under an approximate relaxation superoperator [35], which is completely diagonal in the generalized Pauli basis. In this diagonal form, each non-zero entry in the relaxation superoperator represents the decoherence rate of a generalized Pauli basis operator; the specific values used in simulations are based on measurements of all T1s in the three qubit system as well as the single species T2s.

Given the time scale of one full iteration of the quantum sawtooth map (10^{-1} s) compared to the system's typical decoherence rates (1 s^{-1}), decoherence in this system is in the moderately dissipative regime, which has been shown to cause delocalization in the quantum sawtooth map [65]. The non-unitary, dissipative action of decoherence along with the mixing action of the control sequence causes an essentially uniform damping of the

measured probability distribution, accompanied by a uniform background offset that conserves probability. The background offset in probability appears in the density matrix as an increased identity component, which represents a loss of system purity and a corresponding increase in the von Neumann entropy of the system. In this way, the effect of decoherence is to mimic the diffusive, chaotic dynamics of the classical system described in Sec. 2.1.

Incoherent errors occur when the various members of the experimental ensemble experience a distribution of unitary time evolution operators. Incoherent evolution can be generally expressed as an operator sum

$$\rho_{out}^{inc} = \sum_k p(k) U_k \rho_{in} U_k^\dagger, \quad (2.25)$$

where $p(k)$ is the probability that a member of the ensemble will undergo unitary time evolution under U_k . Under incoherent errors, the individual members of the ensemble evolve coherently, but the ensemble-averaged time evolution of the system is non-unitary. The dominant incoherent errors in the experiment arise due to the inhomogeneity of the rf field over the spatial extent of the liquid state NMR sample. When an rf pulse is applied during the experiment, the members of the ensemble experience a distribution of rf powers, and only a fraction of the ensemble actually experiences precisely the nominal (ideal) rf power. In numerical simulations, we can approximate the effects of the continuous distribution of carbon rf powers by simulating a previously measured distribution of nine discrete bins of rf power, plotted in Fig. 2-5. Bin 6 represents the largest portion of the ensemble and corresponds to the nominal rf power, while the other eight bins result from the inhomogeneity of the rf control field. In the experiment, there are two dimensions of incoherence: one for both the proton and carbon rf-control fields. In numerical simulations presented in Sections 2.4 and 2.5, the continuous distribution of carbon and hydrogen rf power correlations is approximated by a discrete two-dimensional (9×9) rf probability distribution function.

Simulating only the one-dimensional distribution of carbon rf power in Fig. 2-5 is sufficient for gaining a qualitative understanding of the effects of incoherent noise in the experiment. Figure 2-6 shows the results of numerical simulations of the experimentally implemented control sequence for each bin of rf power; the simulations include decoherence effects. Due to the incoherence, the local errors are different for each bin. Consequently, in regions of the ensemble where the rf power is near the nominal rf power (see Bins 6

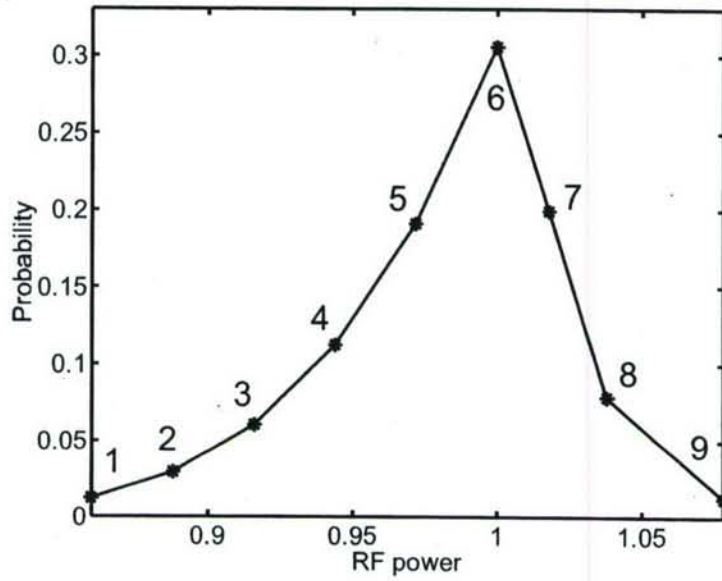


Figure 2-5: The nine point distribution of carbon rf powers measured in previous experiments and used to simulate the experimentally implemented control sequence for the quantum sawtooth map. The carbon rf power is in units of the nominal carbon nutation frequency, 17.5 kHz. The numerals labeling each point in the distribution indicate the associated bin of incoherence in Fig 2-6.

through 8), the fidelity of implementation of the sawtooth map is sufficient that we observe localization. For other regions which constitute a smaller percentage of the ensemble (e.g. Bin 1), the errors are large enough to prevent localization and the momentum distribution is broad. Hence we see that in the experiment, when we observe the weighted average of these distributions, the (more abundant) localized portions of the ensemble will appear as a peak in the $j = 0$ momentum state, and the delocalized portions of the ensemble will contribute an approximately uniform background offset across the momentum distribution.

Another important insight gained from analyzing distributions plotted in Fig. 2-6 is that the bins where the rf power is near ideal are relatively unaffected by decoherence. Consequently, we expect incoherence rather than decoherence to be the principle source of noise compromising our ability to observe localization over the ensemble. This is discussed in more depth in Sec. 2.5.

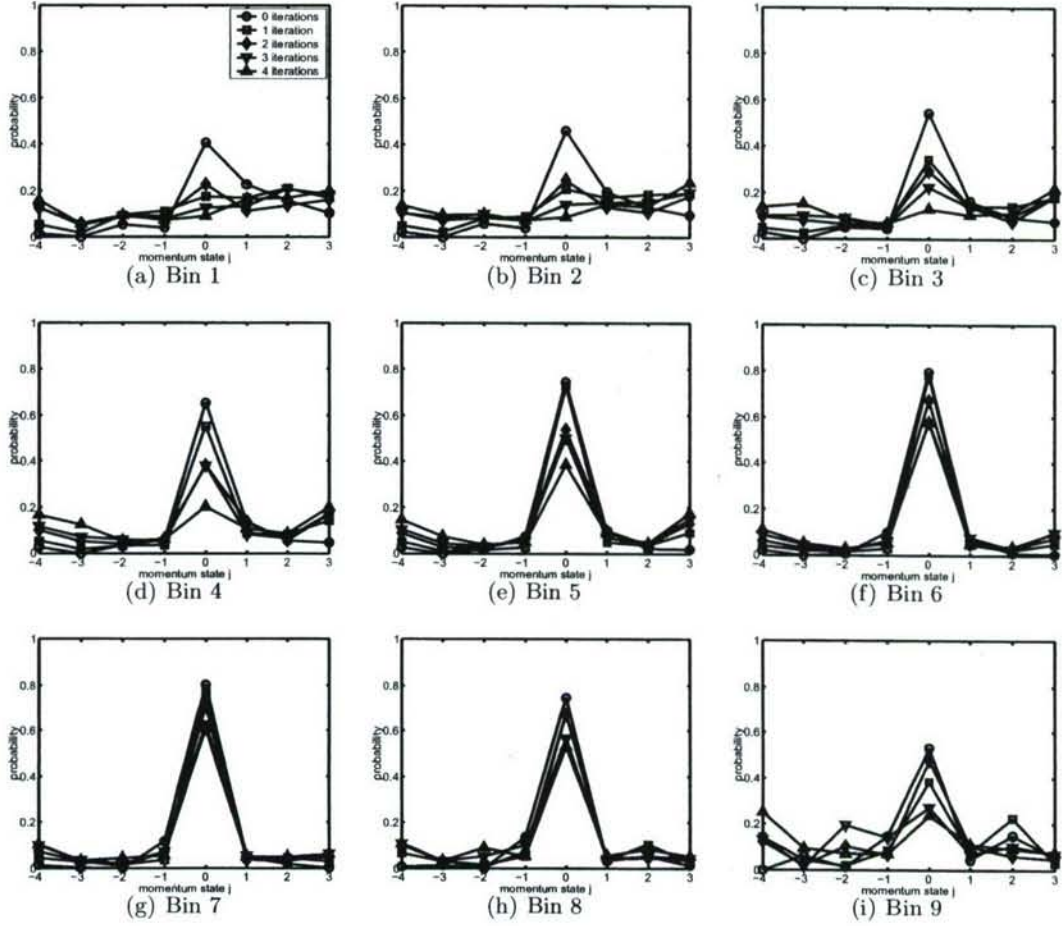


Figure 2-6: Momentum profiles for different regions of the ensemble generated by numerical simulations of the experiment which account for T1 and T2 decoherence. Each plot represents the momentum profile resulting from a numerical simulation of the control sequence (zero through four iterations) with the carbon rf power indicated in Fig. 2-5. Bin 6 represents the nominal rf power, which has the highest fidelity when compared to the ideal quantum sawtooth map. The distributions simulated near the nominal rf power appear to be localized, while those far from the nominal rf power are quickly delocalized. In experiments, the average over the incoherence is observed (weighted by the probability distribution in Fig. 2-5).

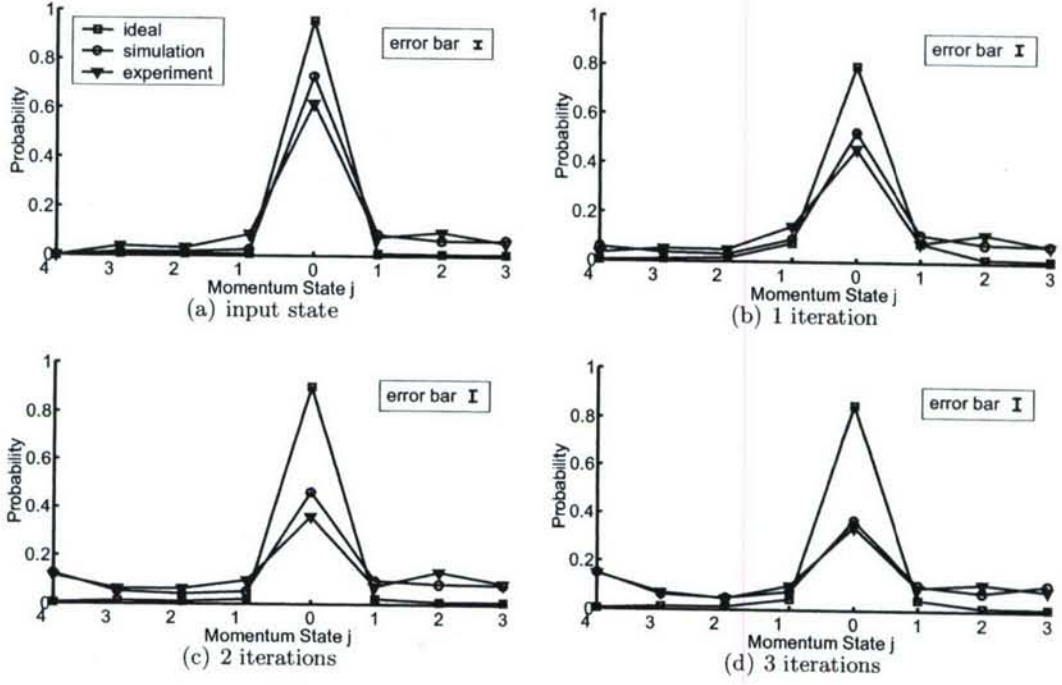


Figure 2-7: The momentum distribution after 0 through 3 iterations of the quantum sawtooth map ($L = 7$, $K = 1.5$, $N = 8$) for the experiment (triangles), a numerical simulation of the experiment which is not affected by noise (squares), and finally a numerical simulation of the experiment which includes coherent errors, decoherence effects, and incoherent errors due to rf inhomogeneity in both the carbon and hydrogen control fields (circles). Error bars are drawn to scale for each iteration. The population of the initial state ($j = 0$) dominates the distribution through 3 iterations of the experiment, and the width of the central peak is essentially unchanged. However, experimental noise clearly causes the ensemble-averaged state to delocalize through the appearance of a baseline offset over the momentum distribution.

2.4 Experimental results

In Fig. 2-7, the experimentally measured probability distributions after zero through three iterations of the quantum sawtooth map are plotted along with the ideal distributions and the distributions obtained by numerical simulations of the experiment which account for decoherence and the full two-dimensional distribution of rf powers. The experimental data reveals that the interior region of the momentum distribution does not broaden, as in a diffusive regime, but rather, the peak maintains roughly the same breadth, as predicted by simulations. Meanwhile, the increasing background probability offset reveals the presence of imperfections in the implemented map, representing those regions of the ensemble which

are not localized due to incoherence. These qualitative features of the experimental data are reflected in the quantitative measures of localization discussed later.

Discrepancies between the ideal and experimentally observed behavior are caused by experimental noise and decoherence influencing the implementation of quantum sawtooth map, in addition to imperfections in the experimentally prepared input state and in the readout steps. Figure 2-7 reveals, on a qualitative level, that these discrepancies are well accounted for by the noise model used in numerical simulations. The relative contribution of the distinct noise mechanisms to the experimentally observed delocalization of the state is discussed further Sec. 2.5.

In light of the incoherent variations of localization properties of the map over the ensemble, we wish to select a measure that can be interpreted as the extent to which some portion of the ensemble demonstrates quantum localization. By measuring the full width at half maximum (FWHM) of the probability distribution in successive iterations, we can observe the presence of any dynamical broadening of the distribution, without regard to the background probability offset caused by incoherence, as discussed in Sec. 2.3. Fig. 2-8 shows a plot of the FWHM for each probability distribution plotted in Fig. 2-7. The FWHM data reveals the dynamical properties of the experimentally measured distribution as distinct from the classical behavior. The relative flatness of the experimentally measured FWHM curve through three iterations of the map is consistent with quantum localization in an incoherent ensemble. Numerical simulations show the progression in peak width from the ideal simulation (most narrow) to simulations where decoherence and incoherence are included in the simulation. The numerical simulation which accounts for decoherence but not incoherence corresponds to the momentum distributions plotted in Bin 6 of Fig. 2-6.

2.5 Discussion

By using numerical simulations to isolate the various types of errors known to influence the experiment, it is possible to measure the relative significance of each type of error by examining the degree to which it leads to delocalization in the system. Figure 2-9 shows the degree to which each type of error causes delocalization in the resulting state, as measured by the second moment of the corresponding probability distribution, thus distinguishing the relative importance of the distinct noise mechanisms in the experiment. The data also

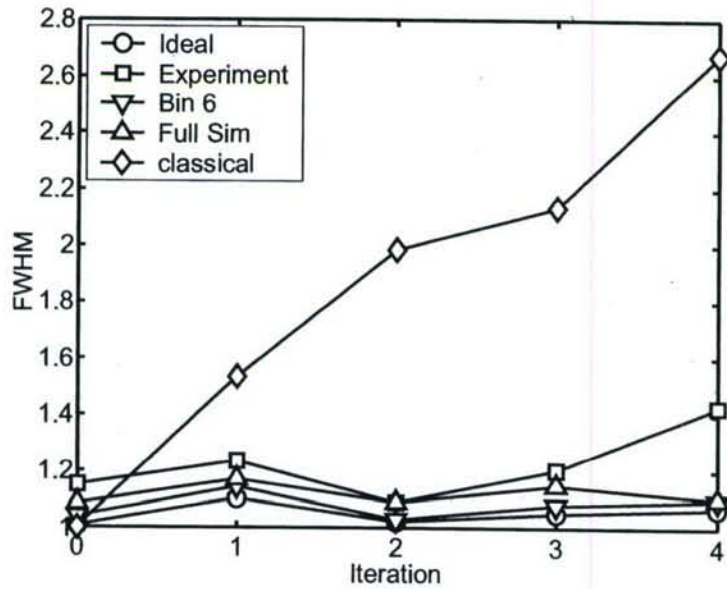


Figure 2-8: The full width at half maximum of the momentum distribution after zero through four iterations of the sawtooth map in various implementations: a numerical simulation of the exact classical map (diamonds), a numerical simulation of the exact quantum map (circles), the experimentally implemented map (squares), a numerical simulation of the experimentally implemented map which accounts for decoherence without incoherence (triangles down), a numerical simulation of the experimentally implemented map which accounts for decoherence with incoherence (triangles up). The FWHM reveals that despite the noise affecting the QIP, the distribution mimics the ideal quantum behavior, and does not broaden in a diffusive manner as in the classical case.

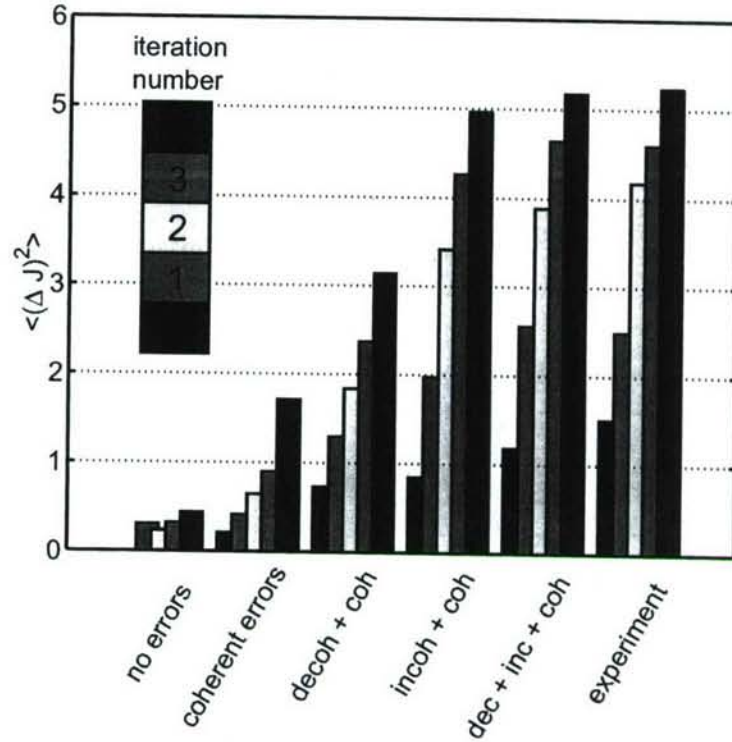


Figure 2-9: The second moment of the probability distribution determined from numerical simulations of the experiment including the error models discussed in the text, compared to the ideal data and the experimental data. This plot demonstrates the relative importance of the individual noise mechanisms as they contribute to the experimentally observed delocalization process. As more errors are included in numerical simulations, the system shows stronger delocalization and more closely emulates the experimental data.

reveals the extent to which the breadth of the distribution is affected by errors in the initial state preparation. Evidently, the coherent errors are essentially inconsequential over at least three iterations of the map. The slope of second moment versus time plot is most strongly affected by incoherent errors, and thus incoherence is determined to be the dominant noise mechanism limiting the degree to which localization is achieved by experimental control, which is consistent with the observations of Sec. 2.3.

Additional insight on the delocalizing effects of experimental noise and decoherence can be gained by examining the superoperators and the corresponding Kraus operators for each type of numerical simulation. A superoperator of dimension $N^2 \times N^2$ which describes a completely positive quantum process can be equivalently expressed as an operator sum, which involves at most N Kraus operators of dimension $N \times N$ [60]. That is to say that for a general quantum process as in Eq. 2.24,

$$|\rho_{out}\rangle = S |\rho_{in}\rangle \quad (2.26)$$

there is an equivalent representation of the form

$$\rho_{out} = \sum_k A_k \rho_{in} A_k^\dagger \quad (2.27)$$

where A_k is the k^{th} Kraus operator, which has a magnitude of $\|A_k\|$. Methods for conversion to and analysis of the Kraus form are given in [47] and [115]. The Kraus form for an ideal implementation of a unitary process would consist of a single Kraus operator which is the corresponding unitary operator describing the process. Therefore, in an implementation where the errors are small, we expect the Kraus operator of largest magnitude to resemble the ideal unitary operator. The numerically simulated superoperators expressed in the momentum basis, along with the largest magnitude Kraus operators, plotted in Fig. 2-10, give a qualitative picture of the differences between a quantum process that leads to localization (in the ideal simulations) and a quantum process that causes some degree of delocalization (in the simulations which include errors). Off-diagonal elements in the unitary or Kraus operator cause transitions between momentum states; diagonal elements alter the magnitude and phase of each momentum state without causing transitions. The qualitative result of the simulated noise is to reduce the bandedness (i.e. the relative magnitude of the

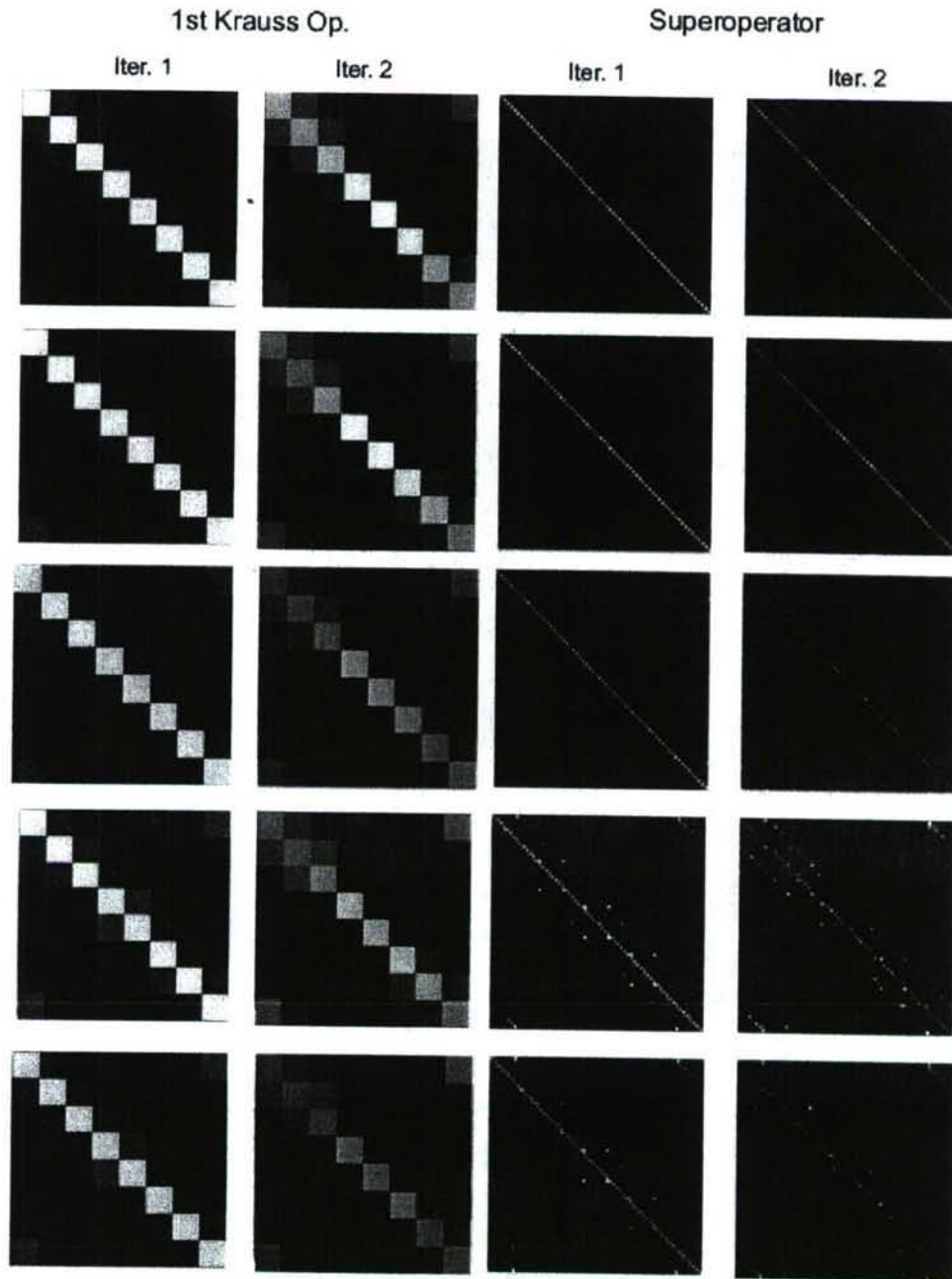


Figure 2-10: The magnitude of each element of the superoperators and most significant Kraus operators for numerical simulations of the quantum sawtooth map experiment which include different types of errors (top to bottom): (1) no errors, (2) coherent errors, (3) coherent errors and decoherent errors due to relaxation, (4) coherent errors and incoherent errors due to rf inhomogeneity, (5) coherent, incoherent, and decoherent errors. The elements are scaled from zero (black) to one (white). The errors in the implementation of the sawtooth map affect the bandedness of each Kraus operator (and similarly of each superoperator).

diagonal and near-diagonal elements compared to the off-diagonal elements) of the operator, thus reducing the degree to which a state is localized under the map. The simulated operators for 1 and 2 iterations are progressively less banded as more errors are included in the simulation, which further attests to the sensitivity of localization to experimental noise effects. As explained in Sec. 2.3, Fig. 2-10 again shows qualitatively that rf inhomogeneity has a greater delocalizing effect than decoherence in this implementation of the quantum sawtooth map.

2.6 Conclusions

The quantum sawtooth map has been emulated on a three qubit liquid state nuclear magnetic resonance quantum information processor in the perturbative localization parameter regime of the map ($K = 1.5$, $L = 7$, $N = 8$). Observing the dynamic behavior of the width of the peak in the momentum probability distribution reveals behavior which is consistent with coherent quantum localization. Due to incoherent noise, this localized peak is superimposed with a uniform background offset over the probability distribution which represents those parts of the ensemble which are not localized due to local unitary errors which vary over the ensemble.

Numerical simulations of the experiment reveal that the decoherent noise known to act on the system is relatively inconsequential in this implementation of the map, in terms of its effect on localization when compared with incoherence. This study serves as a test of the capabilities of coherent control and serves to motivate the refinement of our implementation. Specifically, we see that incoherence is the biggest challenge in implementing localization, a highly sensitive quantum coherence-dependent phenomenon. Given the sensitivity of localization to various types and strengths of errors, the degree to which localization can be created and maintained in a QIP serves as a benchmark of practical relevance for assessing the overall degree of coherent control and for identifying which noise mechanisms most significantly reduce the degree of coherent control achieved in the device.

Chapter 3

Signatures of incoherence

Incoherent noise encodes quantum information into the classical degrees of freedom of an ensemble by a distribution of unitary errors. An incoherent process is tied to a time-independent or slowly varying classical probability distribution of Hamiltonians. Evolution under such a process is naturally described as an operator sum, given in superoperator notation by

$$\hat{S}(t) = \int p(z) e^{i\mathcal{H}(z)t} \otimes e^{-i\mathcal{H}(z)t} dz \quad (3.1)$$

where $p(z)$ is the classical probability distribution of Hamiltonians $\mathcal{H}(z)$. A variety of tools have been developed to counteract incoherent noise in quantum information processors. Optimal control theory minimizes the errors caused by uncertainty in the system Hamiltonian [25, 85]. Dynamical decoupling and bang-bang control actively suppress incoherence by periodically refocusing part of the evolution [109, 111–113]. Strongly modulating pulses [88] and composite pulses [68] have also been used to refocus incoherent noise. Such techniques exploit the reversibility of incoherent errors and are particularly valuable since they do not require access to a larger Hilbert space, as do decoherence free subspaces [32, 70, 122], noiseless subsystems [58, 122] and other quantum error encodings [96, 100]. Decoherent noise by contrast does require the full power of quantum error-correcting codes, so distinguishing the presence of incoherence is important in choosing an error-correction scheme.

Incoherence, which is typically studied for single-qubit errors in $SU(2)$, causes a loss of purity in the ensemble-averaged state while preserving the purity of the individual ensemble members. Decoherence is a distinct process that irreversibly reduces the purity of

the individual ensemble members. In small Hilbert spaces, incoherence is easily detected and controlled either by time reversal of the control field or through creation of echoes. Some classic examples include the rotary echo [53, 91], the Hahn echo [46], the Carr-Purcell and CPMG echo sequences [15, 78]. In these examples, incoherent errors are completely refocused by an inverted incoherent process, and the resulting increase in purity over the ensemble causes an observable echo. Identifying and controlling incoherence is more difficult in Hilbert spaces that support entanglement and in particular, in the presence of an entangling operation. An entangling operation propagates incoherent errors to non-separable states, causing a loss of purity that is not recovered by an inverted incoherent process, so the incoherence mimics a decoherent process.

Here we present an example of incoherence influencing an entangling operation in a three-qubit liquid state NMR QIP, and we show how the incoherence appears as a distinct process from decoherence in the measurement of fidelity decay under imperfect motion reversal. Fidelity decay [86] has previously been shown to be a useful tool for efficiently characterizing errors in a QIP [33]. In the method suggested here, the task of measuring fidelity decay is simplified by studying fidelity decay under a cyclic operation, which removes the need to invert the ideal evolution and admits analysis by Average Hamiltonian Theory [44]. We show that in our experiment incoherence causes recurrences in fidelity that could not arise from a decoherent process. The signature of incoherence observed in experimental data is also analyzed by numerical simulations of the NMR experiment.

3.1 Identifying incoherence by fidelity decay

The fidelity between two quantum states ρ and $\tilde{\rho}$ is defined

$$F = \langle \tilde{\rho} | \rho \rangle, \quad (3.2)$$

where $|\rho\rangle$ is the density matrix represented as a state vector in Liouville space. Given an ideal unitary map \hat{S} , a perturbation \hat{P} and an initial state ρ_0 , the fidelity decay after n iterations of imperfect motion reversal is

$$F_n = \langle \rho_0 | (\hat{S}^{-1})^n (\hat{P}\hat{S})^n | \rho_0 \rangle. \quad (3.3)$$

Here we consider the case where $(\hat{P}\hat{S})$ is a noisy implementation of \hat{S} , and therefore implementing the ideal inverse map \hat{S}^{-1} is impractical. However, if we choose \hat{S} to be cyclic, then for some number of iterations n_c , we have $(\hat{S}^{-1})^{n_c} = \hat{S}^{n_c} = \mathbb{1}$. Now if we constrain the fidelity decay to be measured only after iterations that are an integer multiple of n_c , we have

$$F_n = \langle \rho_0 | (\hat{P}\hat{S})^n | \rho_0 \rangle, \quad (3.4)$$

thus simplifying the fidelity decay expression and measurement.

In our experiment, we are interested in distinguishing incoherence and decoherence in a fidelity decay. Here we derive an expression for the fidelity decay of an ensemble-averaged state evolving under these two types of noise using a simple noise model. For both types of noise, the measurement ensemble \mathcal{E}_z is parameterized by the classical variable z . For decoherent noise, the state fidelity decays exponentially before saturating at $1/N$ where N is the Hilbert space dimension, a well-known result for decoherent noise [51]. For incoherent noise, we will show that the fidelity decay expression has two terms: one term that decreases as the map is iterated, and an additional term that may periodically increase, allowing for fidelity recurrences.

Let \hat{S} and \hat{P}_z represent unitary processes over a Hilbert space of dimension N . The ideal map \hat{S} acting n times on the initial state ρ_0 returns the state $\hat{S}^n |\rho_0\rangle = |\rho_n\rangle$, while the perturbed map returns the state $(\hat{P}_z \hat{S})^n |\rho_0\rangle = |\tilde{\rho}_n\rangle$. \hat{P}_z is a perturbation of the form $\exp(-i\eta_z \hat{V})$, where \hat{V} is an hermitian operator in the N dimensional Hilbert space and η_z is the strength of the noise for a particular member of the ensemble \mathcal{E}_z . We take $\langle \eta_z \rangle_z = 0$, where $\langle \cdot \rangle_z \Rightarrow \int (\cdot) p(z) dz$, and $p(z)$ is the probability of measuring the ensemble member labeled z . The fidelity decay after n iterations is the overlap of the ensemble average state $\langle \tilde{\rho}_n \rangle_z$ and the ideal state ρ_n

$$F_n = \langle \rho_n | \left\langle (\hat{P}_z \hat{S})^n | \rho_0 \right\rangle_z \rangle = \langle \rho_n | \langle \tilde{\rho}_n \rangle_z \rangle. \quad (3.5)$$

3.1.1 Decoherent noise

Decoherence describes a process whereby information is irreversibly lost to an environment. To model decoherent noise, we consider η_z to be random for a given member of the ensemble

on every iteration of the map. The random process is modeled by individually averaging the evolution of each member of the measurement ensemble \mathcal{E}_z over a stochastic ensemble \mathcal{E}_s that samples the distribution of random η_z values. The distribution of random η_z values satisfies $\langle \eta_z \rangle_s = 0$. The stochastic ensemble \mathcal{E}_s is averaged *before* the measurement ensemble \mathcal{E}_z .

We rewrite the input state $\rho_0 = \frac{1}{N}\mathbb{1} + \chi\sigma_0$, where $\langle \mathbb{1}|\sigma_0 \rangle = 0$, $\chi^2 = (N-1)/N^2$ and $\text{trace}(\sigma_0^2) = N$ guarantee the normalization and purity of ρ_0 . Now $\hat{S}^n |\sigma_0\rangle = |\sigma_n\rangle$, where the unitarity of \hat{S} guarantees $\langle \sigma_n|\mathbb{1} \rangle = 0$. Our normalization conditions include $\langle \sigma_n|\sigma_n \rangle = N$. After the first iteration of the decoherent process

$$\begin{aligned} |\tilde{\rho}_1\rangle &= \left\langle \hat{P}_z \hat{S} |\rho_0\rangle \right\rangle_s = \left\langle \frac{1}{N} |\mathbb{1}\rangle + \chi \hat{P}_z |\sigma_1\rangle \right\rangle_s \\ &= \left\langle \frac{1}{N} |\mathbb{1}\rangle + \chi (a_{01} |\sigma_1\rangle + \mu_{01} |\sigma_{\mu 01}\rangle) \right\rangle_s, \end{aligned} \quad (3.6)$$

where we have decomposed $\hat{P}_z |\sigma_1\rangle$ into a component parallel to the ideal state $|\sigma_1\rangle$ and an orthogonal component $|\sigma_{\mu 01}\rangle$ such that $\langle \sigma_1|\sigma_{\mu 01}\rangle = 0$ and $a_{01}^2 + \mu_{01}^2 = 1$. The value μ_{01} is related to the strength of the noise such that for small errors η_z , we have $\langle \mu_{01} \rangle_s = 0$. Averaging over the stochastic ensemble \mathcal{E}_s , we have

$$|\tilde{\rho}_1\rangle = \frac{1}{N} |\mathbb{1}\rangle + \chi \langle a_{01} \rangle_s |\sigma_1\rangle. \quad (3.7)$$

If we allow the measurement ensemble \mathcal{E}_z and the stochastic ensemble \mathcal{E}_s to sample the same distribution $p(z)$, then we can define $\alpha_{01} \equiv \langle a_{01} \rangle_s = \langle a_{01} \rangle_z$. In this case, averaging $\tilde{\rho}_1$ over \mathcal{E}_z has no effect, and $\langle \tilde{\rho}_1 \rangle_z = \tilde{\rho}_1$. For the decoherent model, the fidelity after one iteration of the perturbed map is

$$F_1^{(D)} = \langle \rho_1 | \langle \tilde{\rho}_1 \rangle \rangle_z = \frac{1}{N} + N\chi^2 \alpha_{01} = \frac{1}{N} + \frac{(N-1)}{N} \alpha_{01} \quad (3.8)$$

Now reiterating the process, the state after two iterations is

$$|\tilde{\rho}_2\rangle = \left\langle \hat{P}_z \hat{S} |\tilde{\rho}_1\rangle \right\rangle_s = \left\langle \frac{1}{N} |\mathbb{1}\rangle + \chi \alpha_{01} (a_{12} |\sigma_2\rangle + \mu_{12} |\sigma_{\mu 12}\rangle) \right\rangle_s \quad (3.9)$$

and

$$F_2^{(D)} = \langle \rho_2 | \langle |\tilde{\rho}_2\rangle \rangle_z = \frac{1}{N} + \frac{(N-1)}{N} \alpha_{01} \alpha_{12}. \quad (3.10)$$

Since $0 \leq \alpha_{j,j+1} < 1$, the general expression for the fidelity decay under decoherent dynamics

$$F_n^{(D)} = \langle \rho_n | \langle |\tilde{\rho}_n\rangle \rangle_z = \frac{1}{N} + \frac{(N-1)}{N} \prod_{j=0}^{n-1} \alpha_{j,j+1} \quad (3.11)$$

is an exponentially decreasing function that saturates at $1/N$, as expected for a decoherent map.

3.1.2 Incoherent noise

Incoherence describes a process whereby information is reversibly encoded in the classical degrees of freedom of an ensemble by a static or slowly varying distribution of Hamiltonians. To model incoherent dynamics for a particular member of the measurement ensemble \mathcal{E}_z , we consider η_z to be a static value for each iteration of the map. In this case there is no stochastic ensemble; the local dynamics are deterministic and reversible. After one iteration of the incoherent map the state of an individual ensemble member is given by

$$|\tilde{\rho}_1\rangle = \frac{1}{N} |\mathbb{1}\rangle + \chi (a_{01} |\sigma_1\rangle + \mu_{01} |\sigma_{\mu 01}\rangle), \quad (3.12)$$

and so the ensemble-averaged state

$$\langle |\tilde{\rho}_1\rangle \rangle_z = \frac{1}{N} |\mathbb{1}\rangle + \chi \langle a_{01} \rangle_z |\sigma_1\rangle. \quad (3.13)$$

has a fidelity of

$$F_1^{(I)} = \frac{1}{N} + \frac{(N-1)}{N} \alpha_{01}, \quad (3.14)$$

which is equivalent to the value $F_1^{(D)}$ measured in the decoherent case. The second iteration of the incoherent process returns the state

$$\begin{aligned} |\tilde{\rho}_2\rangle &= \hat{P}_z \hat{S} |\tilde{\rho}_1\rangle = \frac{1}{N} |\mathbb{1}\rangle + \chi \hat{P}_z (a_{01} |\sigma_1\rangle + \mu_{01} |\sigma_{\mu 01}\rangle) \\ &= \frac{1}{N} |\mathbb{1}\rangle + \chi a_{01} (a_{12} |\sigma_2\rangle + \mu_{12} |\sigma_{\mu 12}\rangle) + \chi \mu_{01} (b_{12} |\sigma_2\rangle + \nu_{12} |\sigma_{\nu 12}\rangle) \end{aligned} \quad (3.15)$$

where we have decomposed $\hat{P}_z |\sigma_{\mu 01}\rangle$ into a component parallel to the ideal state $|\sigma_2\rangle$ and an orthogonal component $|\sigma_{\nu 12}\rangle$ such that $\langle \sigma_2 | \sigma_{\nu 12} \rangle = 0$ and $b_{12}^2 + \nu_{12}^2 = 1$. Unlike the decoherent process, the incoherent process preserves the full $|\sigma_{\mu 01}\rangle$ component after the first iteration. The second iteration of the map may then transform some portion of this component into the ideal state $|\sigma_2\rangle$. The possibility of fully “refocusing” errors in the incoherent case is the essential difference between decoherent and incoherent dynamics, and this difference is what leads to observable signatures of incoherence. Collecting terms, we have

$$\begin{aligned} |\tilde{\rho}_2\rangle &= \frac{1}{N} |\mathbb{1}\rangle + \chi (a_{01} a_{12} + \mu_{01} b_{12}) |\sigma_2\rangle + \chi (\mu_{01} \nu_{12} |\sigma_{\nu 12}\rangle + a_{01} \mu_{12} |\sigma_{\mu 12}\rangle) \\ &= \frac{1}{N} |\mathbb{1}\rangle + \chi (A_2 |\sigma_2\rangle + \Gamma_2 |\sigma_{\Gamma 2}\rangle), \end{aligned} \quad (3.16)$$

and in general we can write $\tilde{\rho}_n$ as a pure state

$$|\tilde{\rho}_n\rangle = \left(\hat{P}_z \hat{S} \right)^n |\rho_0\rangle = \frac{1}{N} |\mathbb{1}\rangle + \chi (A_n |\sigma_n\rangle + \Gamma_n |\sigma_{\Gamma n}\rangle), \quad (3.17)$$

where $\langle \sigma_n | \sigma_{\Gamma n} \rangle = 0$ and $A_n^2 + \Gamma_n^2 = 1$. Now after averaging over \mathcal{E}_z , the fidelity is given by

$$F_2^{(I)} = \frac{1}{N} + \frac{N-1}{N} (\langle a_{01} a_{12} \rangle_z + \langle \mu_{01} b_{12} \rangle_z) \quad (3.18)$$

$$F_n^{(I)} = \frac{1}{N} + \frac{N-1}{N} (\langle A_{n-1} a_{n-1,n} \rangle_z + \langle \Gamma_{n-1} b_{n-1,n} \rangle_z). \quad (3.19)$$

The first term in parenthesis $\langle A_{n-1} a_{n-1,n} \rangle_z$ is similar to the term $\prod_{j=0}^{n-1} \alpha_{j,j+1}$ in the expression for $F_n^{(D)}$, as they both cause the fidelity to decrease on each map iteration since $0 \leq a_{n-1,n} < 1$. However, the second term in parenthesis $\langle \Gamma_{n-1} b_{n-1,n} \rangle_z$ may be nonzero and positive, allowing for an increase, or recurrence, in fidelity ($F_n^{(I)} > F_{n-1}^{(I)}$) in some cases. As an example, consider the Carr-Purcell echo experiment where B_0 field inhomogeneities

are fully refocused by π pulses. However, the recurrence in fidelity decay is more general than a simple echo experiment in which incoherence is inverted by local $SU(2)$ operations. Recurrence in fidelity decay allows errors to be refocused from any part of Hilbert space through the repeated action of the perturbed map.

There is also a third type of noise that is not explicitly included in the model for incoherent or decoherent noise. Coherent noise causes non-ideal unitary errors that are uniform over the ensemble and do not cause a loss of purity in the individual ensemble members or in the ensemble-averaged state. In the noise models above, coherent errors could be incorporated by taking $\langle \eta_z \rangle_z \neq 0$. Like incoherent noise, coherent noise can cause recurrences in fidelity decay. However, there is little motivation to distinguish them in this setting since the two types of noise can be treated with the same techniques, which do not require access to a larger Hilbert space.

Recurrences in a fidelity decay are a unique signature of microscopically reversible dynamics. For the case that \hat{S} is an entangling operation, incoherent errors will cause a loss in the purity of the ensemble that is not recovered by single-qubit operations, and therefore is difficult to distinguish from the effects of decoherence. Fidelity decay under imperfect motion reversal provides an efficient means for observing signatures of incoherence even in the presence of an entangling operation.

3.2 Experiment

Quantum Circuit. Figure 3-1 shows the quantum circuit used to study incoherence in an entangling operation. This circuit is an example of a case where incoherence causes errors in the output state that are not easily distinguished from the effects of decoherence. The first three gates in the circuit create the GHZ state $(|000\rangle + |111\rangle) / \sqrt{2}$. Next, an entangling operation on qubits two and three is repeated $4n$ times. The final three gates convert the resulting entangled state to a separable computational basis state. For odd values of n the final state is $|001\rangle$, and for even values of n the final state is $|000\rangle$. Incoherent noise in the repeated entangling operation will propagate through the Hilbert space, creating entangled components in the final state. These errors cause a loss of purity that mimics decoherence since they are not refocused by inverting the incoherence on the output state.

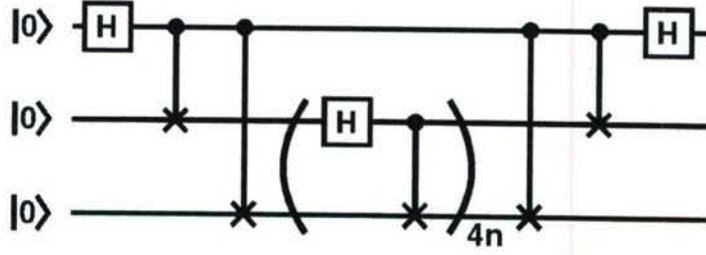


Figure 3-1: The quantum circuit for exploring incoherence in an entangling operation on a QIP. H represents the single-qubit Hadamard operation $(\sigma_z + \sigma_x)/\sqrt{2}$, the two-qubit gate represents a controlled-not operation, which flips the target qubit when the control qubit is in the $|1\rangle$ state. The first three gates create a maximally entangled GHZ state $(|000\rangle + |111\rangle)/\sqrt{2}$, which is followed by $4n$ iterations of a two-qubit entangling operation. The final three gates convert the resulting entangled state to the computational basis state $|000\rangle$ for even values of n and $|001\rangle$ for odd values of n . Incoherence in an entangling operation mimics decoherence by causing a loss of purity that is not refocused in the output state by inverting the incoherence. In our experiment, we observe signatures of incoherence in the two-qubit entangling operation by measuring the fidelity decay of the output state for $n=0$ through 30.

NMR QIP. In NMR quantum information processing, nuclear spins polarized by a strong external magnetic field serve as qubits. The molecule used in this experiment, diagrammed in Fig. 3-2, is tris(trimethylsilyl)silane-acetylene dissolved in deuterated chloroform. The carbon nuclei in the acetylene branch are isotopically enriched ^{13}C , while the methyl carbons are of natural isotopic abundance. The two carbon-13 nuclei and the hydrogen nucleus in the acetylene branch are used as qubits. The full internal Hamiltonian of the nuclear spin system has the form

$$\mathcal{H}_{int} = \sum_{j=1}^{n_q} \pi \nu_j \sigma_z^j + \sum_{j < k} \frac{\pi J_{jk}}{2} \sigma^j \cdot \sigma^k \quad (3.20)$$

where ν_j is the resonance frequency of the j^{th} spin, and J_{jk} is the frequency of scalar coupling between spins j and k . The hydrogen nucleus is labeled qubit number 1, making it the most significant bit in the computational state vector. The repeated entangling operation is applied to the carbon qubits, which are labeled as indicated in Fig. 3-2. Experiments are performed in a 9.4 Tesla magnetic field, where the Carbon qubits are separated by 1.201 kHz. The scalar couplings are $J_{12} = 235.7$ Hz, $J_{23} = 132.6$ Hz, and $J_{13} = 42.9$ Hz.

The initial pseudopure state [20] was created by the technique described in [104] using hard rf pulses and gradient fields. The input state preparation pulse sequence, which is

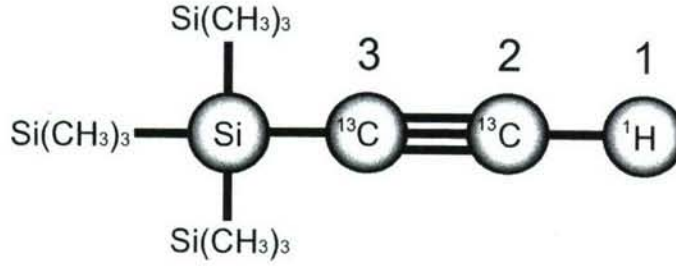


Figure 3-2: A diagram of the tris(trimethylsilyl)silane-acetylene molecule used to implement the quantum circuit in Fig. 3-1 in a liquid state NMR QIP. The two-qubit entangling operation is applied to the two ^{13}C spins in the acetylene branch, labeled qubits 2 and 3. The primary source of incoherence in the experimentally implemented entangling operation is the inhomogeneity of the carbon rf control field.

non-unitary, was optimized based on the state correlation [37] between the numerically simulated input state and the ideal input state. The average gate fidelities [37] of the sequences corresponding to the three sections of the circuit were optimized over the full Hilbert space. In the experiment, representative measurements of the fidelity are taken. A single $\pi/2$ readout pulse on the hydrogen spin was used to measure the σ_z^1 , $\sigma_z^1\sigma_z^2$, $\sigma_z^1\sigma_z^3$, and $\sigma_z^1\sigma_z^2\sigma_z^3$ components of the output density matrix, for $n = 1$ through $n = 30$.

3.3 Numerical simulation

The NMR experiment was numerically simulated on a classical computer. The dominant incoherent noise in the experiment arises due to the inhomogeneity of the rf control field over the spatial extent of the liquid state NMR sample. When an rf pulse is applied during the experiment, the members of the ensemble experience a distribution of rf powers, and only a fraction of the ensemble actually experiences precisely the nominal (ideal) rf power. While the control fields for both the hydrogen and carbon qubits are known to be inhomogeneous, the inhomogeneity of the carbon control field is the dominant source of incoherent errors in the entangling operation. Consequently, our numerical simulations include incoherence for each carbon pulse as a distribution of rf control field strengths. The discrete nine-point distribution used in simulations is plotted in Fig. 3-3. The natural decoherence of the nuclear spin system is simulated by an approximate relaxation superoperator [35], which is completely diagonal in the generalized Pauli basis. In this diagonal form, each non-zero

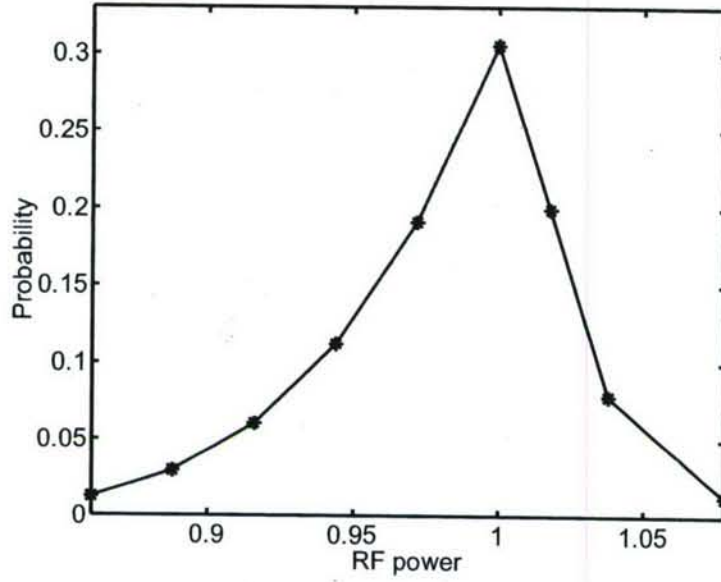


Figure 3-3: The distribution of carbon rf powers measured in previous experiments and used in numerical simulations of the NMR implementation of the circuit in Fig. 3-1. The rf power is in units of the nominal rf nutation frequency (17.5 kHz).

entry in the relaxation superoperator represents the decoherence rate of a generalized Pauli basis operator; the specific values used in simulations are based on measurements of all T1s and the single species T2s.

In numerical simulations, we are interested in the unique features of fidelity decay caused by incoherence. This is accomplished by separating out those parts of the evolution that are uniform over the ensemble. We isolate the effects of incoherence by simulating the rf inhomogeneity in two regimes of dynamics. In the incoherent model, rf inhomogeneity is simulated as it actually occurs in the experiment, as a static distribution of local unitary noise. The output state in this regime is $\left\langle \left(\hat{P}_z \hat{S} \right)^n | \rho_0 \right\rangle_z$. In this model, the full state of each ensemble member is preserved between iterations, which leads to recurrences in fidelity as discussed in Sec. 3.1.2. In the decoherent model, rf inhomogeneity is simulated fictitiously as a stochastic effect, as discussed in Sec. 3.1.1. The output state in this regime is $\left(\left\langle \hat{P}_z \hat{S} \right\rangle_z \right)^n | \rho_0 \rangle$. In this model, averaging the state after each iteration preserves only an average state that is uniform over the ensemble. Differences between the two models arise purely from incoherence. We emphasize that rf inhomogeneity is known to be a static effect, and the fictitious stochastic model is used only to isolate the signatures of incoherence. We also note that the relaxation superoperator, a well-understood source of decoherent noise,

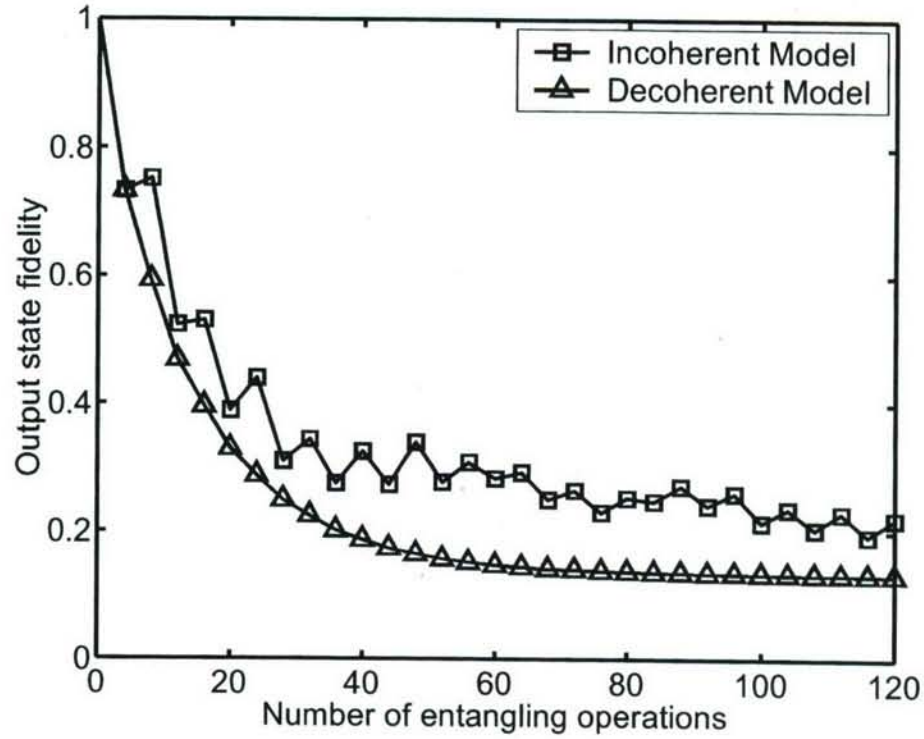


Figure 3-4: The fidelity decay from a numerical simulation of the experiment, where rf inhomogeneity (RFI) is simulated using two different models. RFI is simulated as a static distribution in the incoherent model, while RFI is fictitiously simulated as a stochastic effect in the decoherent model. This fiction allows us to isolate signatures of incoherence. In the incoherent model, fidelity recurrences (which appear as oscillations in the plot) are observed because the purity of the ensemble members is preserved and the repeated action of the entangling map refocuses some of the errors. There are no significant recurrences in the decoherent model because the individual members of the ensemble lose purity, the errors are not refocused, and the fidelity decays steadily and saturates. Comparison of the two plots shows that the fidelity decay recurrences are caused by incoherent noise.

is simulated identically in both models.

The results of numerical simulations are plotted in Fig. 3-4. Although incoherence in entangling operations creates a loss of purity that mimics decoherence, fidelity decay under imperfect reversal of such a process reveals distinguishable properties of the incoherence. The first point in the two fidelity decays are identical, as predicted in Sec. 3.1.2. However, differences in the two models are manifest already in the second point of the fidelity decay, as the fidelity increases only in the incoherent model. Over 120 entangling operations, the numerically simulated fidelity decay for the incoherent case shows rapid oscillations, or recurrences, which are only possible for microscopically reversible dynamics, as discussed in

Section 3.1.2. The decoherent simulation shows a non-oscillatory decay and saturation at a value of the inverse of the dimension of the Hilbert space $1/N$. Differences between the fidelity decays collected in the two regimes reveal a signature of incoherent noise which is also observed in experimental data.

3.4 Results and discussion

Experimental data resulting from an implementation of the optimized control sequences are compared to results of numerical simulations of the experiment for the two models of rf inhomogeneity previously discussed. Rf inhomogeneity is simulated as a static distribution in the incoherent model, while rf inhomogeneity is fictitiously simulated as a stochastic effect in the decoherent model. The fictitious model of a stochastic distribution of rf powers isolates the effects of incoherence from evolution that is uniform over the ensemble. Figure 3-5 shows the sum of the measured magnitudes of four state components (σ_z^1 , $\sigma_z^1\sigma_z^2$, $\sigma_z^1\sigma_z^3$, and $\sigma_z^1\sigma_z^2\sigma_z^3$) obtained by experiment and by numerical simulations. Under the ideal unitary evolution, the value of the plotted sum is 0.5. The experimentally observed value decreases for about 24 iterations of the entangling operation, and then begins to oscillate and later becomes nearly constant. The incoherent model reproduces the important features of the experimental data. The value simulated by the incoherent model oscillates over many iterations, and finally settles to a nearly constant value. By contrast the value simulated by the decoherent model decreases rapidly and steadily, never oscillates, and saturates to zero. This comparison demonstrates that incoherence in the entangling operation appears with distinct signatures in the experimental data.

Some insight is gained by comparing the the individually measured state components of the density matrix (σ_z^1 , $\sigma_z^1\sigma_z^2$, $\sigma_z^1\sigma_z^3$, and $\sigma_z^1\sigma_z^2\sigma_z^3$) in the frequency domain by Fourier transforming the data, as plotted in Fig. 3-6. In each set of axes, the frequency is represented on the horizontal axis in units of oscillation periods per entangling operation. The highest observable (Nyquist) frequency is $1/8$, since the state was measured after every four entangling operations. Comparing the experimental data with the two types of simulation, we see again that the incoherent model of rf inhomogeneity accurately reproduces key features of the experimental data which are not reproduced by the decoherent model. The dominant signal in all twelve plots is the zero frequency peak, which is caused by the initial decline

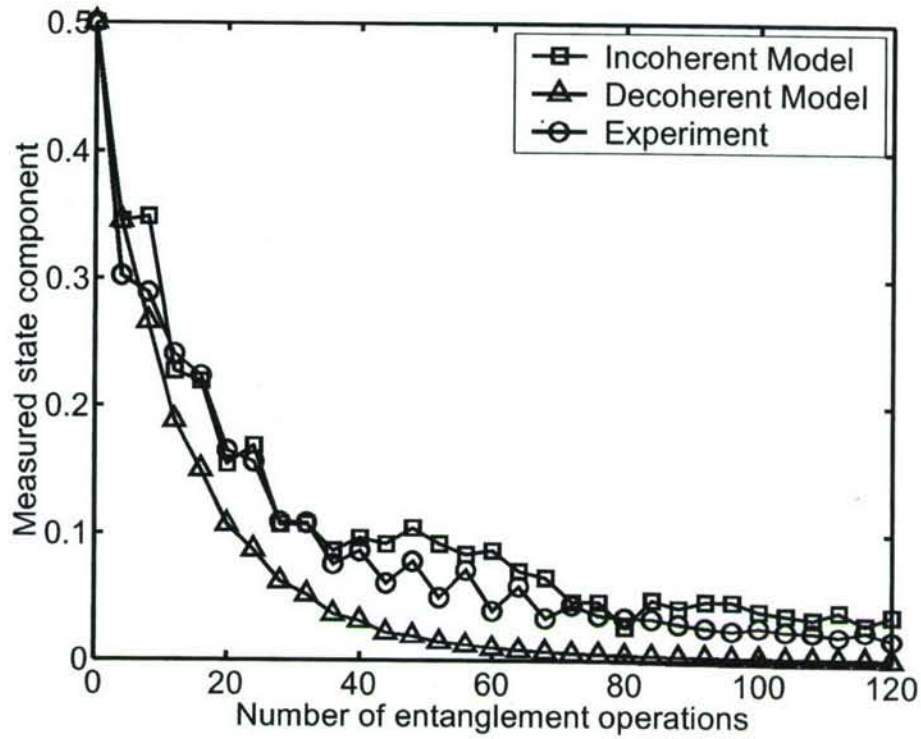


Figure 3-5: The sum of the absolute value of the density matrix components measured in the experiment and in numerical simulations. This measurement is a representative measure of state fidelity for the map under consideration. Rf inhomogeneity is numerically simulated using an incoherent model and a fictitious decoherent model as discussed in the text. For the ideal map with no noise, the sum of the density matrix components is a constant value of 0.5. Experimental noise and decoherence cause the measured value to initially decrease. However, as the map is iterated, the measured value increases and begins to oscillate. This behavior is well-reproduced by the incoherent model, while the decoherent model does not predict the oscillatory behavior. This plot shows that incoherence in the entangling operation appears with distinct signatures in the experimental data.

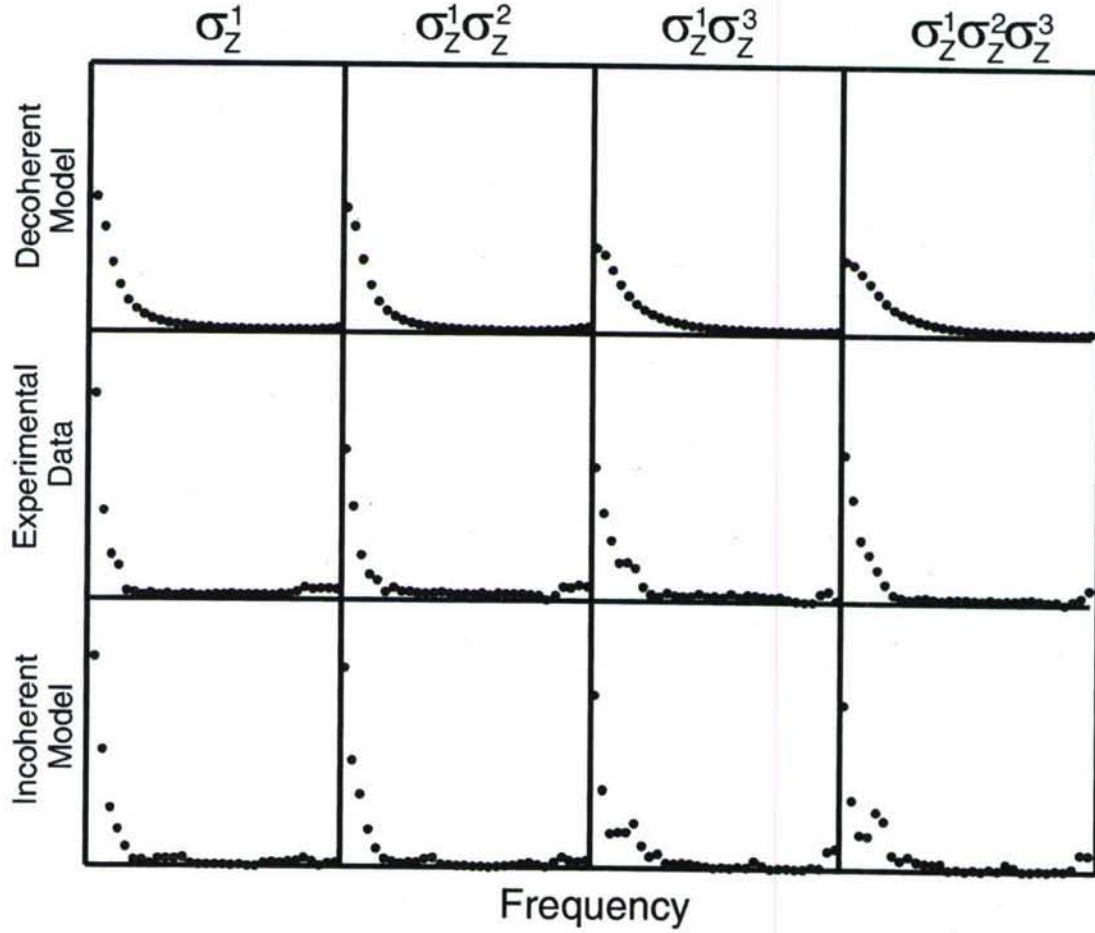


Figure 3-6: The Fourier transform of each experimentally measured component of the density matrix (middle row), compared to numerical simulations of the experiment using two models of rf inhomogeneity discussed in the text. The horizontal axis represents frequency in units of oscillation periods per entangling operation, with values ranging from 0 (left) to $1/8$ (right). Resolved high frequency components, which represent fidelity recurrences, are observed in the experimental data and in numerical simulations of the incoherent model, but not in numerical simulations of the decoherent model. The dominant high frequency components are observed in the three-body term $\sigma_z^1\sigma_z^2\sigma_z^3$ at the Nyquist frequency. This plot shows that incoherence in the experimentally implemented entangling operation appears as high frequency components in the Fourier transform of a state fidelity measurement.

in fidelity observed for all three plots in Fig. 3-5. The zero frequency peak is somewhat broader in the decoherent model, which reflects the rapid decay to zero of that data in the time-domain. The important features in the time-domain data, namely the oscillatory fidelity recurrences, are represented in the high frequencies of the Fourier domain. The oscillatory behavior in the experimental data and in the incoherent model simulations in Fig. 3-5 appear as resolved high frequency components of the individual state measurements in Fig. 3-6. The largest high frequency component occurs in the $\sigma_z^1 \sigma_z^2 \sigma_z^3$ measurement at the Nyquist frequency.

Incoherence in an entangling operation causes a loss of purity over the ensemble that is not recovered by an inverted incoherent process, and therefore is difficult to distinguish from decoherence. However, incoherence due to inhomogeneity in the rf control field during the implemented entangling operation appears as a distinct process in our experimental data in the form of fidelity recurrences. Numerical simulations are used to identify the recurrences as a purely incoherent effect. Incoherent errors are isolated in numerical simulations by separating out those parts of the evolution that are identical over the ensemble in a fictitious decoherent model, and we see that the decoherent process does not give rise to fidelity recurrences.

3.5 Conclusions

We have shown that incoherence can lead to recurrences in a fidelity decay, whereas decoherence cannot lead to such behavior, which provides an efficient framework for identifying signatures of incoherence. In our experiment, a two-qubit entangling operation was repeated 120 times on a three-qubit GHZ state in a liquid state NMR QIP, and fidelity recurrences in the experimental data were created by incoherence due to inhomogeneity of the rf control field. The experiment was numerically simulated modeling rf inhomogeneity in two regimes: as a static distribution of Hamiltonians and fictitiously as a stochastic distribution of Hamiltonians. The stochastic model mimics a decoherent process, allowing us to isolate the incoherent effects of rf inhomogeneity. The comparison identifies the experimentally observed recurrences as an incoherent process. The approach for detecting incoherence described here will be a valuable resource in QIPs operating in larger Hilbert spaces with entangled states over many qubits, where the effects of incoherence and decoherence are

difficult yet important to distinguish.

Chapter 4

Liquid crystal solvent NMR QIPs

Some materials exhibit a liquid crystal phase, or mesophase, which has properties of both liquid and solid phases. Liquid crystals are like liquids in that the constituent molecules undergo rapid translational diffusion, and they are like solids in that the molecules demonstrate some amount of long-range ordering. The particular nature of the microscopic ordering varies among materials, but the most commonly observed type of ordering is the nematic mesophase. Nematic materials are typically made of long, rod-like organic molecules which, in nematic mesophase temperature regimes, prefer to self-align as illustrated in Figure 4-1. When a sample of nematic mesophase material is subject to a uniform external magnetic field, the field acts as a director for the aligned particles, and the material adopts molecular orientational preferences which are uniform over the sample [29, 34].

4.1 NMR with liquid crystal solvents

The NMR spectrum of a typical nematic liquid crystal material is very broad and has little structure. These characteristics arise due to the presence of many non-equivalent dipolar-coupled protons in the liquid crystal material. By contrast when a smaller, rigid molecule is dissolved in a liquid crystal, the solute adopts the orientational ordering of the solvent, and a resolved NMR spectrum is observed. The resolved peaks of the solute spectrum appear with a broad baseline due to the liquid crystal material, as seen in Figure 4-2(a). The figure shows the proton spectrum of *o*-chloronitrobenzene (CNB) partially oriented by the liquid crystal solvent ZLI-1132 at 600 MHz. The resolved peaks are from the four protons of CNB, and the baseline modulation arises from the many non-equivalent dipolar-coupled protons

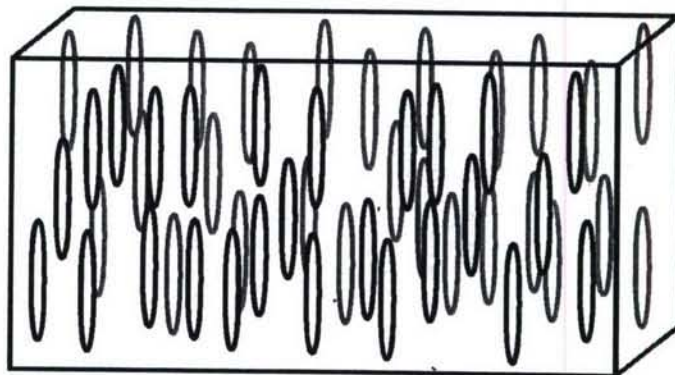


Figure 4-1: Illustration of the order properties of a nematic liquid crystal phase, showing orientational but not positional ordering. The material is composed of long, rod-like molecules that become self-aligned at certain temperatures. When the nematic phase is subject to an external magnetic field, the field acts as a director for the molecular alignment. Solutes dissolved in a nematic liquid crystal adopt preferred orientations that restrict thermal rotation, causing nuclear spins within the molecule to retain non-zero dipolar interactions which are not present in an isotropic liquid. The intramolecular dipolar couplings are useful for NMR quantum information processing.

of ZLI-1132.

The baseline due to the liquid crystal solvent can be removed by inserting a time suspension sequence, such as the Cory-48 pulse sequence [22], before acquiring an FID. This technique works because the dipolar coupling of the liquid crystal solvent spins, whose signal we want to suppress, is much stronger than the dipolar coupling of the solute spins, whose signal we want to observe ($d_{supp} \gg d_{obs}$). By selecting a pulse sequence that refocuses the solute spins ($\tau d_{obs} \ll 1$) but not the solvent spins ($\tau d_{supp} \gg 1$), the unwanted signal is removed. In our experiments we found that one cycle of the Cory-48 pulse sequence, using $\tau = 30\mu s$ and a $(\pi/2)$ pulse time of $6.85\mu s$, worked well. The results of the baseline suppression technique for CNB dissolved in ZLI-1132 are shown in Figure 4-2(b).

After removing the baseline, we are left with a complicated spectrum of many resolved transitions. The dominant features in the resolved spectrum arise due to the presence of strong magnetic dipolar couplings among nuclear spins in the solute material. This strong dipolar interaction is the principal difference between liquid and liquid crystal solvent NMR. The secular homonuclear dipolar interaction between two spins (j and k) in a strong magnetic field is given by

$$\mathcal{H}_{Dip}^{jk} = \frac{D_{jk}}{2} \left(2\sigma_z^j \sigma_z^k - \sigma_x^j \sigma_x^k - \sigma_y^j \sigma_y^k \right) \quad (4.1)$$

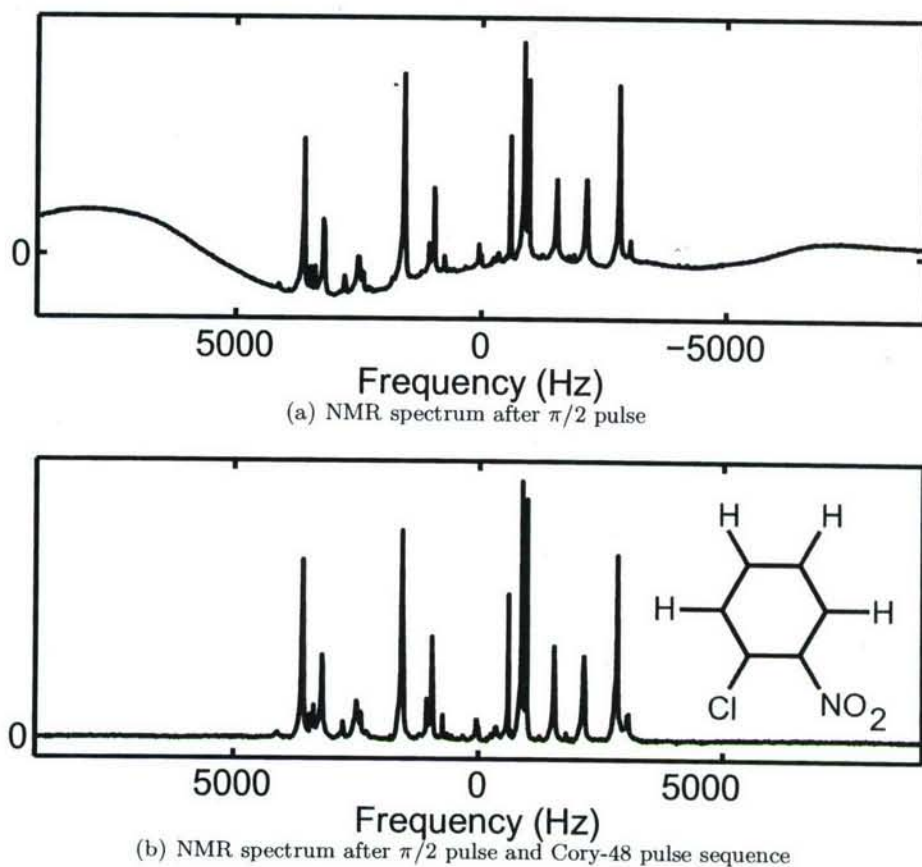


Figure 4-2: 600 MHz proton spectrum of o-chloronitrobenzene (CNB) partially oriented by the liquid crystal solvent ZLI-1132. (Top) The spectrum after a single ($\pi/2$) pulse features a broad baseline due to the liquid crystal solvent, which contains many nonequivalent strongly dipolar-coupled protons. The resolved peaks are the four dipolar coupled protons of the CNB solute material. The dipolar coupling among solvent protons is much stronger than among solute protons. (Bottom) The spectrum after a ($\pi/2$) pulse and one cycle of the Cory-48 pulse time suspension sequence ($\tau = 30\mu\text{s}$, $\pi/2$ pulse = $6.85\mu\text{s}$). The baseline is suppressed because the pulse sequence is parameterized to refocus the dipolar couplings among solute protons but not among solvent protons.

where D_{jk} is the dipolar coupling strength (in units of Hz)

$$D_{jk} = \left(\frac{\mu_0 \hbar \gamma_j \gamma_k}{8\pi^2} \right) \left(\frac{1 - 3 \cos^2 \theta_{jk}}{r_{jk}^3} \right), \quad (4.2)$$

$r_{jk} = ||\vec{r}_{jk}||$ is the length of the internuclear vector, θ_{jk} is the angle between the internuclear vector and the B_0 field, μ_0 is the permeability of free space, and \hbar is Planck's constant divided by 2π . The value of the expression in the first set of parenthesis in equation (4.2) is determined by the type of nuclear species; for two protons $(\mu_0 \hbar \gamma_j \gamma_k / 8\pi^2) = 120 \text{ kHz } \text{\AA}^3$.

For an ensemble of rigid molecules, the internuclear distances are fixed by the structure of the molecule, and the angular terms in the dipolar coupling strength are averaged over the distribution of molecular orientations in the ensemble

$$d_{jk} = \left(\frac{\mu_0 \hbar \gamma_j \gamma_k}{8\pi^2 r_{jk}^3} \right) \langle 1 - 3 \cos^2 \theta_{jk} \rangle, \quad (4.3)$$

where the angular brackets denote the ensemble average. In both liquid and liquid crystal solvents, the solute molecules move about with rapid, diffusive translational motion, which averages the intermolecular dipolar couplings to zero. In addition to translational motion, the molecules in a liquid are randomly rotating, averaging out the intramolecular dipolar couplings as well. By contrast, a molecule dissolved in a liquid crystal has a preferred orientation, so rotational motion is restricted, and intramolecular dipolar couplings are retained, as the bracketed term in equation (4.3) averages to some non-zero value.

4.2 Dipolar coupling in a partially oriented system

Emsley and Lindon's text [34] gives a detailed derivation of the effective NMR dipolar Hamiltonian for partially oriented systems. The observed nuclear dipolar couplings arise from an ensemble average over the distribution of molecular orientations. The order parameter $S_{\alpha\beta}$ provides a convenient framework for representing the ensemble averaging. In general, the order parameter varies with temperature and depends heavily on the liquid crystal solvent and the symmetry of the solute molecule. In order to express the observed dipolar couplings in terms of the order parameter, we first define two Cartesian coordinate systems. The lab frame coordinate axes are labeled x, y, and z, and the molecular frame coordinate axes are labeled a, b, and c. The lab frame is defined by the external B_0 field,

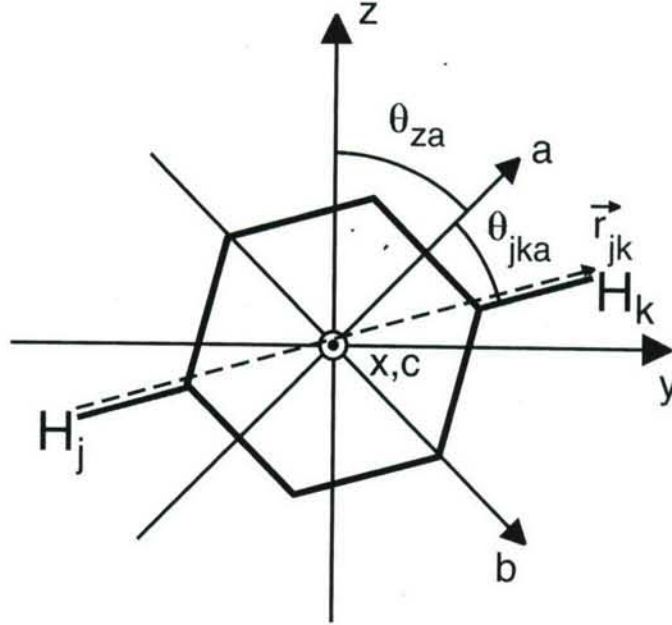


Figure 4-3: Coordinate frames used in the expression of the order parameter. The molecule is fixed in the molecular frame, whose axes are labeled a, b, and c. Thermal energy causes the molecular frame to rotate with respect to the lab frame, whose axes are labeled x, y, and z. The z-axis is parallel to the external B_0 field; the x- and c-axes are perpendicular to the yz-plane. The internuclear vector \vec{r}_{jk} makes an angle θ_{jka} with the molecular a-axis. The molecular a-axis makes an angle θ_{za} with the lab z-axis. The order parameter given in equation (4.4) describes the distribution of molecular frame orientations in an ensemble of molecules. Equation (4.5) relates the order parameter to the observed dipolar couplings d_{jk} .

which is parallel to the z-axis. The molecular frame is defined by the orientation of the molecule, as the molecule is fixed in the molecular frame. The indices α and β will be used to represent a generic axis in the molecular frame. The order parameter is expressed

$$S_{\alpha\beta} = \frac{1}{2} \langle 3 \cos \theta_{\alpha z} \cos \theta_{\beta z} - \delta_{\alpha\beta} \rangle \quad (4.4)$$

where the angled brackets indicate the ensemble average, $\delta_{\alpha\beta}$ is the Kronecker delta, and $\theta_{\alpha z}$ is the angle between the lab z axis and the molecular α axis. These angles and their relationship to the lab and molecular frames are illustrated in Figure 4-3 for a benzene molecule. The effective dipolar couplings for a partially oriented system can now be expressed

$$d_{jk} = \left(\frac{\mu_0 \hbar \gamma_j \gamma_k}{8\pi^2 r_{jk}^3} \right) \sum_{\alpha\beta} S_{\alpha\beta} \langle \cos \theta_{jka} \cos \theta_{jk\beta} \rangle \quad (4.5)$$

where θ_{jka} is the angle between the internuclear vector \vec{r}_{jk} and the molecular α -axis, illustrated in Figure 4-3. In a liquid, all elements of $S_{\alpha\beta}$ are zero, and there is no dipolar coupling.

The order parameter is a traceless rank-two tensor, so the diagonal elements are often expressed as two independent terms S_{aa} and $(S_{bb} - S_{cc})$. Also, because $S_{\alpha\beta}$ is symmetric, the off-diagonal terms can be reduced to three independent terms S_{ab} , S_{ac} and S_{bc} . In this representation, the dipolar couplings are given by

$$\begin{aligned} D_{jk} = \left(\frac{\mu_0 \hbar \gamma_j \gamma_k}{8\pi^2 r_{jk}^3} \right) [& S_{aa} \langle \cos^2 \theta_{jka} \rangle + (S_{bb} - S_{cc}) \langle \cos^2 \theta_{jkb} - \cos^2 \theta_{jkc} \rangle \\ & + 2S_{ab} \langle \cos \theta_{jka} \cos \theta_{jkb} \rangle + 2S_{ac} \langle \cos \theta_{jka} \cos \theta_{jkc} \rangle \\ & + 2S_{bc} \langle \cos \theta_{jkb} \cos \theta_{jkc} \rangle]. \end{aligned} \quad (4.6)$$

which is often used in literature and texts. The order parameter is a convenient representation of the ensemble average orientation because it characterizes the molecular orientation in the molecular frame. The molecular frame can be chosen to exploit symmetries in the molecule, which reduces the number of independent parameters necessary to characterize molecular motion in the molecular frame. Consequently, the order parameter can often be reduced to fewer than five independent terms. For example, the symmetry of the benzene molecule reduces the order parameter to a single nonzero term S_{aa} . The proton NMR spectrum of benzene partially oriented by the liquid crystal ZLI-1132 is shown in Figure 4-4. The symmetry of the spectrum is a result of the benzene molecule's symmetry.

Now the internal Hamiltonian of the solute spin system can be written

$$\mathcal{H} = \sum_j \pi \nu_j \sigma_z^j + \sum_{j < k} \frac{\pi}{2} (J_{jk} + 2d_{jk}) \sigma_z^j \sigma_z^k + \sum_{j < k} \frac{\pi}{2} (J_{jk} - d_{jk}) (\sigma_x^j \sigma_x^k + \sigma_y^j \sigma_y^k) \quad (4.7)$$

where ν_j is the resonance frequency of the j^{th} spin, d_{jk} is the dipolar coupling strength (modified by $S_{\alpha\beta}$) between spins j and k , and J_{jk} is the corresponding scalar coupling strength. In liquid crystal solvent systems, dipolar coupling strengths can reach a few kilohertz. For a given pair of spins the dipolar coupling is typically one to two orders of

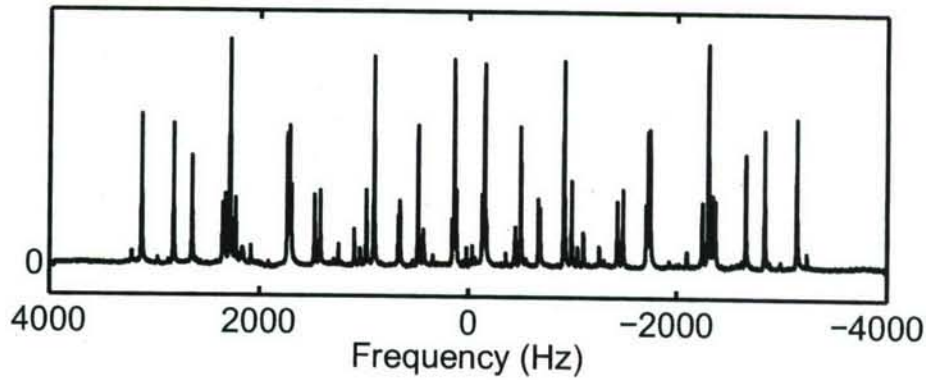


Figure 4-4: 600 MHz proton spectrum of benzene partially oriented by the liquid crystal solvent ZLI-1132. The symmetry of the NMR spectrum is a result of the symmetry of the benzene molecule. The order parameter for this system has one independent parameter which uniformly scales the dipolar couplings among all six protons and therefore determines the spectral breadth.

magnitude larger than the scalar coupling.

For ordered systems, the chemical shift difference between two nuclear spins $\Delta\nu_{jk} = |\nu_j - \nu_k|$ is often smaller than or comparable to the dipolar coupling strength d_{jk} , so we have $\Delta\nu_{jk} \approx d_{jk}$. This contrasts with the liquid state, where typically $d_{jk} = 0$ and $\Delta\nu_{jk} \gg J_{jk}$. The effect is that the nuclear Zeeman energy levels in the partially ordered system are mixed by the anisotropic coupling terms of the internal Hamiltonian. The peak heights and positions in the resulting NMR spectrum are affected by the mixing, and the physical parameters of the internal Hamiltonian are not trivially extracted from the NMR spectrum, as they usually can be in liquid state systems.

4.3 Liquid crystal solvent NMR QIPs

The solute material in a liquid crystal solvent system can be used for NMR quantum information processing to some advantage over liquid state systems [120]. One primary advantage is a direct result of the large dipolar couplings in partially oriented systems. The computing speed of an NMR quantum processor is related to the inverse of the nuclear spin coupling strength, and therefore the computing speed of a liquid crystal solvent NMR QIP (LNQ) is much faster than that of a liquid state system. Another advantage is the greater availability of molecules bearing large networks of strongly coupled nuclear spins. In order to perform conditional quantum logic gates, the nuclear spins in an NMR QIP

must exchange information. Nuclei in the liquid state exchange information by through-bond scalar couplings, so nuclei that are not directly bonded must exchange information indirectly, traversing multiple bonds. Dipolar coupling is a spatial effect, and in a partially ordered system, even distant nuclei that are not directly bonded can directly exchange information, simplifying multiple-qubit quantum logic gates. In addition, the coherence times of nuclear spins in an LNQ can be hundreds of milliseconds long, providing sufficient time to perform many quantum logic operations before the system decoheres.

From liquids to solids There are additional reasons, other than their performance, for developing coherent control in LNQs. The future direction of NMR quantum information processing (discussed in Chapter Six), aspires to implement coherent control in large Hilbert spaces using solid state devices. However, adapting the tools of liquid state NMR QIPs to these systems is not a trivial task. Figure 4.3 shows how LNQs fit into the broad picture of NMR quantum information processing as a bridge from liquid to solid state implementations. The left and middle columns of the figure illustrate liquid crystal as a *mesophase* of matter, in the *middle* of a liquid and solid phase. The third column of Figure 4.3 shows that the nuclear spin dynamics of an LNQ are in a *meso*-regime between liquid state and solid state dynamics. Liquid state dynamics are typically dominated by the Zeeman interaction ($\Delta\nu_{jk} \gg J_{jk}, d_{jk} = 0$), whereas solid state dynamics are typically dominated by the dipolar interaction ($\Delta\nu_{jk} \ll d_{jk}$). Materials dissolved in a liquid crystal are typically in a regime between these two extrema ($\Delta\nu_{jk} \approx d_{jk}$). From this perspective, LNQs provide a natural setting for translating liquid state methodologies to dipolar coupled systems and for addressing some of the other important challenges in solid state NMR quantum information processing.

Challenges Just as the advantages of LNQs arise due to the presence of strong dipolar couplings, so do the some of the challenges. LNQs provide moderately large networks of dipolar-coupled nuclear spins, and a significant challenge in these systems is to characterize and coherently control the dipolar interaction. Multiple pulse techniques and magic angle spinning have both been used with great success to effectively average out the dipolar Hamiltonian [43, 77]. Other work has demonstrated coherent control in dipolar coupled systems [4, 5, 73, 89]. However, as the number of spins increases, the size of the Hilbert

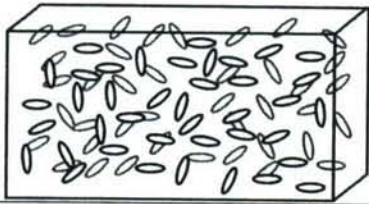
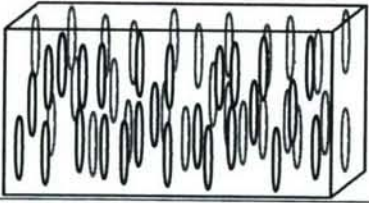
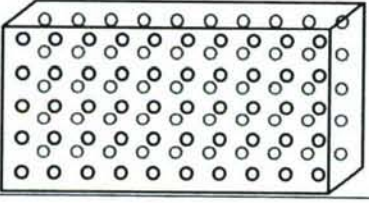
	Liquids -translational diffusion -random reorientation	$\Delta\nu \gg J_{jk}$ $d_{jk} = 0$ up to 12 qubits
	Liquid Crystals -translational diffusion -partially oriented	$\Delta\nu \approx d_{jk}$ $d_{jk} \neq 0$ 15-30 qubits
	Solids -no diffusion -highly ordered	$\Delta\nu \ll d_{jk}$ $d_{jk} \neq 0$ many qubits

Figure 4-5: Comparison of three regimes of NMR QIP, showing liquid crystal solvent NMR QIPs as a bridge between liquid and solid state implementations. Liquid state NMR QIPs explore coherent control with a small number of weakly coupled nuclear spins. Solids host large networks of strongly dipolar-coupled nuclear spins, an attractive setting for implementing coherent control of large Hilbert spaces. Liquid crystal solvent systems provide a middle-ground, where the dynamics approach solid state conditions, and the available Hilbert spaces are larger than those available in the liquid state. LNQs provide a natural setting for addressing some of the important challenges in solid state NMR quantum information processing.

space grows exponentially, and pushing coherent control techniques to large Hilbert space implementations remains a significant challenge. Another effect of increasing the number of dipolar coupled spins in an LNQ is the added difficulty of analyzing the NMR spectrum and parameterizing the internal Hamiltonian [34, 102, 103].

An additional challenge arises due to the relatively small differences in nuclear spin resonance frequencies in an LNQ. For a molecule in a liquid crystal solvent, chemically distinct nuclear spins are distinguishable by their resonance frequencies ν_j . However, the chemical shift differences $\Delta\nu_{jk} = |\nu_j - \nu_k|$ may be very small, and the time required to distinguish among the spins is proportional to $1/\Delta\nu_{jk}$. Consequently, control sequences which distinguish among the spins are long in time, negating the enhancement in computing speed enabled by strong dipolar couplings and augmenting the effects of decoherence. This challenge is addressed in Chapter Five of this thesis by encoding logical qubits in a decoherence free subspace (DFS). Logical qubit rotations are implemented by the dipolar interaction and need not distinguish the resonance frequencies of the nuclear spins, which allows shorter control sequences [31]. In addition, by storing quantum information in a DFS, the effects of decoherence are minimized, as the state of the logical qubits is immune to certain types of noise [32, 70, 122].

Prior work with LNQs The potential advantages of an LNQ were first demonstrated in an implementation of the Grover search algorithm using partially oriented chloroform [120]. Since then, more complex systems have been explored. LNQs have been used to implement adiabatic quantum algorithms [79], entangled states [76], universal coherent control [72], quantum information processing with spins greater than $1/2$ [27, 28, 56, 97], and demonstrations with up to seven nuclear spins [64]. Recent work [73] has shown the success of strongly modulating pulses [37] for coherent control of dipolar-coupled nuclear spins in an LNQ.

In previous studies of LNQs involving multiple homonuclear spins- $1/2$, the physical parameters of the internal Hamiltonian (d_{jk} , ν_j , and J_{jk}) were not measured. Instead, a two-dimensional NMR method, HET-Z-COSY [26], identified connectivities among the eigenstates of the internal Hamiltonian, and these states were used as the computational basis of the LNQ. In some of these studies, transition selective pulses were used to implement the desired unitary evolution [26, 72]. More recent work has combined the HET-Z-COSY

method with spectral fitting procedures to determine a “guess” Hamiltonian [73], but the physical parameters of the Hamiltonian are not determined. In Chapter Five of this thesis we demonstrate control sequences that are robust to variations in Hamiltonian parameters, and high fidelity control of two logical qubits is achieved even when the Hamiltonian parameters are known with some uncertainty.

Chapter 5

Enhanced control by logical qubit encoding

The successful transition from quantum information processing to quantum computation will require the ability to efficiently control qubits in the presence of noise. Decoherence free subspaces (DFSs) are some of the most efficient schemes of avoiding decoherence from noise sources with underlying symmetries [32, 70, 122]. There have been considerable experimental demonstrations of coherent control in DFSs including demonstrations of multiple qubit control [13, 37, 38, 45, 49, 57, 61, 63, 80, 83]. However most examples were not the natural encodings, in that the dominant noise source was not of the proper symmetry, and the control method did not simply match the available control elements. Here we explore a DFS encoding of strongly dipolar-coupled spins where the logical encoding quite naturally fits the internal Hamiltonian structure. This work builds on the extensive theoretical investigations of DFS encoding for systems with time-dependent exchange couplings [3, 31, 119, 121]. To achieve similar internal Hamiltonian structure we employ liquid crystal solvents to partially align the spin system and to reintroduce the spin-spin dipolar coupling [34].

5.1 System model

Liquid crystals in a strong external magnetic field are partially ordered. This partial ordering restricts the thermal motion of molecules dissolved in the liquid crystal material, and consequently, the solute molecules have a preferred orientation, and the orientationally-

dependent intramolecular dipolar interactions

$$\mathcal{H}_{\text{Dip}} = \sum_{j < k} \frac{\pi}{2} d_{jk} \left(2\sigma_z^j \sigma_z^k - \sigma_x^j \sigma_x^k - \sigma_y^j \sigma_y^k \right) \quad (5.1)$$

$$d_{jk} = \left(\frac{\mu_0 \hbar \gamma_j \gamma_k}{8\pi^2} \right) \left(\frac{1 - 3\cos^2 \theta_{jk}}{r_{jk}^3} \right) \quad (5.2)$$

do not average to zero. However the translational motion of solute molecules is not restricted, and intermolecular dipolar couplings do average to zero. The resulting internal Hamiltonian for a liquid crystal solvent system is

$$\mathcal{H} = \sum_j \pi \nu_j \sigma_z^j + \sum_{j < k} \frac{\pi}{2} (J_{jk} + 2d_{jk}) \sigma_z^j \sigma_z^k + \sum_{j < k} \frac{\pi}{2} (J_{jk} - d_{jk}) \left(\sigma_x^j \sigma_x^k + \sigma_y^j \sigma_y^k \right) \quad (5.3)$$

where ν_j is the resonance frequency of the j^{th} spin, d_{jk} is the dipolar coupling strength between spins j and k , J_{jk} is the corresponding scalar coupling strength, and the sums are restricted to spins within the molecule. In liquid crystal solvent systems, dipolar coupling strengths can reach multiple kHz, and for a given pair of spins the dipolar coupling is typically one to two orders of magnitude larger than the scalar coupling. The resonance frequencies and scalar couplings can be directly measured using multiple pulse sequences that average out the dipolar interaction, such as the MREV-8 sequence [74, 75, 90]. The intramolecular dipolar coupling strengths for a partially ordered system are a result of the structure of the molecule as modified by the order parameters of the system [29, 34].

We are interested in the control of two logical qubits that are encoded to protect against collective σ_z noise. The logical subspace S_L for this encoding is the zero-quantum subspace of the Zeeman energy eigenstates

$$|00\rangle_L = |0101\rangle \quad (5.4)$$

$$|01\rangle_L = |0110\rangle \quad (5.5)$$

$$|10\rangle_L = |1001\rangle \quad (5.6)$$

$$|11\rangle_L = |1010\rangle. \quad (5.7)$$

We describe the system in terms of the following set of logical subspace Pauli operators

$$\begin{aligned}
\sigma_x^{L1} &= \frac{1}{2}(\sigma_x^1 \sigma_x^2 + \sigma_y^1 \sigma_y^2) & \sigma_x^{L2} &= \frac{1}{2}(\sigma_x^3 \sigma_x^4 + \sigma_y^3 \sigma_y^4) \\
\sigma_y^{L1} &= \frac{1}{2}(\sigma_y^1 \sigma_x^2 - \sigma_x^1 \sigma_y^2) & \sigma_y^{L2} &= \frac{1}{2}(\sigma_y^3 \sigma_x^4 - \sigma_x^3 \sigma_y^4) \\
\sigma_z^{L1} &= \sigma_z^1 - \sigma_z^2 & \sigma_z^{L2} &= \sigma_z^3 - \sigma_z^4
\end{aligned}$$

along with the identity term and the nine bipartite terms such as $\sigma_x^{L1} \sigma_y^{L2}$. Recently we have reported on liquid state NMR experiments to demonstrate coherent control for a Bell state with this encoding [49]. We have discussed leakage out of the logical subspace under the control operations [12], and we have described a convenient subsystem pseudopure state [13]. The liquid crystal system extends these studies by offering a new symmetry for the internal spin Hamiltonian that led us to expect that the logical encoding will be a more natural and efficient subspace for manipulating quantum information. The dipolar Hamiltonian has a portion that transforms as the exchange operator which has been shown to be particularly convenient for subsystem encodings [3, 31, 119, 121].

The goal of this work is to demonstrate three results: (1) improved quantum information processing by using logical qubits, (2) an implementation of a DFS with dipolar-coupled spins, and (3) high fidelity control even when we have limited knowledge of the system Hamiltonian. The spin system used in these studies is the four protons of o-chloronitrobenzene (CNB) dissolved in Merck ZLI-1132 liquid crystal at 600 MHz field and a temperature of 300 K. The proton spins are strongly coupled to each other, and all of the resonances are not resolved in the 1-D NMR spectrum shown in Figure 5-1. The order parameters for CNB aligned in a liquid crystal solvent have not been measured previously so we do not have this information on which to determine the internal Hamiltonian. We have made the following simple measurements to obtain reasonable estimates of the internal Hamiltonian: (1) a 1-D MREV-8 spectrum shown in Figure 5-1, and (2) 2-D correlation spectra between the chemical shifts under MREV-8 line narrowing and the full internal Hamiltonian. The MREV-8 spectrum indicates the chemical shifts, and the 2-D measurement provides a means of assigning the largest dipolar couplings to the appropriate chemical shifts. We measured the chemical shifts (in units of Hz) $\nu_1 = 115$, $\nu_2 = -234$, $\nu_3 = 204$, and $\nu_4 = -86$ relative to an arbitrary transmitter frequency, and an incomplete set of approximate dipolar couplings (in units of Hz) $d_{12} = -729$, $d_{23} = -503$, and

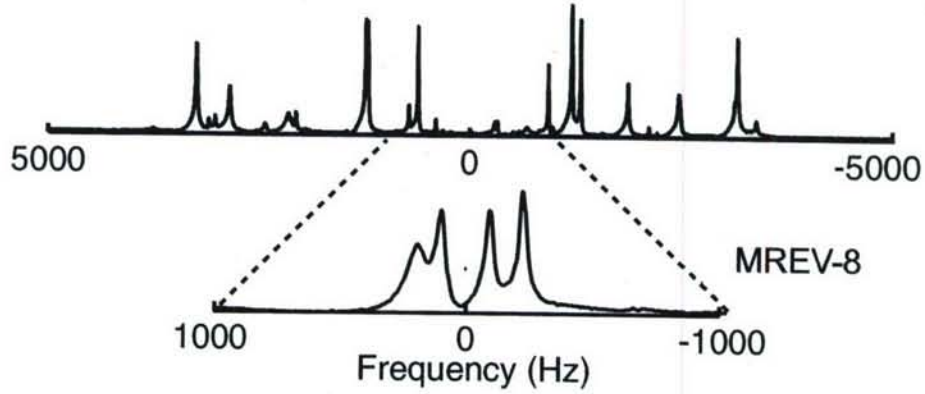


Figure 5-1: 600 MHz proton spectrum of o-chloronitrobenzene (CNB) partially oriented by the liquid crystal solvent ZLI-1132, where the signal due to solvent protons has been suppressed by inserting a single cycle of the Cory-48 pulse sequence before the acquisition. The inset spectrum, collected stroboscopically under the MREV-8 sequence ($\tau = 15\mu\text{s}$, $\pi/2$ pulse = $6.85\mu\text{s}$), shows the four spins uncoupled with chemical shifts scaled by approximately 0.50. The spectrum after a single ($\pi/2$) pulse (not shown) features a broad baseline due to the liquid crystal solvent, which contains many nonequivalent strongly dipolar-coupled protons. The baseline is suppressed in the spectra shown above because the Cory-48 pulse sequence was parameterized ($\tau = 30\mu\text{s}$, $\pi/2$ pulse = $6.85\mu\text{s}$) to refocus the weaker couplings among solute protons but not the much stronger couplings among solvent protons.

$d_{34} = -1875$. Although this limited description gives a very incomplete picture of the total system dynamics it is sufficient for our purposes.

5.2 Experiment

We encoded the four spin system into two logical qubits where d_{12} provided the control elements to rotate the first logical qubit, d_{34} similarly controlled the second logical qubit and d_{23} controlled the interactions between qubits. To achieve the desired control fidelity we found pulse sequences via the GRAPE algorithm [54]. Pulses were optimized for robustness to scalar couplings, the unknown dipolar couplings (d_{13} , d_{14} , d_{24}), and rf inhomogeneity. The three unknown dipolar couplings were set to a distribution of values centered about a “best guess” (in units of Hz) $d_{13} = 116$, $d_{14} = -64$, and $d_{24} = -170$. Although the most accurately known parameters in the internal Hamiltonian are the chemical shifts, we did not rely on them for control of the logical qubits. There is a final complication in that the three specified dipolar couplings (d_{12} , d_{23} , d_{34}) are not precisely determined. We designed the control sequences to be robust against small (± 100 Hz) variations of each of these.

The experimental goal was to create a pseudo-pure state over the logical qubits and then to entangle them in the form of a Bell state. We directly created the pseudo-pure state over the logical qubits via temporal averaging. This was accomplished in two steps. Under MREV-8 decoupling we prepared the states

$$\sigma_z^{L1} + \sigma_z^{L2} = \sigma_z^1 - \sigma_z^2 + \sigma_z^3 - \sigma_z^4 \quad (5.8)$$

$$\sigma_z^{L2} = \sigma_z^3 - \sigma_z^4 \quad (5.9)$$

relying on the differences in the chemical shifts of the four spins. To complete the pseudo-pure state preparation we used a numerically optimized GRAPE pulse to implement

$$\sigma_z^{L2} \xrightarrow{U_{prep}} \sigma_z^{L1} \sigma_z^{L2}. \quad (5.10)$$

The entangling operator we attempted to implement in the logical space is

$$U_{ent}^L = \frac{1}{\sqrt{2}} \begin{pmatrix} 1 & 0 & -i & 0 \\ 0 & -i & 0 & -1 \\ 0 & i & 0 & -1 \\ -1 & 0 & -i & 0 \end{pmatrix} \quad (5.11)$$

which takes the input state vector $|00\rangle_L$ to the logical Bell state $(|00\rangle_L - |11\rangle_L)/\sqrt{2}$. A numerically optimized (GRAPE) pulse was found which performs this unitary operation over the logical subspace with high fidelity. The fidelity of the pulse, accounting for coherent errors and the uncertainty in Hamiltonian parameters, is 0.99. In addition to the preparation and entangling pulses, we found fourteen readout pulses that transform every operator in the logical space into observables. The full experiment is outlined in Fig. 5-2.

Information stored in a DFS respects a direct sum representation over the full Hilbert space. Ideal control operations over the logical qubits have the structure $S \equiv S_L \oplus S_R$, where S_L is the logical subspace of interest, and S_R is the remainder of the space. We attempted to prepare the initial state $\rho_{in} = |00\rangle_L \langle 00|_L \oplus 0^R$, where 0^R is an explicit representation that the state has no component in S_R . The entangling operation over the full Hilbert space should also respect this symmetry $U_{ent} \equiv U_{ent}^L \oplus U_{ent}^R$ where we have complete flexibility in our choice of U_{ent}^R . The challenge of course is that if the direct sum representation is

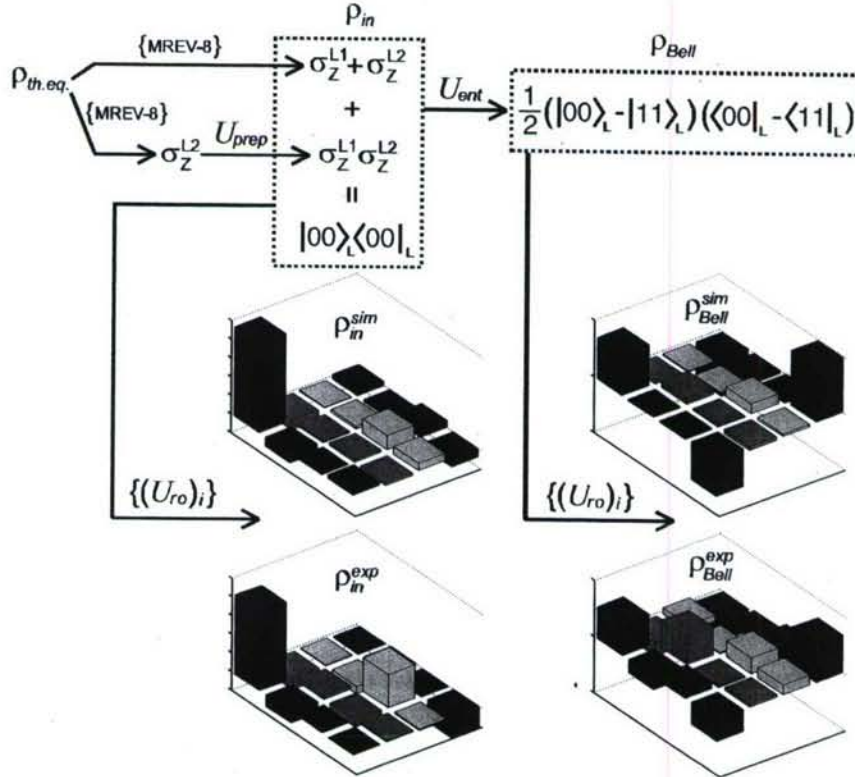


Figure 5-2: The procedure and experimental results of creating a Bell state over two logical qubits encoded in the four dipolar-coupled protons of the CNB molecule. MREV-8 sequences along with a numerically optimized preparation pulse are used to create the pseudopure input state $|00\rangle_L$ over the logical subspace. A numerically optimized entangling operation pulse converts the input state to the logical Bell state $(|00\rangle_L + |11\rangle_L)/\sqrt{2}$. A set of 14 numerically optimized readout pulses were used to reconstruct the density matrices shown above. The experimentally measured logical input and Bell states have correlations of 0.90 and 0.84 (respectively) with the numerically simulated states shown above.

not maintained, the logical information can be corrupted or can leak out of the logical subspace [12, 106, 118].

U_{prep} and U_{ent} were optimized over the range of dipolar couplings and rf inhomogeneity described above. The goodness function maximized by the GRAPE optimization algorithm was the logical subspace fidelity, which includes a penalty for pulses that permit leakage. The logical subspace fidelity expression is derived in Appendix A. U_{ent}^R was chosen arbitrarily. Finally, the readout pulses necessarily operated over the entire Hilbert space. They were simply designed to efficiently transform selected logical operators into observables and to be robust over the dispersion of coupling constants and rf inhomogeneity.

The reconstructed density matrices over the logical degrees of freedom are shown in Fig. 5-2. As expected, most of the observed errors arise from the initial state preparation and the readout sequences. The normalized state correlations over the logical subspace are:

$$\text{Corr}(\rho_{in}^{sim}, \rho_{in}^{exp}) = 0.90 \quad (5.12)$$

$$\text{Corr}(\rho_{Bell}^{sim}, \rho_{Bell}^{exp}) = 0.84 \quad (5.13)$$

The normalized correlations between the experimentally measured states and the ideal states are of course lower since they include more of the errors due to state preparation and readout

$$\text{Corr}(\rho_{|00\rangle_L}, \rho_{in}^{exp}) = 0.83 \quad (5.14)$$

$$\text{Corr}(\rho_{|Bell\rangle_L}, \rho_{Bell}^{exp}) = 0.76 \quad (5.15)$$

5.3 Analysis

To further explore the robust nature of our control over the logical subspace we have simulated the average state correlations that would be expected as the dipolar frequencies are varied. This information is shown in Figure 5-3. The loss in correlation is most pronounced for the step of creating the pseudopure state in the logical subspace. The entangling operation suffers only a small additional loss in correlation. Finally we compare our control over the encoded logical qubits to that we have over the individual spins. Figure 5-4 shows data from numerical simulations of the logical qubit entangling pulse implemented in the

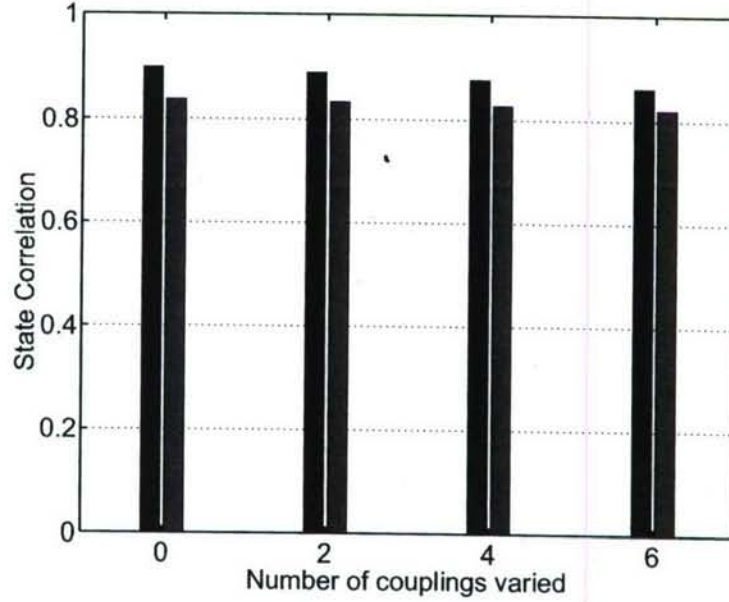


Figure 5-3: Correlation of the numerically simulated and experimentally measured density matrices for the logical input state (black) and the logical output state (green). The correlations shown are averaged over a dispersion of simulated Hamiltonian parameters. The horizontal axis indicates the number of dipolar couplings that are varied in the Hamiltonian dispersion. The individual coupling strengths are known with some uncertainty that is approximated by a dispersion centered at d_{jk} having a full width at half maximum = 200 Hz. Three points of each dispersion are sampled (d_{jk} and $d_{jk} \pm 100$ Hz), taking only those combinations of coupling strengths that have the same sum. As more couplings are varied, the correlations decrease only slightly since the pulse sequences were engineered to be robust to these variations, and the loss in correlation is most pronounced for the input state.

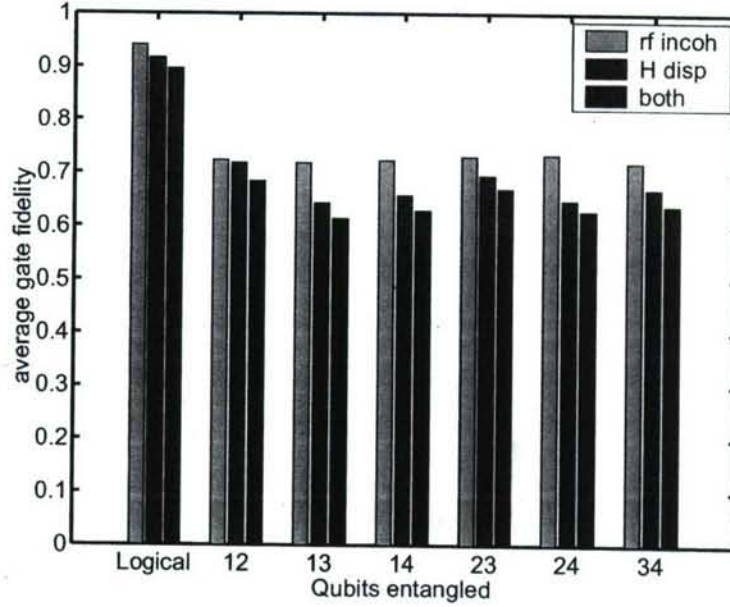


Figure 5-4: Fidelity of two-qubit entangling operation pulses numerically simulated under various conditions, comparing control of two logical qubits versus all pairs of spin qubits. The horizontal axis indicates the pair of qubits entangled. Bar color indicates the conditions of the simulation: (yellow, left) rf inhomogeneity is included in the simulation, (red, middle) a dispersion of Hamiltonians are simulated with no rf inhomogeneity, (blue, right) a dispersion of Hamiltonians are simulated with rf inhomogeneity. All fidelities are attenuated by $\exp(-t_{\text{pulse}}/T_2)$. For logical qubits, the estimated decoherence time of the zero quantum subspace is used ($T_2=80$ ms), and for spin qubits, the longest estimated single spin decoherence time is used ($T_2=40$ ms). The fidelity under each set of conditions is significantly better in the case of logical qubits than for any pair of spin qubits.

experiment, compared to numerical simulations of the best spin qubit entangling pulses found by the same pulse optimization methods, optimizing over the full Hilbert space. The fidelity under each set of simulated conditions is significantly better in the case of logical qubits than for any pair of spin qubits.

5.4 Conclusions

In conclusion, we have shown that improved coherent control is achieved by encoding logical qubits in our system of four dipolar-coupled protons. Control in this system was demonstrated experimentally by creating a pseudopure state in the DFS and applying a unitary transformation to create a logical Bell state. Some of the system Hamiltonian parameters are imprecisely known, and high fidelity control was achieved by engineering pulse

sequences that are robust to these uncertainties. The structure of the system Hamiltonian for molecules dissolved in liquid crystal solvents provides a natural setting for experimental studies of logical qubit encodings. In the future, liquid crystal solvent NMR QIPs could be used to explore more complex logical encodings in larger Hilbert spaces.

Chapter 6

Future direction

The long-term goals of quantum computing research include the realization of scalable, fault-tolerant coherent control. This goal is motivated by the idea that quantum computers will offer exciting and unique possibilities that are not available from classical computers. In the near term, existing implementations will move toward this goal by incorporating more complexities and broader capabilities. Specifically, efforts are focused on the development of QIPs that have access to larger Hilbert spaces. Many of these ongoing experimental efforts utilize nuclear and electron spin networks in solids, where spin addressability can present an additional challenge.

Facing these challenges, a logical approach is to utilize and adapt the tools that have enabled control in smaller, less complicated systems. In this regard, liquid crystal solvent NMR QIPs (LNQs) provide a fertile ground for progress. LNQs provide modestly large Hilbert spaces for studying complex system dynamics and quantum control with limited addressability. As discussed in Chapter Four, the natural system dynamics of an LNQ are in a middle-regime, between liquid and solid state dynamics, where the tools of liquid state NMR QIP can be applied to challenges related to scalable systems.

6.1 Larger Hilbert spaces

In liquid state NMR QIP, the Hilbert space is defined by nuclear spins in an ensemble of molecules. Because each molecule is approximately isolated from its environment, a molecule with a small number of scalar-coupled nuclear spins creates a well-defined Hilbert space, which enables precise coherent control. In solids, nuclear spin coupling is not limited

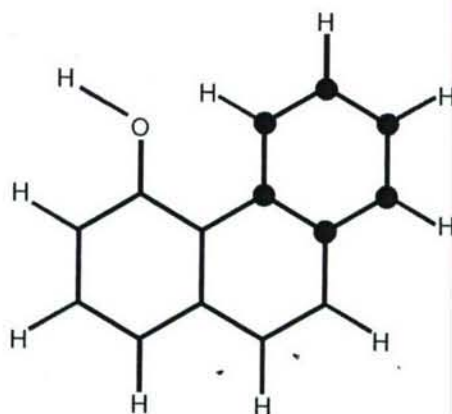


Figure 6-1: Diagram of the 4-hydroxyphenanthrene molecule which could be used as a 16 qubit heteronuclear LNQ. ^{13}C labeled spins are highlighted in red. Such a system will be useful for developing control techniques in large Hilbert spaces and for exploring control in dipolar-coupled nuclear spin systems.

to nearest neighbor interactions, and each spin is coupled to many other spins by the dipolar interaction. Experiments have identified interacting spin clusters containing as many as 100 spins [18,19]. While these large spin clusters present the advantages of a large Hilbert space, approximating a well-defined, isolated Hilbert space for quantum computing is a significant challenge in these systems. Liquid crystals will enable studies in moderately large networks of dipolar-coupled spins that are small enough that the dynamics are tractable. Figure 6-1 shows a molecule that could be used for such work. Future work with molecules such as 4-hydroxyphenanthrene could help identify methods for approximating a well-defined Hilbert space within a large network of dipolar-coupled spins.

6.2 Limited addressability

In liquid state NMR QIP, the difference in spin resonance frequency between two spins $\Delta\nu_{jk}$ is typically on the order of kHz, while the coupling strengths J_{jk} are typically one to two orders of magnitude smaller. In this regime, each spin-qubit is addressable by its resonance frequency, and arbitrary single-qubit manipulations are implemented by numerically optimized rf control sequences [37]. In solids, $\Delta\nu_{jk}$ is orders of magnitude less than the dipolar coupling strength d_{jk} , and individual spins are often indistinguishable, making single spin-qubit manipulations virtually impossible.

The solution to this problem is to encode single qubits in the state of many nuclear spins, which allows single qubit manipulations to be accomplished by controlling the interaction among the spins rather than by addressing individual spin resonance frequencies [3, 31]. As demonstrated in Chapter Five, liquid crystals provide a natural setting for exploring coherent control of logical qubits. Figure 6-2 demonstrates that liquid crystals are in a regime of addressability between liquids and solids. In a liquid crystal, individual transitions are resolved in the spectrum, but individual spins are not efficiently manipulated, since the coupling strengths are comparable to and often greater than the differences in resonance frequencies $\Delta\nu_{jk}$. Future studies with LNQs will progress to larger spin systems, incorporating more complex logical encodings involving more than two spins per logical qubit, which provides protection from a larger class of noise generators.

6.3 Complex dynamics

In liquid state NMR QIPs, dipolar couplings among nuclear spins are averaged out naturally by the thermal motion of the molecules, and nuclear spins interact through scalar coupling. The interaction is often in the weak coupling regime where the coupling term $J_{jk}\sigma^j \cdot \sigma^k$ is well approximated by $J_{jk}\sigma_z^j\sigma_z^k$. In such a regime, simulating a strongly mixing anisotropic Hamiltonian can require many transformations and long coupling times. In LNQs, strong dipolar couplings provide a natural setting for simulating and controlling a wider variety of Hamiltonians. As an example, the dipolar Hamiltonian can be transformed to study evolution under XY-Heisenberg couplings [14].

Many promising approaches to scalable control involve nuclear spins in the solid state, some of which incorporate electron spins via the hyperfine interaction [21, 52, 55, 62, 94, 101]. In these systems, it will be necessary to control and precisely manipulate large anisotropic coupling terms in the system Hamiltonian. LNQs provide a means for exploring control methods for such applications.

6.4 Conclusions

The challenge of building a quantum computer is a significant motivation to study and control complex quantum systems. Experimental methods have been developed to enable precise coherent control in liquid state NMR QIPs, and adapting these methods to solid

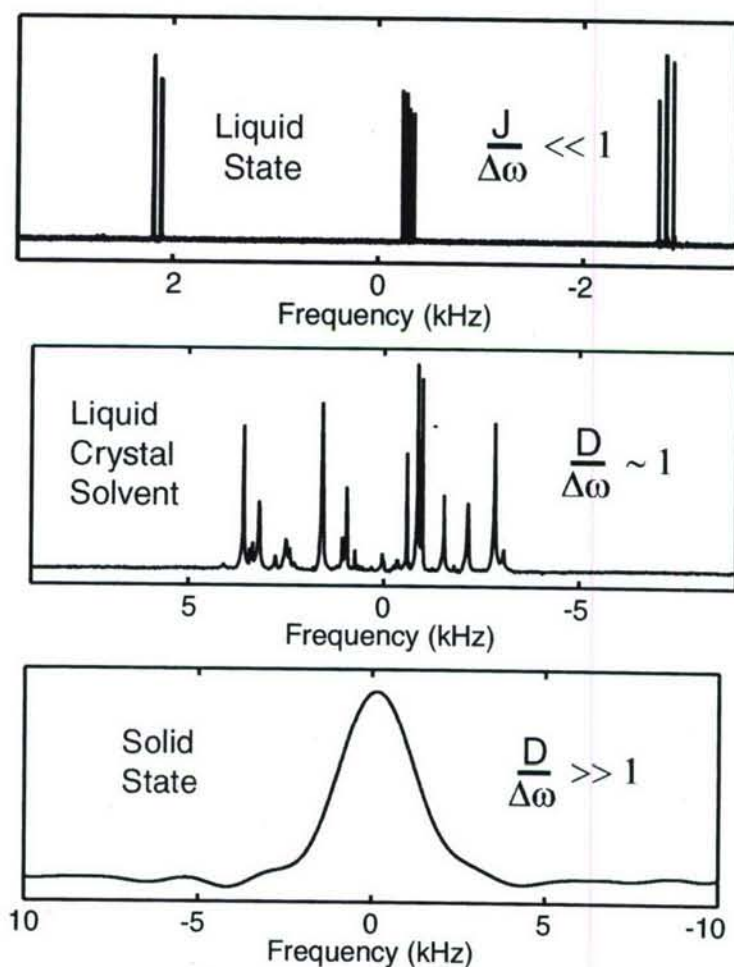


Figure 6-2: NMR spectra showing different regimes of Hamiltonians. (Top) A spectrum typical of liquid state NMR QIPs, showing three groups of peaks from three labeled ^{13}C nuclei in crotonic acid. Each group of peaks is split due to scalar coupling among the spins. The couplings are orders of magnitude smaller than the chemical shift differences. (Middle) A spectrum typical of liquid crystal solvent NMR QIPs, showing many resolved peaks over a broad spectral range from the four protons of o-chloronitrobenzene. Each proton is strongly dipolar coupled to the three other protons. The couplings are similar in magnitude to the chemical shift differences, and individual spins are not identifiable in the spectrum. (Bottom) An NMR spectrum typical of solid state systems that have been proposed for QIPs [21, 55, 62, 94, 101], showing many ^{29}Si nuclear spins, strongly coupled through the dipolar interaction in a rigid crystal lattice. Though there are many spins and many transitions in the system, a single peak, broadened by dipolar interactions, is observed.

state systems will lead to QIPs with greater capabilities. Liquid crystal solvent NMR QIPs provide a setting for this task, where the system dynamics are tractable but complex enough to present meaningful challenges and opportunities for significant progress.

Appendix A

Fidelity of logical qubit control

A.1 Measures of control

In an experiment, the control sequence optimized to implement U_{ideal} is modified by experimental noise. Under a noisy implementation, the resulting state can be expressed by a Kraus decomposition of the experimentally implemented process

$$\rho_{exp} = \sum_{\mu} A_{\mu} \rho_{in} A_{\mu}^{\dagger}. \quad (\text{A.1})$$

where the A_{μ} must satisfy

$$\sum_{\mu} A_{\mu} A_{\mu}^{\dagger} = \mathbb{1}, \quad (\text{A.2})$$

Expression (A.1) may represent a unitary operator sum for an incoherent process or any other completely positive quantum process. The experimentally implemented quantum process can also be fully described in a Liouville space representation by the superoperator S_{exp} , where

$$S_{exp} = \sum_{\mu} \bar{A}_{\mu} \otimes A_{\mu}. \quad (\text{A.3})$$

In the superoperator notation, states are represented by columnized density matrices $|\rho\rangle$ that are formed by stacking the columns of ρ from left to right, and state evolution is expressed

$$|\rho_{exp}\rangle = S_{exp} |\rho_{in}\rangle. \quad (\text{A.4})$$

The superoperator describing a unitary process U is given by $S = \bar{U} \otimes U$, where the overbar denotes complex conjugation.

Typically, three measures of control are of interest in quantum computation. The correlation between two quantum states

$$C(\rho_{ideal}, \rho_{exp}) = \frac{\text{trace}(\rho_{ideal} \rho_{exp})}{\sqrt{\text{trace}(\rho_{ideal}^2) \text{trace}(\rho_{exp}^2)}} \quad (\text{A.5})$$

indicates the overlap of the two states in Hilbert space. The attenuated correlation between two quantum states

$$A(\rho_{ideal}, \rho_{exp}, \rho_{in}) = C(\rho_{ideal}, \rho_{exp}) \sqrt{\frac{\text{trace}(\rho_{exp}^2)}{\text{trace}(\rho_{in}^2)}} \quad (\text{A.6})$$

includes a penalty for loss of state purity. Finally, the fidelity of the implemented quantum process is defined

$$F = \overline{A(\rho_{ideal}, \rho_{exp}, \rho_{in})}, \quad (\text{A.7})$$

the average attenuated correlation over a complete set of input basis states (average denoted by overbar). There are multiple equivalent expressions for the fidelity. For example, as derived in [37],

$$F = \sum_{\mu} \left| \text{trace}(U_{ideal}^{\dagger} A_{\mu}) / N \right|^2, \quad (\text{A.8})$$

where N is the Hilbert space dimension. Following from equation (A.8), when the implemented process is unitary, the fidelity is given by

$$F = \left| \text{trace}(U_{ideal}^{\dagger} U_{exp}) / N \right|^2 \quad (\text{A.9})$$

When U_{ideal} is represented in the Liouville space $S_{ideal} = \bar{U}_{ideal} \otimes U_{ideal}$ (overbar denotes complex conjugation), the fidelity is given by

$$F = \text{trace}(S_{exp}^{\dagger} S_{ideal}) / N^2 \quad (\text{A.10})$$

A.2 Control in the logical subspace

When implementing control in a logical subspace, measures of control need to be modified. The system Hamiltonian is defined over the full Hilbert space $S \equiv S_L \oplus S_R$, where S_L is the logical subspace of interest, and S_R is the remainder of the space. An operator \mathcal{O} in S has a component in S_L which is extracted by the projection operation

$$\mathcal{O}^L = \sum_{jj'=1}^{N_L} |L_j\rangle \langle L_j| \mathcal{O} |L_{j'}\rangle \langle L_{j'}| \quad (\text{A.11})$$

where the $|L_j\rangle$ form a complete set of N_L basis vectors in S_L . The component of \mathcal{O} in S_R is given similarly by

$$\mathcal{O}^R = \sum_{tt'=1}^{N_R} |R_t\rangle \langle R_t| \mathcal{O} |R_{t'}\rangle \langle R_{t'}| \quad (\text{A.12})$$

where the $|R_t\rangle$ form a complete set of N_R basis vectors in S_R .

It is assumed that the initial state resides in S_L , such that $\rho_{in} = \rho_{in}^L \oplus 0^R$, where 0^R is an explicit representation that the state has no component in S_R . The ideal unitary evolution has the form $U_{ideal} \equiv U_{ideal}^L \oplus U_{ideal}^R$, which implies that there is no leakage into S_R . This means that no instantaneous state has elements in S_R , and the final state after ideal evolution $\rho_{ideal} = U_{ideal} \rho_{in} U_{ideal}^\dagger = \rho_{ideal}^L \oplus 0^R$ also resides in S_L .

Errors in the implementation of U_{ideal} may cause leakage into S_R . In this case, the logical component of the Kraus operators representing the noisy process A_μ are sufficient for describing the component of the resulting state in the logical space. Given that $\rho_{in} = \rho^L \oplus 0^R$, the component of ρ_{exp} in S_L is

$$\rho_{out}^L = \sum_{\mu} A_\mu^L \rho_{in}^L A_\mu^{L\dagger}. \quad (\text{A.13})$$

The set of operators A_μ^L contains information about errors in the logical subspace and is affected by leakage to S_R . Consequently, we are only interested in the fidelity of A_μ^L , the process which affects the evolution of the component of the state in S_L . The fidelity of the process A_μ^L is given by

$$F_L = \sum_{\mu} \left| \text{trace} \left(U_{ideal}^{L\dagger} A_\mu^L \right) / N_L \right|^2. \quad (\text{A.14})$$

F_L has the three necessary qualities of a good measure of control in the logical subspace: (1)

there is a penalty for leakage out of the logical subspace, (2) there is no penalty for errors restricted to the space S_R , and (3) F_L is equivalent to the full space fidelity when errors are restricted to the logical subspace. We now prove that F_L is equivalent to the fidelity of the full Hilbert space operator A_μ as in equation (A.8), but where the trace sum is restricted to S_L . That is to say that the quantity in equation (A.14) is equivalent to the attenuated correlation averaged over a complete set of input basis states in the logical subspace. We begin with an explicit expression of equation (A.8) with the restricted trace sum

$$F = \sum_{\mu} \left| \text{trace}_L \left(U_{ideal}^\dagger A_\mu \right) / N_L \right|^2 \quad (\text{A.15})$$

$$= \sum_{\mu} \left| \left(\sum_{j=1}^{N_L} \langle L_j | U_{ideal}^\dagger A_\mu | L_j \rangle \right) / N_L \right|^2 \quad (\text{A.16})$$

We now insert three operators which correspond to identity in the full space S

$$F = \sum_{\mu} \left| \left(\sum_{j=1}^{N_L} \sum_{\{k\}=1}^N \langle L_j | k \rangle \langle k | U_{ideal}^\dagger | k' \rangle \langle k' | A_\mu | k'' \rangle \langle k'' | L_j \rangle \right) / N_L \right|^2 \quad (\text{A.17})$$

Given that $\langle L_j | k \rangle = 0$ unless $|k\rangle \in S_L$ and $\langle k'' | L_j \rangle = 0$ unless $|k''\rangle \in S_L$, the sums over k and k'' are restricted to elements in S_L , and we rewrite the expression

$$F = \sum_{\mu} \left| \left(\sum_{\{j\}=1}^{N_L} \sum_{k'=1}^N \langle L_j | L_{j'} \rangle \langle L_{j'} | U_{ideal}^\dagger | k' \rangle \langle k' | A_\mu | L_{j''} \rangle \langle L_{j''} | L_j \rangle \right) / N_L \right|^2 \quad (\text{A.18})$$

Finally, because the ideal unitary U_{ideal} does not create leakage of states from S_L to S_R , the elements of $\langle L_{j'} | U_R | k' \rangle$ will be zero unless $|k'\rangle \in S_L$. Now

$$F = \sum_{\mu} \left| \left(\sum_{\{j\}=1}^{N_L} \langle L_j | L_{j'} \rangle \langle L_{j'} | U_{ideal}^\dagger | L_{j''} \rangle \langle L_{j''} | A_\mu | L_{j''} \rangle \langle L_{j''} | L_j \rangle \right) / N_L \right|^2 \quad (\text{A.19})$$

and by (A.11), this is equal to

$$F = \sum_{\mu} \left| \left(\sum_{j=1}^{N_L} \langle L_j | U_{ideal}^{L\dagger} A_\mu^L | L_j \rangle \right) / N_L \right|^2 \quad (\text{A.20})$$

which is equivalent to (A.14).

In our numerical optimization scheme in Chapter Five, we optimize over an incoherent process and a dispersion of Hamiltonians, where the dynamics for each member of the ensemble are unitary, and the operators in the sum of equation (A.13) may be expressed $A_\mu = \sqrt{p_\mu} U_\mu$, where $\sum_\alpha p_\alpha = 1$. In this case, our fidelity is given by

$$F = \sum_\alpha p_\alpha \left| \text{trace} \left(U_{ideal}^{L\dagger} U_\alpha^L \right) / N_L \right|^2 \quad (\text{A.21})$$

Bibliography

- [1] D. S. Abrams and S. Lloyd. Simulation of many-body fermi systems on a universal quantum computer. *Physical Review Letters*, 79(13):2586–2589, Sep 1997.
- [2] D. S. Abrams and S. Lloyd. Quantum algorithm providing exponential speed increase for finding eigenvalues and eigenvectors. *Physical Review Letters*, 83(24):5162–5165, Dec 1999.
- [3] D. Bacon, J. Kempe, D. A. Lidar, and K. B. Whaley. Universal fault-tolerant quantum computation on decoherence-free subspaces. *Physical Review Letters*, 85(8):1758–1761, Aug 2000.
- [4] J. Baugh, O. Moussa, C. A. Ryan, R. Laflamme, C. Ramanathan, T. F. Havel, and D. G. Cory. Solid-state nmr three-qubit homonuclear system for quantum-information processing: Control and characterization. *Physical Review A*, 73(2):022305, 2006.
- [5] J. Baugh, O. Moussa, C. A. Ryan, A. Nayak, and R. Laflamme. Experimental implementation of heat-bath algorithmic cooling using solid-state nuclear magnetic resonance. *Nature*, 438:470–473, 2005.
- [6] G. Benenti, G. Casati, and S. Montangero. Quantum computing and information extraction for dynamical quantum systems. *Quantum Information Processing*, 3:273–293, 2004.
- [7] G. Benenti, G. Casati, S. Montangero, and D. L. Shepelyansky. Efficient quantum computing of complex dynamics. *Physical Review Letters*, 87(22):227901, 2001.
- [8] G. Benenti, G. Casati, S. Montangero, and D. L. Shepelyansky. Dynamical localization simulated on a few-qubit quantum computer. *Physical Review A*, 67(5):052312, 2003.

- [9] N. Boulant, K. Edmonds, J. Yang, M. A. Pravia, and D. G. Cory. Experimental demonstration of an entanglement swapping operation and improved control in nmr quantum-information processing. *Physical Review A*, 68(3):032305, Sep 2003.
- [10] N. Boulant, J. Emerson, T. F. Havel, D. G. Cory, and S. Furuta. Incoherent noise and quantum information processing. *Journal of Chemical Physics*, 121(7):2955–2961, 2004.
- [11] N. Boulant, L. Viola, E. M. Fortunato, and D. G. Cory. Experimental implementation of a concatenated quantum error-correcting code. *Physical Review Letters*, 94(13):130501, Apr 2005.
- [12] P. Cappellaro, J. S. Hodges, T. F. Havel, and D. G. Cory. Principles of control for decoherence-free subsystems. *Journal of Chemical Physics*, 125(4):044514, 2006.
- [13] P. Cappellaro, J. S. Hodges, T. F. Havel, and D. G. Cory. Subsystem pseudopure states. *Physical Review A*, 75(4):042321, 2007.
- [14] Paola Cappellaro. *Quantum Information Processing in Multi-Spin Systems*. PhD dissertation, Massachusetts Institute of Technology, Department of Nuclear Science and Engineering, 2006.
- [15] H. Y. Carr and E. M. Purcell. Effects of diffusion on free precession in nuclear magnetic resonance experiments. *Physical Review*, 94(3):630–638, May 1954.
- [16] G. Casati, B. V. Chirikov, F. M. Izraelev, and J. Ford. Stochastic behavior in classical and quantum hamiltonian systems. *Lecture Notes in Physics*, 93:334, 1979.
- [17] Z. Chen, J. Yezpez, and D. G. Cory. Simulation of the burgers equation by nmr quantum-information processing. *Physical Review A*, 74(4):042321, Oct 2006.
- [18] H. Cho, P. Cappellaro, D. G. Cory, and C. Ramanathan. Decay of highly correlated spin states in a dipolar-coupled solid: Nmr study of caf_2 . *Physical Review B*, 74(22):224434, Dec 2006.
- [19] H. Cho, T. D. Ladd, J. Baugh, D. G. Cory, and C. Ramanathan. Multispin dynamics of the solid-state nmr free induction decay. *Physical Review B*, 72(5):054427, Aug 2005.

- [20] D. G. Cory, A. F. Fahmy, and T. F. Havel. Ensemble quantum computing by nmr spectroscopy. *Proceedings of the National Academy of Sciences of the United States of America*, 94:1634, 1997.
- [21] D. G. Cory, R. Laflamme, E. Knill, L. Viola, T. Havel, N. Boulant, G. Boutis, E. Fortunato, S. Lloyd, R. Martinez, C. Negrevergne, M. Pravia, Y. Sharf, G. Teklemariam, Y.S. Weinstein, and W.H. Zureck. NMR based quantum information processing: Achievements and prospects. *Fortschritte der Physik-progress of physics*, 48:875, 2000.
- [22] D. G. Cory, J. B. Miller, and A. N. Garroway. Time-suspension multiple-pulse sequences: applications to solid-state imaging. *Journal of Magnetic Resonance*, 90:205–213, 1990.
- [23] D. G. Cory, M. D. Price, W. Maas, E. Knill, R. Laflamme, W. H. Zurek, T. F. Havel, and S. S. Somaroo. Experimental quantum error correction. *Physical Review Letters*, 81(10):2152–2155, Sep 1998.
- [24] H. K. Cummins, G. Llewellyn, and J. A. Jones. Tackling systematic errors in quantum logic gates with composite rotations. *Physical Review A*, 67(4):042308, Apr 2003.
- [25] M. Dahleh, A. P. Peirce, and H. Rabitz. Optimal control of uncertain quantum systems. *Physical Review A*, 42(3):1065–1079, Aug 1990.
- [26] R. Das, R. Bhattacharyya, and A. Kumar. Quantum information processing by nmr using a 5-qubit system formed by dipolar coupled spins in an oriented molecule. *Journal of Magnetic Resonance*, 170(2):310–321, October 2004.
- [27] R. Das and A. Kumar. Use of quadrupolar nuclei for quantum-information processing by nuclear magnetic resonance: Implementation of a quantum algorithm. *Physical Review A*, 68(3):032304, Sep 2003.
- [28] R. Das and A. Kumar. Experimental implementation of a quantum algorithm in a multiqubit nmr system formed by an oriented $7/2$ spin. *Applied Physics Letters*, 89:024107, 2006.
- [29] P. Diehl and C. Khetrapal. *NMR Basic Principles and Progress, Vol. 1*. Springer-Verlag, Berlin, 1969.

- [30] D. P. DiVincenzo. The physical implementation of quantum computation. *Fortschritte der physik-progress of physics*, 48:771–783, 2000.
- [31] D. P. DiVincenzo, D. Bacon, J. Kempe, G. Burkard, and K. B. Whaley. Universal quantum computation with the exchange interaction. *Nature*, 408:339–342, 2000.
- [32] L.-M. Duan and G.-C. Guo. Preserving coherence in quantum computation by pairing quantum bits. *Physical Review Letters*, 79(10):1953–1956, Sep 1997.
- [33] J. Emerson, Y. S. Weinstein, S. Lloyd, and D. G. Cory. Fidelity decay as an efficient indicator of quantum chaos. *Physical Review Letters*, 89(28):284102, Dec 2002.
- [34] J. W. Emsley and J. C. Lindon. *NMR Spectroscopy Using Liquid Crystal Solvents*. Pergamon, Oxford, 1975.
- [35] R. R. Ernst, G. Bodenhausen, and A. Wokaun. *Principles of Nuclear Magnetic Resonance in One and Two Dimensions*. Clarendon Press, Oxford, 1987.
- [36] R. P. Feynman. Simulating physics with computers. *International Journal of Theoretical Physics*, 21(6-7):467–488, 1981/82.
- [37] E. M. Fortunato, M. A. Pravia, N. Boulant, G. Teklemariam, T. F. Havel, and D. G. Cory. Design of strongly modulating pulses to implement precise effective hamiltonians for quantum information processing. *Journal of Chemical Physics*, 116(17):7599–7606, 2002.
- [38] E. M. Fortunato, L. Viola, M. A. Pravia, E. Knill, R. Laflamme, T. F. Havel, and D. G. Cory. Exploring noiseless subsystems via nuclear magnetic resonance. *Physical Review A*, 67(6):062303, Jun 2003.
- [39] B. Georgeot and D. L. Shepelyansky. Exponential gain in quantum computing of quantum chaos and localization. *Physical Review Letters*, 86(13):2890–2893, Mar 2001.
- [40] B. Georgeot and D. L. Shepelyansky. Stable quantum computation of unstable classical chaos. *Physical Review Letters*, 86(23):5393–5396, Jun 2001.
- [41] N. A. Gershenfeld and I. L. Chuang. Bulk spin-resonance quantum computation. *Science*, 275(5298):350–356, 1997.

- [42] L. K. Grover. Quantum mechanics helps in searching for a needle in a haystack. *Physical Review Letters*, 79(2):325–328, Jul 1997.
- [43] U. Haeberlen. *High Resolution NMR in Solids: Selective Averaging*. Academic Press Inc., 1976.
- [44] U. Haeberlen and J. S. Waugh. Coherent averaging effects in magnetic resonance. *Physical Review*, 175(2):453–467, Nov 1968.
- [45] H. Haffner, F. Schmidt-Kaler, W. Hansel, C. F. Roos, T. Kober, M. Chwalla, M. Riebe, J. Benhelm, U. D. Rapol, C. Becher, and R. Blatt. Robust entanglement. *Applied Physics B: Lasers and Optics*, 81:151, 2005.
- [46] E. L. Hahn. Spin echoes. *Physical Review*, 80(4):580–594, 1950.
- [47] T. F. Havel. Robust procedures for converting among lindblad, kraus and matrix representations of quantum dynamical semigroups. *Journal of Mathematical Physics*, 44:534, 2003.
- [48] M. K. Henry, J. Emerson, R. Martinez, and D. G. Cory. Localization in the quantum sawtooth map emulated on a quantum-information processor. *Physical Review A*, 74(6):062317, 2006.
- [49] J. S. Hodges, P. Cappellaro, T. F. Havel, R. Martinez, and D. G. Cory. Experimental implementation of a logical bell state encoding. *Physical Review A*, 75(4):042320, 2007.
- [50] L. M. K. Vandersypen I. L. Chuang, X Zhou, D. W. Leung, and S. Lloyd. Experimental realization of a quantum algorithm. *Nature*, 393:143–146, 1998.
- [51] Ph. Jacquod, P.G. Silvestrov, and C.W.J. Beenakker. Golden rule decay versus lyapunov decay of the quantum loschmidt echo. *Physical Review E*, 64(5):055203, Oct 2001.
- [52] B. E. Kane. A silicon-based nuclear spin quantum computer. *Nature*, 393:133–137, 1998.
- [53] H. Kessemeier and W.-K. Rhim. Nmr line narrowing by means of rotary spin echoes. *Physical Review B*, 5(3):761–768, Feb 1972.

- [54] N. Khaneja, T. Reiss, C. Kehlet, T. Schulte-Herbruggen, and S. J. Glaser. Optimal control of coupled spin dynamics: design of nmr pulse sequences by gradient ascent algorithms. *Journal of Magnetic Resonance*, 172(2):296–305, 2005.
- [55] A. K. Khitrin, V. L. Ermakov, and B. M. Fung. Information storage using a cluster of dipolar-coupled spins. *Chemical Physics Letters*, 360:161–166, 2002.
- [56] A. K. Khitrin and B. M. Fung. Nuclear magnetic resonance quantum logic gates using quadrupolar nuclei. *Journal of Chemical Physics*, 112:6963, 2000.
- [57] D. Kielpinski, V. Meyer, M. A. Rowe, C. A. Sackett, W. M. Itano, C. Monroe, and D. J. Wineland. A decoherence-free quantum memory using trapped ions. *Science*, 291:1013–1015, 2001.
- [58] E. Knill, R. Laflamme, and L. Viola. Theory of quantum error correction for general noise. *Physical Review Letters*, 84(11):2525–2528, Mar 2000.
- [59] E. Knill, R. Laflamme, and W. H. Zurek. Resilient quantum computation. *Science*, 279:342–345, 1998.
- [60] K. Kraus. *States, Effects, and Operations*. Springer, Berlin, FRG, 1983.
- [61] P. G. Kwiat, A. J. Berglund, J. B. Altepeter, and A. G. White. Experimental verification of decoherence-free subspaces. *Science*, 290:498–501, 2000.
- [62] T. D. Ladd, J. R. Goldman, F. Yamaguchi, Y. Yamamoto, E. Abe, and K. M. Itoh. All-silicon quantum computer. *Physical Review Letters*, 89(1):017901, Jun 2002.
- [63] C. Langer, R. Ozeri, J. D. Jost, J. Chiaverini, B. DeMarco, A. Ben-Kish, R. B. Blakestad, J. Britton, D. B. Hume, W. M. Itano, D. Leibfried, R. Reichle, T. Rosenband, T. Schaetz, P. O. Schmidt, and D. J. Wineland. Long-lived qubit memory using atomic ions. *Physical Review Letters*, 95(6):060502, 2005.
- [64] J. S. Lee and A. K. Khitrin. Resurrection of schrodinger’s cat. *New Journal of Physics*, 8:144, 2006.
- [65] J. W. Lee and D. L. Shepelyansky. Quantum chaos algorithms and dissipative decoherence with quantum trajectories. *Physical Review E*, 71(5):056202, 2005.

- [66] B. Levi and B. Georgeot. Quantum computation of a complex system: The kicked harper model. *Physical Review E*, 70(5):056218, 2004.
- [67] B. Levi, B. Georgeot, and D. L. Shepelyansky. Quantum computing of quantum chaos in the kicked rotator model. *Physical Review E*, 67(4):046220, 2003.
- [68] M. Levitt. Composite pulses. *Progress in Nuclear Magnetic Resonance Spectroscopy*, 18:61, 1986.
- [69] D. A. Lidar and O. Biham. Simulating ising spin glasses on a quantum computer. *Physical Review Letters*, 56(3):3661–3681, Sep 1997.
- [70] D. A. Lidar, I. L. Chuang, and K. B. Whaley. Decoherence-free subspaces for quantum computation. *Physical Review Letters*, 81(12):2594–2597, Sep 1998.
- [71] S. Lloyd. Universal quantum simulators. *Science*, 273(5278):1073–1078, 1996.
- [72] T. S. Mahesh, N. Sinha, K. V. Ramanathan, and A. Kumar. Ensemble quantum-information processing by nmr: implementation of gates and the creation of pseudopure states using dipolar coupled spins as qubits. *Physical Review A*, 65(2):022312, Jan 2002.
- [73] T. S. Mahesh and D. Suter. Quantum-information processing using strongly dipolar coupled nuclear spins. *Physical Review A*, 74(6):062312, 2006.
- [74] P. Mansfield. Symmetrized pulse sequences in high resolution nmr in solids. *Journal of Physics C: Solid State Physics*, 4(11):1444–1452, 1971.
- [75] P. Mansfield, M. J. Orchard, D. C. Stalker, and K. H. B. Richards. Symmetrized multipulse nuclear-magnetic-resonance experiments in solids: Measurement of the chemical-shift shielding tensor in some compounds. *Physical Review B*, 7(1):90, Jan 1973.
- [76] M. Marjanska, I. L. Chuang, and M. G. Kubinec. Demonstration of quantum logic gates in liquid crystal nuclear magnetic resonance. *Journal of Chemical Physics*, 112(11):5095–5099, 2000.
- [77] Michael Mehring. *Principle of High Resolution NMR in Solids*. Springer-Verlag, 1983.

- [78] S. Meiboom and D. Gill. Modified spin-echo method for measuring nuclear relaxation times. *Review of Scientific Instruments*, 29(8):688–691, 1958.
- [79] A. Mitra, A. Ghosh, R. Das, A. Patel, and A. Kumar. Experimental implementation of local adiabatic evolution algorithms by an nmr quantum information processor. *Journal of Magnetic Resonance*, 177:285–298, 2005.
- [80] M. Mohseni, J. S. Lundeen, K. J. Resch, and A. M. Steinberg. Experimental application of decoherence-free subspaces in an optical quantum-computing algorithm. *Physical Review Letters*, 91(18):187903, Oct 2003.
- [81] C. Negrevergne, T. S. Mahesh, C. A. Ryan, M. Ditty, F. Cyr-Racine, W. Power, N. Boulant, T. Havel, D. G. Cory, and R. Laflamme. Benchmarking quantum control methods on a 12-qubit system. *Physical Review Letters*, 96(17):170501, May 2006.
- [82] M. A. Nielsen and I. L. Chuang. *Quantum Computation and Quantum Information Processing*. Cambridge University Press, Cambridge, 2000.
- [83] Jason E. Ollerenshaw, Daniel A. Lidar, and Lewis E. Kay. Magnetic resonance realization of decoherence-free quantum computation. *Phys. Rev. Lett.*, 91(21):217904, Nov 2003.
- [84] E. Ott, T. M. Antonsen, and J. D. Hanson. Effect of noise on time-dependent quantum chaos. *Physical Review Letters*, 53(23):2187–2190, 1984.
- [85] A. P. Peirce, M. A. Dahleh, and H. Rabitz. Optimal control of quantum-mechanical systems: Existence, numerical approximation, and applications. *Physical Review A*, 37(12):4950–4964, Jun 1988.
- [86] A. Peres. Stability of quantum motion in chaotic and regular systems. *Physical Review A*, 30(4):1610–1615, Oct 1984.
- [87] J. G. Powles and P. Mansfield. Double-pulse nuclear-resonance transients in solids. *Physics Letters*, 2:58, 1962.
- [88] M. A. Pravia, N. Boulant, J. Emerson, A. Farid, E. M. Fortunato, T. F. Havel, R. Martinez, and D. G. Cory. Robust control of quantum information. *Journal of Chemical Physics*, 119(19):9993–10001, 2003.

- [89] C. Ramanathan, S. Sinha, J. Baugh, T. F. Havel, and D. G. Cory. Selective coherence transfers in homonuclear dipolar coupled spin systems. *Physical Review A*, 71(2):020303, Feb 2005.
- [90] W-K. Rhim, D. D. Elleman, and R. W. Vaughan. Analysis of multiple pulse nmr in solids. *Journal of Chemical Physics*, 59(7):3740–3749, 1973.
- [91] W.-K. Rhim and H. Kessemeier. Transverse-magnetization recovery in the rotating frame. *Physical Review B*, 3(11):3655–3661, Jun 1971.
- [92] W-K. Rhim, A. Pines, and J. S. Waugh. Time-reversal experiments in dipolar-coupled spin systems. *Physical Review B*, 3(3):684–696, Feb 1971.
- [93] R. Schack. Using a quantum computer to investigate quantum chaos. *Physical Review A*, 57(3):1634–1635, Mar 1998.
- [94] M. S. Shahriar, P. R. Hemmer, S. Lloyd, P. S. Bhatia, and A. E. Craig. Solid-state quantum computing using spectral holes. *Physical Review A*, 66(3):032301, Sep 2002.
- [95] P. W. Shor. Algorithms for quantum computation: Discrete logarithms and factoring. *Proceedings of the 35th Annual Symposium on Foundations of Computer Science*, pages 124 – 134, 1994.
- [96] P. W. Shor. Scheme for reducing decoherence in quantum computer memory. *Physical Review A*, 52(4):R2493–R2496, Oct 1995.
- [97] N. Sinha, T. S. Mahesh, K. V. Ramanathan, and A. Kumar. Toward quantum information processing by nuclear magnetic resonance: Pseudopure states and logical operations using selective pulses on an oriented spin 3/2 nucleus. *Journal of Chemical Physics*, 114(10):4415–4420, 2001.
- [98] S. Somaroo, C. H. Tseng, T. F. Havel, R. Laflamme, and D. G. Cory. Quantum simulations on a quantum computer. *Physical Review Letters*, 82(26):5381–5384, Jun 1999.
- [99] P. H. Song and D. L. Shepelyansky. Quantum computing of quantum chaos and imperfection effects. *Physical Review Letters*, 86(10):2162–2165, 2001.

- [100] A. M. Steane. Error correcting codes in quantum theory. *Physical Review Letters*, 77(5):793–797, Jul 1996.
- [101] D. Suter and K. Lim. Scalable architecture for spin-based quantum computers with a single type of gate. *Physical Review A*, 65(5):052309, Apr 2002.
- [102] R. T. Syvitski, N. Burlinson, E. E. Burnell, and J. Jeener. Simultaneous selective detection of multiple quantum spectra. *Journal of Magnetic Resonance*, 155:251–256, 2002.
- [103] R. T. Syvitski and E. E. Burnell. Multiple quantum and high-resolution nmr, molecular structure, and order parameters of partially oriented ortho and meta dimethyl-, dichloro-, and chloromethylbenzenes codissolved in nematic liquid crystals. *Journal of Magnetic Resonance*, 144:58–73, 2000.
- [104] G. Teklemariam, E. M. Fortunato, M. A. Pravia, T. F. Havel, and D. G. Cory. Nmr analog of the quantum disentanglement eraser. *Physical Review Letters*, 86(26):5845–5849, 2001.
- [105] G. Teklemariam, E. M. Fortunato, M. A. Pravia, Y. Sharf, T. F. Havel, D. G. Cory, A. Bhattaharyya, and J. Hou. Quantum erasers and probing classifications of entanglement via nuclear magnetic resonance. *Physical Review A*, 66(1):012309, Jul 2002.
- [106] L. Tian and S. Lloyd. Resonant cancellation of off-resonant effects in a multilevel qubit. *Physical Review A*, 62(5):050301, Oct 2000.
- [107] C. H. Tseng, S. Somaroo, Y. Sharf, E. Knill, R. Laflamme, T. F. Havel, and D. G. Cory. Quantum simulation of a three-body-interaction hamiltonian on an nmr quantum computer. *Physical Review A*, 61(1):012302, Dec 1999.
- [108] L.M.K. Vandersypen, M. Steffen, G. Breyta, C.S. Yannoni, M.H. Sherwood, and I.L. Chuang. Experimental realization of shor’s quantum factoring algorithm using nuclear magnetic resonance. *Nature*, 414:883–887, 2001.
- [109] L. Viola. Quantum control via encoded dynamical decoupling. *Physical Review A*, 66(1):012307, Jul 2002.

- [110] L. Viola, E. M. Fortunato, M. A. Pravia, E. Knill, R. Laflamme, and D. G. Cory. Experimental realization of noiseless subsystems for quantum information processing. *Science*, 293(5537):2059–2063, 2001.
- [111] L. Viola, E. Knill, and S. Lloyd. Dynamical decoupling of open quantum systems. *Physical Review Letters*, 82(12):2417–2421, Mar 1999.
- [112] L. Viola and S. Lloyd. Dynamical suppression of decoherence in two-state quantum systems. *Physical Review A*, 58(4):2733–2744, Oct 1998.
- [113] L. Viola, S. Lloyd, and E. Knill. Universal control of decoupled quantum systems. *Physical Review Letters*, 83(23):4888–4891, Dec 1999.
- [114] W. S. Warren. The usefulness of nmr quantum computing. *Science*, 277:1688–1690, 1997.
- [115] Y. S. Weinstein, T. F. Havel, J. Emerson, N. Boulant, M. Saraceno, S. Lloyd, and D. G. Cory. Quantum process tomography of the quantum fourier transform. *Journal of Chemical Physics*, 121(13):6117–6133, 2004.
- [116] Y. S. Weinstein, S. Lloyd, J. Emerson, and D. G. Cory. Experimental implementation of the quantum baker’s map. *Physical Review Letters*, 89(15):157902, Sep 2002.
- [117] Y. S. Weinstein, M. A. Pravia, E. M. Fortunato, S. Lloyd, and D. G. Cory. Implementation of the quantum fourier transform. *Physical Review Letters*, 86(9):1889–1891, 2001.
- [118] L.-A. Wu, M. S. Byrd, and D. A. Lidar. Efficient universal leakage elimination for physical and encoded qubits. *Physical Review Letters*, 89(12):127901, Aug 2002.
- [119] L.-A. Wu and D. A. Lidar. Power of anisotropic exchange interactions: Universality and efficient codes for quantum computing. *Physical Review A*, 65(4):042318, Apr 2002.
- [120] C. S. Yannoni, M. H. Sherwood, D. C. Miller, I. L. Chuang, L. M. K. Vandersypen, and M. G. Kubinec. Nuclear magnetic resonance quantum computing using liquid crystal solvents. *Applied Physics Letters*, 75(22):3563–3565, 1999.

- [121] P. Zanardi and S. Lloyd. Universal control of quantum subspaces and subsystems. *Physical Review A*, 69(2):022313, 2004.
- [122] P. Zanardi and M. Rasetti. Noiseless quantum codes. *Physical Review Letters*, 79(17):3306–3309, Oct 1997.